



HAL
open science

PMU based situation awareness for smart distribution grids

Rodrigo José Albuquerque Frazao

► **To cite this version:**

Rodrigo José Albuquerque Frazao. PMU based situation awareness for smart distribution grids. Electric power. Université Grenoble Alpes, 2015. English. NNT : 2015GREAT061 . tel-01224221

HAL Id: tel-01224221

<https://theses.hal.science/tel-01224221>

Submitted on 4 Nov 2015

HAL is a multi-disciplinary open access archive for the deposit and dissemination of scientific research documents, whether they are published or not. The documents may come from teaching and research institutions in France or abroad, or from public or private research centers.

L'archive ouverte pluridisciplinaire **HAL**, est destinée au dépôt et à la diffusion de documents scientifiques de niveau recherche, publiés ou non, émanant des établissements d'enseignement et de recherche français ou étrangers, des laboratoires publics ou privés.

THÈSE

Pour obtenir le grade de

DOCTEUR DE L'UNIVERSITÉ GRENOBLE ALPES

Spécialité : **Génie Électrique**

Arrêté ministériel : 7 août 2006

Présentée par

Rodrigo José ALBUQUERQUE FRAZÃO

Thèse dirigée par **Prof. Nouredine HADJSAÏD**
et codirigée par **Dr. Raphaël CAIRE**

préparée au sein du **Laboratoire de Génie Électrique de Grenoble (G2Elab)**
dans l'**École Doctorale Électronique, Électrotechniques, Automatique et Traitement du Signal - EEATS**

PMU based situation awareness for smart distribution grids

Thèse soutenue publiquement le **14 October 2015**,
devant le jury composé de :

Prof. Jean-Pascal Cambronne

Toulouse University, France, Présidente

Prof. Christian Rehtanz

Dortmund University, Germany, Rapporteur

Prof. Lars Nordström

Royal Institute of Technology (KTH), Sweden, Rapporteur

Pierre Mallet

Director of Innovation and Technical strategy at ERDF, France, Examineur

Prof. Nouredine HadjSaïd

Grenoble Alpes University, France, Directeur de thèse

Dr. Raphaël Caire

Grenoble Alpes University, France, Co-Directeur de thèse



To my lovely wife and to my superhero brother, this thesis is affectionately dedicated.

CONTENTS

	3
TABLE OF CONTENTS	i
ACKNOWLEDGMENT	vii
LIST OF SYMBOLS	ix
GENERAL INTRODUCTION	1
I FUNDAMENTALS OF SYNCHRONIZED PHASOR MEASUREMENTS ESTIMATION: STATE OF THE ART	5
I.1 INTRODUCTION	6
I.2 PHASOR REPRESENTATION OF SINUSOIDAL SIGNALS	7
I.3 FOURIER SERIES APPROACH AND PHASOR REPRESENTATION	9
I.4 MAJOR FOURIER TRANSFORM (FT) PROPERTIES FOR PHASOR ESTIMATION	15
I.5 SAMPLED DATA, ALIASING EFFECT, AND LEAKAGE PHENOMENON BACKGROUND	21
I.6 DISCRETE FOURIER TRANSFORM (DFT) FOR ESTIMATING FUNDAMENTAL AND HARMONIC PHASORS	25
I.7 IMPROVING PHASOR ESTIMATION USING FAST FOURIER TRANSFORM (FFT)	28
I.7.i Mathematical formulation	29
I.7.ii Radix-2 Decimation in Time (DIT) FFT	33
I.8 RECURSIVE UPDATE FOR FUNDAMENTAL PHASOR USING DFT AND RADIX-2 FFT	35
I.8.a Nominal frequency signals	36
I.8.b Off-nominal frequency signals (leakage phenomenon)	37
I.9 LEAKAGE PHENOMENON REDUCTION TECHNIQUES REVIEW	39
I.10 POWER SYSTEM FREQUENCY ESTIMATION METHODS REVIEW	41
I.11 THE PHASOR MEASUREMENT UNIT (PMU)	42
I.11.a Definition of synchronized phasor measurements according to IEEE Std. C37.118	44
I.11.b The Global Positioning System (GPS) as time synchronization source for synchrophasor estimation	46
I.11.c Synchronized phasor measurements estimation	48

I.11.d	Performance metrics for PMUs	51
I.12	PHASOR ESTIMATION ALGORITHMS REVIEW FOR POWER DISTRIBUTION SYSTEMS	52
I.13	CURRENT CONJUNCTURE OF TIME-SYNCHRONIZED MEASUREMENTS IN POWER DISTRIBUTION SYSTEMS	54
I.14	CONCLUSION	57
II	MAIN CHALLENGES OF THE SYNCHRONIZED PHASOR MEASUREMENTS DEPLOYMENT IN ACTIVE POWER DISTRIBUTION ENVIRONMENT	59
II.1	INTRODUCTION	60
II.2	IEEE STD.C37.118.1-2011 VERSUS ACTIVE DISTRIBUTION SYSTEM REQUIREMENTS: THE PROBLEMATIC OF THE TVE METRIC	63
II.2.a	Primary distribution system topology overview	66
II.2.b	Voltage angle difference between adjacent primary busbars <i>versus</i> TVE metric	69
II.3	FREQUENCY DEVIATION	75
II.4	HARMONIC CONTENT ISSUES	76
II.5	MEASUREMENT POINTS	77
II.6	OVERVIEW OF THE DEPLOYMENT COST-BENEFIT RATIO	78
II.7	CONCLUSION	78
III	PROPOSITIONS OF FREQUENCY-ADAPTIVE ALGORITHMS TO ESTIMATE SYNCHRONIZED PHASOR MEASUREMENTS IN ACTIVE POWER DISTRIBUTION SYSTEMS	81
III.1	INTRODUCTION	82
III.2	ANTI-ALIASING LOWPASS FILTER DESIGN	85
III.3	FREQUENCY-ADAPTIVE MODIFIED PARK'S TRANSFORMATION-BASED ALGORITHM	88
III.3.a	Park's transformation mathematical basis	89
III.3.b	Park's transformation for estimating fundamental positive-sequence phasor	91
III.3.c	Filtering harmonic and interharmonic components before estimating fundamental positive-sequence phasor	94
III.3.c.i	Phasor estimates of balanced input signals at nominal frequency	95
III.3.c.ii	Phasor estimates of unbalanced input signals at nominal frequency	96
III.3.c.iii	Phasor estimates of balanced input signals at off-nominal frequency	99
III.3.c.iv	Phasor estimates of unbalanced input signals at off-nominal frequency	100
III.3.d	Frequency estimation and ROCOF based on Park's transformation	103
III.3.e	Overcoming undefined frequency estimates	105
III.3.f	Frequency estimation error analysis and calibration factor	108
III.4	AN ENHANCED SYNERGISTIC FREQUENCY-ADAPTIVE ALGORITHM (4F-ALGORITHM)	112

III.4.a	Characteristics of the FIR bandpass filter bank	113
III.4.a.i	Classical linear trigonometric interpolation technique and its extended version	114
III.4.b	Half-cycle Radix-2 DIT FFT for computing selective phasor measurements	116
III.5	FREQUENCY-ADAPTIVE ALGORITHM BASED ON WEIGHTED LEAST SQUARES (WLS) APPROACH (AWLS-ALGORITHM)	118
III.5.a	Weighted Least Squares estimation overview	119
III.5.b	AWLS-algorithm for computing phasor measurements	121
III.6	IEEE STD. C37.118.1-2011 REQUIREMENTS AND COMPLIANCE VERI- FICATION FOR MONITORING APPLICATIONS	124
III.6.a	Performance of the algorithms under static and/or dynamic conditions . .	128
III.6.a.i	<i>Test cases concerning the modified Park's transformation- based algorithm</i>	129
III.6.a.ii	<i>Test cases concerning the 4F-algorithm</i>	134
III.6.a.iii	<i>Test cases concerning the AWLS-algorithm</i>	136
III.7	CONCLUSION	138
IV	APPLICATIONS OF SYNCHRONIZED PHASOR MEASUREMENTS TO IN- CREASE THE SITUATIONAL AWARENESS IN ACTIVE POWER DISTRIBU- TION SYSTEMS	141
IV.1	INTRODUCTION	142
IV.2	CONTRIBUTIONS FOR REAL-TIME ESTIMATION OF THÉVENIN'S EQUIV- ALENT USING ACCURATE PMU DATA	144
IV.2.a	Classical method for evaluating the Thévenin's equivalent using PMU data	146
IV.2.b	Evaluation of the TE circuit based on accurate PMU data for steady- or <i>quasi</i> -steady state conditions	151
IV.2.b.i	Optimal solution of the Thévenin's impedance based on Recursive Weighted Least Squares (RLS) estimation	152
IV.2.c	Main objective: Online tracking of the grid model based on the Thévenin's equivalent and enhanced operating point assessment on generation capa- bility curves	154
IV.3	PRACTICAL ONLINE EXTERNAL EQUIVALENTS IN RADIAL ACTIVE DIS- TRIBUTION GRIDS USING PMU DATA	160
IV.3.a	Ward linear equivalent overview	162
IV.3.b	Practical on-line external equivalent based on PMU data	163
IV.3.c	Main objective: Reduction of the grid size and online evaluation of the external network	166
IV.4	ASSESSMENT OF THREE-PHASE VOLTAGE DROP IN PRIMARY RADIAL DISTRIBUTION GRIDS USING PMU DATA	169
IV.4.a	Overall voltage drop of a radial feeder calculated from PMU data taken at the feeder ends	171
IV.4.b	Main objective: Online three-phase voltage drop assessment	173
IV.5	ASSESSMENT OF HARMONIC ISSUES USING PMU DATA	175
IV.5.a	Main objective: Enhanced detection of both harmonic power flow direc- tion and main source of harmonic pollution under frequency deviation . .	178

IV.6 CONCLUSION	184
CONCLUSION	187
BIBLIOGRAPHY	198
PUBLICATIONS	199
Part Appendixes	1
A DISCRETE FOURIER TRANSFORM AND PHASOR REPRESENTATION	1
B PHASOR ESTIMATION ERROR DUE TO LEAKAGE PHENOMENON	3
C CLASSICAL METHOD FOR ESTIMATING FUNDAMENTAL POSITIVE-SEQUENCE PHASOR	7
D PARK'S TRANSFORMATION-BASED FUNDAMENTAL POSITIVE-SEQUENCE PHASOR	9
E FEEDER'S DATA OF THE DISTRIBUTION GRID MODEL	13
Part Abstracts	15

Acknowledgment

Above all, utmost appreciation to God the Father Almighty for the divine providence during the three years of my academic endeavor. Thanks God, I wanna be your glow!

I would like to acknowledge and thank Prof. Nouredine HadjSaïd, the thesis advisor, for giving me the extraordinary privilege to join the G2Elab team. His academic guidance, valuable advice, suggestions, and support were paramount in making this thesis a reality.

I would also like to express my sincere gratitude and thanks to Dr. Raphaël Caire, the thesis co-advisor, for his unwavering guidance, support, and cooperation on different aspects of my research. Thank you so much for sharing several expertise with value-added insights that indeed, contributed imperatively and directly to the development of this thesis.

I specially want to thank the honorable Jury members for accepting the invitation, for their invaluable corrections, comments, and advice to further increase the quality of this work.

A very special thank you to my family (José Frazão, Venância Albuquerque, Roberta Maria and Rômulo José) whose support and encouragement have been overwhelming. Without their motivational force, this thesis could never have been completed.

I would like to seize this opportunity to extend my deep gratitude to my wife Dyenny Albuquerque. Her encouragement, support, tolerance, loyalty, affection and unwavering love are incontestably the necessary conditions so that I can perform my activities efficiently. I am very grateful to you. You make a difference!

Thank you for all, dear Brazilian and French friends, for the support and for the bittersweet moments that we have spent together. In particular, I gratefully acknowledge Prof. Maria da Guia da Silva for believing in me and my young researcher skills. My sincere thanks and appreciation are also extended to my friend Tiago Staudt for his help and support during troubled waters of my stay in Grenoble. You are a phenomenal guy!

Finally, I would like to thank the CAPES Foundation of Brazil and SO-GRIG project for their valuable financial and technical support.

List of Symbols

Acronyms

ADC	Analog-to-Digital Converter
CF	Calibration Factor
DER	Distributed Energy Resource
DFT	Discrete Fourier Transform
DIT	Decimation-in-Time
DPLL	Digital Phase-Locked Loop
DMS	Distribution Management System
DSP	Digital Signal Processor
EDSO	European Distribution System Operator
EN	External Network
ENTSO-E	European Network of Transmission System Operators for Electricity
FE	Frequency Error
FIR	Finite Impulse Response
FFT	Fast Fourier Transform
FPGA	Field-Programmable Gate Array
FT	Fourier Transform
FS	Fourier Series
GPS	Global Positioning System
IED	Intelligent Electronic Device
IN	Internal Network
IRIG-B	Inter-Range Instrumentation Group - format B
MAF	Moving Average Filter
PCC	Point of Common Coupling
PDC	Phasor Data Concentrator
PPS	Pulse per Second
PMU	Phasor Measurement Unit
ROCOF	Rate of Change of Frequency
RLS	Recursive Weighted Least Squares
SCDR	Symmetrical Component Distance Relay
SNR	Signal-to-Noise Ratio
TE	Thévenin's equivalent
TVE	Total Vector Error

UTC	Coordinated Universal Time
WAMS	Wide-Area Management System
WLS	Weighted Least Squares

General introduction

Voltage, current, power, and energy measurements have been in use since the dawn of power system infrastructure. At the turn of the 20th century, the analog measurement devices were in the midst of a fierce battle (“War of the Currents”) ensued between the advocates of the direct current (DC), headed by J. P. Morgan and Thomas Edison, and the alternating current (AC), headed by George Westinghouse and Nicolai Tesla. Due to several technical and economic aspects, the AC technology won the DC for generation, delivery, and utilization of the electricity.

In this context, the mathematical theory of the power system via AC-based model needed to be formulated to simplify, without loss of generality, the analyzes and calculations. This task was successfully performed by Charles Proteus Steinmetz with the development of a symbolic method used to represent alternating current [1]. This event is the birth of the phasor representation in electric power systems.

This fact has given rise to the need for calculating ‘off-line’ phasors provided by analog devices. The operating principle of these devices is based on the electromagnetic interaction able to produce mechanical movement’s approaches over a properly graduated scale. Thus, single and three-phase voltage and current magnitude measurements could be obtained with good precision, however the phase angle measurements were conveniently obtained by clever methods using wattmeters to measure both active and reactive power consumption (two and/or three-wattmeter methods).

The phase angle of the load was then defined as the inverse tangent of the ratio between the reactive and active power, being numerically identical to the angular aperture between voltage and current angles. Generally, the *a*-phase has been applied as angular reference based on a counterclockwise sense of rotation (*abc*-sequence). In this way, complex quantities related to voltage, current and apparent power have been calculated. Nowadays, this analysis has yet been employed for educational purposes [2].

A special regard to frequency measurements must also be directed. The speed of rotation of synchronous generator rotors is directly related to the frequency of the voltages they generate, thus mechanical feedback controls were performed to ensure a relatively narrow range of speeds to produce the nominal power frequency (50-Hz or 60-Hz). The earliest power system frequency measurements were performed by mechanical and/or electrical resonators tuned to a range of frequencies around the nominal, in which typical resolution of the order of 0.25 Hz could be obtained [3].

In the course of time, the measuring technology evolved enabling the quasi-complete

shift from analog to digital domain, however these nostalgic devices are still present in several parts of the electric networks (substations, power system control centers, homes, buildings, and so on), due to their robustness and efficiency. Unfortunately, for online monitoring, control, and protection applications in active and smart power distribution systems, the analog measurement devices have a tendency to fall into disuse because they are not endowed with the required capabilities of communication and interoperability. Therefore, this makes room for the massive use of digital measurement devices. With the deployment of modern Distribution Management System (DMS), digital measurements will be utilized to enable and improve the situational awareness.

The definition of situational awareness in electric power systems can be understood as the perception of the elements in the network, the comprehension of their current states, and the projections of their future status to make decisions in a timely manner [4]. In the context of active power distribution systems - characterized by a high integration of distributed energy resources (DERs) - situational awareness might allow the implementation of emerging advancements in online monitoring, adaptive control schemes of distribution assets, and optimized automation to achieve a high operational efficiency, an enhanced security, an improved flexibility, and an increased reliability for these electric grids.

Actually, robust metering infrastructure based on classical digital measurements has been used to enable a comprehensive power distribution network management, however synchronized phasor measurements, also known as *synchrophasors*, are especially welcome to improve the overall framework capabilities (Chapter I provides the state of the art concerning synchronized phasor measurements). A synchrophasor is a phasor¹ digitally computed from data samples using an absolute and accurate time source as reference. In this way, since the absolute time source has sufficient accuracy to synchronize voltage and current measurements at geographically distant locations it is possible to extract valuable informations of the real grid operating status without full knowledge of its characteristics.

Due to this fact, applications of synchronized phasor measurements in wide-area management systems (WAMSs) have been achieved [5]. Angular separation, linear state estimation, islanding detection, oscillatory stability, and disturbance location identification are some of the several applications that have been proposed. Thus, we could be lead to believe that to bring the well-known benefits of the synchronized measurements toward electric distribution grids it is only required to place in a straightforward manner conventional PMUs into the electric distribution environment. Unfortunately, this is not as simple as it seems.

Electric power distribution systems and high-voltage power systems have different operational characteristics. Hence, PMUs or PMU-enabled IEDs (Intelligent Electronic Devices) dedicated to distribution systems should have different features from those devoted to the high-voltage systems. Active distribution grids with shorter line lengths produce smaller angular aperture between their adjacent busbars. In addition, high harmonic content and frequency deviation impose more challenges for estimating phasors. Generally, frequency deviation is related to high-voltage power systems, however, due to the interconnected nature of the overall power system, frequency deviation can be propagated toward the distribution grid. The integration of multiple high-rate DERs with poor control ca-

¹A phasor is a steady-state representation of physical quantities that vary over time [1].

pabilities can also impose local frequency drift. Advanced synchronized devices dedicated to smart monitoring framework must overcome these challenges in order to lead the measurement accuracy beyond the levels stipulated by current standard requirements [6]-[7] (Chapter II).

This overall problematic is treated and evaluated in the present thesis. Phasor estimation accuracy is directly related to the algorithm's performance used for processing the incoming data. Robustness against pernicious effects that can degrade the quality of the estimates is highly desired. Due to this fact, three frequency-adaptive algorithms are proposed aiming to boost the phasor estimation process in active distribution grids. Several simulations using spurious and distorted signals are performed for evaluating their performances under static and/or dynamic conditions (Chapter III).

Taking into account accurate phasor estimates provided by the proposed frequency-adaptive algorithms, four potential applications are presented seeking to increase situation awareness in distribution environment. Contributions are presented concerning online Thévenin's equivalent (TE) circuit seen by the Point of Common Coupling (*PCC*) between DERs and the grid side, online external equivalents and online three-phase voltage drop assessment in primary radial distribution grids, as well as assessment of harmonic issues for improving the classical P_H method (harmonic active power) to detect both the main source of harmonic pollution and true power flow direction under frequency deviation (Chapter IV).

The issue of synchronized phasor measurements in electric power distribution system is still underexplored and suspicions about its applicability are common, however this thesis aims to provide contributions for the advent of phasor measurements in electric distribution environment.

Chapter I

Fundamentals of synchronized phasor measurements estimation: state of the art

L'étude approfondie de la nature est la source la plus féconde des découvertes mathématiques.

Jean Baptiste Joseph Fourier

CONTENTS

I.1	INTRODUCTION	6
I.2	PHASOR REPRESENTATION OF SINUSOIDAL SIGNALS	7
I.3	FOURIER SERIES APPROACH AND PHASOR REPRESENTATION	9
I.4	MAJOR FOURIER TRANSFORM (FT) PROPERTIES FOR PHASOR ESTIMATION	15
I.5	SAMPLED DATA, ALIASING EFFECT, AND LEAKAGE PHENOMENON BACKGROUND	21
I.6	DISCRETE FOURIER TRANSFORM (DFT) FOR ESTIMATING FUNDAMENTAL AND HARMONIC PHASORS	25
I.7	IMPROVING PHASOR ESTIMATION USING FAST FOURIER TRANSFORM (FFT)	28
I.8	RECURSIVE UPDATE FOR FUNDAMENTAL PHASOR USING DFT AND RADIX-2 FFT	35
I.8.a	Nominal frequency signals	36
I.8.b	Off-nominal frequency signals (leakage phenomenon)	37
I.9	LEAKAGE PHENOMENON REDUCTION TECHNIQUES REVIEW	39
I.10	POWER SYSTEM FREQUENCY ESTIMATION METHODS REVIEW	41
I.11	THE PHASOR MEASUREMENT UNIT (PMU)	42
I.11.a	Definition of synchronized phasor measurements according to IEEE Std. C37.118	44
I.11.b	The Global Positioning System (GPS) as time synchronization source for synchrophasor estimation	46
I.11.c	Synchronized phasor measurements estimation	48
I.11.d	Performance metrics for PMUs	51
I.12	PHASOR ESTIMATION ALGORITHMS REVIEW FOR POWER DISTRIBUTION SYSTEMS	52
I.13	CURRENT CONJUNCTURE OF TIME-SYNCHRONIZED MEASUREMENTS IN POWER DISTRIBUTION SYSTEMS	54
I.14	CONCLUSION	57

Abstract

The current state of synchronized phasor measurements estimation is widely vast, rich, and diverse, however the powerful Fourier's methods are the cornerstone of this subject in such a manner that the data processing techniques used to estimate phasors are divided into two categories: Fourier-based and Non-Fourier-based. Considering this statement, in this chapter, the state of the art related to the phasor estimation in electric power system is presented. The main key points of Fourier series (FS) approach, Fourier transform (FT) properties, discrete Fourier transform (DFT) and fast Fourier transform (FFT) are reported in details to provide an intuitive mathematical basis for phasor representation in continuous and discrete-time domain. The main drawbacks concerning phasor estimation in electric power systems are also outlined and an extended review of methods applied to circumvent them are presented and discussed. In addition, the characteristics and features of the emblematic Phasor Measurement Unit (PMU) are described taking into account the overall informations provided by the IEEE standards for synchronized phasor measurements for power systems. The survey of some algorithms dedicated to estimate phasors in distribution networks, as well as, the current conjuncture of the major projects related to the deployment of time-synchronized measurements in the distribution environment are equally carried out. This chapter is the result of an extensive reading and research of outstanding academic works, however, it has been intentionally written in a different manner for increasing the comprehension of the key points which are of direct interest for phasor estimation. It is of paramount importance to emphasize that the state of the art presented in this chapter will serve as theoretical support for the propositions presented in this thesis concerning accurate synchronized phasor estimation, whose goal is to ability potential applications to increase situational awareness in active power distribution systems.

I.1 Introduction

Intriguing issues may arise regarding the synchronized phasor measurement estimation. What are the mathematical methods employed? How are they estimated? What is the time source used in the synchronization process? How to associate time information with the measurement? How to ensure that measurements are accurate? For these issues, and for others that may arise, this chapter deals with the state of the art of the synchronized phasor measurements.

Talk directly about phasor measurements without mentioning Jean Baptiste Joseph Fourier (the renowned *préfet de l'Isère*) could leave a considerable gap, because Fourier's methods are the cornerstone of this subject. To get an idea, the data processing techniques used to estimate phasors are divided into two categories: Fourier-based and Non-Fourier-based. Thus, the current chapter begins with the analysis of sinusoidal and non-sinusoidal wave forms by Fourier series approach using complex wave analysis. This analysis needs be performed to demonstrate, in an intuitive manner, that the phasor representation of a sinusoid is equal to its Fourier series in the exponential form, as well as it is possible to decompose the signal to determine what are its phasor harmonic components (I.3).

Rather than series, the Fourier Transform analysis will also be performed to recover the signal from the integral, thus providing the basis for convolution properties and sampling

operation (I.4). The problematic of the conversion from continuous-time to discrete-time domain is addressed, whose goal is to assess whether the information associated with the signal in the time-domain is correctly converted into the resulting finite sequence in the discrete domain after performing the sampling operation (I.5). If this condition is not fulfilled, it is necessary to evaluate how far the information is modified and which kind of errors the sampling operation introduces in the measuring process [8].

In order to obtain valuable data in the discrete-time domain, the discrete Fourier transform (DFT) and the fast Fourier transform (FFT) are explained. Generally, the DFT uses few samples inside an observation interval or “data window” to extract knowledge of each frequency component of the sampled signal (I.6). The FFT presents some advantages because it decomposes the DFT into smaller DFTs whose calculation requires less computational burden (I.7).

The theory of the Radix-2 decimation in time (DIT) FFT is then presented in (I.7.ii) due to its simplicity, elegance and accuracy to compute phasors. The phasor estimation process under synchronous and asynchronous sampling conditions will also be evaluated, in which the latter will produce the pernicious leakage phenomenon that affects the quality of the estimation (I.8). For overcoming this problem, classical techniques applied to reduce the leakage (I.9) and a review of frequency estimation methods (I.10) are shown and discussed.

A background knowledge of the emblematic Phasor Measurement Unit (PMU) is described and explained taking into account the overall informations provided by the IEEE standards for synchrophasor measurements for power systems. The classical definition of synchrophasor measurements, the use of the Global Positioning System (GPS) as synchronization source, the correct manner to estimate synchrophasor measurements related to the GPS-time-tag, and the specification of the following performance metrics: Total Vector Error (TVE), Frequency Error (FE), and Rate of Change of Frequency (ROCOF) error (RFE) will be outlined. The reported metrics are applied for static and/or dynamic power system conditions (I.11).

Additionally, a survey of some algorithms dedicated for estimating phasors in distribution networks (I.12), as well as, the current conjuncture of the major projects related to the deployment of time-synchronized measurements in the distribution environment (I.13) are equally carried out.

I.2 Phasor representation of sinusoidal signals

In most practical applications involving AC circuit analysis, it is necessary to deal with average quantities that provide valuable information about the circuit’s features during several cycles. To calculate these quantities, instantaneous values are integrated over time to express the desired average value. Clearly, this statement involves quantities related to voltage and current. In this way, the Root Mean Square (RMS) is a powerful statistical measure used to represent time-varying quantities, being also particularly employed for calculating active and reactive power.

The RMS value of a sinusoid is numerically equal to the ratio between the peak amplitude and $\sqrt{2}$, in other words, increasing the number of instantaneous values, the RMS tends closely to 70.71% of the maximum value. Therefore, it represents the magnitude of the time-varying quantity. In essence, the RMS value do not provide any explicit informa-

tion about frequency and phase angle, however the latter is essential to enable a timing of events over the course of some cycles.

For a detailed analysis of an AC circuit, it is useful to know the magnitude, frequency and phase angle of the time-varying quantities during a specific time interval. The mathematical tool used to accomplish this task is called *Phasor* [1]. Let us consider a pure sinusoidal quantity given by

$$y(t) = Y_m \cos(\omega t + \phi) \quad (\text{I.1})$$

where Y_m represents the maximum value or peak amplitude; $\omega = 2\pi f_o$ is the angular frequency of the signal in radians per second (f_o is the fundamental frequency); and ϕ is the phase angle in radians.

Keeping in mind the Euler's identity ($e^{jx} = \cos x + j \sin x$), one can observe that Eq. (I.1) can also be rewritten as

$$y(t) = \text{Re}\{Y_m e^{j(\omega t + \phi)}\} = \text{Re}\{e^{j2\pi f_o t}\} Y_m e^{j\phi} \quad (\text{I.2})$$

once the system frequency is known, the term $e^{j2\pi f_o t}$ can be neglected. Therefore, Eq. (I.2) may be represented by a complex number V given by

$$y(t) \longleftrightarrow V = Y_m e^{j\phi} = Y_m [\cos \phi + j \sin \phi]. \quad (\text{I.3})$$

Assuming that both voltage and current signals are given by Eq. (I.3), one can observe that this representation is at odds with the calculation of average power, therefore the RMS quantities must be taken into account for the correct phasor representation of sinusoidal signals, as illustrated by the complex number Y that follows

$$y(t) \longleftrightarrow Y = \left(\frac{Y_m}{\sqrt{2}}\right) e^{j\phi} = \left(\frac{Y_m}{\sqrt{2}}\right) [\cos \phi + j \sin \phi]. \quad (\text{I.4})$$

The phase angle of a phasor brings the information about the fraction of the sinusoid's period in which the time, or the angular displacement ωt , is advanced or delayed to an arbitrary reference. It is very important to correlate different alternating-waves between them, thus, the phasors represent an *equilibrium point* or the steady-state condition of the AC circuit, that is, one can assume that the phasors are time-invariant, as illustrated in Fig. I.1.

However, in practical cases, a time interval must be considered to perform the phasor calculation. This time interval is also known as "data window" or "observation interval", being fundamental in phasor estimation of practical waveforms. In essence, the phasor representation is related to a pure sinusoidal signal, but the existing signals in electric power systems may be distorted by harmonics. In this way, it is advised to extract the envisaged frequency component(s) of the signal to also be represented by phasor notation. These tasks have been properly performed by the classical Fourier's theory. Due to the fact, the main key points about phasor representation using the aforementioned theory is presented and discussed in greater detail in the later sections.

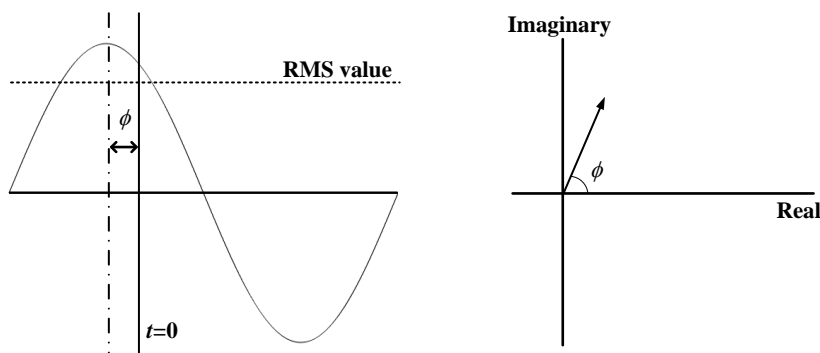


Figure I.1: Phasor representation of a sinusoid. The phase angle of a phasor depends upon the choice of the axis $t=0$ taking into account the peak amplitude of the sinusoid. (adapted of [3])

I.3 Fourier series approach and phasor representation

Even having as his main focus on the heat theory, in which his work entitled *Mémoire sur la Théorie Analytique de la Chaleur* is considered as the milestone on the way to describe mathematically how heat diffuses in a continuous medium, *Baron Fourier* also provided the mathematical basis to the generalization of the notion of function. He showed that the sines and cosines are the elementary periodic functions able to express all the others, that is, it is possible to express some interval of an arbitrary periodic function as an infinite trigonometric series of sines and cosines (functions can be truncated to the observation interval, however they may merely be extended periodically for wrapping the vanished portion outside of the interval) [9].

Objections were made by his contemporaries as Lagrange, Legendre and Laplace because they had already published important contributions related to the problem based on “convergent trigonometric series”. Fortunately, Fourier had a different vision of the things. He did not want to prove that his series converged, but that any periodic function $y: [-\pi, \pi] \rightarrow \mathbb{R}$, even being wildly discontinuous, could be written as a trigonometric series. Fourier asserted that even though sines and cosines are periodic, this does not impose a severe limitation to represent non-differentiable piecewise functions. This triumphant assumption changed the history of the analysis. Dirichlet’s test proved effectively that trigonometric and Fourier series are not necessarily equal because they could differ in respect to the convergence mode due to their coefficients [9].

The Fourier series circumvented the problem of Taylor series related to a very restrictive condition of functions infinitely differentiable inside the observation interval. In addition, the representation by sines and cosines give the capability to look behind the periodic function what are its prime elements, in which it is not possible with polynomials. Only a few constraints hinder the Fourier series applicability, the most emblematic are related to the infinite number of maximum and minimum values around any point inside the interval and a finite number of finite discontinuities. Excluding these restrictions any time-varying periodic function with a period T , $y: [-\frac{T}{2}, \frac{T}{2}] \rightarrow \mathbb{R}$, could be represented by the Fourier series given by

$$y(t) = A_0 + A_1 \cos(\omega t) + B_1 \sin(\omega t) + A_2 \cos(2\omega t) + B_2 \sin(2\omega t) + A_3 \cos(3\omega t) \quad (\text{I.5}) \\ + B_3 \sin(3\omega t) + \dots + A_k \cos(k\omega t) + B_k \sin(k\omega t)$$

being A_0 , A_1 , B_1 , and son on, the coefficients of the series; and $\omega=2\pi f_o$ represents the angular frequency ($f_o=\frac{1}{T}$ is the frequency in Hz).

Theoretically, an infinite number of components is required for a “perfect” representation of a periodic function. In practice, however, only some components are effectively used for a trustworthy approximation due to the small effect of the higher frequency components. It is remarkable that the Fourier series expresses a linear combination (superposition principle) of sinusoidal components with different frequencies, in which the results are appropriately combined to form the composite or final complex wave.

From this perspective, each component can be treated in accordance with the laws that govern the pure sinusoid calculation. Thereby, Fourier series is also known as *harmonic analysis*, being widely applied in digital measurement theory for electric power networks. Based on [10], an efficient manner for understanding the calculation of the Fourier series coefficients may be performed using the complex wave analysis. Assuming that the definite integral of $y(t)$ function from $-\frac{T}{2}$ to $\frac{T}{2}$ is numerically equal to the sum of the integrals of the harmonic components taking into account the same integration interval for each of them, we have

$$\int_{-\frac{T}{2}}^{\frac{T}{2}} y(t) dt = \int_{-\frac{T}{2}}^{\frac{T}{2}} A_0 dt + \int_{-\frac{T}{2}}^{\frac{T}{2}} A_1 \cos(\omega t) dt + \int_{-\frac{T}{2}}^{\frac{T}{2}} B_1 \sin(\omega t) dt + \int_{-\frac{T}{2}}^{\frac{T}{2}} A_2 \cos(2\omega t) dt \\ + \int_{-\frac{T}{2}}^{\frac{T}{2}} B_2 \sin(2\omega t) dt + \int_{-\frac{T}{2}}^{\frac{T}{2}} A_3 \cos(3\omega t) dt + \int_{-\frac{T}{2}}^{\frac{T}{2}} B_3 \sin(3\omega t) dt + \dots \\ + \int_{-\frac{T}{2}}^{\frac{T}{2}} A_k \cos(k\omega t) dt + \int_{-\frac{T}{2}}^{\frac{T}{2}} B_k \sin(k\omega t) dt. \quad (\text{I.6})$$

Using the classical definition of integral based on a geometric point of view related to the summation of areas (Riemann Sum), one can observe that the definite integral of each harmonic component will be equal to zero, because their resulting area over the period T will be null. In this way, the only component that is not null is A_0 , therefore Eq. (I.6) becomes

$$\int_{-\frac{T}{2}}^{\frac{T}{2}} y(t) dt = \int_{-\frac{T}{2}}^{\frac{T}{2}} A_0 dt \Rightarrow \int_{-\frac{T}{2}}^{\frac{T}{2}} y(t) dt = A_0 \left[\frac{T}{2} + \frac{T}{2} \right] \Rightarrow A_0 = \frac{1}{T} \int_{-\frac{T}{2}}^{\frac{T}{2}} y(t) dt. \quad (\text{I.7})$$

It is clear that the A_0 coefficient is the average or mean value of the periodic function. In other words, it represents the “area under the function” for a period T . Frequently, the terms DC component, DC bias, DC offset or zero frequency component have also been employed. It is important to mention that if a periodic function does not have A_0 component, the Fourier series may be evaluated using the concept of symmetry (odd or

even). For calculating the other coefficients, it is necessary to perform some mathematical manipulations in Eq. (I.5), such that the desired coefficient can be maintained while the others are discarded. For example, to find A_1 , Eq. (I.5) must be multiplied by $\cos(\omega t) dt$ and integrated from $-\frac{T}{2}$ to $\frac{T}{2}$, therefore

$$\begin{aligned} \int_{-\frac{T}{2}}^{\frac{T}{2}} y(t)\cos(\omega t) dt &= \int_{-\frac{T}{2}}^{\frac{T}{2}} A_0\cos(\omega t) dt + \int_{-\frac{T}{2}}^{\frac{T}{2}} A_1\cos^2(\omega t) dt + \int_{-\frac{T}{2}}^{\frac{T}{2}} B_1\sin(\omega t)\cos(\omega t) dt \\ &+ \int_{-\frac{T}{2}}^{\frac{T}{2}} A_2\cos(2\omega t)\cos(\omega t) dt + \int_{-\frac{T}{2}}^{\frac{T}{2}} B_2\sin(2\omega t)\cos(\omega t) dt \\ &+ \int_{-\frac{T}{2}}^{\frac{T}{2}} A_3\cos(3\omega t)\cos(\omega t) dt + \int_{-\frac{T}{2}}^{\frac{T}{2}} B_3\sin(3\omega t)\cos(\omega t) dt + \dots \\ &+ \int_{-\frac{T}{2}}^{\frac{T}{2}} A_k\cos(k\omega t)\cos(\omega t) dt + \int_{-\frac{T}{2}}^{\frac{T}{2}} B_k\sin(k\omega t)\cos(\omega t) dt. \end{aligned} \quad (\text{I.8})$$

Looking closely at Eq. (I.8), one can note five types of definite integrals, given by Eqs. (I.9)-(I.13), whose features tend to be similar during the calculation of each coefficient. These integrals have been used to allow a generalized mathematical approach to calculate the coefficients of the harmonic components

$$1. \int_{-\frac{T}{2}}^{\frac{T}{2}} A_0\cos(\omega t) dt = 0 \quad (\text{I.9})$$

$$2. \int_{-\frac{T}{2}}^{\frac{T}{2}} A_1\cos^2(\omega t) dt = A_1 \int_{-\frac{T}{2}}^{\frac{T}{2}} \left[\frac{1}{2} + \frac{1}{2}\cos(2\omega t) \right] dt = A_1 \int_{-\frac{T}{2}}^{\frac{T}{2}} \frac{1}{2} dt = \frac{A_1 T}{2} \quad (\text{I.10})$$

$$3. \int_{-\frac{T}{2}}^{\frac{T}{2}} B_1\sin(\omega t)\cos(\omega t) dt = \frac{B_1}{2} \int_{-\frac{T}{2}}^{\frac{T}{2}} \sin(2\omega t) dt = 0 \quad (\text{I.11})$$

$$4. \int_{-\frac{T}{2}}^{\frac{T}{2}} A_2\cos(2\omega t)\cos(\omega t) dt, \text{ which is of the general type:} \quad (\text{I.12})$$

$$\int_{-\frac{T}{2}}^{\frac{T}{2}} A_m\cos(mt)\cos(nt) dt = \frac{A_m}{2} \int_{-\frac{T}{2}}^{\frac{T}{2}} [\cos(m-n)t + \cos(m+n)t] dt = 0 \quad \forall m \neq n \in \mathbf{Z}$$

$$5. \int_{-\frac{T}{2}}^{\frac{T}{2}} B_2\sin(2\omega t)\cos(\omega t) dt, \text{ which is of the general type:} \quad (\text{I.13})$$

$$\int_{-\frac{T}{2}}^{\frac{T}{2}} B_m\sin(mt)\cos(nt) dt = \frac{B_m}{2} \int_{-\frac{T}{2}}^{\frac{T}{2}} [\sin(m-n)t + \sin(m+n)t] dt = 0 \quad \forall m \neq n \in \mathbf{Z}.$$

From the performed manipulations only the integral (I.10) is not null. It is clear that the Fourier series forms a set of orthogonal functions over $[-\frac{T}{2}, \frac{T}{2}]$. In this way, Eq. (I.8) reduces to

$$\frac{A_1 T}{2} = \int_{-\frac{T}{2}}^{\frac{T}{2}} y(t)\cos(\omega t) dt \Rightarrow A_1 = \frac{2}{T} \int_{-\frac{T}{2}}^{\frac{T}{2}} y(t)\cos(\omega t) dt. \quad (\text{I.14})$$

A similar procedure must be performed to evaluate the coefficient B_1 , however the Eq. (I.5) must be multiplied by $\sin(\omega t) dt$ and integrated from $-\frac{T}{2}$ to $\frac{T}{2}$, as illustrated in Eq. (I.15). For evaluating the other desired coefficients, Eq. (I.5) must be multiplied by the respective function related to the coefficient, in other words, to evaluate A_2 a multiplication by $\cos(2\omega t) dt$ must be realized, to evaluate B_2 a multiplication by $\sin(2\omega t) dt$ is performed, and so on and so forth. For all cases, the indicated operations produce a set of orthogonal functions over the function's period that simplify and clarify the procedures to calculate the coefficient envisaged

$$\begin{aligned} \int_{-\frac{T}{2}}^{\frac{T}{2}} y(t)\sin(\omega t) dt &= \int_{-\frac{T}{2}}^{\frac{T}{2}} A_0\sin(\omega t) dt + \int_{-\frac{T}{2}}^{\frac{T}{2}} A_1\cos(\omega t)\sin(\omega t) dt + \int_{-\frac{T}{2}}^{\frac{T}{2}} B_1\sin^2(\omega t) dt \\ &+ \int_{-\frac{T}{2}}^{\frac{T}{2}} A_2\cos(2\omega t)\sin(\omega t) dt + \int_{-\frac{T}{2}}^{\frac{T}{2}} B_2\sin(2\omega t)\sin(\omega t) dt \\ &+ \int_{-\frac{T}{2}}^{\frac{T}{2}} A_3\cos(3\omega t)\sin(\omega t) dt + \int_{-\frac{T}{2}}^{\frac{T}{2}} B_3\sin(3\omega t)\sin(\omega t) dt + \dots \\ &+ \int_{-\frac{T}{2}}^{\frac{T}{2}} A_k\cos(k\omega t)\sin(\omega t) dt + \int_{-\frac{T}{2}}^{\frac{T}{2}} B_k\sin(k\omega t)\sin(\omega t) dt. \end{aligned} \quad (\text{I.15})$$

Carrying out the indicated relations given by the Eqs. (I.9)-(I.13) taking into consideration the sinus function, Eq. (I.15) becomes

$$\frac{B_1 T}{2} = \int_{-\frac{T}{2}}^{\frac{T}{2}} y(t)\sin(\omega t) dt \Rightarrow B_1 = \frac{2}{T} \int_{-\frac{T}{2}}^{\frac{T}{2}} y(t)\sin(\omega t) dt. \quad (\text{I.16})$$

In this way, the generalized equations for calculating the Fourier series coefficients, regardless of the sinusoidal component order, are given as follows

$$A_k = \frac{2}{T} \int_{-\frac{T}{2}}^{\frac{T}{2}} y(t)\cos(k\omega t) dt = \frac{2}{T} \int_0^T y(t)\cos(k\omega t) dt \quad (\text{I.17})$$

$$B_k = \frac{2}{T} \int_{-\frac{T}{2}}^{\frac{T}{2}} y(t)\sin(k\omega t) dt = \frac{2}{T} \int_0^T y(t)\sin(k\omega t) dt. \quad (\text{I.18})$$

Several procedures for finding the Fourier series coefficients have been devised. Graphical procedures use a photographic record of the wave obtained through oscillographic analysis or other means. The function's equation is not commonly known, however it may be determined using the basic method of successive approximations related to a standardized system in tabular form. The tables which are employed are called *analyzing tables*. This procedure has a good performance even for waves very distorted by harmonics, in which it would be very laborious to establish equations for portions of the wave [10].

Both mechanical and electronic devices have also been applied. The mechanical ones have an operation principle similar to that of a planimeter (device able to measure the area of closed regions in the plane) based on harmonically related rotating wheels, where the amplitudes of Fourier coefficients could be properly set from a scale and the sum computed. Nowadays, powerful digital harmonic analyzers have been largely applied to

track the wave's components aiming to produce an approximate graph which matches with the wave's function [11],[12].

If the representative equation of the wave is known over the interval of periodicity, analytical procedures may be applied. This statement becomes clear that it is not necessary to know any information of the wave outside its interval of periodicity for computing the Fourier series. Even if the wave is formed by piecewise functions, the Fourier coefficients are obtained from a sum of integrals of the several functions taking into account the interval of periodicity in which each function is analyzed [10]. Fig. I.2 depicts the Fourier series based on analytical procedures for representing classical wave forms.

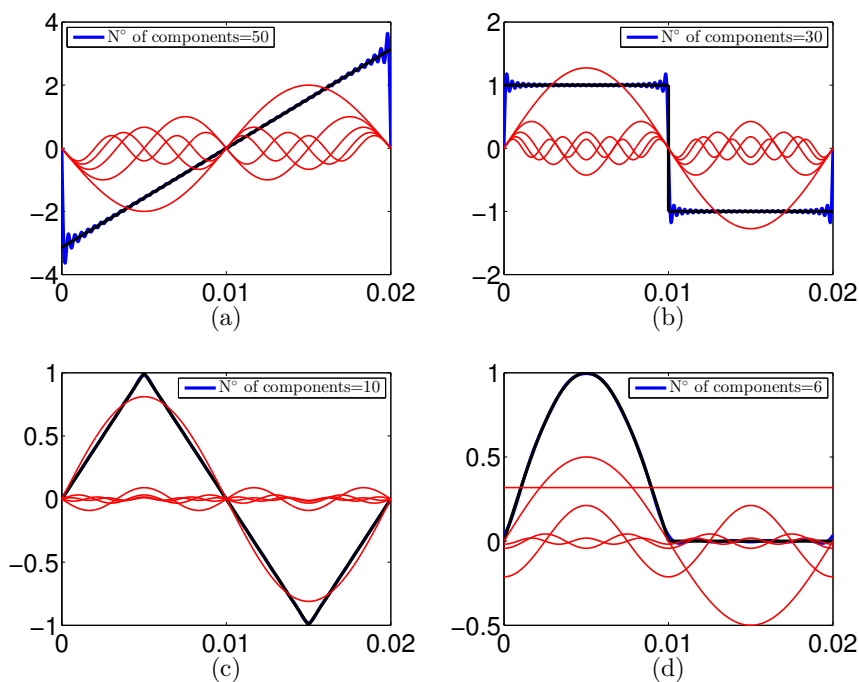


Figure I.2: Function approach using Fourier series (blue line): (a) sawtooth wave, (b) symmetrical rectangular wave, (c) symmetrical triangular wave, (d) half-wave rectification of a sine wave (black lines). The fundamental frequency is $f_o=50$ -Hz and the first five components of the Fourier series to each waveform are displayed in red lines.

An interesting effect can be noted in Fig. I.2 (a)-(b) related to overshoots in the vicinity of discontinuity points. This effect is called the ‘‘Gibbs phenomenon’’ or ‘‘Gibbs-Wilbraham phenomenon’’ and it asserts that any discontinuous periodic function represented by a truncated Fourier series will present results that oscillate closely to the discontinuity, being the maximum overshoot value proportional to the size of the jump discontinuity.

Increasing the number of components into the series the oscillations persist, however the overshoot tends to approach of the discontinuity itself. Even if the number of components into the series tends to infinity, the phenomenon will still be present. This assumption brings the concept of nonuniform convergence [12], [9]. When a function does not have any discontinuity into the interval of periodicity, for instance Fig. I.2 (c)-(d), the convergence of the Fourier series is fast and accurate, because fewer components are necessary to produce a faithful wave representation.

The general coefficients A_k and B_k can be employed for rewriting the trigonometric

Fourier series in its compact form given by

$$y(t) = \frac{A_0}{2} + \sum_{k \in \mathbb{N}} A_k \cos(k\omega t) + \sum_{k \in \mathbb{N}} B_k \sin(k\omega t). \quad (\text{I.19})$$

A special attention needs to be directed to the A_0 coefficient. It has been written in a special form as a matter of formality. The reason is quite simple: the factor that multiplies the integral of Eq. (I.7) is $\frac{1}{T}$, however the factor that multiplies the integral of Eqs. (I.17)-(I.18) is $\frac{2}{T}$, in this way, performing a division of A_0 by 2 preserves the similarity with A_k , that is, the same coefficient formula may be employed.

According to [13], there is another way to represent the Fourier series. For this purpose, let us consider the following trigonometric identities

$$\cos(k\omega t) = \frac{1}{2} \left(e^{jk\omega t} + e^{-jk\omega t} \right) \quad (\text{I.20})$$

$$\sin(k\omega t) = \frac{1}{2j} \left(e^{jk\omega t} - e^{-jk\omega t} \right) \quad (\text{I.21})$$

replacing Eqs. (I.20)-(I.21) into Eq. (I.19) and reorganizing the general coefficients with the complex exponentials yields

$$y(t) = \frac{1}{2} \sum_{k \in \mathbb{N}} (A_k - jB_k) e^{jk\omega t} + \frac{1}{2} \sum_{k \in \mathbb{N}} (A_k + jB_k) e^{-jk\omega t} \quad (\text{I.22})$$

one can observe that Eq. (I.22) may be further simplified by taking into account the interval from $-\infty$ to $+\infty$, thus

$$y(t) = \frac{1}{2} \sum_{k=-\infty}^{+\infty} (A_k - jB_k) e^{jk\omega t} = \sum_{k=-\infty}^{+\infty} \alpha_k e^{jk\omega t} \quad (\text{I.23})$$

where Eq. (I.23) represents the Fourier series in the exponential form with complex coefficients. Since

$$\alpha_k = \frac{1}{2} (A_k - jB_k) \quad k = 0, \pm 1, \pm 2, \dots \quad (\text{I.24})$$

an effective manner to compute the parameter α_n is integrating $y(t)$ over the exposure period, yielding

$$\alpha_k = \frac{1}{T} \int_{-\frac{T}{2}}^{\frac{T}{2}} y(t) e^{-jk\omega t} dt \quad k = 0, \pm 1, \pm 2, \dots \quad (\text{I.25})$$

The Fourier series in exponential form (I.23) and the coefficients in the complex form (I.24) are the approaches frequently used in wave analyzes. Using these representations, it is possible to lay down an important conclusion about the Fourier series of pure sinusoids. Considering the wave given by Eq. (I.1), it is possible to notice that the result of α_0 is null, due to the facts already mentioned about the average value of sinusoidal quantities. Remembering the trigonometric identity (I.20), the complex coefficients α_{-1} and α_1 may be directly obtained by integration, yielding

$$\alpha_{-1} = \frac{Y_m}{2T} \int_{-\frac{T}{2}}^{\frac{T}{2}} \left[e^{j(\omega t + \phi)} + e^{-j(\omega t + \phi)} \right] e^{j\omega t} dt = \frac{Y_m}{2} e^{-j\phi} \quad (\text{I.26})$$

$$\alpha_1 = \frac{Y_m}{2T} \int_{-\frac{T}{2}}^{\frac{T}{2}} \left[e^{j(\omega t + \phi)} + e^{-j(\omega t + \phi)} \right] e^{-j\omega t} dt = \frac{Y_m}{2} e^{j\phi} \quad (\text{I.27})$$

in this way, the exponential Fourier series (I.23) can be rewritten as follows

$$y(t) = \left(\frac{Y_m}{2} e^{-j\phi} \right) e^{-j\omega t} + \left(\frac{Y_m}{2} e^{j\phi} \right) e^{j\omega t} \quad (\text{I.28})$$

the function $y(t)$ is *real* and it has *even symmetry*, thus the following manipulation can be performed

$$y(t) = 2 \left(\frac{Y_m}{2} \text{Re} \left[e^{j\omega t} e^{j\phi} \right] \right) = Y_m \text{Re} \left[e^{j\omega t} e^{j\phi} \right] \quad (\text{I.29})$$

once the system frequency is known, the term $e^{j\omega t}$ can be omitted, furthermore, dividing Eq. (I.29) by $\sqrt{2}$ we just came back to phasor notation. In other words, one can conclude that the phasor representation of a pure sinusoidal quantity is also its exponential Fourier series.

I.4 Major Fourier transform (FT) properties for phasor estimation

The Fourier transform claims for an extensive and rigorous mathematical background, however, in this section, it will be present only the major properties which are of direct interest for phasor estimation in electric power system. In the references [9], [13], and [14] an excellent and complete description of the Fourier transform theory have been devoted.

Up till now Fourier series has been used to represent periodic functions that vanish outside of the observation interval. Now suppose that $y(t)$ is defined for all real t , and it is not possible to truncate this function into a finite interval for some reason. For $y \in \mathbb{R}$, instead of integrating from $-\frac{T}{2}$ to $\frac{T}{2}$, one can integrate over \mathbb{R} [9], therefore

$$Y(f) = \int_{-\infty}^{+\infty} y(t) e^{-j2\pi ft} dt. \quad (\text{I.30})$$

Eq. (I.30) is called the *Fourier transform* or *Fourier integral* of $y(t)$. It is possible to note that, rather than series, $y(t)$ is recovery from the integral. Looking closely at this equation, a direct conclusion may be drawn: the Fourier transform can extract any envisaged single frequency component of a signal, thus it may be interpreted as a complex quantity for each frequency component

$$Y(f) = R(f) + jI(f) = |Y(f)| e^{j\theta(f)} \quad (\text{I.31})$$

being $R(f)$ the real part of the Fourier transform; $I(f)$ is the imaginary part of the Fourier transform; $|Y(f)|$ represents the *amplitude* or *Fourier spectrum* of $y(t)$ being equal to

$\sqrt{R^2(f) + I^2(f)}$; and $\theta(f)$ represents the phase angle of the Fourier transform being given by $\tan^{-1}[I(f)/R(f)]$ [13].

Inversion transformation (I.32) allows the representation of the time function, piecewise or not, from its Fourier transform. Representing the functions $Y(f)$ and $y(t)$ through the notations (I.30) and (I.32), respectively, the two functions are termed as *Fourier transform pair* and the relationship $y(t) \iff Y(f)$ may be established for stable functions (limited in amplitude)

$$y(t) = \int_{-\infty}^{+\infty} Y(f)e^{j2\pi ft} df. \quad (\text{I.32})$$

The Fourier transform provides the basis for sampling and convolution approaches. For a comprehensive understanding of both the concept of distribution must be applied. In mathematical analysis, a distribution can be understood as a process that assigns to an arbitrary function a response or number, therefore, a distribution is also known as *generalized function*. The Dirac's distribution, also called as *unit distribution*, is a powerful mathematical tool in the Fourier theory, because it simplifies the calculus which would otherwise require a complex and laborious solution [13],[8],[14]. Let us assume the sampling distribution $h(t)$ formed as a proper combination of Dirac impulses properly spaced by t_d

$$h(t) = \sum_{k=-\infty}^{+\infty} \delta(t - kt_d) \quad (\text{I.33})$$

the sampling process of a continuous-time signal $y(t)$ may be represented by the product between the time function and the sampling distribution, as given by (I.34)

$$y_s(t_d) = \int_{-\infty}^{+\infty} \delta(t - t_d)y(t) dt \equiv h(t) * y(t) \quad (\text{I.34})$$

where $y_s(t_d)$ is an impulse train, called the sampling signal, whose amplitude is modulated by the value taken by function $y(t)$ at each t_d instant. The integrals of the type illustrated in Eq. (I.34) are named as *convolution*. In other words, it is possible to represent the value taken by any function at each t_d instant based on the convolution sum, i.e, taking into account the intersection between the continuous-time function and the shifting of the Dirac's impulse function with step t_d over time from $-\infty$ to $+\infty$.

Three properties of the Fourier transform are directly related to the previous statements, thereby, based on [3] and [13], in the following paragraphs the properties are appropriately addressed.

Property 1: *The Fourier transform of a periodic function is a series of impulses located at multiples of the fundamental frequency of the periodic function.*

To illustrate this property, let us consider a periodic function given by

$$y(t) = Y_m \cos(2\pi f_o t) \quad (\text{I.35})$$

computing the Fourier transform of Eq. (I.35) yields

$$\begin{aligned}
 Y(f) &= \int_{-\infty}^{+\infty} Y_m \cos(2\pi f_o t) e^{-j2\pi f t} dt \\
 &= \frac{Y_m}{2} \int_{-\infty}^{+\infty} [e^{j2\pi f_o t} + e^{-j2\pi f_o t}] e^{-j2\pi f t} dt \\
 &= \frac{Y_m}{2} \int_{-\infty}^{+\infty} [e^{-j2\pi(f-f_o)t} + e^{-j2\pi(f+f_o)t}] dt \\
 &= \frac{Y_m}{2} \delta(f - f_o) + \frac{Y_m}{2} \delta(f + f_o)
 \end{aligned}
 \tag{I.36}$$

applying the inversion formula (I.32) gives

$$\begin{aligned}
 y(t) &= \int_{-\infty}^{+\infty} \left[\frac{Y_m}{2} \delta(f - f_o) + \frac{Y_m}{2} \delta(f + f_o) \right] e^{j2\pi f t} df \\
 &= \frac{Y_m}{2} e^{j2\pi f_o t} + \frac{Y_m}{2} e^{-j2\pi f_o t} \\
 &= Y_m \cos(2\pi f_o t)
 \end{aligned}
 \tag{I.37}$$

in this way, the Fourier transform pair is determined. It is important to note that the Fourier transform is *real*

$$Y_m \cos(2\pi f_o t) \iff \frac{Y_m}{2} \delta(f - f_o) + \frac{Y_m}{2} \delta(f + f_o).
 \tag{I.38}$$

Performing a similar procedure for a sine wave the obtained Fourier transform pair is given by Eq. (I.39). For this case, the Fourier transform is *imaginary*

$$Y_m \sin(2\pi f_o t) \iff j \frac{Y_m}{2} \delta(f + f_o) - j \frac{Y_m}{2} \delta(f - f_o).
 \tag{I.39}$$

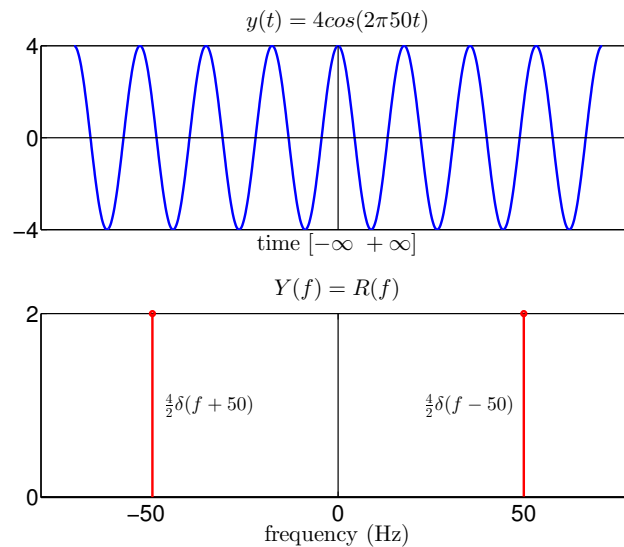


Figure I.3: Fourier transform of a cosine wave at fundamental frequency $f_o=50$ -Hz. Impulses located at ± 50 -Hz, ± 100 Hz, ± 150 Hz, and so on and so forth.

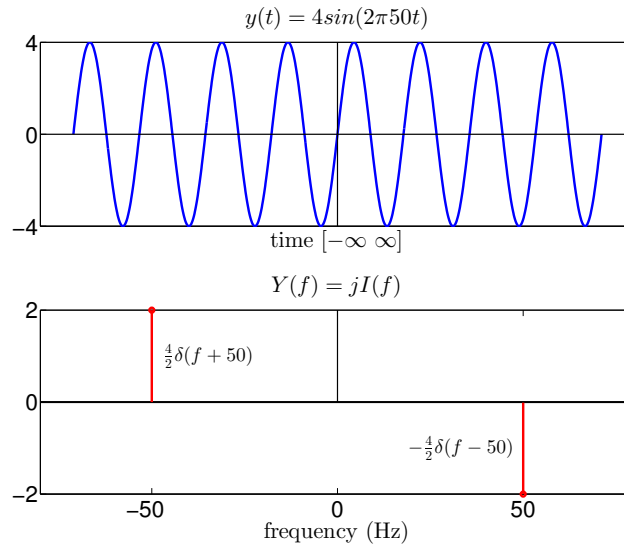


Figure I.4: Fourier transform of a sine wave at fundamental frequency $f_o=50$ -Hz. Once again the impulses are located at ± 50 -Hz, ± 100 Hz, ± 150 Hz, and so on and so forth.

Figs. I.3-I.4 display the graphical representation of the Fourier transform for both functions, respectively. Clearly, one can observe that the Fourier transform of a continuous-time signal produces impulses at multiples of its fundamental frequency.

Property 2: *The Fourier transform of a periodic series of impulses with interval T is a series of impulses in the frequency domain located at multiples of $\frac{1}{T}$.*

To illustrate this property, it is necessary to keep in mind that any periodic function may be represented by the exponential Fourier series, therefore, the sampling distribution given by Eq. (I.33) can be rewrite as follows

$$h(t) = \sum_{k=-\infty}^{+\infty} \delta(t - kT) = \sum_{k=-\infty}^{+\infty} \alpha_k e^{j2\pi fkt} \quad (\text{I.40})$$

with α_k being given by Eq. (I.25). Expressing the Fourier transform of $h(t)$ in the exponential form gives

$$\begin{aligned} H(f) &= \int_{-\infty}^{+\infty} h(t) e^{-j2\pi ft} dt \\ &= \int_{-\infty}^{+\infty} \left[\sum_{k=-\infty}^{+\infty} \alpha_k e^{j\frac{2\pi kt}{T}} \right] e^{-j2\pi ft} dt \\ &= \sum_{k=-\infty}^{+\infty} \int_{-\infty}^{+\infty} \alpha_k e^{j\frac{2\pi kt}{T}} e^{-j2\pi ft} dt \\ &= \sum_{k=-\infty}^{+\infty} \int_{-\infty}^{+\infty} \alpha_k e^{-j2\pi(f - \frac{k}{T})t} dt. \end{aligned} \quad (\text{I.41})$$

In the third form of Eq. (I.41) has been assumed that the order of the summation and integration can be reversed. The integral of the exponential term in the last form is the impulse function $\delta(f - \frac{k}{T})$, and thus the Fourier transform of the periodic function $h(t)$ is

$$H(f) = \sum_{k=-\infty}^{+\infty} \alpha_k \delta\left(f - \frac{k}{T}\right). \quad (\text{I.42})$$

It is clear that the Eq. (I.42) represents a series of impulses in the frequency domain located at integer multiples of $\frac{1}{T}$. To determine the coefficients α_k , we recall Eq. (I.25) taking into account the impulse function $\delta(t)$, therefore

$$\alpha_k = \frac{1}{T} \int_{-\frac{T}{2}}^{\frac{T}{2}} \delta(t) e^{-j\frac{2\pi kt}{T}} dt \quad k = 0, \pm 1, \pm 2, \dots \quad (\text{I.43})$$

One can notice that the impulse function in the integrand yields an unitary sample only at $t=0$, thereby, α_k is equal to $\frac{1}{T}$ for all k . In other words, the Fourier transform of $h(t)$ will have a magnitude of $\frac{1}{T}$ for each interval being the final equation given by

$$H(f) = \frac{1}{T} \sum_{k=-\infty}^{+\infty} \delta\left(f - \frac{k}{T}\right). \quad (\text{I.44})$$

The Fourier transform pair is illustrated in Eq. (I.45) and its graphical representation is displayed in Fig. I.5.

$$\sum_{k=-\infty}^{\infty} \delta(t - kT) \iff \frac{1}{T} \sum_{k=-\infty}^{+\infty} \delta\left(f - \frac{k}{T}\right) \quad (\text{I.45})$$

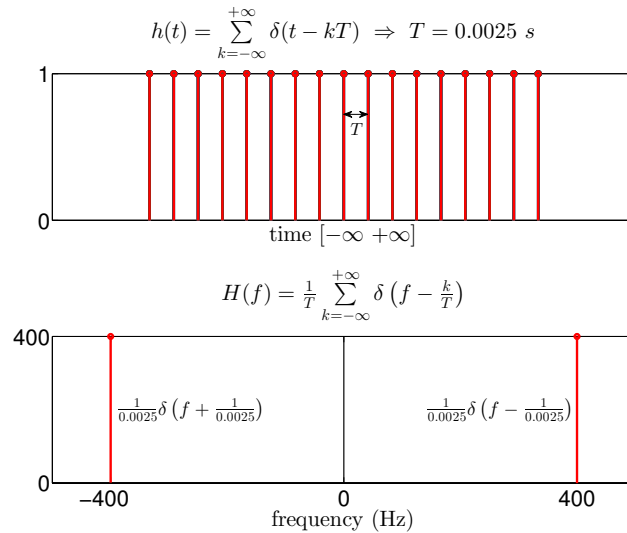


Figure I.5: Fourier transform of a distribution sampling with $T=0.0025$ s.

Property 3: *The Fourier transform of a convolution of two functions in time domain is equal to the product of the Fourier transform of the functions being convolved (time convolution theorem), and similarly, the Fourier transform of the product of two functions in time domain is equal to the convolution of the Fourier transform of the functions being multiplied (frequency convolution theorem).*

One of the most important and powerful mathematical tool in modern scientific analysis is the relationship between Eq. (I.34) and its Fourier transform because this relationship is

the basis of the *convolution theorem*. This theorem can be split into two categories: time and frequency convolution. The first one allows the possibility to convolve mathematically in the time domain by simple multiplication in the frequency domain, and the second may be interpreted as the converse, in which a simple multiplication in the time domain yields a convolution in the frequency domain. Both play an essential role in digital signal processing and they allow a comprehensive understanding about sampled data, *aliasing* effect and *leakage* phenomenon that will be presented in Section I.5.

The Fourier transform pair given by the time convolution theorem is represented by the following equation

$$x(t) = y(t) * h(t) \iff X(f) = Y(f) \times H(f). \quad (\text{I.46})$$

To establish the above relationship, the Fourier transform of both sides related to the time domain functions must be performed, therefore

$$\int_{-\infty}^{+\infty} x(t)e^{-j2\pi ft} dt = \int_{-\infty}^{+\infty} \left[\int_{-\infty}^{+\infty} y(\tau)h(t-\tau) d\tau \right] e^{-j2\pi ft} dt. \quad (\text{I.47})$$

Assuming that the order of integration can be changed, Eq. (I.47) may be rewritten as

$$X(f) = \int_{-\infty}^{+\infty} y(\tau) \left[\int_{-\infty}^{+\infty} h(t-\tau)e^{-j2\pi ft} dt \right] d\tau \quad (\text{I.48})$$

by substituting $\sigma = t - \tau$, the brackets becomes

$$X(f) = \int_{-\infty}^{+\infty} y(\tau) \left[\int_{-\infty}^{+\infty} h(\sigma)e^{-j2\pi f\sigma} e^{-j2\pi f\tau} d\sigma \right] d\tau \quad (\text{I.49})$$

thus, Eq. (I.49) can then be rewritten as follows

$$X(f) = \int_{-\infty}^{+\infty} y(\tau)e^{-j2\pi f\tau} \left[\int_{-\infty}^{+\infty} h(\sigma)e^{-j2\pi f\sigma} d\sigma \right] d\tau. \quad (\text{I.50})$$

Looking closely at Eq. (I.50), one can notice that it may be rewritten in a compact form taking into account the product of the Fourier transform of the functions convolved, therefore

$$X(f) = Y(f) \times H(f). \quad (\text{I.51})$$

The frequency convolution theorem may also be similarly proven to ensure the Fourier transform pair given by

$$x(t) = y(t) \times h(t) \iff X(f) = Y(f) * H(f). \quad (\text{I.52})$$

for this purpose, it is advised to replace $t = \sigma + \tau - \tau$ into the Eq. (I.48) and perform the following manipulations

$$X(f) = \int_{-\infty}^{+\infty} y(\tau) \left[\int_{-\infty}^{+\infty} h(\sigma-\tau)e^{-j2\pi f(\sigma-\tau)} e^{-j2\pi f\tau} d\sigma \right] d\tau \quad (\text{I.53})$$

thereby, Eq. (I.53) can then be rewritten as follows

$$X(f) = \int_{-\infty}^{+\infty} y(\tau) e^{-j2\pi f\tau} \left[\int_{-\infty}^{+\infty} h(\sigma - \tau) e^{-j2\pi f(\sigma - \tau)} d\sigma \right] d\tau \quad (\text{I.54})$$

into the brackets σ is the variable of integration and outside the brackets τ is the variable. It is possible to note the existence of an inherent relationship between the integrands, therefore Eq. (I.54) can be rewritten taking into account the integral of the product between the Fourier transforms of the functions, yielding

$$X(f) = \int_{-\infty}^{+\infty} Y(\tau) H(f - \tau) d\tau \equiv Y(f) * H(f) \quad (\text{I.55})$$

in fact, Eq. (I.55) is closely linked to the Eq. (I.34), therefore, it also represents a convolution but in the frequency domain.

I.5 Sampled data, aliasing effect, and leakage phenomenon background

Physical phenomena can be observed and analyzed according to the physical quantities that describe the particular phenomenon. For most phenomena, the time is the independent variable, and even evaluating a small interval of the physical quantity, an infinite amount of data will be found inside of the interval analyzed. For this reason, these phenomena are mathematically represented by temporal functions that belongs to the set of the real numbers, and these functions are referred to as belonging to the *continuous-time domain*. Therefore, the data that bring the associated information of the phenomena are called *continuous-time signals* [8].

When the independent variable is time, however, the data are defined only for a finite set of discrete values of the independent variable, the data belong to the *discrete-time domain* and they are called as *discrete-time signals* or *discrete-time sequence*. Generally, a discrete sequence is obtained after performing a constant sampling process on a continuous-time signal, and, theoretically, the sequence must contain the true continuous-time signal information [8]. The discrete-time signals are the basis for the digital signal processing for measurements, computer science and also for the modern information theory, in which, the works developed by Alan Turing have been changed the course of the computer age (*and also of the history*).

In the preceding section, the Fourier series has been applied to periodic functions in the continuous-time domain, however it is possible to transform these functions in discrete-time periodic sequences in order to enable the applicability of Fourier series for digital signal processing. Based on Eq. (I.34), the sampled data may be interpreted as a time function $y_s(t)$ consisting of uniformly spaced and modulated impulses, each with a magnitude $y(kT_s)$

$$y_s(t) = \sum_{k=-\infty}^{+\infty} y(kT_s) \delta(t - kT_s) \quad (\text{I.56})$$

where T_s is the uniform time interval between samples, that is, the sampling period.

It can be immediately recognized that Eq. (I.56) represents the product at uniform intervals between the continuous-time signal and the distribution sampling. It is notewor-

thy to point out that Eq. (I.56) is in keeping with **Property 3** of the Fourier transform related to the frequency convolution theorem. Hence, the Fourier transform $Y_s(f)$ of $y_s(t)$ is the convolution between the Fourier transforms of $y(t)$ and of the sampling distribution $h(t)$, thereby

$$\begin{aligned} Y_s(f) &= \frac{Y_m}{2T_s} \int_{-\infty}^{+\infty} Y(v) \sum_{k=-\infty}^{+\infty} \delta\left(f - \frac{k}{T_s} - v\right) dv \\ &= \frac{Y_m}{2T_s} \sum_{k=-\infty}^{+\infty} \int_{-\infty}^{+\infty} Y(v) \delta\left(f - \frac{k}{T_s} - v\right) dv \\ &= \frac{Y_m}{2T_s} \sum_{k=-\infty}^{+\infty} Y\left(f - \frac{k}{T_s}\right) \quad \forall k. \end{aligned} \quad (\text{I.57})$$

Once again, it has been assumed that the order of summation and integration can be reversed, and the integral is evaluated using the **Property 2** related to the Fourier transform of the sampling distribution. Eq. (I.57) shows that the Fourier transform of the sampled data will be equal to the Fourier transform of the continuous-time signal (**Property 1**) centered at integer multiples of the sampling frequency $f_s = \frac{1}{T_s}$ and modulated by the factor $\frac{Y_m}{2T_s}$. Taking into account the graphical representation of the **Properties 1-2**, Fig. I.6 depicts an intuitive graphical representation of the aforementioned statements.

One can observe that the sampled signal is obtained by the product between the continuous-time signal and the sampling distribution ($y(t) \times h(t)$). Performing the Fourier transform of the sampled signal ($Y_s(f)$), one can obtain the same result if the convolution between the Fourier transforms of the continuous-time signal and the sampling distribution is performed ($Y(f) * H(f)$). Recall that the Fourier transform of $y(t)$ is band-limited at $f_o=50$ -Hz, thus, if the f_o is less than or equal to one-half of the sampling frequency f_s ($f_o \leq \frac{f_s}{2}$), in essence, the sampling process could be performed without errors.

If this condition is not satisfied, an overlapping between the regions of the frequency spectrum will appear causing errors on the estimated frequency components, this phenomenon is known as *aliasing*. In order to avoid errors due to aliasing, the bandwidth of the continuous signal must be less than half the sampling frequency. This requirement is known as the ‘‘Nyquist-Shannon theorem’’ [8]. Fig. I.7 shows a graphical representation of the aliasing effect taking into account the **Properties 1-2-3**.

In order to avoid aliasing errors, analog anti-aliasing low-pass filter is commonly employed in all sampled data systems used in phasor estimation. The goal of this filter is to band-limit the input signals to below half the sampling frequency chosen. In practice, the signal input cut-off frequency must be *much less than* one half the sampling frequency to ensure that aliasing does not occur. Although analog filters are widely used, active and digital filters have been used to accomplish this task.

A sharp cut-off characteristic can be obtained using active filters. Digital filters (with oversampling and decimation) may also be employed in special cases. It is important to mention that all anti-aliasing filters introduce frequency-dependent magnitude and phase shift in the input signal which must be compensated during the phasor estimation process

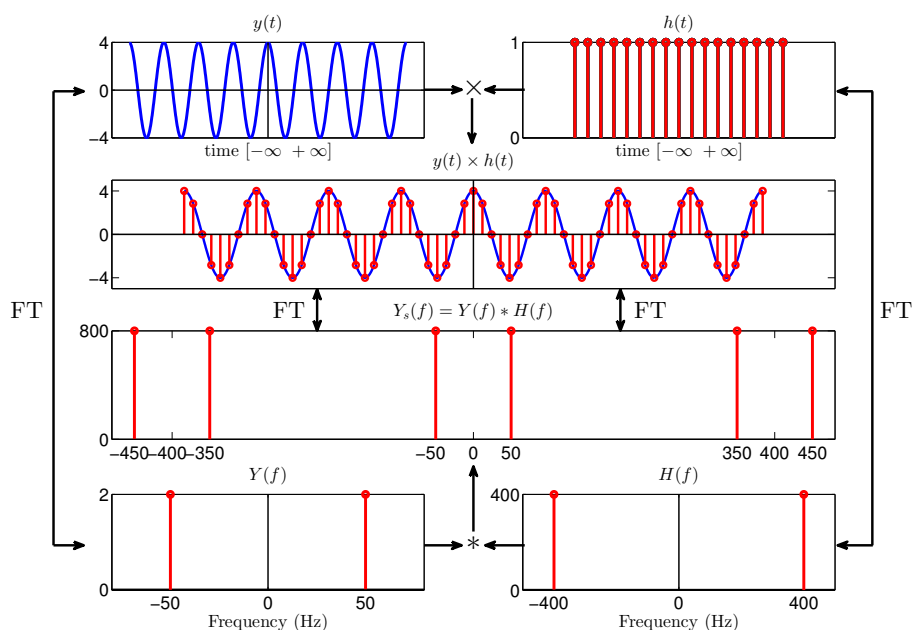


Figure I.6: Graphical representation of the frequency convolution theorem. For this case, the signal $y(t)$ is sampled with a sampling frequency of $f_s=400$ Hz, that is, $T_s=0.0025$ s.

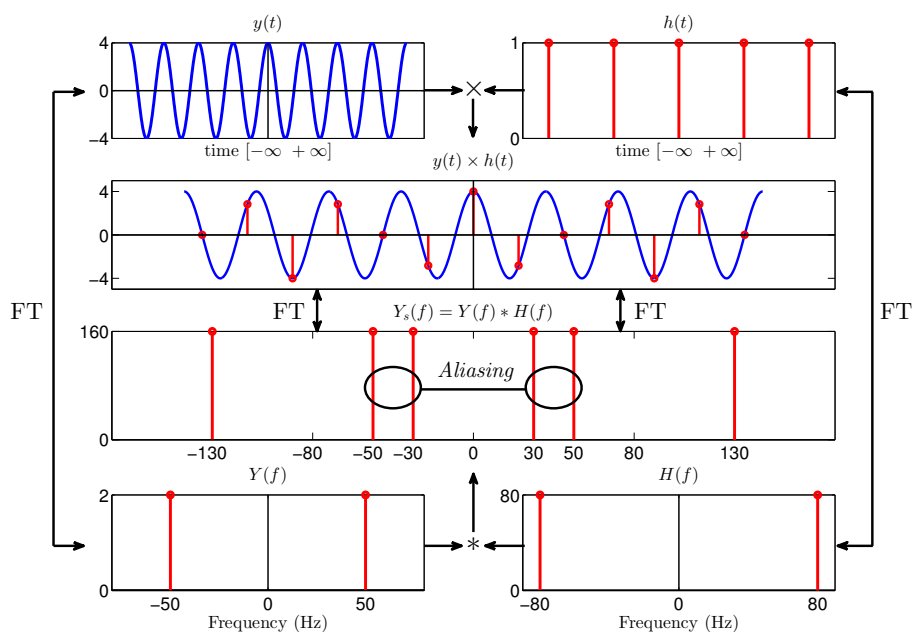


Figure I.7: Graphical representation of the aliasing effect. In this case, the signal $y(t)$ is sampled with a sampling frequency of $f_s=80$ Hz, that is, $T_s=0.0125$ s.

[3]. This will be discussed further in Chapter III where the proposed frequency-adaptive algorithms are described.

Once the aliasing effect is avoided, we are led to believe that the information contained in the sampled sequence is the same of the continuous-time signal, however, another pernicious problem related to the lack of synchronism between the input signal period and the sampling period can also degrade the phasor estimates. It is important to mention that

an uniform sampling of a continuous-time signal is a periodic sequence that repeats itself in a constant period along time, as shown below

$$y[k] = y[k + N] \quad \forall k \quad (\text{I.58})$$

being $N \in \mathbf{Z}$, the number of samples inside the interval of periodicity.

To clarify the foregoing, let us rewrite the continuous-time signal represented by Eq. (I.1) taking into account its interval of periodicity T , as follows

$$y(t) = Y_m \cos\left(\frac{2\pi}{T}t + \phi\right). \quad (\text{I.59})$$

Let $y(t)$ be sampled with a sampling period T_s . Evaluating Eq. (I.59) for each sampling time kT_s gives

$$y(kT_s) = Y_m \cos\left(2\pi \frac{kT_s}{T} + \phi\right) \Rightarrow y[k] = Y_m \cos\left(\frac{2\pi}{N}k + \phi\right). \quad (\text{I.60})$$

It is clear that $T = N \times T_s$ or $f_s = N \times f_o$. These simple relationships provide the necessary and sufficient condition for a correct sampling of a periodic continuous-time signal. In other words, the only way to obtain a correlated periodic sequence is ensuring that N be an integer or a rational number, in this case, the associated information from the continuous-time signal is transferred to the discrete-time sequence.

Concerning Eq. (I.60), Fig. I.8 (a)-(b) depicts the synchronous and asynchronous sampling condition, respectively, where $N = 8$ samples have been taken over a period of 0.02 ms, which corresponds to one period of the 50-Hz signal. For a synchronous sampling, one can observe that any sample taken at instant k will be matched with the sample at $k + N$. For example, a sample taken at $k=0$ (peak value) will be numerically equal to the sample taken at $k=8$ ($8 \times T_s = 0.02$ ms, that also corresponds to peak value). For this case, a correct sampling will produce samples properly taken at uniform intervals including the zero-crossings.

For an asynchronous sampling, the samples are not properly taken. Clearly, it can be seen that the definition of periodic sequence given by Eq. (I.58) is not fulfilled. An interesting issue arises regarding the Fourier transform for signals obtained by asynchronous sampling: What is the impact of the lack of synchronism on the Fourier transform? Unfortunately, the answer for this issue is not good, because the lack of synchronism will provoke a spurious energy across the frequency spectrum (spectral leakage). Fig. I.8 (c) displays this pernicious phenomenon that must be overcome for providing correct phasor estimates. In Section I.9, several techniques employed to reduce the leakage phenomenon will be addressed.

It can be immediately recognized that the theory presented in this section is the basis of the sampling theorem. In essence, it claims that the original information of the continuous-time signal can be uniquely retrieved from the sequence of sample data *if, and only if*, the Fourier transform of a continuous-time signal is zero for all frequencies greater than the maximum frequency found in this signal (aliasing removal) and the leakage phenomenon is avoided [8]. Based on this theory, in Sections I.6 and I.7 the classical mathematical tools used to compute phasors in electric power system will be presented.

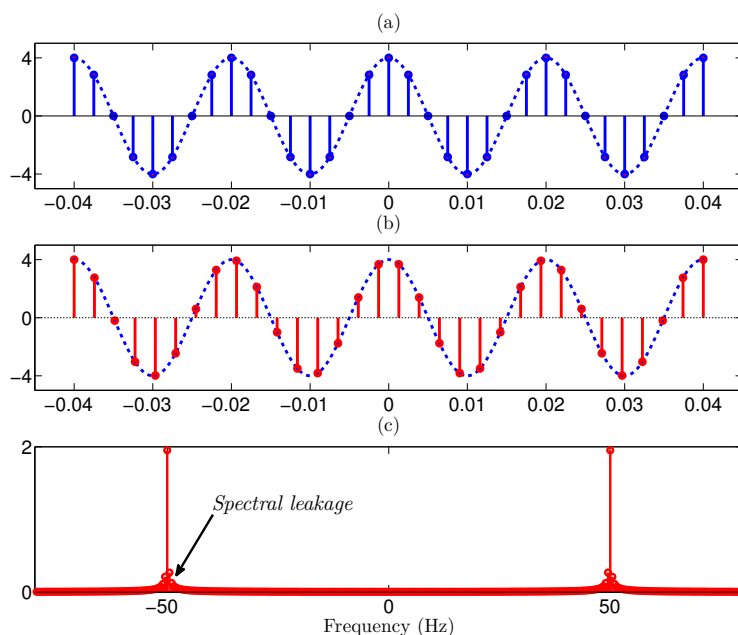


Figure I.8: (a) Synchronous sampling, (b) asynchronous sampling, and (c) Fourier transform of a non-periodic sequence.

I.6 Discrete Fourier transform (DFT) for estimating fundamental and harmonic phasors

Digital signal processing uses a finite amount of data to perform any calculation envisaged. In this way, the estimation of voltage and current phasors in digital domain must have a limited number of samples taken at uniform intervals $y(nT_s)$ ($n=0, 1, 2, \dots, N-1$). Recalling that the Fourier series claims for the knowledge of the periodic waveform only over the interval of periodicity, it can be concluded that the samples must be taken inside of the waveform's period T . From now, the concept of *data window* will be used, also known as observation interval, that represents the time span in which the samples are obtained.

In the preceding section, the performed calculations have been based on an infinite amount of data, however, the data window truncates the amount of data yielding a process called *windowing*, being represented by a function $w(t)$ [3]. Since the ranging of the samples is from 0 to $N-1$, a finite number of samples can be obtained by the product of the continuous-time signal $y(t)$, the sampling distribution $h(t)$, and the windowing function $w(t)$, as follows

$$y_{sw}(t) = y(t)h(t)w(t) = \sum_{n=0}^{N-1} y(nT_s)\delta(t - nT_s). \quad (\text{I.61})$$

It is very important to evaluate the Fourier transform of the windowed sampled data $y_{sw}(t)$. Thus, the frequency convolution theorem may be applied to accomplish this task. The Fourier transforms of $y(t)$ and $h(t)$ have been calculated in the previous section, thereby, only the Fourier transform of $w(t)$ must be evaluated. Based on Eq. (I.30), and taking into account Eq. (I.21) to simplify the calculation, the Fourier transform of an unitary rectangular function is

$$W(f) = \int_{-\infty}^{+\infty} w(t)e^{-j2\pi ft} dt = \int_{-\frac{T}{2}}^{\frac{T}{2}} e^{-j2\pi ft} dt = T \frac{\sin(2\pi f \frac{T}{2})}{(2\pi f \frac{T}{2})} \equiv T \text{sinc}(fT) \quad (\text{I.62})$$

in this way, the Fourier transform pair is determined as follows

$$w(t) = 1, \quad -\frac{T}{2} \leq t \leq \frac{T}{2} \iff T \text{sinc}(fT). \quad (\text{I.63})$$

Eq. (I.62) have been tidied up in terms of the sinus cardinal function, also called *sinc* function. It presents two major characteristics: an oscillating effect and *zero crossings* at all nonzero integer values that are related to the nominal frequency of the continuous signal. Fig. I.9 displays the graphical representation of the Fourier transform pair.

Forthwith, the Fourier transform of a windowed sampled data $y_{sw}(t)$ can be obtained. Hence, it is only necessary to perform the convolution between the Fourier transforms $Y(f)$, $H(f)$, and $W(f)$ to provide the $Y_{sw}(f)$, as illustrated in Fig. I.10 (a). The *sinc* function provides an efficient manner for evaluating the sampling process. Fig. I.10 (a) also shows that when the synchronous sampling condition is ensured, the position of $Y(f)$ coincides exactly with the peak of the main lobe of $Y_{sw}(f)$ at fundamental frequency (the impulse's amplitude of $Y(f)$ has been extended by a factor 8 for easy viewing).

Otherwise, when the synchronous sampling condition is not satisfied, the position of $Y(f)$ does not coincides with the peak of the main lobe, and spurious harmonic frequencies may be generated according to the degree of asynchronism. In this way, the location of these harmonic frequencies do not coincide with the zero-crossings of $Y_{sw}(f)$. This displacement between the Fourier transforms is caused by the leakage effect, as illustrated in Fig. I.10 (b) [8].

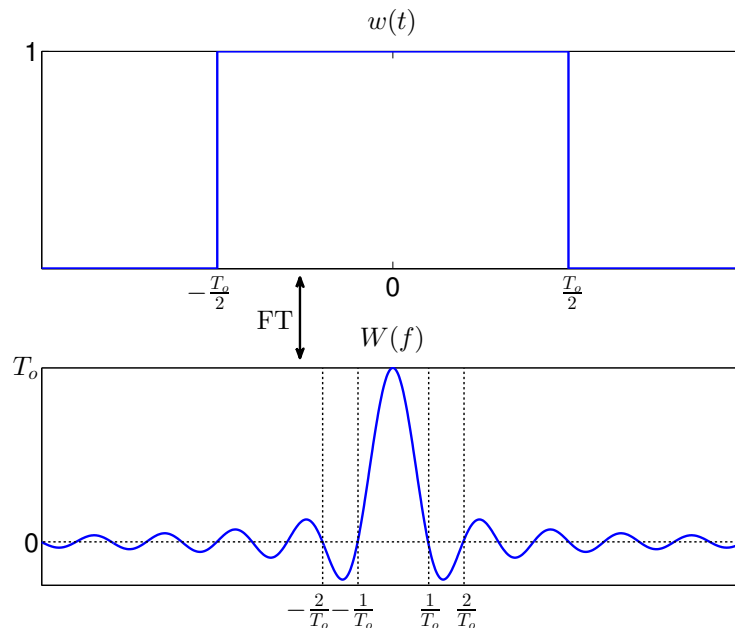


Figure I.9: Rectangular time function $w(t)$ and its Fourier transform $W(f)$. Note the oscillating effect in frequency-domain caused by the truncation process in time-domain.

Using a finite sequence obtained by asynchronous sampling condition for computing voltage and current phasors, the estimates will present severe errors. The leakage phenomenon is one of the major sources of error in the phasor estimation in electric power systems, because the voltage and current signals have constantly changing fundamental frequency provoked by dynamic variations on the power system.

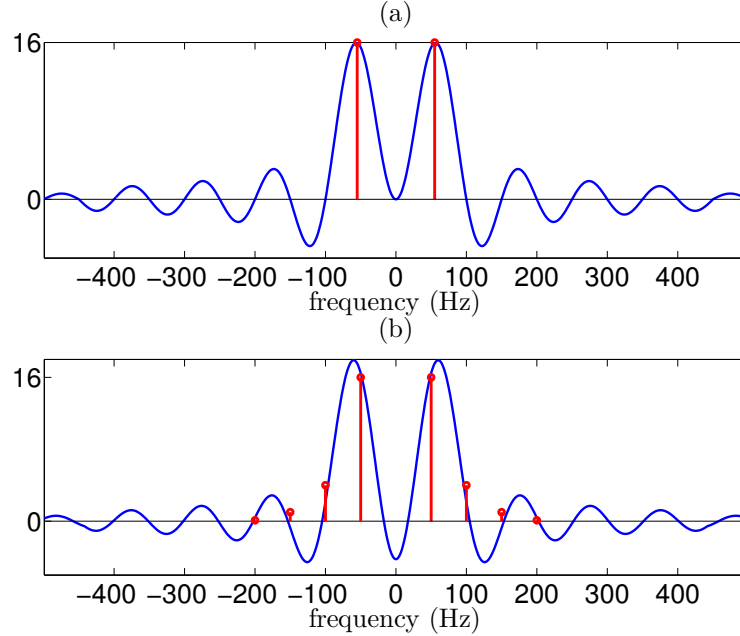


Figure I.10: (a) Synchronous sampling, (b) asynchronous sampling, and (c) The Fourier transform of a non-periodic sequence (obtained results concerning $N=8$ samples by cycle at 50-Hz).

In Section I.3, it has been demonstrated that the phasor representation of a pure sinusoidal quantity is also its exponential Fourier series. Looking back at Eqs. (I.24)-(I.25), one can observe that the complex coefficients of the Fourier series can be obtained directly, thus

$$A_k - jB_k = \frac{2}{T} \int_{-\frac{T}{2}}^{\frac{T}{2}} y(t) e^{-jk\omega t} dt \quad k = 0, \pm 1, \pm 2, \dots \quad (\text{I.64})$$

For a data window with samples $\{n=0,1,2,\dots, N-1\}$ obtained at sampling period T_s , Eq. (I.64) can be rewritten as

$$Y(k) = A_k - jB_k = \frac{2}{N} \sum_{n=0}^{N-1} y(nT_s) e^{-j\left(\frac{2\pi nk}{N}\right)}. \quad (\text{I.65})$$

The coefficients of the Fourier series may be understood as complex amplitudes, thereby, by dividing Eq. (I.65) by the factor $\sqrt{2}$ and expressing the result, we have

$$Y(k) = \frac{2}{\sqrt{2}N} \sum_{n=0}^{N-1} y(nT_s) e^{-j\left(\frac{2\pi nk}{N}\right)} = \frac{\sqrt{2}}{N} \sum_{n=0}^{N-1} y(nT_s) e^{-j\left(\frac{2\pi nk}{N}\right)} \quad (\text{I.66})$$

thereupon, splitting Eq. (I.66) into real and imaginary parts will provide the classical method for calculating the Fourier transform of a limited number of samples taken from a periodic continuous-time signal. This method is known as Discrete Fourier Transform (DFT) for phasor representation [3]. Eqs. (I.67)-(I.68) are the formulas for estimating the real and imaginary phasor components, respectively (see Appendix A)

$$Y_r = \frac{\sqrt{2}}{N} \sum_{n=0}^{N-1} y(nT_s) \cos\left(\frac{2\pi nk}{N}\right) \quad (\text{I.67})$$

$$Y_i = \frac{\sqrt{2}}{N} \sum_{n=0}^{N-1} y(nT_s) \sin\left(\frac{2\pi nk}{N}\right) \quad (\text{I.68})$$

being n the sample index, k the frequency component, and $\frac{2\pi}{N}$ represents the angle between the samples, that is, the sampling angle based on the period of the fundamental frequency component.

For the generalized DFT representation the factor $\frac{\sqrt{2}}{N}$ must be omitted, Eq. (I.69), to allow the entire frequency spectrum evaluation. One can notice the intrinsic relationship between the Fourier series and the spectrum of the DFT

$$Y(k) = \sum_{n=0}^{N-1} y(nT_s) e^{-j\left(\frac{2\pi nk}{N}\right)}. \quad (\text{I.69})$$

According to [3], it is possible to obtain the coefficients of the Fourier series performing a division between the DFT's spectrum, for each frequency component k , and the number of samples N . For example, $N=24$ samples are taken over a window of 0.02 ms from a pure sinusoidal input signal, which corresponds to one period of the 50-Hz signal. In this case, the sampling frequency is 1200 Hz, and the maximum harmonic component k that can be estimated to obey the sampling theorem is 600 Hz.

In this way, the DFT's spectrum need to be evaluated for the frequency components from 0 to 11th order. Due to the pure sinusoidal feature of the input signal, only the DFT's spectrum for $k = 1$, related to the nominal frequency, will not be null. Consequently, the obtained complex result must be divided by N and multiplied by 2 (to cover the negative and positive parts of the spectrum) for computing the Fourier series coefficients A_1 and B_1 . If the signal have harmonic components the procedure to compute the other coefficients is quite similar.

I.7 Improving phasor estimation using Fast Fourier transform (FFT)

In 1960, I. J. Good published a pioneering work for computing Fourier series using an iterative algorithm that has been considered a breakthrough in digital signal processing [15]. Having this work as reference, several other high-performance algorithms were proposed. Nevertheless, the algorithm that stood out among all the others is credited to J. W. Cooley and J. W. Tukey, because their algorithm had far-reaching effects on the computational efficiency and accuracy [16]. This algorithm is known as Fast Fourier transform (FFT).

In essence, the FFT is a particular algorithm that performs a series of computations much more rapidly than other algorithms, such as the DFT-based. The secret of the success of FFT is related to the properties of factorization, recursivity, and identity that are used in a very clever manner to drastically reduce the computational burden. FFT is explained in an intuitive mathematical formulation to demonstrate its performance features. In addition, the Radix-2 DIT FFT algorithm, belonging to the class *decimation in time*, is presented and evaluated for estimating phasors.

I.7..i Mathematical formulation

The theory presented in the current subsection has been based on the first class reference [13]. Consider the generalized DFT given by Eq. (I.69) with slight modifications for convenience of notation, hence

$$Y(k) = \sum_{n=0}^{N-1} y_0(n)e^{-j\theta nk} \quad (\text{I.70})$$

where $\theta = \frac{2\pi}{N}$ is the sampling angle.

Now, let us consider $N=4$ samples inside a data window matched with the period of the fundamental signal component, thus, the sampling angle is equal to 90° and the frequency component k varies from 0 to 3 to cover the entire frequency spectrum. Like this, it is clear that Eq. (I.70) may be rewritten as follows

$$Y(0) = y_0(0) + y_0(1) + y_0(2) + y_0(3) \quad (\text{I.71})$$

$$Y(1) = y_0(0) + y_0(1)e^{-j\theta} + y_0(2)e^{-j2\theta} + y_0(3)e^{-j3\theta} \quad (\text{I.72})$$

$$Y(2) = y_0(0) + y_0(1)e^{-j2\theta} + y_0(2)e^{-j4\theta} + y_0(3)e^{-j6\theta} \quad (\text{I.73})$$

$$Y(3) = y_0(0) + y_0(1)e^{-j3\theta} + y_0(2)e^{-j6\theta} + y_0(3)e^{-j9\theta} \quad (\text{I.74})$$

Eq.(I.71)-(I.74) may be represented in matrix notation, hence

$$\begin{bmatrix} Y_0 \\ Y_1 \\ Y_2 \\ Y_3 \end{bmatrix} = \begin{bmatrix} 1 & 1 & 1 & 1 \\ 1 & e^{-j\theta} & e^{-j2\theta} & e^{-j3\theta} \\ 1 & e^{-j2\theta} & e^{-j4\theta} & e^{-j6\theta} \\ 1 & e^{-j3\theta} & e^{-j6\theta} & e^{-j9\theta} \end{bmatrix} \begin{bmatrix} y_0(0) \\ y_0(1) \\ y_0(2) \\ y_0(3) \end{bmatrix} \quad (\text{I.75})$$

or more compactly as

$$Y(k) = \left[e^{-j\theta nk} \right] y_0(n). \quad (\text{I.76})$$

Assuming that all elements of the square matrix $[e^{-j\theta nk}]$ and the column vector $y_0(n)$ are possibly complex, then N^2 complex multiplications and $N(N-1)$ complex additions are required to cover the matrix computation. The FFT is very performance-focused, therefore, it reduces the number of complex multiplications and additions required for computing (I.70). For a comprehensive and intuitive understanding of the FFT mathematical formulation, let us take a closer look at the matrix system (I.75).

Some direct conclusions can be drawn, for instance, one can notice that the elements $e^{-j\theta}$ and $e^{-j9\theta}$ are equal. The aforementioned equality can be proved in an insightful manner replacing θ angle by the sampling angle 90° , thus $e^{-j90^\circ} = e^{-j810^\circ} = e^{-j720^\circ} e^{-j90^\circ}$, that is, $e^{-j720^\circ} = 1$ because it represents two revolutions along the unit circle. Other equalities may be guaranteed considering this trigonometric identity, therefore: $e^{-j2\theta} = e^{-j6\theta}$ ($e^{-j180^\circ} = e^{-j540^\circ} = e^{-j360^\circ} e^{-j180^\circ}$) and $e^{-j4\theta} = e^{-j360^\circ} = 1$. Like this, the matrix system (I.75) can be rewritten as

$$\begin{bmatrix} Y_0 \\ Y_1 \\ Y_2 \\ Y_3 \end{bmatrix} = \begin{bmatrix} 1 & 1 & 1 & 1 \\ 1 & e^{-j1\theta} & e^{-j2\theta} & e^{-j3\theta} \\ 1 & e^{-j2\theta} & 1 & e^{-j2\theta} \\ 1 & e^{-j3\theta} & e^{-j2\theta} & e^{-j1\theta} \end{bmatrix} \begin{bmatrix} y_0(0) \\ y_0(1) \\ y_0(2) \\ y_0(3) \end{bmatrix} \quad (\text{I.77})$$

the square matrix in (I.77) may be conveniently factored yielding

$$\begin{bmatrix} Y_0 \\ Y_2 \\ Y_1 \\ Y_3 \end{bmatrix} = \begin{bmatrix} 1 & e^{-j0} & 0 & 0 \\ 1 & e^{-j2\theta} & 0 & 0 \\ 0 & 0 & 1 & e^{-j\theta} \\ 0 & 0 & 1 & e^{-j3\theta} \end{bmatrix} \begin{bmatrix} 1 & 0 & e^{-j0} & 0 \\ 0 & 1 & 0 & e^{-j0} \\ 1 & 0 & e^{-j2\theta} & 0 \\ 0 & 1 & 0 & e^{-j2\theta} \end{bmatrix} \begin{bmatrix} y_0(0) \\ y_0(1) \\ y_0(2) \\ y_0(3) \end{bmatrix} \quad (\text{I.78})$$

this factored matrix is the main key related to the efficiency of the FFT algorithm. The element e^{-j0} has been considered in strategic positions only to facilitate and allow some identity and recursivity manipulations that will be shown below. One can note that the column vector $Y(k)$ has been interchanged for ensuring a correlation due to the factorization process. Clearly, the multiplication of the two square matrices of (I.78) provides the square matrix of (I.77), however the rows 2 and 3 have been changed their positions (the rows are renumbered from 1 to 4 for ease of reference).

Based upon this statement, one should then evaluate the number of complex multiplications and additions required to compute each frequency component relative to the factored matrix. For accomplish this goal, let us split the analysis into two steps. First let

$$\begin{bmatrix} y_1(0) \\ y_1(1) \\ y_1(2) \\ y_1(3) \end{bmatrix} = \begin{bmatrix} 1 & 0 & e^{-j0} & 0 \\ 0 & 1 & 0 & e^{-j0} \\ 1 & 0 & e^{-j2\theta} & 0 \\ 0 & 1 & 0 & e^{-j2\theta} \end{bmatrix} \begin{bmatrix} y_0(0) \\ y_0(1) \\ y_0(2) \\ y_0(3) \end{bmatrix} \quad (\text{I.79})$$

the column vector $y_1(n)$ is equal to the product between the last two matrices on the right side of (I.78). For computing the element $y_1(0)$ is only required one complex multiplication and one complex addition (note that e^{-j0} is not reduced to unity to provide a generalized approach), thus

$$y_1(0) = y_0(0) + y_0(2)e^{-j0}. \quad (\text{I.80})$$

For computing $y_1(1)$, one complex multiplication and one complex addition are required. However, to compute $y_1(2)$ only one complex addition is demanded, because the identity and recursivity properties can be applied. This may be proved from the fact that $e^{-j2\theta} = e^{-j180^\circ} = -e^{-j\theta}$, hence

$$y_1(2) = y_0(0) + y_0(2)e^{-j2\theta} = y_0(0) - y_0(2)e^{-j\theta} \quad (\text{I.81})$$

one can note that the complex multiplication $y_0(2)e^{-j\theta}$ has been computed in the calculation of $y_1(0)$, thereby a recursive updating may be applied. By the same reasoning, for computing $y_1(3)$ only one addition is required. One can conclude that for computing the column vector $y_1(n)$ two complex multiplication and four complex additions must be carry out.

The second step of the procedure aims for completing the computation of (I.78), hence

$$\begin{bmatrix} Y_0 \\ Y_2 \\ Y_1 \\ Y_3 \end{bmatrix} = \begin{bmatrix} y_2(0) \\ y_2(1) \\ y_2(2) \\ y_2(3) \end{bmatrix} = \begin{bmatrix} 1 & e^{-j\theta} & 0 & 0 \\ 1 & e^{-j2\theta} & 0 & 0 \\ 0 & 0 & 1 & e^{-j\theta} \\ 0 & 0 & 1 & e^{-j3\theta} \end{bmatrix} \begin{bmatrix} y_1(0) \\ y_1(1) \\ y_1(2) \\ y_1(3) \end{bmatrix} \quad (\text{I.82})$$

the element $y_2(0)$ can be computed by one complex multiplication and one complex addition

$$y_2(0) = y_1(0) + y_1(1)e^{-j\theta} \quad (\text{I.83})$$

and the element $y_2(1)$ requires only one complex addition for its computation due to the equality $-e^{-j\theta} = e^{-j2\theta}$ whose value has been determined in Eq. (I.83). Similarly, the element $y_2(2)$ requires one complex multiplication and one addition, whereas the element $y_2(3)$ requires only one addition.

Now, it is possible to evaluate the number of complex operations. Taking into account the two complex multiplications and the four complex additions for the first and second steps, the computation of the column vector $Y(k)$ requires twelve operations (four complex multiplications and eight complex additions), whilst the number of operations by means of Eq. (I.70) is twenty-eight (sixteen complex multiplications (N^2) and twelve complex additions $N(N-1)$). It is clear that the huge reduction of the number of required operations to compute the frequency components is directly related to the sparsity of the factored matrices. In digital signal processing the computational burden is directly linked with the amount of mathematical operations, especially the number of multiplications, thus one can remark the effectiveness of this powerful algorithm.

For ensuring the robustness of the FFT, N must be a power of two. This statement is more evident if we consider the representation given by $N = 2^\kappa$. In this way, one can conclude that the FFT algorithm is a procedure for factoring an $N \times N$ matrix into κ matrices of order $N \times N$, in which the factored matrices bring the aforementioned properties for reducing the number of mathematical operations. For the presented formulation, the number of samples is $N=4$, therefore the factorization process will yield $\kappa=2$ matrices, as illustrated in (I.78).

The amount of complex operations can be determined in terms of the parameters N

and κ . For the previous example, $\frac{N\kappa}{2}=4$ represents the number of multiplications and $N\kappa=8$ is the number of additions. Assuming that the computing time is proportional to the number of complex multiplications, then an approximative ratio related to the FFT computing time is given by

$$\frac{N^2}{N\kappa/2} = \frac{2N}{\kappa}. \tag{I.84}$$

Fig. I.11 depicts an approximate comparison between the number of complex multiplications required to the FFT algorithm and the number of multiplications demanded by the classical DFT. A very large reduction can be obtained when the number of samples inside a data window increases.

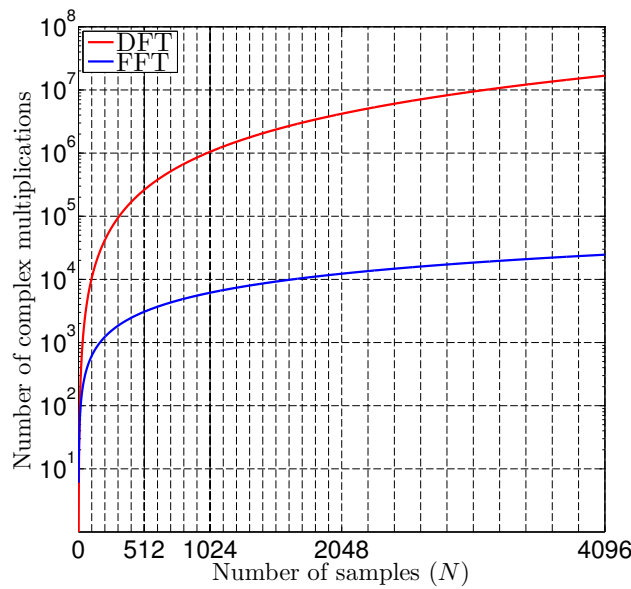


Figure I.11: Comparison between the number of complex multiplications required by the DFT and FFT algorithms (adapted of [13]).

Another way to easily describe the factoring process given by (I.78) is in term of a *flow*

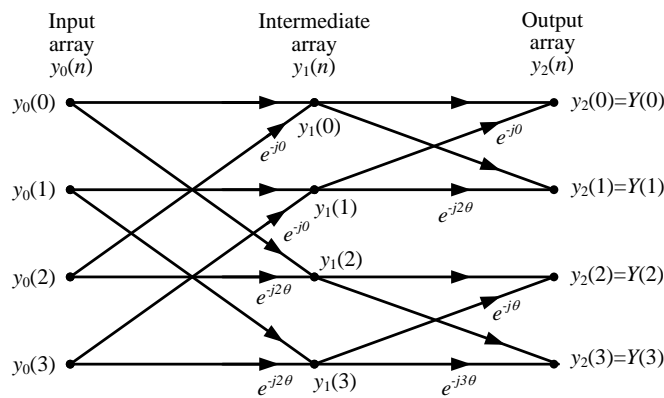


Figure I.12: FFT signal flow graph for $N=4$ (adapted of [13]).

graph, as depicted in Fig. I.12. The input array $y_0(n)$ formed by the samples is a vertical column of nodes on the left side of the graph. The intermediate array of nodes is the column vector given by (I.79). The output array of nodes $y_2(n)$, numerically equal to the frequency component vector $Y(k)$, is computed according to (I.82). The flow graph interpretation is quite simple. The nodes are linked by solid lines representing the *transmission path*. A path sends the information of the node, multiplies the quantity by the factor e^{-jz} that appears near the arrowhead, and inputs the result into the node of the subsequent array. The input information arriving on a given node are combined additively. When the factor e^{-jz} is absent, this indicates that it is equal to one.

The signal flow graph also provides an interesting method to determine the amount of mathematical computations demanded in the factored system (I.78). In this section a mathematical formulation for $N=4$ has been presented, however, based on the shown analyzes, it is possible to develop a general approach for any value to N (as power of two) to provide a mathematical framework for implementing FFT algorithms.

I.7..ii Radix-2 Decimation in Time (DIT) FFT

The theory presented in this subsection has been based on [13] and [17]. There are many ways to perform the FFT decomposition, however, the algorithm called Radix-2 decimation in time (DIT) FFT has been largely used to accomplish this task due to its accurate, efficient and simple form of implementation. Radix-2 DIT FFT algorithm have two main features: the first is related to the splitting of periodic time sequences into even and odd samples, and the second is based on bit-reversed data ordering.

In essence, the Radix-2 algorithm divides the classical DFT of size N into two smallest DFTs of size $N/2$, in other words, the Radix-2 applies the *divide-and-conquer* strategy. In order to exemplify, let us consider $N=4$ samples inside a data window, thus, Radix-2 DIT computes the DFT for the sets of even and odd-indexed samples given by $y_{even}=\{y_0(0), y_0(2)\}$ and $y_{odd}=\{y_0(1), y_0(3)\}$, respectively. Consequently, the Radix-2 DIT divides the DFT into two summations over the even and odd-indexed samples, yielding

$$Y(k) = \sum_{m=0}^{\frac{N}{2}-1} y_{even}(m) e^{-j\frac{2\pi}{N}mk} + \sum_{m=0}^{\frac{N}{2}-1} y_{odd}(m) e^{-j\frac{2\pi}{N}(m+\frac{1}{2})k} \quad (\text{I.85})$$

the exponential function in the second summation has been written with a slight modification merely to cover the odd-indexed samples. In a compact form, Eq. (I.85) can be rewritten as

$$Y(k) = \sum_{m=0}^{\frac{N}{2}-1} y_{even}(m) e^{-j2\theta mk} + \sum_{m=0}^{\frac{N}{2}-1} y_{odd}(m) e^{-j2\theta(m+\frac{1}{2})k} \quad (\text{I.86})$$

one can notice that the common factor $e^{-j\theta k}$ may be withdrawn of the second summation

yielding

$$Y(k) = \sum_{m=0}^{\frac{N}{2}-1} y_{\text{even}}(m)e^{-j2\theta mk} + e^{-j\theta k} \sum_{m=0}^{\frac{N}{2}-1} y_{\text{odd}}(m)e^{-j2\theta mk} = A(k) + e^{j\theta k}B(k) \quad (\text{I.87})$$

$$\forall 0 \leq k < N.$$

Eq. (I.87) represents the classical Radix-2 DIT FFT synthesis equation used for algorithms development. Each summation represents the DFT for $N/2$ -point of the sequences y_{even} and y_{odd} , respectively. Thereby, $\text{DFT}[y_{\text{even}}]=A(k)$ for even-indexed samples, and $\text{DFT}[y_{\text{odd}}]=B(k)$ for odd-indexed samples. Looking closely at Eq. (I.87) some interesting insights on the periodicity, symmetrical and recursivity properties may be drawn.

For $A(k)$ the computed frequency components within $0 \leq k < N/2$, taking into account a DFT of length $N/2$, is numerically identical to a DFT from the range $N/2 \leq k < N$, that is, the periodicity property is present. However, for $B(k)$, the factor $e^{j\theta k}$ will introduce a symmetry between the DFTs computed from the ranges $0 \leq k < N/2$ and $N/2 \leq k < N$, respectively. In this way, it is only necessary to compute the DFTs from the range $0 \leq k < N/2$ and perform the recursivity property. Thus, the whole DFT's spectrum may be calculated as given by

$$Y(k) = A(k) + e^{j\theta k}B(k) \Rightarrow Y\left(k + \frac{N}{2}\right) = A(k) - e^{j\theta k}B(k) \quad \forall 0 \leq k < \frac{N}{2}. \quad (\text{I.88})$$

Once again, one should then examine the number of complex mathematical operations required to compute the Radix-2 DIT. In order to achieve this goal, Eq. (I.87) can be rewritten as

$$Y(0) = y_0(0) + y_0(2) + y_0(1) + y_0(3) \quad (\text{I.89})$$

$$Y(1) = y_0(0) + y_0(2)e^{-j2\theta} + y_0(1)e^{-j\theta} + y_0(3)e^{-j3\theta} \quad (\text{I.90})$$

$$Y(2) = y_0(0) + y_0(2)e^{-j4\theta} + y_0(1)e^{-j2\theta} + y_0(3)e^{-j6\theta} \quad (\text{I.91})$$

$$Y(3) = y_0(0) + y_0(2)e^{-j6\theta} + y_0(1)e^{-j3\theta} + y_0(3)e^{-j9\theta}. \quad (\text{I.92})$$

Doubtlessly, Eqs. (I.89)-(I.92) are identical to Eqs. (I.71)-(I.74). In this way, it can be seen the reason for the efficiency of the Radix-2 DIT FFT algorithm, because it presents the special properties of minimizing the amount of complex mathematical operations, as shown in the previous section. As declared earlier in this section, the Radix-2 DIT claims for a bit-reversed data ordering, however, an important question may be raised: What is the role of bit reversal? The answer for this issue concerns the reverse indexed addressing bits for *read/write* of data used by the Digital Signal Processor (DSP) or Field-Programmable Gate Array (FPGA).

Recall that the matrix factoring introduces an interchange between some rows of the frequency component column vector, as shown in (I.78). The procedure consists of replacing the index k by its binary equivalent for all components of the frequency component vector obtained by the factored matrices, then the binary arguments are *flipped* (that is, 01

becomes 10, 10 becomes 01, and so on and so forth) to provide the corrected positions, as illustrated in (I.93).

One can remark that $Y(00)$ does not move its first position, $Y(10)$ moves to the third position, $Y(01)$ moves to the second position, and $Y(11)$ does not move its fourth position (the positions have been numbered from 1 to 4 for convenience). Based on this example, a generalized approach may be obtained to implement Radix-2 DIT FFT algorithm considering high order of data.

$$Y'(k) = \begin{bmatrix} Y(0) \\ Y(2) \\ Y(1) \\ Y(3) \end{bmatrix} = \begin{bmatrix} Y(00) \\ Y(10) \\ Y(01) \\ Y(11) \end{bmatrix} \text{ flips to } \begin{bmatrix} Y(00) \\ Y(01) \\ Y(10) \\ Y(11) \end{bmatrix} = \begin{bmatrix} Y(0) \\ Y(1) \\ Y(2) \\ Y(3) \end{bmatrix} = Y(k) \quad (\text{I.93})$$

To represent phasors using this algorithm is solely required to multiply Eq. (I.88) by the factor $\frac{\sqrt{2}}{N}$. One can see that the multiplicative factor is the same used by the classical DFT, therefore

$$Y_s(k) = \frac{\sqrt{2}}{N} \left(A(k) + e^{j\theta k} B(k) \right) \Rightarrow Y_s \left(k + \frac{N}{2} \right) = \frac{\sqrt{2}}{N} \left(A(k) - e^{j\theta k} B(k) \right) \quad (\text{I.94})$$

$$\forall 0 \leq k < \frac{N}{2}.$$

A signal flow graph may be also employed to represent Radix-2 DIT. In general, this graphical representation is called *butterfly* and its interpretation is quite similar to Fig. I.12. A frequency-adaptive algorithm will be proposed further in Chapter III where the Radix-2 DIT FFT is developed together with frequency estimation routine, FIR (Finite Impulse Response) filtering process, and fast linear trigonometric interpolation.

I.8 Recursive update for fundamental phasor using DFT and Radix-2 FFT

An efficient manner to reduce the computational burden in phasor estimation is using recursive programming. This powerful technique uses the data previously calculated to update the subsequent data, therefore the number of mathematical operations is widely reduced. In the previous section, it was shown that the recursion is an intrinsic property of the fast Fourier transform to update the elements of the factored matrix, however, without loss of generality, this property may also be applied to update phasors previously estimated.

The procedure consists of moving the data window from sample by sample, in this way, the phasor computed in the previous data window is updated taking into account only two samples of the subsequent data window. Recursive programming is able to ensure the achievement of stationary phasors [3]. An important issue that may arise in the context of phasor estimation is: Can we obtain the same stationary phasor estimate computing full-DFT for each moving data window?

Unfortunately, it is not possible, because the displacement between each sample is related to the sampling angle, thus, performing full-DFT for each independent data window,

the phasor estimate will rotate at the uniform rate related to the sampling angle. For this case, the algorithm is called non-recursive and its application is not envisaged for practical applications. In subsections I.8.a and I.8.b, general informations are addressed about the recursive DFT and Radix-2 DIT FFT to estimate phasors under nominal and off-nominal signals.

I.8.a Nominal frequency signals

The signals at nominal frequency satisfy Eq. (I.58), that is, a periodic sequence may be properly taken of a continuous-time signal. Based on Fig. I.13, it should be noted that the number of samples N inside each moving window are common (for this example, there are 12 samples per cycle). Special attention must be paid to the transition between windows. Looking closely at the window 1, one can observe that it has two new samples, $y(1)$ and $y(12)$, which did not exist in the window 0. All others samples are common between them.

A similar analysis may be performed between windows 1 and 2. It is possible to note that into window 2 the new samples are $y(2)$ and $y(13)$, which did not exist in the window 1. In this way, a recursive DFT algorithm may be implemented according to

$$\hat{Y}^{N+r} = \hat{Y}^{N+r-1} + \frac{\sqrt{2}}{N} (y(N+r) - y(r)) e^{-jr\theta} \quad (\text{I.95})$$

where r represents the recursion index.

The analysis of Eq. (I.95) may be performed as follows: for $r=1$, the phasor estimate of window 1 (\hat{Y}^{N+1}) is equal to the phasor estimate of window 0 (\hat{Y}^N) taking into account an angular retardation of θ , furthermore the samples $y(N+1)$ and $y(1)$ are identical because the signal is a pure sinusoid. Therefore, the second term in Eq. (I.95) disappears. The same analysis could be performed between the windows 1 and 2. For both analyzes, the

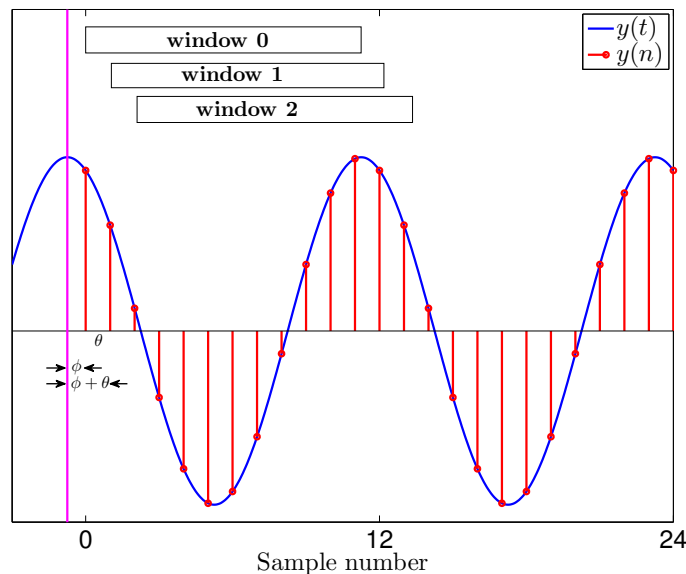


Figure I.13: Sliding window applied to recursive updating of phasor measurements. Note that the angle ϕ is the phase angle of the phasor, whereas θ represents the sampling angle between successive samples.

phasor estimates are the same providing a stationary representation.

Considering the number of mathematical operations, it can be seen that $(N-1)$ multiplications in the new data window are the same as those used in the previous window. The recursive DFT algorithm for computing phasor estimates has been credited to *prof.* Arun Phadke [3]. In I.7.ii, it has been noticed that the Radix-2 algorithm splits the full-DFT into smallest DFTs whose results are the same as those provided by full-DFT. In this way, the recursion property shown in Eq. (I.95) may also be applied to Radix-2 DIT FFT, in which Eq. (I.94) must be employed to compute the phasor estimate for the window 0.

I.8.b Off-nominal frequency signals (leakage phenomenon)

The Fourier theory presented in Section I.5 demonstrates the harms of the leakage phenomenon over the frequency spectrum. In this context, it is interesting to determine the impact of the leakage phenomenon when the estimation is dynamically performed. For this, let us assume a continuous-time signal at off-nominal frequency $f_o + \Delta f$ (fundamental frequency and frequency deviation, respectively), hence

$$y(t) = Y_m \cos(2\pi(f_o + \Delta f)t + \phi) \quad (\text{I.96})$$

that can be rewritten as follows

$$\begin{aligned} y(t) &= \text{Re} \left[Y_m e^{j(2\pi f_o t)} e^{j(2\pi \Delta f t + \phi)} \right] \\ &= \text{Re} \left[e^{j2\pi f_o t} Y_m e^{j(2\pi \Delta f t + \phi)} \right]. \end{aligned} \quad (\text{I.97})$$

The phasor representation for this waveform is shown in Eq. (I.98), hence

$$Y = \frac{Y_m}{\sqrt{2}} e^{j(2\pi \Delta f t + \phi)}. \quad (\text{I.98})$$

Phasor represents the steady state condition of time-varying physical quantities, however, in Eq. (I.98), it can be seen that this statement is not valid, because the independent variable t (*time*) is already present. Thus, one can state that the leakage phenomenon will cause a rotation on the phasor estimate at the uniform rate Δf . This concept is illustrated in Fig. I.14. Consider a sinusoid at off-nominal power frequency (51 Hz) sampled at intervals $T_s=3.33$ ms, that is, six samples obtained over a window of 0.02 ms, which corresponds to one period of the nominal 50-Hz signal.

The phase angle of this signal has been stipulated at $\phi=45^\circ$. The compact Eq. (I.98) claims to a constant magnitude of the estimated phasor, but the phase angle changes uniformly at a rate $2\pi(51-50)t$. Taking into account the values reported over time, one can observe that the phase angle estimates continuously increase until they reached 180° and after they wrap around to -180° . This pernicious process repeats itself over time, thus the phasor estimate can not be correlated with a steady state condition.

Eq. (I.98) is a compact form to evaluate the leakage phenomenon on the phasor estimate. However, applying the recursive DFT or recursive Radix-2 DIT FFT algorithms for computing dynamically phasors, other effects caused by the leakage phenomenon may be founded. Figs. I.15 (a)-(b) display a zoomed view of magnitude and phase angle estimation

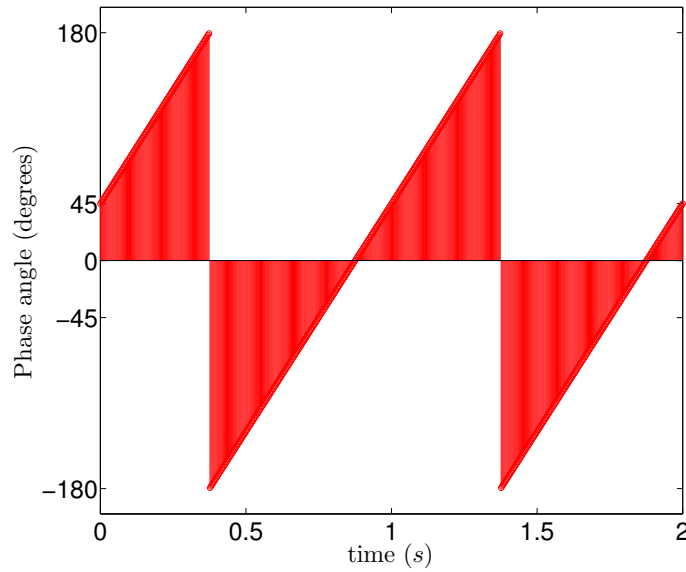


Figure I.14: Impact of the leakage phenomenon on the phase angle estimate. Sampling process of a power signal at off-nominal frequency (51 Hz).

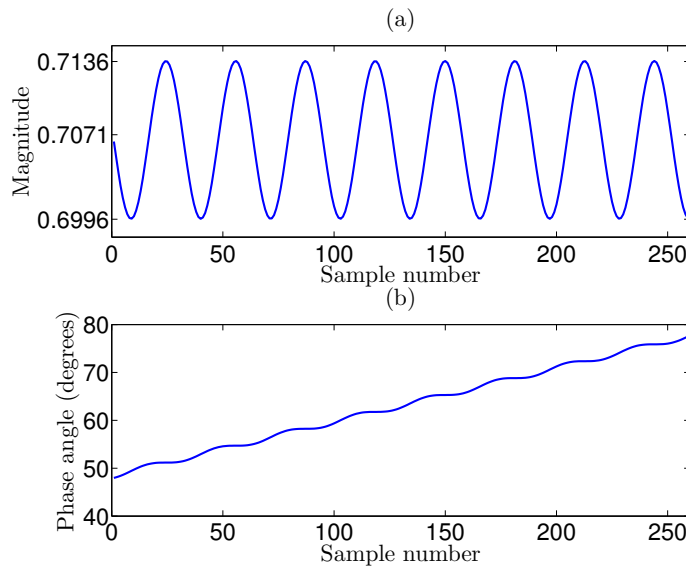


Figure I.15: (a) Magnitude estimate and (b) phase angle estimate using recursive DFT. For both the leakage phenomenon introduces a second order harmonic component.

using the recursion formula (I.95), respectively. The peak value and the initial phase angle of a voltage signal has been stipulated as $Y_m=1$ V and $\phi=45^\circ$.

The leakage phenomenon introduces a second harmonic component that yields oscillations varying over time on the amplitude and phase angle estimates. This effect has been properly reported in [3] and it must be eliminated or *alleviated* by filtering process in order to ensure the accuracy of the phasor estimate. In Appendix B, the mathematical background of the leakage phenomenon impact on the phasor estimates computed from sampled data is presented.

I.9 Leakage phenomenon reduction techniques review

We have seen that the only manner to avoid the leakage phenomenon is ensuring the synchronization between the signal period and the sampling period. However, for electric power systems, this task is not quite as simple as it appears. According to [8], the synchronization can hardly be attained in practice, due to the following reasons: the signal period is generally unknown, the sampling clock could not have a high resolution to satisfy Eq. (I.58), and, once known the signal period, it may vary around its nominal value along the whole measurement process. Indeed, great challenges must be overcome for ensuring a correct synchronization. In this section, several methods dealing with non-synchronous sampling condition for computing phasor estimates from sampled data are presented. Among the various techniques published in the technical literature, the methods discussed in this section have a strong plea for practical applications.

Three classical techniques - weighing windows, frequency tracking and resampling - have frequently been applied to give back to Fourier transform its inherent robustness to estimate the parameters of interest. In Section I.6, the concept of window function has been introduced for computing DFT. It has been demonstrated that the Fourier transform of an unitary rectangular window contains *ripples* over the frequency spectrum caused by abrupt truncation of the signal outside the required data window. To circumvent this effect, other window functions may be used to produce less ripples over the spectrum.

Generally, cosine windows are applied for **weighing** the sampled signal and, consequently, for reducing the effects of the lack of synchronism between the signal period and the sampling period. Among several cosine windows, one can quote the most employed: Hanning, Hamming, Blackman, Blackman-Harris, and Flat-top windows [8]. In essence, these windows have a similar mathematical formulation, however, some slight variations concerning their coefficients and order are responsible to distinguish them. The major drawback of any weighing window is that they could not have a consistent performance against large signal frequency drifts.

The basic idea of **frequency tracking** is to use the estimated frequency to synchronize the sampling rate to the power signal period. Practical applications claim for Digital Phase-Locked Loop (DPLL). The DPLL is a hardware device able to synchronize the sampling period to the power signal period such that Eq. (I.58) be fulfilled. Basically, this device is a frequency multiplier whose operation is based on the following steps: the DPLL's output signal is divided by a constant factor M (being M the desired multiplying factor) and compared with the frequency of the power signal by a Digital Phase Comparator (DPC). A Loop Filter (LF) is employed to convert the digital output of the DPC into an analog reference signal to be used by a Voltage Controlled Oscillator (VCO). Then, the VCO's output frequency is adjusted to M times that of the power signal. The DPLL must be designed in order to satisfy the following requirements: the ratio between the output and input frequency must be properly adjusted to avoid aliasing, and the output frequency must be stable and accurate when the input frequency is stable in order to avoid timing variations on the sampling period (jitter errors). Unfortunately, the frequency tracking method could face difficulties with clock resolution and noise rejection [8].

Numerical interpolation methods aim to create an adjusted **samples sequence** (amplitude corrections) whose sampling frequency is matched to the power signal frequency.

The goal is to obey Eq. (I.58) for ensuring that there are no errors in the phasor estimates. Several techniques have been developed to perform time-domain or frequency-domain interpolation. Linear, cosine, and cubic interpolation are the methods commonly applied in time-domain. The simplest method is the linear interpolation, because only two original samples are required to yield an adjusted sample with corrected position between the original data. Aiming to avoid discontinuities between adjacent samples and improve accuracy, this method claims that the signal be well approximated by a linear function within the sampling period, thus a higher sampling rate is demanded [8].

Cosine interpolation is similar to the linear, however it applies a cosine function to shape the curve and smooth the transition between adjacent samples. This method uses the two end-samples of the sampling period and other two samples on either side of them for modeling approximately a curve. In this way, any adjusted sample may be retrieved within the sampling period. Interpolation based on cubic spline approach seeks to fit piecewise third-order polynomials to adjacent pairs of samples to get an approximated curve between them [18].

These classical interpolation methods could provide good results, however they may demand a high computational burden. In Chapter III, a modified linear interpolation method using trigonometric identities, proposed by [3], is presented. It provides good features to ensure the accuracy and overcome the computational effort for computing phasors under frequency deviation. It is the basis for the generalized approach that has been addressed in this thesis to interpolate harmonic components independently under power frequency drift. Performing an independent analysis for each harmonic component, new algorithms dedicated to estimate only envisaged harmonics under several frequency deviation scenarios may be implemented.

It has been shown, in the previous Section I.6, that the leakage phenomenon introduces a displacement on the relative position between the Fourier transforms of the continuous-time signal and the windowed sampled data in frequency domain. As it has been already discussed, the nominal frequency of the continuous-time signal does not longer correspond to the peak of the main lobe related to the truncated sampled data. Similarly, the harmonic frequencies of the continuous signal are not located at the zero-crossings harmonic frequencies of the sampled data. Due to the different relative position between the Fourier transforms at each step of convolution, the harmonic component of the sampled data may be linearly correlated to the harmonic component of the continuous-time signal taking into account two weighting coefficients, α and β .

The value of α depends upon how displaced is the nominal frequency of the signal with respect to the center of the main lobe, that is, it provides the relative distance of the actual sampling condition from the synchronous one. The β coefficient concerns the harmonic components of the continuous signal that are not located at the zero-crossings providing, generally, non-zero contribution to convolution. The value of the α and β coefficients depend also of the shape of the main lobe and the side lobes, respectively, thus the weighting window employed must be evaluated during the coefficients estimation. With these informations, interpolation in the frequency domain may be performed such that the positions of the Fourier transforms components might be properly adjusted [8].

Resampling methods using Finite Impulse Response (FIR) filter may also be used to reduce the leakage phenomenon. Since the period of the continuous-time signal is known,

resampling is obtained by the combination of interpolation and decimation filtering to change the sampling rate of the signal by a rational coefficient (FI/FD). Interpolation is performed prior to decimation, in other words, the interpolation increases the sampling rate by a factor FI and after the decimation (sometimes called *downsampling*) reduces the sampling rate by a factor FD such that the adjusted samples are matched with the input continuous signal period.

The theoretical basis about FIR filter can be found in [19]. FIR bandpass filtering method with frequency-adaptive coefficients, in which the measured frequency is used to retune the center of the filter bank, is another robust technique for reducing the leakage phenomenon [20], [21]. The performance analysis between FIR bandpass filtering, extended Kalman filtering (EKF), and discrete Fourier transform techniques are properly presented in [22]. It is important to mention that the FIR filter bank design must be carefully implemented to avoid a large amount of filter's taps that will impact on the filtering latency.

I.10 Power system frequency estimation methods review

In Section I.1, we have commented that power system frequency measurements are present from the beginnings of the alternating current circuit. In essence, electric frequency represents the instantaneous rate of change of synchronous generator rotor angular displacement with respect to time (radians/second or Hz). Depending upon the type of synchronous generator, it may produce single or three-phase voltages whose electric frequency is directly related to the speed of rotation of the generator.

The frequency is the only quantity whose value tends to be common for the whole power grid (generation, transmission, and distribution) providing an effective manner to evaluate the status and stability of the grid. Several frequency estimation techniques can be found in the technical literature based on various mathematical formulations, nevertheless, the frequency estimation methods discussed in this section have been developed concerning the intrinsic relationship between frequency, precise time measurement and voltage phasor representation.

Electric frequency may also be understood as the number of complete oscillations of a voltage waveform within a time interval of one second. For an electric power system operating at 50-Hz or 60-Hz, these values provide the number of oscillations (periods) during one second. In this way, determining the time interval between consecutive zero-crossings of voltage waveform periods may provide an effective manner to estimate frequency. In general, this method is often applied to single-phase voltage waveform. The accuracy of the frequency estimation depends upon the precision of time measurement to track zero-crossings, thus, for accomplishing this task, two techniques may be used: precise sampling clock or high sampling rate.

Actually, commercial chip scale atomic clock provides high accuracy and stable signals that may be used to *indoctrinate* precise sampling process to efficiently compute the interval between zero-crossings, however, the main drawback of this technique is related to the cost. High sampling rate based on oven-controlled crystal oscillators (OCXOs) and temperature-controlled crystal oscillators (TCXOs) have frequently been applied. The obtained results may satisfactorily fulfill the needs of zero-crossings computation, despite the computational

burden be clearly higher. Although the zero-crossing method is still widely used, it presents some drawbacks concerning spike noises on the waveform and the performance of the zero-crossing detector circuits and algorithms [3], [23], [24].

The pioneering work concerning the power system frequency estimation based on the sensitivity of voltage phasor measurements has been proposed in [25]. This robust computation method estimates local system frequency at a power bus from the positive sequence voltage phase angle provided by a Symmetrical Component Distance Relay (SCDR). The principle behind this method is based on the sensitivity of the phasor angle due to the variations in the power system frequency, in other words, it leverages the phasor angular displacement caused by the leakage phenomenon to infer the real frequency deviation of the power grid taking into account the finite derivative approximation of the phase displacement. Another point to note is the capability of this method to estimate the rate of change of frequency (ROCOF) - this parameter will be presented in details in [I.11.d](#).

Many of the error sources that degrade the zero-crossing methods are eliminated when the power frequency is estimated from positive-sequence voltage phasor measurements, in addition, harmonic components do not affect the frequency estimation process, because the phasors employed reflect the fundamental frequency components [3]. In practice, the finite derivative of the phase angle could lead to noisy frequency estimates, thus, for overcoming this problem, in [26] was proposed the application of FIR moving-average filter to alleviate the frequency deviation estimates.

As will be discussed further in Chapter [III](#), the method to track accurate local system frequency proposed in the present thesis also employs the finite derivative phase angle displacement, however the positive-sequence phasors are computed from the Park's transformation under balanced and unbalanced system conditions even considering off-nominal signals distorted by high harmonic content and Gaussian white noise. FIR bandpass and cascaded moving average filter are to be used for upgrading the estimation capabilities.

Another method for estimating frequency deviation from phasor has also been outlined [3]. This method models the phasor angular displacement according to the principle of uniformly varying motion to estimate the frequency deviation using weighted least squares approach over a data window. The phase angle is modeled as the integral of the frequency, in this way, beyond the frequency deviation, other parameters as initial phase angle and rate of change of frequency (ROCOF) could also be estimated. The length of the data window is directly related to the precision of the estimates, thus, the phasors computed using consecutive data windows over a span of 3-6 cycles are frequently used for inferring the power system frequency. This method provides good performance even when the voltage signals are distorted by Gaussian noise.

I.11 The Phasor Measurement Unit (PMU)

The necessity to measure time refers since the dawn of humanity, because time is an omnipresent and independent quantity. Voltage and current quantities are time-based, then, since that time is precisely determined, a correlation between these quantities may be harmoniously accomplished. Within the context of voltage and current phasor representation is well known that phasors represent the steady state condition of a power system, thus, we could be led to believe that they will never be related to time.

In essence, this statement is true only for theoretical definition, however, in the digital signal processing this statement is not acceptable, because accurate time is a mandatory prerequisite to ensure phasor measurement synchronization, especially to perform direct analysis of phase angle. Time measurement may be acquired with high degree of accuracy using a stable, accurate, and reliable Cesium atomic clock. Unfortunately, the high cost of these clocks restrict their massive application.

With the advent of the Global Positioning System (GPS), that has a powerful capability to widespread precise time information based on Cesium atomic clocks, the phasor measurement technology for power system protection, monitoring, and control had its genesis [27]. The first researches and implementation of the PMU technology were led by Virginia Tech Team, spearheaded by *prof.* Arun Phadke, James Thorp, and their co-workers, in early 1980s.

The PMU has been developed from the invention of the Symmetrical Component Distance Relay (SCDR), because it was recognized that the positive-sequence component constitute the state vector of a power system, having a fundamental role in analyzes focused especially on state estimation and adaptive relaying [28], [29]. The work published in [25] has been considered as the starting point of modern synchronized phasor measurement technology. In Appendix C, one can find the classical mathematical model to estimate fundamental positive-sequence phasors based on the symmetrical components.

Deployment of PMUs, for the first time, allowed the real possibility of acquisition of the positive-sequence voltage and current phasor estimates with temporal precision based on the same GPS time-stamp. The measurements provided by these devices ensure an adequate manner to monitor the real-time operation status of a wide-area measurement system (WAMS) improving substantially their reliability, observability and security [5]. WAMS with monitoring, protection, and control is referred to as wide-area monitoring, protection, and control (WAMPAC) system [30].

Several applications of PMUs in electric power systems have been addressed in the technical literature, among which one can quote some examples: real time voltage and frequency stability monitoring, online transient stability assessment, fault location and identification, efficient real-time congestion management, automated real-time control of assets, wide-area grid monitoring and visualization, alarming for situation awareness tools, dynamic line ratings and VAR support, automatically manage frequency and voltage response from load, system reclosing and power system restoration, protection system and device commissioning, static and dynamic models benchmarking, and post-mortem event analysis [31].

According to [27], several utilities and regional market operators around the world are making efforts to develop action plans for large-deployment of synchronized measurements technology. It is important to mention that other intelligent electronic devices that have PMU measurement capabilities, for instance, digital fault records (DFRs), digital protective relays (DPRs), and digital disturbance recorders (DDRs) will also be considered to improve monitoring, protection, control and operation of the power system. In subsections I.11.a-I.11.d, the essential informations about the synchronized phasor measurement concerning its definition according to the IEEE standard, GPS-based synchronization technique, estimation process, and the performance metrics are presented in more details.

I.11.a Definition of synchronized phasor measurements according to IEEE Std. C37.118

Before providing the definition of synchronized phasor measurements, it is necessary to comment about the standards in which these measurements are based. In 1995, the first standard for synchrophasor for power system entitled IEEE Std. 1344-1995 was published [32]. It provides the first parameters required to ensure the phasor measurement estimation and data communication. It specified the requirements for the timing signal used in the synchronization process, in which the GPS was recommended as a major time source and the IRIG-B time code (Inter-Range Instrumentation Group - format B) was chosen as the basic format for time-data communication.

This standard has also introduced the early analyzes for estimating phasors from non-synchronous and synchronous sampling condition. The IEEE Std. 1344-1995 was replaced by IEEE Std. C37.118-2005 [33]. The 2005 version of the standard specifies the performance of phasor measurements under steady-state conditions, being the metric called *Total Vector Error* (TVE) one of the most important contributions for evaluating the accuracy of synchrophasor estimates. The IEEE Std. C37.118-2005 was updated giving rise to the IEEE Std. C37.118-2011.

The 2011 version of the standard has been split into two other standards: IEEE Std. C37.118.1-2011 [6], concerning only measurements, and IEEE Std. C37.118.2-2011 [34], concerning only data communication. In [6], new performance metrics have been introduced to cover dynamic power system conditions. Frequency error (FE), rate of change of frequency (ROCOF), and ROCOF error (RFE) are the metrics that bring the capability to accomplish this dynamic evaluation (see I.11.d).

New measurement requirements for test cases related to frequency step, linear frequency ramp, amplitude step, phase step, and modulated input signals have also been introduced to assess the performance of phasor estimation algorithms under transient conditions. In [34], new communication requirements are presented, especially to ensure a compatibility with the IEC 61850 standard [35]. In 2014, an amendment to IEEE Std. C37.118.1-2011 has been introduced yielding the newer standard IEEE Std. C37.118.1a-2014 [7]. It introduces several modifications of selected performance requirements, although these new requirements are less rigorous than those demanded in 2011, see [6].

Once the review of the major standards has been carried out, the classical definition of synchronized phasor measurement may be addressed. According to [6], a synchrophasor is “*a phasor computed from data samples using a standard time signal as the reference for the measurement*”. Based on this statement, one can notice that the synchrophasor is a complex representation of voltage and/or current waveforms correlated with a common *time-tag* concerning the precise instant of time in which the measurements have been performed.

It is of paramount importance to mention that the time-tag is based on the Coordinated Universal Time (UTC). In I.11.c, the synchrophasor estimation is presented, however, at this moment, let us consider a synchronization signal (1PPS) able to trigger the start-of-conversion of the synchrophasor estimation. The 1PPS must be perfectly correlated with the time-tag, that is, to UTC. In order to exemplify, let us rewrite here the continuous-time signal given by Eq. (I.1) and its phasor representation in Eq. (I.4), hence

$$y(t) = Y_m \cos(\omega t + \phi) \longleftrightarrow Y = \left(\frac{Y_m}{\sqrt{2}} \right) e^{j\phi} \quad (\text{I.99})$$

where Y_m is the waveform peak value, $\omega = 2\pi f_o$ is the angular frequency, ϕ represents the phase angle of the signal, and $\frac{Y_m}{\sqrt{2}}$ concerns the RMS value of the signal.

According to [6], the synchrophasor representation of the continuous-time signal $y(t)$ in Eq. (I.99) is the complex value Y where the phase angle ϕ is the offset from a cosine function at the nominal system frequency synchronized to UTC. Fig. I.16 depicts the phase angle related to UTC time and the convention for synchrophasor representation.

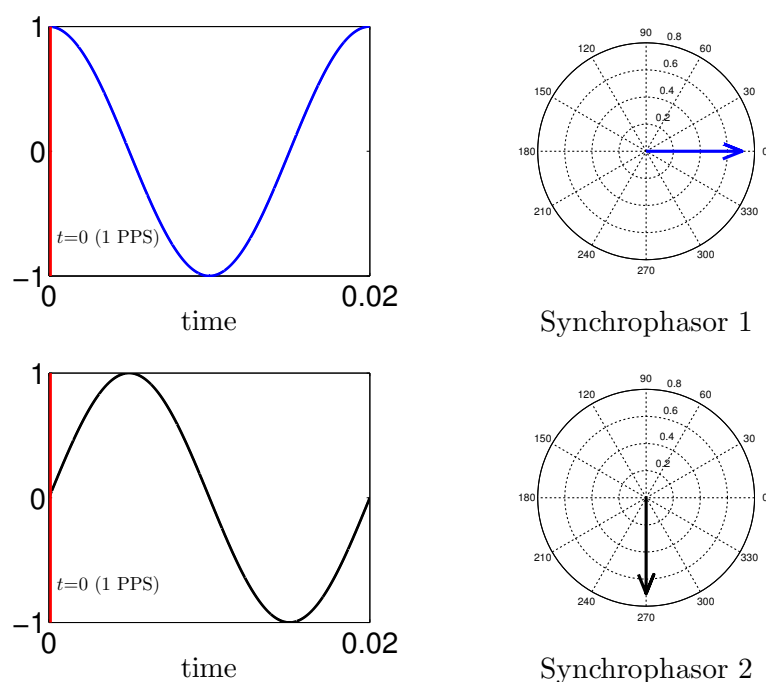


Figure I.16: Established convention for synchrophasor representation (adapted of [6]).

When the UTC second rollover (1 PPS) occurs at $t=0$ s, the phase angle ϕ is 0° , likewise when the 1 PPS occurs at the positive zero crossing the phase angle is -90° (sine wave). Performing the same analysis, when the 1 PPS occurs at the instant that coincides with the negative peak value and the negative zero crossing, the obtained phase angles are -180° and 90° , respectively. One can note that the phase angle for synchrophasor representation are commonly reported in angles from -180° to $+180^\circ$.

In I.8.b, it has been shown that the leakage phenomenon imposes rotating and oscillating effects on the phasor estimate, thus, we can ask ourselves the following question: What is the impact of the leakage phenomenon over the synchrophasor estimate? It is necessary to keep in mind that the only difference between phasor and synchrophasor is that the latter is time-referenced. In this way, the leakage phenomenon also imposes errors on the magnitude and phase angle estimates of the synchrophasor.

Generally, the magnitude error may be neglected, however, phase angle error is critical because the synchrophasor will also rotate at the uniform rate given by the difference between the actual and off-nominal frequency. In this way, the theory presented in Appendix B is also valid for synchrophasor measurements.

I.11.b The Global Positioning System (GPS) as time synchronization source for synchrophasor estimation

In the previous section, it was stated that the synchronized phasor measurements are “attached” to a time-tag traceable to UTC. This means that the synchronization source must provide time information with high degree of accuracy, reliability and availability in order to accomplish the power system requirements and keep the performance metrics (see I.11.d) within the required limits. The main issue remains, however, in the fact that the synchronization source needs to operate continuously and be accessible for several devices placed at remote measurement points on the power grids.

The technology that has been employed to meet these requirements and provide widespread availability is the GPS. It is a navigation system developed by U.S. Department of Defense (DoD) that uses satellites equipped with accurate Cesium atomic reference clocks for broadcasting precise signals for location identification and time synchronization. It has been developed, *a priori*, for radio-navigation that, since 2007, contains a complete constellation of 30 active satellites in orbit providing high accuracy for spatial coordinates estimation of the receivers [3], [27].

The GPS optimal time accuracy is of the order of $\pm 0.2 \mu\text{s}$ or less [36]. This means that the broadcast signals may reach anywhere on the Earth within this time interval. In practice, however, the GPS achieves a precision of around $\pm 1 \mu\text{s}$. In effect, the signals sent by the GPS contain the synchronizing pulse (1 PPS), the time information traceable to UTC (time-tag), and the satellite clock status. The 1 PPS signal is a train of positive pulses at a rate of one pulse per second. The rising edge of the pulses is matched with the seconds change in the GPS atomic clock, due to this fact, it provides a very precise time reference.

It should be emphasized that the 1PPS does not provide any information of time (day, month, year, hour, minute, second and fraction of a second). These informations are inside the UTC-time-tag, therefore, to ensure proper data receiving, the GPS receiver clock must be *correlated* with the satellite atomic clock. Thereby, the GPS receiver must estimate the *clock offset* (t_{co}) for adjusting its internal clock taking into account the received information of the satellite clock status, as illustrated in Fig. I.17.

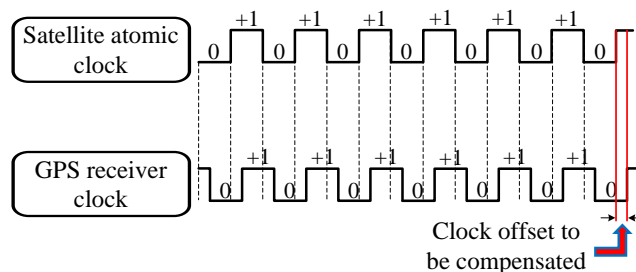


Figure I.17: Clock offset between the satellite atomic clock and the GPS receiver clock. Note that this offset must be compensated by the GPS receiver to ensure a proper data receiving.

The clock synchronization must be performed because most of the commercial GPS receivers applied to synchronize measurements are not equipped with accurate reference

clock, thus, a clock offset will be generated based on the difference between the signals sent by the satellite (atomic clock-based) and the signals received by the GPS receiver (local clock-based). Generally, the GPS receivers use an internal quartz crystal clock, however, external clock such as rubidium frequency standard or cesium beam frequency standard may be used to improve the local reference [37].

The GPS receiver may estimate its position coordinates and clock offset using the trilateration method, as given by Eqs. (I.100)-(I.102) [38]. Through this method, the GPS receiver estimates the *range* equivalent (distance from receiver to satellite) multiplying the broadcasted signal transit time by the signal propagation speed in vacuum, that is, the speed of light. Hypothetically, under ideal error and noise free condition, three satellites would be used to estimate the GPS receiver position, in this case, an accurate synchronization between the satellite and receiver clocks would be accomplished and the distances computed by the GPS receiver would be the true *ranges*.

Unfortunately, this is not always feasible. In practical applications, at least four satellites are required to estimate the unknown parameters: position Earth Centered Earth Fixed (ECEF) coordinates (x_r, y_r, z_r) and clock offset of the GPS receiver [39]. Considering four or more satellites, the estimation process in the weighted least square sense is formulated as follows

$$d_i \equiv l_i + ct_{co} + \omega_i \quad i = 1, 2, \dots, n \quad (\text{I.100})$$

where,

$$l_i = \sqrt{(x_i - x_r)^2 + (y_i - y_r)^2 + (z_i - z_r)^2} \quad (\text{I.101})$$

hence,

$$\text{Min} \quad J(x_r, y_r, z_r, t_{co}) = \sum_{i=0}^n \left(\frac{(d_i - l_i - ct_{co})^2}{\sigma_{ii}^2} \right). \quad (\text{I.102})$$

The i th satellite's coordinates (x_i, y_i, z_i) are parameters known because the GPS receiver compute these values based on the ephemeris data included in the broadcast GPS signal; c is the speed of light (299792458 m/s); n represent the number of visible satellites; d_i and l_i are the i th satellite's corrected *pseudorange* and geometric distance to the receiver, respectively; and ω_i is the i th zero-mean Gaussian pseudorange measurement noise with variance σ^2 .

The following assumptions are commonly made, regarding the statistical properties of the measurement errors: $E[\omega_i] = 0$, $E[\omega_i^2] = \sigma^2$ for all measurements, and the noise terms between satellites are independent, $E[\omega_i \omega_j] = 0$ for $i \neq j$ [38]. The GPS receiver solves this system of nonlinear equations by iterative algorithms, for instance, Newton-Raphson method for $n = 4$ (the system of nonlinear equations has a unique solution) and Gauss-Newton method for $n \geq 5$ (overdetermined system) [40].

Looking closely at the mathematical formulation of the GPS receiver estimation problem we are led to believe that it will always be necessary at least four satellites for estimating the position coordinates and clock offset, however, this assumption is true if we consider the spacial displacement of the receiver. Since the GPS receivers employed

to synchronize PMUs and PMU-enabled IEDs are in fixed locations, and knowing their positions, they need to receive the data arising from only one GPS satellite to compute the clock offset, therefore the GPS receivers dedicated for measurements synchronization may have modified algorithms [37].

Once the clock offset is estimated, the GPS receiver adjusts its internal clock to properly handle the incoming data. In this stage, the IRIG-B time protocol is used to ensure precise time data transfer between the GPS receiver and the device to be synchronized. We have seen that in practical applications the GPS achieves a precision of around $\pm 1 \mu\text{s}$, in this way, an important issue may be raised : Why does synchrophasor estimation process demands a precision on the order of $\pm 1 \mu\text{s}$? The answer for this issue is quite simple, for instance, if the GPS broadcast signal arrives with a time delay of $\pm 1 \mu\text{s}$, the phase angle error (*pae*) of the estimated synchrophasor is around $\pm 0.018^\circ$ and $\pm 0.0216^\circ$ for a signal at 50-Hz and 60-Hz, respectively. These errors are directly achieved by the following equation: $pae = 2 \times 180^\circ \times f_o \times t$.

Now, assuming that the signal arrives with a time delay of $\pm 1 \text{ ms}$, for this case, the error is around $\pm 18^\circ$ and $\pm 21.6^\circ$ for a signal at 50-Hz and 60-Hz, respectively. Clearly, one can observe that the phase angle error caused by a synchronization process within the range of milliseconds may be discarded for practical applications in electric power systems, which does not happen when the synchronization process falls into the range of microseconds.

I.11.c Synchronized phasor measurements estimation

The synchrophasor estimation process may be modeled taking into account two parameters: the synchronizing pulse (1PPS), and the time-tag in which the synchrophasor must be associated. The 1 PPS synchronizing signal and the time-tag information have been explained in I.11.a and I.11.b. Now, we are able to present the role of each of these parameters in the synchrophasor estimation process. The 1 PPS is a signal responsible for triggering the start-of-conversion of the Analog-to-Digital Converter (ADC) located inside the Digital Signal Processor (DSP) or Field-Programmable Gate Array (FPGA) to enable the synchrophasor estimation, that is, the sampling clock is phase-locked with the 1 PPS.

This statement establishes an important information regarding the synchronized measurements: the synchronization process is performed inside the ADC, as illustrated in Fig I.18. ADCs in PMUs and PMU-enabled IEDs often have a resolution of 16 bits [28], however, a higher resolution is encouraged. We take advantage to show the main components of a generic PMU regarding its instrumentation channel, as depicted in Fig. I.19.

Concerning the time-tag, first of all, it is necessary to warn that it is a parameter that often causes confusion, therefore, let us explain in a comprehensive manner. This parameter provides the time and time quality in which the measurement must be associated. The time status includes time quality traceable to UTC, time accuracy, and leap second status. The time-tag must coincide with the 1 PPS signal and with integer sub-multiples of the fundamental power system frequency period, however, one can notice that these integer sub-multiples are not measured from the sampling process, instead they are measured from the GPS signal [3].

The standard [6] claims that the PMU data reporting (record or output) must also be correlated to integer sub-multiples of the fundamental frequency period, due to this fact,

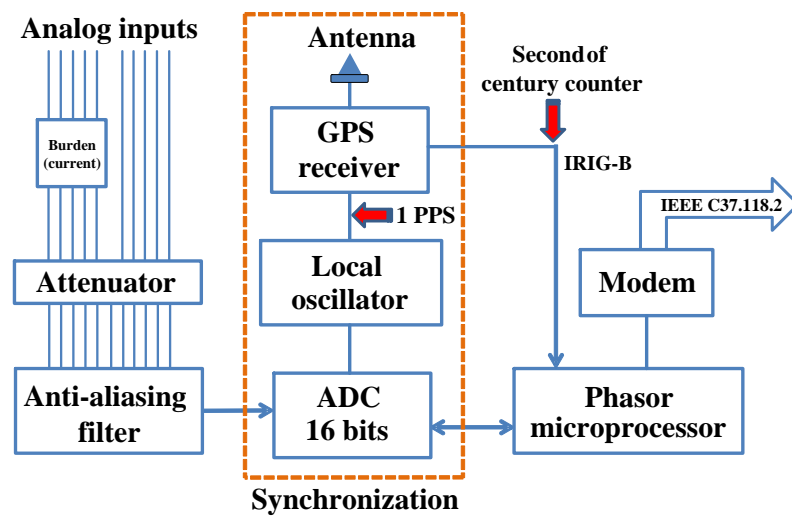


Figure I.18: PMU synchronization process performed inside the ADC (Adapted of [3]).

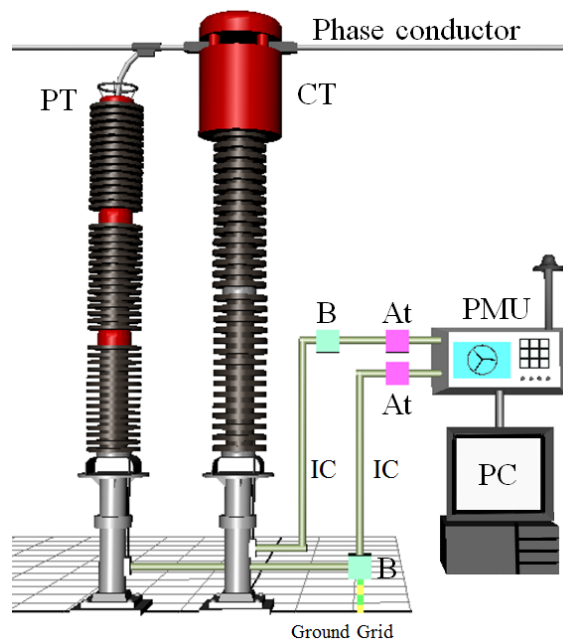


Figure I.19: Main components of a generic PMU regarding its instrumentation channel [41]. PT: voltage transformer; CT: current transformer; IC: instrumentation cables (coaxial cable RG-8 with default parameters at 50Ω impedance, mesh protection against electromagnetic effects, and low signal loss [42]); B: burden (protection impedance against overcurrent, besides protecting for avoiding CT saturation [42]); At: attenuator (for reducing the amplitude of the analog signal measurement without significant distortion of its shape).

the time-tag is also known as *reporting time*. Table I.1 shows the advised number of PMU output synchrophasors by second that may be user selectable.

Another mandatory information about the time-tags is that they are to be used for

Table I.1: Required PMU reporting rates

System frequency	50 Hz			60 Hz					
Reporting rates (F_s)	10	25	50	10	12	15	20	30	60

estimating the synchrophasor instantaneous value, as defined in I.11.a. This is envisaged because the synchrophasor estimation process requires sampling the waveform over some interval of time that can lead to some doubts about which time within the data window is the correct time-tag to be correlated with the synchrophasor. For example, let us consider a reporting rate of 50 synchrophasors by second at 50-Hz fundamental frequency. Fig. I.20 illustrates the allowable time-tags related to the GPS clock.

Taking into account one data window, one can note that, *in theory*, the synchrophasor angle estimate is θ , being the angle between the first sample and the sinusoid peak value. This angle remains constant for all other subsequent synchrophasors when a recursive updating is performed (without leakage). Concerning the standard [6], it states that the synchrophasor is an estimate of the sinusoid parameters (RMS value and phase angle) over the data window, thereby, the estimate covers a short period of time representing some kind of ‘average’ of the parameters that may change during the window.

In this way, this standard advises to correlate the synchrophasor estimate with a time in the middle of the data window. Then, it becomes necessary to determine the time interval between the first sample and the theoretical (advised) time-tag in the middle of the data window so that the phase angle, related to this theoretical time-tag, be reported as the phase angle of the synchrophasor. In short, due to the time-tag concept, a synchrophasor is a theoretical phasor that represents the phasor estimated.

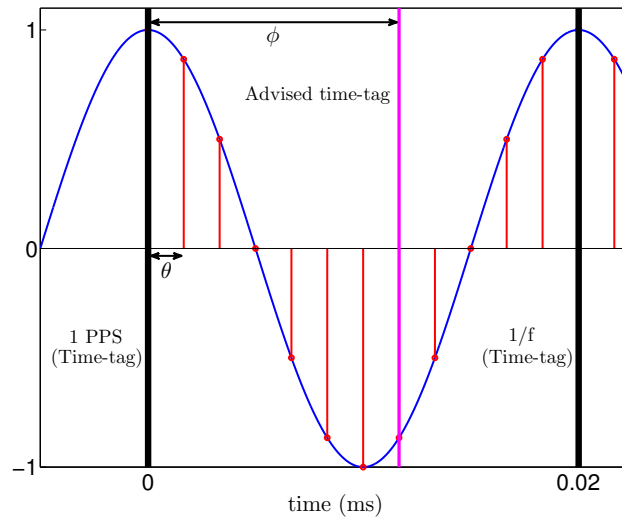


Figure I.20: Time-tags matched with sub-multiples of the fundamental power system frequency period. Theoretically, the synchrophasor phase angle estimate is θ , however, the phase angle which must be associated with the synchrophasor is ϕ .

Once the synchrophasors have been estimated according an UTC-time-tag they are able to be employed for inferring the power system status, however, the delays caused by, for example, analog input filtering, sampling, digital filtering, and estimation group delay will

change the synchrophasor estimates. Due to this reason, the concept of *time-stamp* must be carried out.

According to [6], “the time-stamp of the PMU output represents the phasor equivalent, frequency, and ROCOF of the power system signal at the time it is applied to the PMU input”. It is clear that all of these estimates must be compensated to provide valuable informations. Since the measurements are time-stamped with a high degree of precision, the communication medium between PMUs and Phasor Data Concentrators (PDCs) is no longer a critical factor to allow the use of this measurements [3]. The PDC saves and treats the set of measurements with the same time-stamp for power system application purposes. (see [43] for specific informations about PDCs).

I.11.d Performance metrics for PMUs

According to [6], the performance metrics concerning synchrophasor measurements are called Total Vector Error (TVE), Frequency Error (FE), and Rate of Change of Frequency (ROCOF) error (RFE). These metrics are employed to evaluate the estimates in order to ascertain whether they fall within of acceptable limits under static and dynamic conditions. The TVE gives the error between the theoretical synchrophasor value of the signal being measured and the synchrophasor estimate at the same instant of time, in other words, the theoretical values of a synchrophasor representation may differ in both magnitude and phase angle from the values provided by the PMU.

It can be seen that the magnitude and phase angle errors could be specified separately, however, the TVE metric is more inclusive because the synchronization time, phase angle, and magnitude estimation errors are combined together. The TVE value is normalized and expressed as percentage of the theoretical synchrophasor as follows

$$TVE(t) = \frac{|\underline{Y}_{estimate}(t) - \underline{Y}_{theoretical}(t)|}{|\underline{Y}_{theoretical}(t)|} \times 100\% \quad (I.103)$$

or,

$$TVE(t) = \sqrt{\frac{(\hat{Y}_r(t) - Y_r(t))^2 + (\hat{Y}_i(t) - Y_i(t))^2}{(Y_r(t))^2 + (Y_i(t))^2}} \times 100\% \quad (I.104)$$

where $\hat{Y}_r(t)$ and $\hat{Y}_i(t)$ are the synchrophasor estimates given by the unit under test, and $Y_r(t)$ and $Y_i(t)$ represent the theoretical values of the input signal at the instants of time (t) assigned by the unit to those values. The values $Y_r(t)$ and $Y_i(t)$ can be determined in closed form by calibration taking into account certain well-defined situations, such as constant frequency or phase offsets.

A maximum TVE value of 1% has been stipulated in [6], thus, based on this information, one can determine the maximum individual error for the magnitude, phase angle, and synchronization time estimates. For the first example, let us assume that there are no errors on the phase angle and synchronization time estimates, in which 1% TVE is related only to the magnitude estimate. In this case, one can conclude that 1% TVE produces $\pm 1\%$ magnitude measurement error.

In the second case, there are no errors on the magnitude and synchronization time estimates, in this case, 1% TVE related to the phase angle estimate provides a maximum

admissible error of $\pm 0.573^\circ$ (0.01 radian). Based on this assumption, the maximum phase angle measurement error may be correlated with a synchronization time error that may be interpreted like analogous to clock offset. In this way, a maximum synchronization time error of $\pm 31 \mu\text{s}$ and $\pm 26 \mu\text{s}$ at 50-Hz and 60-Hz have been obtained, respectively. Within the context of active power distribution system, 1% TVE imposes some restrictions for the deployment of PMUs in these grids, as will be seen further in II.2, therefore, the researches carried out in this thesis aim to circumvent this problematic.

According to [6], frequency and ROCOF errors are defined as the absolute value of the difference between the theoretical and the estimated values given in Hz and Hz/s, respectively. In general, frequency error represents a narrow range around the nominal power system frequency, although it may become excessively high under specific power system operating conditions as islanding, faults, and load shedding.

The FE estimation is of utmost importance to overcome the problems imposed by the leakage phenomenon. ROCOF evaluates the frequency changes over time, thereby, it provides an excellent way to assess dynamic frequency variations (especially linear frequency ramp) in the electric grid. Frequency and ROCOF errors may be evaluated using the following definitions:

- Frequency measurement error:

$$FE \equiv |f_{theoretical} - f_{estimated}| = |\Delta f_{theoretical} - \Delta f_{estimated}| \quad (\text{I.105})$$

- ROCOF measurement error:

$$RFE \equiv \left| \left(\frac{df}{dt} \right)_{theoretical} - \left(\frac{df}{dt} \right)_{estimated} \right|. \quad (\text{I.106})$$

One can assume that the estimated and theoretical values are taken at the same instant of time, therefore, the time-tag of the estimated values will be the same for the theoretical values. These performance metrics will be considered further in Chapter III for evaluating the performance of the proposed frequency-adaptive algorithms.

I.12 Phasor estimation algorithms review for Power Distribution Systems

Regarding the algorithms, the IEEE Standards cited in I.11.a do not specify or require a specific type of algorithm that may be applied to estimate synchrophasors. In Appendix C of [6], it is possible to find some recommendations to develop algorithms to verify the performance requirements that have been introduced by this standard. Some evidences suggest that many of the developed PMUs from the major vendors use Fourier-based algorithms (DFT or FFT) or their slight variations (see I.6-I.8). Currently, several research groups around world, including the G2Elab team, seek to develop high-performance algorithms (Fourier-based or not) to allow the applicability of synchrophasors in active power distribution systems.

There are many challenges to estimate synchrophasors in these electric grids, as will be shown in Section II.1, however, this thesis aims to contribute for overcoming these

challenges by means of frequency-adaptive algorithms for tracking accurate synchrophasor estimates in smart power distribution networks. In the present section, a review of published works concerning new algorithms for estimating phasors in power distribution environment is presented. These algorithms are based on several estimation methods, however, evidences suggest that many of them have one point in common: phasor estimation with small TVE value (See Chapter II).

In [44], an algorithm called Interpolated-Modulated Sliding DFT (IpMSDFT) has been proposed. In essence, this algorithm is a variation of the classical DFT method, in which, high sampling rate and interpolation are employed to mitigate the leakage phenomenon. The authors claim for a high accuracy, reduced latency, high synchrophasor reporting rate per second, and low-computational complexity. The algorithm has been tailored to allow a feasible deployment on an FPGA-based PMU.

The main reference of [44] is the work proposed in [45], in which, an enhanced interpolation method in frequency domain considering a long-range spectral leakage has been performed. In [46], a modified version of the Taylor-Fourier-transform (TFT)-based algorithm has been proposed, wherein the employed mathematical formulation considers the phasor as a second order Taylor expansion around each estimation point within the data window. In this way, an overdetermined linear system is obtained whose solution is based on the Weighted Least Squares (WLS) approach (TFT-WLS).

An architecture that aims to allow the requirements of P- and M-class PMU models (protection and monitoring oriented applications, respectively) is proposed in [47]. This architecture processes in parallel the acquired samples using two digital channels, both based on the TFT-WLS algorithm, however different lengths and parameters of data windows are employed. The first channel is able to estimate accurate measurements of steady state signals, while the second one is suited to track the fast signal variations. Then, a fast changes detector identifies a potential dynamic condition and selects the most suited output for the actual system operation status.

A real-valued version of the Taylor Weighted Least Squares (TWLS) algorithm is addressed in [48]. Once again the Taylor approach is employed, however, the authors claim that the algorithm is a generalization to both windowing and dynamic waveform model of the three-parameter sine-fitting (3PSF) algorithm when the offset is not present. According to the authors, their proposed algorithm requires a lower processing effort.

Recursive Least Squares (RLS) and the Least Means Squares (LMS) algorithms have been properly proposed in [26] for providing dynamic phasor and frequency deviation estimates. A non-linear and time-varying model of the system voltage is modeled assuming a zero mean Gaussian noise. This model is appropriately linearized using Taylor series to allow that the RLS and the LMS algorithms (endowed with forgetting and adaptation factors) provide dynamic voltage phasor. The frequency deviation estimate has been taken based on the finite derivative approximation of the voltage phasor phase angle displacement. RLS and LMS algorithms aim to overcome the problems founded on Kalman-filters-based algorithms concerning high computational requirements.

In [20], alternative algorithms for P- and M-class PMU models using adaptive cascaded filters with high sampling rates (up to 10 kHz) are presented and discussed. The authors state that the phasor estimates allow consistent accuracy providing less computational burden compared to the traditional FIR filter, in addition, the ROCOF metric could be

detected more efficiently.

In [49], adaptive-window PMU algorithms using cascaded boxcar filters have also been proposed to meet and exceed the IEEE standards requirements. Boxcar filter is a moving average smoother applied in frequency domain, thus it can be understood as a rectangular data window used to convolve the frequency spectrum. Initial results show that the calculation rate does not increase for longer-window, since the number of cascaded boxcar filter remains constant, moreover, it might be extended to applications involving harmonic components.

Several of these proposed algorithms have been presented or cited in a pioneering workshop - *Synchrophasor estimation processes for Phasor Measurement Units: algorithms and metrological characterization* - focused on methods for synchrophasors estimation and their deployment specially intended for active power distribution systems [50]. The workshop was organized by Swiss Federal Institute of Technology of Lausanne (EPFL) and by Swiss Federal Institute of Metrology (METAS) within the context of the Euramet European research project - *Measurement tools for Smart Grid stability and quality ENG52 SmartGrid*.

Concurrently with the development of clever real-time algorithms, researches are ongoing on applications of PMUs and PMU-enabled IEDs dedicated to power distribution systems. In Section I.13, the current conjuncture of some projects related to the deployment of time-synchronized measurements in the power distribution environment are reported.

I.13 Current conjuncture of time-synchronized measurements in Power Distribution Systems

In Section I.11, we have seen that the PMUs have the capability to increase the situational awareness on power systems regarding the improved applications that can be realized, in this way, some pioneering researches and projects attempt to apply the synchronized measurements technology to also increase the situational awareness in power distribution systems.

A satisfactory deployment of synchronized measurements in power distribution environment might allow the implementation of real-time monitoring, control, and protection functions to achieve an improved operational efficiency, an enhanced flexibility and an increased reliability for these systems. In this sense, PMUs, PMU-enabled IEDs, and other GPS-enabled Intelligent Electronic Devices (IEDs-GPS) will have a fundamental role to play in the attainment of these objectives.

Efforts are being made to move the synchronized measurements from high voltage power networks to power distribution systems, in which the features and peculiarities of the latter have been carefully taken into account in order to obtain reliable advanced analytic informations. In [51], the first analyzes of the synchronized phasor measurement system prototype entitled MEDFASEE has been presented, in which PMUs are connected at low-voltage level to estimate phasors, system frequency, and record events, whose goal is to monitor dynamic conditions in the Brazilian interconnected power grid.

In [52] and [53], the concept of Internet-based real-time GPS-synchronized wide-area frequency monitoring (FNET) is shown. The FNET system consist of frequency disturbance recorders integrated with an information management system for monitoring the

entire USA power network. The FNET devices are also placed at low-voltage whose goal is to measure power system frequency dynamics with high degree of accuracy enabling the power system status evaluation.

One can observe that the synchronized measurements provided by the abovementioned references are not necessarily employed to monitor the distribution grids, however, an indirect conclusion that can be obtained from these researches is the need of adequate immunity against leakage phenomenon for the PMUs, PMU-enabled IEDs, and IEDs-GPS dedicated exclusively to monitor the distribution level.

In [54] and [55], the investigation regarding the deployment of PMUs in industrial distribution networks in East Germany are reported. A survey concerning the optimal PMU placement has been taken into account to identify the most susceptible busbars for PMU installation. Some units were placed at medium voltage level (20 kV) and, additionally, one PMU was utilized to perform low voltage (0.4 kV) measurements. The synchronized measurements taken at the industrial network are processed and treated by a local PDC that transmits the data online to the PDC placed at Otto-von-Guericke University in Magdeburg using a VPN connection. Visualization tools and calculations are performed to monitor the industrial grid status, in which the authors state that the obtained results may be used to analyze steady state and disturbance conditions.

In [56], a FPGA-based PMU prototype has been conceived for monitoring active distribution grids. The authors point out the need to achieve a very low TVE value to ensure the applicability of the synchronized measurements in distribution environment. Experimental applications related to intentional islanding and reconnection tests are performed to evaluate the performance of the prototype. The authors claim that the obtained results are useful to facilitate the operator maneuvers and for the development of an improved monitoring, control and protection frameworks dedicated to active distribution grid.

The state estimation is one of the most important function to evaluate the operation condition of a power system. Unfortunately, the vast majority of works concerning state estimation in distribution systems have a poor performance in practical applications, due to the several constraints related to few number of measurements, unbalanced circuits, high insertion of decentralized and renewable production, and so on. In addition, the proposed algorithms for state estimation in distribution systems are not perfectly adapted, because they are based on the algorithms developed for high voltage power system.

To emerge from the darkness, a real-time state estimator using only synchrophasor measurements has been developed in [57]. In this project, several PMU prototypes are placed at EPFL-campus medium-voltage grid. Smart monitoring framework makes possible to infer about the grid status based on the measured synchrophasors, in addition, active and reactive power are also computed to allow a real-time power flow evaluation.

A pioneering project dedicated for developing PMUs focused exclusively for the distribution systems has been carried out in [58]. This project was funded in part by the Advanced Research Projects Agency-Energy (ARPA-E) with the intent to increase the visibility and the situational awareness of the distribution network using micro-synchrophasors (μ PMU) to measure voltage phase angle with precision of millidegree ($\pm 0.01^\circ$ typical). It is important to mention that several challenges for measuring millidegree phase angle such as cable transit time, quantization errors and signal attenuation must be circumvented. Therefore, accurate calibration and compensations must be performed in order to obtain

valuable results. The goal of this project is to explore several applications based on the μ PMU data to improve operation status identification and increase reliability.

It is expected that several advanced functions may be effectively implemented, among which one can cite: faster grid restoration during faults, reverse power flow detection, Volt-VAR optimization, real-time monitoring and control, power quality issues, distribution system resilience capability, optimized integration of distributed and renewable resources, topology detection, state estimation, and fault location (for instance, high-impedance fault). The devices will be placed in field sites to meet the need of the circuit characteristics that the utility wishes to better understand (high decentralized and renewable penetration and some unexpected behavior). The first tests and validation of the device were realized in pilot site at Lawrence Berkeley National Laboratory (LBNL) and results with high degree of accuracy have been reported. Fig. I.21 shows the μ PMU prototype.

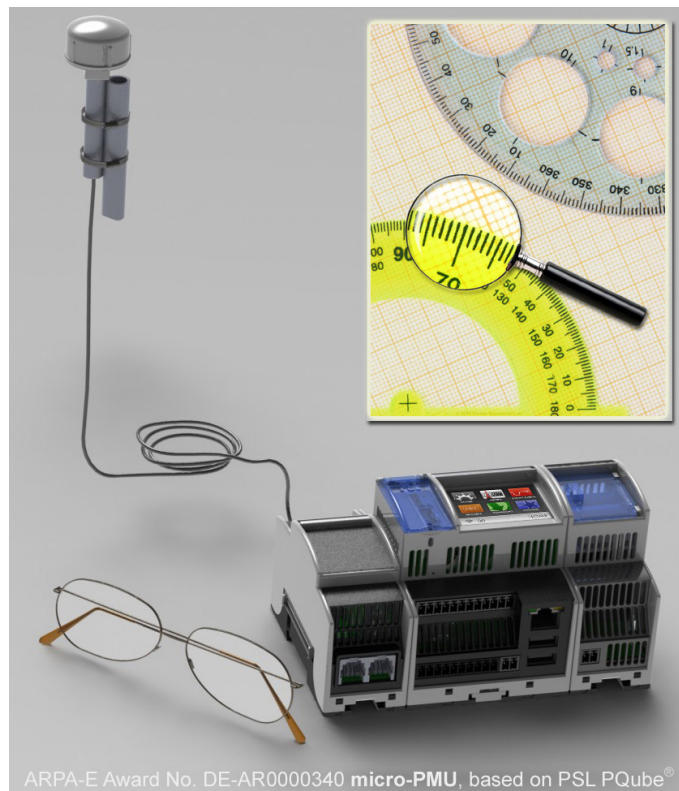


Figure I.21: μ PMU prototype developed for distribution networks (public domain picture [58]).

In the technical literature, other projects may be found concerning the deployment of synchronized measurements in distribution systems, however, the background about them are not properly explained making difficult their inclusion in the present section. One can state that the overall amount of projects is still non significant, nonetheless, they are opening the doors to allow, for the first time, new perspectives and initiatives to ensure an effective situational awareness in power distribution systems. It is also important to mention that these projects are breaking an established “premise” that claims for the non-applicability of PMUs, PMU-enabled IEDs and other GPS-IED devices in power distribution environment because they could not bring concrete advantages.

I.14 Conclusion

In the current chapter, the state of the art concerning the synchronized phasor measurements estimation has been outlined. The background regarding the Fourier's methods is addressed due to the fact that they represent the cornerstone of the data processing techniques employed to estimate phasor measurements in electric power systems. In this way, a thorough review of the main key points with respect to Fourier series (FS) approach, Fourier transform (FT) properties, discrete Fourier transform (DFT) and fast Fourier transform (FFT) (including the Radix-2 DIT FFT) have been presented in details to provide an intuitive mathematical basis for phasor representation in continuous and discrete-time domain. This review aims to provide a theoretical support for the accurate frequency-adaptive algorithms that have been proposed in the current thesis.

The main drawbacks concerning phasor estimation in electric power systems are also shown with a special regard to the system frequency deviation responsible for introducing the pernicious leakage phenomenon, whose impact on the phasor estimation accuracy is relentless. Thus, an extended review of methods applied to circumvent this phenomenon has been presented and discussed. Additionally, the characteristics of the classical Phasor Measurement Unit (PMU) are carried out taking into account the informations provided by the IEEE C37.118 standards for synchronized phasor measurements for power systems. Concerning the state of art of synchronized measurements in distribution grids, a survey of some tailored algorithms and the current conjuncture of the major projects related to the deployment of synchronized devices in the distribution environment are equally presented.

In this thesis, the proposed works are engaged to demonstrate the effectiveness of synchronized measurements to enable real-time monitoring functions for distribution systems in order to overcome the major operational challenges of these networks. For accomplishing this task, firstly, it is necessary to evoke the drawbacks that may effectively impose restrictions for the synchronized measurements deployment, therefore, in Chapter II, the main problematics are reported in details. These problematics may impose restrictions, but this does not mean that they can not be circumvented.

Chapter II

Main challenges of the synchronized phasor measurements deployment in active power distribution environment

Life is combat therefore only the brave men will can exalt.

Gonçaves Dias

CONTENTS

II.1	INTRODUCTION	60
II.2	IEEE STD.C37.118.1-2011 VERSUS ACTIVE DISTRIBUTION SYSTEM REQUIREMENTS: THE PROBLEMATIC OF THE TVE METRIC	63
II.2.a	Primary distribution system topology overview	66
II.2.b	Voltage angle difference between adjacent primary busbars <i>versus</i> TVE metric	69
II.3	FREQUENCY DEVIATION	75
II.4	HARMONIC CONTENT ISSUES	76
II.5	MEASUREMENT POINTS	77
II.6	OVERVIEW OF THE DEPLOYMENT COST-BENEFIT RATIO	78
II.7	CONCLUSION	78

Abstract

The integration of DERs has been considered as a flagship of the new scenarios concerning the future distribution grids. Due to this fact, new paradigms of communication infrastructures, advanced metering, and a modern automation and control frameworks must be created to effectively allow the evolution of electric distribution grids from passive to active networks. The need of real-time monitoring and control will play a special role, thus, the deployment of PMUs and PMU-enabled IEDs in active distribution environment to perform these tasks must be carefully evaluated in order to identify and overcome the challenges that can be met. A special regard to the problematic concerning the requirements demanded by the IEEE Std. C37.118 versus the active distribution system operational requirements is presented and discussed. It will be shown that the admissible phasor measurement errors stated by this standard is not conceivable for distribution grids and it is essential to reduce the measurement errors in order to obtain valuable phasor estimates in distribution environment. Other challenges regarding the frequency deviation, out-of-band disturbances (harmonic, interharmonic and subharmonic), measurement points, and cost-benefit ratio of the synchronized devices deployment are also reported.

II.1 Introduction

Since the beginnings of its development, the distribution system (medium and low-voltage) has been considered as a passive element in the whole electric grid, in other words, it has been seen solely in terms of a grid element able to absorb energy produced by power plants. With the advent of the electric deregulation and the onset of competitive electricity markets, several changes in the way of producing and delivering energy have emerged. Nowadays, more and more elements of the overall network, including consumers, are capable of participating actively and directly in the grid operation provided that they comply with specific requirements.

New possibilities of electricity generation are envisaged, thereupon, profound changes in the architecture and management of the electric grids must be carried out. In distribution environment, the load (consumers) endowed with local production or storage system could be considered as a small-scale generator and DERs throughout the service territory could be used to inject energy at different layers of the grid. In this context, new paradigms of communication infrastructures, advanced metering, and a modern automation and control frameworks must be created to effectively allow the evolution of electric distribution grids from passive to active networks.

The integration of DERs may be considered as one of the main actors on active power distribution grid. They will play an essential role for improving the energy efficiency of these networks. According to [59], DERs may be applied to defer or eliminate the need to build additional central generating plants, voltage support and improved power quality, reduction in power system load losses, transmission and distribution capacity release, deferments of new or upgraded infrastructure, relief of transmission system congestion, and smooth peaks in demand patterns.

One can cite that the benefits of DERs are for both transmission and distribution systems. Achieving the aforementioned system benefits requires that the DERs be integrated in a reliable manner with the electric network, being the three key system integration issues reported as follows [59]

- Topological design and operation impacts of active power grid infrastructure for DER integration.
- Communication and control for strategic system operation and support with DER.
- Physical interconnection of DER with electric power grids.

According to [59], the first issue deals with changes of the electric grid topological design and the system operation scope due to the integration of the DERs. Impacts related to voltage regulation, flicker, harmonics, and reliability are commonly focused, in which studies such as load flow, harmonic, and short-circuit analysis must be performed. The second issue deals how to increase DER's capabilities by providing means for controlling and dispatching of their services strategically, in other words, data and control signals must be transferred between DER equipments and control centers for safe and optimal energy integration into the grid.

The third issue addresses safe practices for the physical connection of DER equipment to electric grids, that is, all matters concerning control relays, transformer interfaces, disconnect switches, and other-site specific DER hardware required for successful operation of the DER. It is of paramount importance to comment that all three key issues are closely inter-related. Several types of energy sources and generation technologies may be employed as ‘distributed energy resources’, where the most common generation technologies include:

- Gas combustion turbine-generators,
- Gas combustion microturbines with alternators-inverters,
- Gas to hydrogen fed fuel cells and electronic inverters,
- Gas and oil fired reciprocating engine-generators,
- Wind-driven turbines with induction generators or alternators-inverters,
- Solar photovoltaic cells and inverters,
- Solar thermal-electric power plants,
- Hydroelectric micro- and small-scale power plants,
- Geo-thermal driven steam turbine-generators.

Other generation technologies can also be considered as DERs. These include different energy storage system as: mechanical (compressed air energy storage, flywheels), electro-chemical (lead-, nickel-, high temperature salts-, redox-batteries, hydrogen), and electrical (capacitors, supercapacitors, super-conductive magnetic energy storage (SMES)) [60]. In essence, a DC storage system employs solid state converters to get the features of an AC generator to dispatch AC power to the load when requested. Storage systems may operate in two schemes: *off-line* (backup system working only when the main grid is not available) or *grid-tie* (operating together with the grid).

Looking closely at the European perspectives on the future of electric distribution, the DERs are one of the mainstays of this electric revolution. In most European countries, DERs based on renewable generation are being developed at an accelerated pace, leading to a total current installed capacity of 106 GW of wind and 70 GW of solar energies in the year 2015. The first perspectives point out that 20% target renewable energy sources in total energy consumption will be integrated until 2020. A large portion of these resources will be connected at low- and medium-voltage distribution grids [61].

Considering all these changes, evidences suggest that the classical distribution system management is not envisaged because active systems will become more complex, for instance, the power flow will not be exclusively unidirectional (from power plants to consumers), but also from the consumers to the grid (bi-directional power flow), as illustrated in Fig. II.1. One can state that the current distribution grid was not designed to absorb a high penetration of DERs, therefore, problems related to technical limits may occur more frequently requiring network reinforcement and advanced adaptive relaying and control

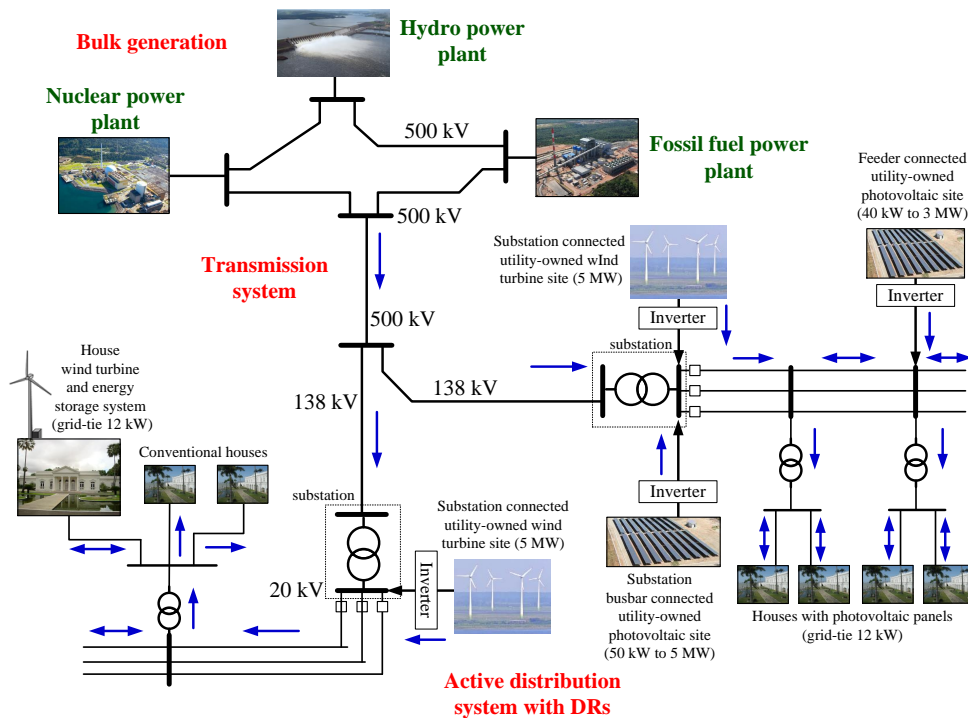


Figure II.1: Classical electricity infrastructure with special regard to the active distribution system with DERs integration (blue arrow indicates possible power flows).

systems. DERs, flexible loads and storage system will be the basis to reach a very flexible and active distribution grids [61].

The *European distribution system operators association* (EDSO) advocates that an optimized distribution grid might be achieved regarding an intrinsic interaction among the following key grid processes: *planning, connection and access*, and *operation*. In addition, greater flexibility on supply and demand sides will be a key tool concerning this assumption. In this way, such flexibility could enable the optimum use of the existing network whose goal is to minimize distribution grid extensions. Some key elements have been listed by EDSO concerning active distribution management [61]:

- ***A variety of network planning and access options that would reduce the need for investment:*** An optimized network planning taking into account a coordination among all relevant actors (transmission system operators (TSOs) and DSOs) may make the network investment more economically viable.
- ***An adequately designed connection requirement for DERs:*** DERs must fulfill some technical criteria to ensure a proper integration into the grid (dispatching optimized of the power injection, local reactive power production, local frequency tracking, local voltage and phase angle requirements). In essence, they must be able to help the distribution system during several scenarios such as islanding and peak demand.
- ***A new role of services in distribution grid operation:*** The flexibility from DERs and consumers may result in new market mechanism, in which basic system

conditions should be considered to select the appropriate actions for various system conditions. Under normal condition, the DSOs would operate according to the market procedures. Under ‘insecure’ condition, the DSOs would take actions to incentive the consumers to adapt their production and consumption according to the system status. In emergency mode, the DSOs should be able to manage immediately the loads and DERs after the contracted options have been exhausted. It is clear that the *demand response* will play an important role in active distribution management.

- **Technical tools that let DSOs become real ‘grid operators’:** the real advent of the aforementioned active distribution management tools depend on the ability of the DSO to monitor in real-time the operation status of the grid given increasing complexity. Unfortunately, in the present conjuncture, DSOs have several difficulties to control, monitor and acquire real-time data over the overall distribution territory. In this way, advanced real-time monitoring and protection schemes are demanded and the synchronized phasor measurements may open the doors for a new age of active distribution grids.

According to the abovementioned statements, it is of paramount importance to emphasize that the active power distribution system is not a ‘new’ electric system that may be developed from scratch for ensuring all capabilities, functionalities, and benefits that have been outlined. Active distribution system is a *natural evolution* of the current distribution grid, in other words, upgrading gradually the current system regarding the introduction of some elements (communication, advanced metering and control, DERs, and so forth) it is possible to achieve the envisaged active distribution systems.

In this way, the classical particularities and features of the current distribution grid must be taken into account. It has been seen that the real-time monitoring and control will play a special role, thus, the deployment of PMUs and PMU-enabled IEDs in active distribution environment must be carefully evaluated in order to identify and overcome the problematics that can be found.

The most important challenges for deploying synchronized measurements in distribution environment are related to the topology (shorter feeder lengths), buses separated by short distances causing smaller angular difference, higher harmonic content, the pernicious frequency deviation caused by many events in the high-voltage power system and/or sub-transmission systems, as well as faults in the distribution grids yielding islands supplied by high rate of DERs. These challenges are analyzed and discussed in Sections II.2- II.6 for determining their impacts over the phasor measurement estimates in distribution environment. To this end, the IEEE Std.C37.118.1-2011 [6] has been taken into account in order to evaluate if its maximum allowed errors requirements may comply with the distribution system operational requirements.

II.2 IEEE Std.C37.118.1-2011 versus Active Distribution System requirements: the problematic of the TVE metric

The performance metrics shown in I.11.d aim to evaluate whether the synchronized measurements provided by a PMU or PMU-enabled IED are accurate and reliable in order

to fulfill strict requirements. Looking closely at the newest IEEE Std. C37.118.1a-2014 [7], some evidences suggest that many commercial devices with integrated PMU functionalities could undergo severe estimate errors during transients conditions, especially under frequency deviation. This assumption might justify the reduction of criteria from the initial requirements found in the previous IEEE Std. C37.118.1-2011 [6].

The reduction of the measurement requirements may limit the deployment of synchronized devices in active distribution systems, due to that, the requirements imposed by [6] (more strictly rigorous) will be employed in this thesis. Thus, it remains for us to consider the following issue: Are the IEEE Std. C37.118.1-2011 requirements sufficiently accurate to allow the applicability of the PMUs and PMU-enabled IEDs in active distribution systems? A proper analysis of this issue must be carried out aiming to evaluate whether the current requirements may comply with the operational constraints imposed by the active distribution networks.

In this context, the TVE metric will play a key role in achieving this analysis because it indicates the *quality* of the phasor measurement estimates in order to assess the real operational status of the active distribution grids. In I.11.d, the concept of TVE metric has been properly addressed. One can recall that the TVE aggregates three source of errors combined together: magnitude error, phase angle error, and synchronization time error, in which the permissible range is within of 1%. Hypothetically, when only one source of error is present, the 1% TVE may be obtained for either a magnitude estimation error equal to $\pm 1\%$, a phase angle estimation error of $\pm 0.573^\circ$ and a synchronization time error of $\pm 31 \mu\text{s}$ and $\pm 26 \mu\text{s}$ at 50-Hz and 60-Hz, respectively. It is necessary to keep in mind that the phase angle estimation error and the synchronization time error are closely related.

The aggregation of different terms inside this metric does not allow individually inferring the contribution of each of them. In other words, the TVE value does not provide any information about the major source error(s) responsible for its determination. Indeed, a high TVE value may be caused by a high magnitude estimation error and a low phase angle estimation error, however, it is possible to mistakenly infer that the major source error is related to the phase angle estimates or even through a poor synchronization (GPS unavailability or inaccuracy of instrument transformers).

Figs II.2-II.3 depict the procedure involved to estimate the TVE value. The magnitude and phase angle differences have been enlarged in order to better illustrate the behavior of the estimate. In Fig. II.2, for the *base-case*, let us consider that the estimated and theoretical synchrophasors have the same magnitude and phase angle. Now, assuming that an error of $\pm 1\%$ is imposed only over the magnitude estimated. In this case, two possible magnitudes may be obtained being equal to $|\underline{Y}_{estimated} \pm 0.01\underline{Y}_{estimated}|$ (from origin to the interception points between the green vectors and the complex error circle).

One can observe that there is no margin for phase angle estimation error, because even a small portion of this error will contribute to exceed the TVE limit. Within the complex error circle, yielded by the rotation of the error vector (red), one can find the 1% TVE (non-normalized) related to the combined magnitude and phase angle estimation errors.

A similar analysis may be performed taking into account a *base-case* related to a theoretical and estimated synchrophasors having same magnitude but different phase angle estimates. For this case, 1% TVE will yield an isosceles triangle with vertex angle given by twice the value of the angular aperture ($2\Delta\phi$), thus, no margin for magnitude esti-

mation error is allowed. Once again, considering the rotation of the vector error, it is possible to obtain a TVE value (non-normalized) with aggregated magnitude and phase angle estimation errors.

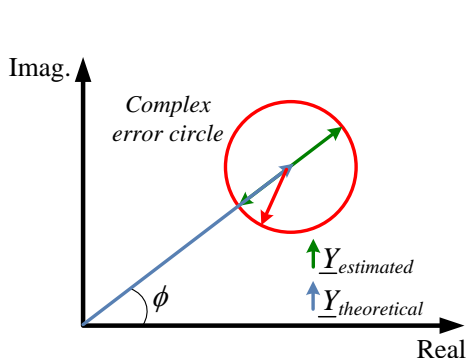


Figure II.2: TVE value based on the magnitude estimation error.

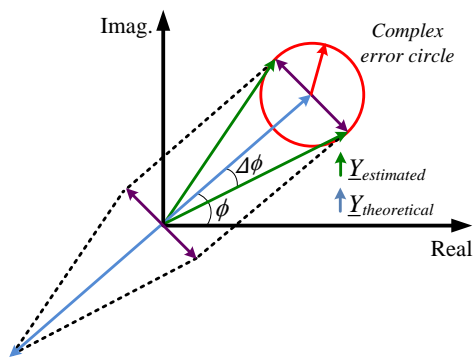


Figure II.3: TVE value based on the phase angle estimation error.

For clarity, Figs II.4-II.5 display the behavior of the TVE value concerning the complex error circle. For this example, the normalized TVE value given by Eq. I.103 has been taken into account. In the Fig. II.4, one can observe that without phase error (0°), 1% TVE is provoked exclusively by $\pm 1\%$ magnitude estimation error. Considering a phase angle error of 0.15° (equivalent to a synchronization error of about $8.33 \mu\text{s}$ for a power system frequency at 50-Hz), the margin of magnitude difference is within the range of $\pm 0.96\%$. For a phase angle error of 0.3° (related to a synchronization error around $16.66 \mu\text{s}$), the margin of magnitude difference is around $\pm 0.85\%$.

Increasing the phase angle error until reaching the maximum allowed value of $\pm 0.573^\circ$, the margin of the magnitude estimation error tends to be more and more narrow until reaching zero (matched with the maximum allowed phase angle error). Once again, a similar analysis may be performed regarding the variation of the phase angle estimation taking into account fixed magnitude errors, as illustrated in Fig. II.5.

It is clear that for 0% of magnitude error, 1% TVE is caused by the maximum allowed phase angle estimation error ($\pm 0.573^\circ$). Increasing the magnitude estimation error until $\pm 1\%$ (matched with the 1% TVE) will yield a progressive reduction of the phase angle errors until no margin of error can be allowed. One can notice that, in some specific cases, the analyzes of the percent magnitude and phase angle estimation errors could be evaluated separately in order to assert certain results.

The classical TVE metric must be employed when the synchrophasors represent a steady-state condition of the electric grid, thus, for information purposes, a non-standardized alternative metric called *TVE settling time* has been proposed in the technical literature [62], whose goal is to evaluate the impact of abrupt step changes in the synchrophasor estimation. It represents the time interval between the old and the new TVE estimates whose values are bigger than a predefined threshold Th , in other words, the TVE settling time describes the duration of the transient behavior of the synchrophasor estimation process [63], as given by Eq. (II.1)

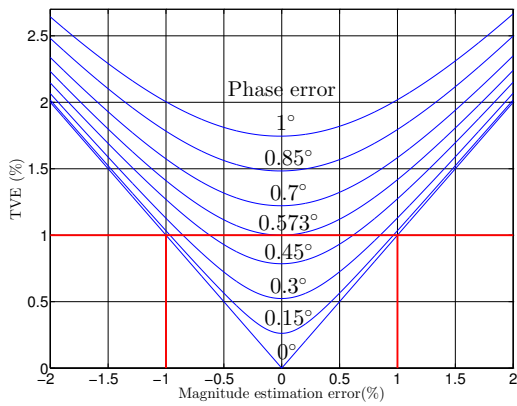


Figure II.4: TVE value obtained by the variation of the magnitude estimation error related to a fixed phase angle error.

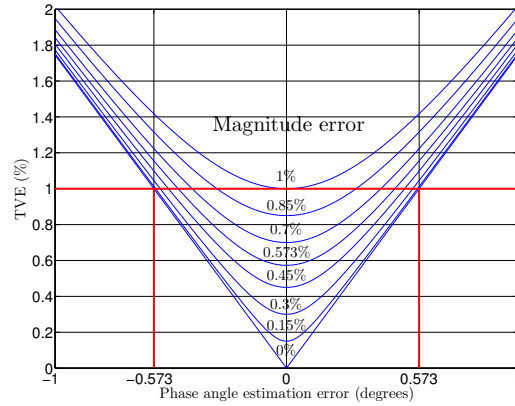


Figure II.5: TVE value obtained by the variation of the phase angle estimation error related to a fixed magnitude error.

$$\Delta t_t = new_t\{TVE\% > Th\} - old_t\{TVE\% > Th\}. \quad (II.1)$$

In active power distribution systems, the phase angle measurement provided by PMUs and PMU-enabled IEDs will be one of the most useful information to effectively allow the development of specific applications focused on these networks, in this way, a high accuracy on the phase angle estimates is envisaged. Taking into consideration the aforementioned informations regarding the classical TVE metric that requires a maximum phase angle estimation error of $\pm 0.573^\circ$ (without magnitude error), one can observe that this error margin could be considerably excessive for applications in active distribution systems, due to the fact that the angular aperture between the busbars of these networks could be lower than the maximum allowed phase angle error, thereby, large errors over the synchrophasor estimates may be produced.

This problematic of the TVE metric imposes restrictions for the placement of PMUs and PMU-enabled IEDs in distribution environment, however, as cited in Section I.12, new algorithms have been proposed aiming to overcome it. In the following section, the distribution system topology features are analyzed in order to evaluate the impact of TVE value estimates.

II.2.a Primary distribution system topology overview

The starting point of the power distribution systems are the distribution substations (**SS**). They can be considered as nodes for terminating and reconfiguring subtransmission lines, in addition, they use power transformers that step down voltage to primary distribution levels. Primary distribution systems, or medium voltage networks, consists mainly of *feeders*. A feeder, also called *mains* or *mainline*, is a three-phase backbone, protected by circuit-breakers (**CBs**), that deliver power from distribution substations to distribution transformers (retail customers) [64].

Aiming an increased reliability, a feeder from a substation may be connected to other feeders, originated from same substation or from other substations, within the distribution service territory. To accomplish this task, in general, normally-open switches (**NO**),

remotely or manually controlled, are placed in specific points for load transferring after a system fault or due to preventive maintenance activities.

These switches allow several routed paths in order to reduce the number of consumers affected by interruptions. Lateral taps - often called *taps*, *branches*, or *branch lines* - emerge out of the feeder to cover a wider service area. Owing to the fact that the loads on the feeders are more distributed, the laterals may be single and two-phase (especially for residential service), or three-phase (especially for commercial and industrial service). In effect, this feature imposes that the distribution systems be unbalanced in nature. The laterals normally are protected by fuses (**F**) to separate them from the main feeder when they are under fault condition [64], [65].

The most common wiring of the distribution primaries is composed by three-phase conductors in conjunction with a multigrounded neutral (specially for North American types of medium voltage). In this way, the transformers connected at the feeder may be single-phase (phase-neutral), two-phase (two-phase and neutral), and three-phase (with neutral). According to the type of transformer, single-phase, two-phase and three-phase loads are served. The neutral is used as a return conductor and as an equipment safety ground, that is, it is grounded periodically along the distribution service territory and at all equipment for security purposes. One can find primary distribution networks with only three-wire conductors (without neutral). For these networks, the loads are connected between phases (phase-phase connection), however, care should be taken because the absence of the neutral might generate undervoltage or overvoltage along the feeder [64].

The feeder wiring may be broadly categorized into two groups: overhead and underground. Generally, overhead wiring are chosen because it is less expensive to implement and maintain, however, it has a lower reliability (compared to the underground wiring) due to its direct exposition to natural weather and pernicious human actions. Underground wiring have a high reliability, however some constraints related mainly to implementation cost may impose some difficulties for its wide use by the distribution utilities around the world. Fortunately, the costs between overhead and underground wiring reduces progressively, thus, underground wiring are becoming more attractive [64].

Several primary distribution topologies with different shapes and sizes may be implemented, however, the most used topology is mainly radial. In this context, an issue that may be raised is: Why radial topology is often employed in primary distribution systems? According to [64], the answer for this issue is quite simple because radial circuits present many advantages including: easier fault current protection, lower fault currents over most of the circuit, easier voltage control, easier prediction and control of power flows, and lower implementation cost. Common distribution primary arrangements operated radially are classified as follows and illustrated in Figs. II.6-II.9:

- **Single feeder:** main backbone with several extensive lateral taps to serve the loads wherever they are demanded.
- **Express feeder:** it serves load concentrations located at more distant geographical area from the substation.
- **Branched feeder:** it presents some branches along the distribution service territory.

- **Very branched feeder:** backbone that presents several branches within a wide-spread distribution service territory.

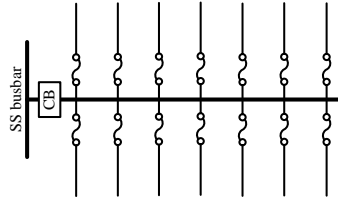


Figure II.6: Single feeder [64].

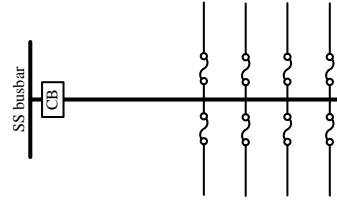


Figure II.7: Express feeder [64].

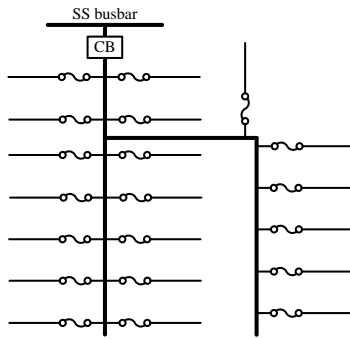


Figure II.8: Branched feeder [64].

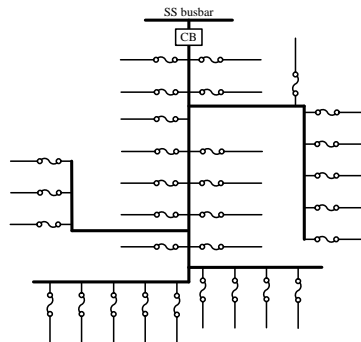


Figure II.9: Very branched feeder [64].

Normally, three classical overhead primary radial schemes are used. The first one is illustrated in Fig. II.10. The protection and restoration of this scheme is quite simple, for instance, if a fault occurs in one of the feeders, the **CB** isolates it, the **NC** switches of the faulted feeder portion is opened and the **NO** switch is closed to allow a quickly supplying.

Loops on the primary distribution have been applied to increase reliability of critical distribution areas yielding the overhead primary-loop scheme or open-loop design. This arrangement is normally open in some points using **NO** switches. It is important to mention that this scheme is not necessarily operated in a closed loop, however, under a system fault, the **CB** of the faulted feeder is opened, the damaged section is isolated through the opening of the **NC** switches, the **NO** switches are properly closed so that the largest possible number of consumers can be supplied, and after clearing the fault the **CB** is closed. Thus, alternative paths may be created reducing the fault effects, as shown in Fig. II.11. It is worthy to emphasize that even performing loops within the primary distribution network, it will still be considered weakly meshed [66].

Another overhead arrangement frequently employed is called *primary selective*. In general, this design uses transfer switch (open-switch and closed-switch operated in parallel) placed between the feeders along its extension, as depicted in Fig. II.12. The selective design aims to ensure the power supply even when one of the feeders is in failure mode.

One can state that this design must be properly implemented because each feeder must be able to absorb all loads of the other feeder.

Concerning the underground primary radial scheme, a very reliable arrangement called *spot network* is usually applied. This design is frequently applied to secondary distribution circuits, however, it may be satisfactorily employed in primary circuits. The secret of this scheme is a special switch called *network protector* (NP) connected between the feeders and the distribution transformer busbar, as shown in Fig. II.13. The NP aims to detect the current flow in the reverse direction flowing through it.

Under fault condition, the NPs connected to the faulted feeder will be crossed by inverse current flow, in consequence, they will isolate the transformer busbars from the faulted feeder. In short, for all primary topologies, an advanced coordination of the switchgear must aiming an efficient protection and operation [66], [64].

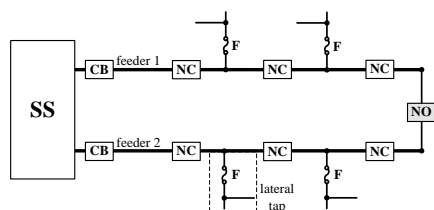


Figure II.10: Normally open overhead primary radial scheme [66].

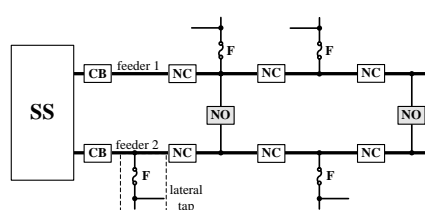


Figure II.11: Overhead primary loop radial scheme [66].

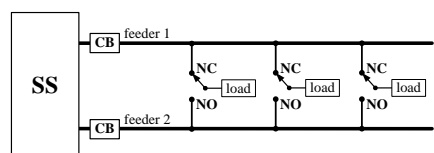


Figure II.12: Overhead primary selective radial scheme [66].

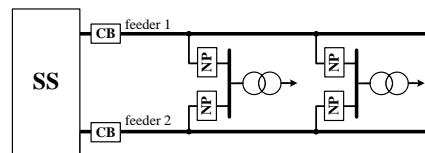


Figure II.13: Underground primary spot radial scheme [66].

Regardless of the topology employed, feeder sections are untransposed and predominantly shorter having a high R/X (resistance/reactance) ratio. These features may impose major challenges concerning the synchronized phasor measurements deployment in active distribution grids because the voltage angle difference between busbars may be small depending upon the line section parameters and the current operation status of the grid. In the following section the requirements of the IEEE standard [6] concerning the TVE metric are analyzed and evaluated taking into account the features and particularities of the classical active distribution grid topology.

II.2.b Voltage angle difference between adjacent primary busbars *versus* TVE metric

For performing the present analysis, let us consider a practical case concerning an *express feeder* section between a substation busbar and a load concentration busbar, in which PMUs are placed at the section ends to record phasor measurements. The feeder's section

impedance is equal to $0.18 + j 0.2 \Omega/\text{km}$ ($\frac{R}{X} = 0.9$) and the section's length is 2 km. It has been considered that the feeder's section is a three-phase backbone with maximum transmission capacity of 30 MVA delivered at the load point. Assuming that 26.73 MVA (26.5 MW + j 3.5 MVar yielding a power factor close to 1) is served at the load point. The base power and the base voltage are equal to 100 MVA and 20 kV, respectively. Fig. II.14 illustrates the single-line diagram of the feeder's section, as well as its quadrupole network based on the short transmission line model

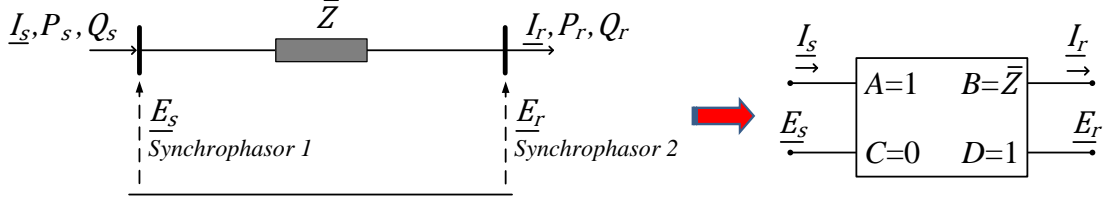


Figure II.14: Representation of the *express feeder* section between the substation- and load busbar. Likewise, one can note the quadrupole network based on the short transmission line model.

where P_s and Q_s are the active and reactive power injections in the substation busbar; P_r and Q_r represent the active and reactive power flows delivered at the load concentration point, respectively; \bar{Z} is the feeder's section impedance; \underline{E}_s and \underline{I}_s are the positive-sequence voltage and current phasor measurements taken at the substation busbar; \underline{E}_r and \underline{I}_r are the positive-sequence voltage and current phasor measurements at the load busbar, respectively.

For evaluating the impact of the TVE value related to the voltage phasors over the power flow, the mathematical relationship among the quadrupole parameters must be performed, thereby, the equation that describes the network model is given by

$$\underline{E}_s = \underline{E}_r + \bar{Z}\underline{I}_r \quad (\text{II.2})$$

hence, the equation related to the current phasor at the receiver point is

$$\underline{I}_r = \frac{\underline{E}_s - \underline{E}_r}{\bar{Z}}. \quad (\text{II.3})$$

Representing the voltage phasor measurements in polar form and rewritten Eq. (II.3) yields

$$\underline{I}_r = \frac{|E_s| \angle \phi_s - |E_r| \angle \phi_r}{|Z| \angle \alpha} = \frac{|E_s|}{|Z|} \angle (\phi_s - \alpha) - \frac{|E_r|}{|Z|} \angle (\phi_r - \alpha). \quad (\text{II.4})$$

The complex power delivered at the load busbar is represented as follows

$$S_r = P_r + jQ_r = \underline{E}_r \underline{I}_r^* = \frac{|E_s| |E_r|}{|Z|} \angle (\alpha - \phi_s + \phi_r) - \frac{|E_r|^2}{|Z|} \angle \alpha \quad (\text{II.5})$$

assuming that $\delta = \phi_s - \phi_r$ (angular aperture between the busbars), the active and reactive

power flows can be evaluated separately according to the following equations

$$P_r = \frac{|E_s| |E_r|}{|Z|} \cos(\alpha - \delta) - \frac{|E_r|^2}{|Z|} \cos(\alpha) \quad (\text{II.6})$$

$$Q_r = \frac{|E_s| |E_r|}{|Z|} \sin(\alpha - \delta) - \frac{|E_r|^2}{|Z|} \sin(\alpha). \quad (\text{II.7})$$

These components may be more easily evaluated using the phasor diagram representation given by the difference between the terms of Eq. (II.5), as depicted in Fig. II.15. Assuming that the feeder's section impedance is a true value, the phasor magnitude and phase angle estimates may vary regarding the 1% TVE range, therefore, it is envisaged to evaluate the impact of these variations over the active and reactive power flows.

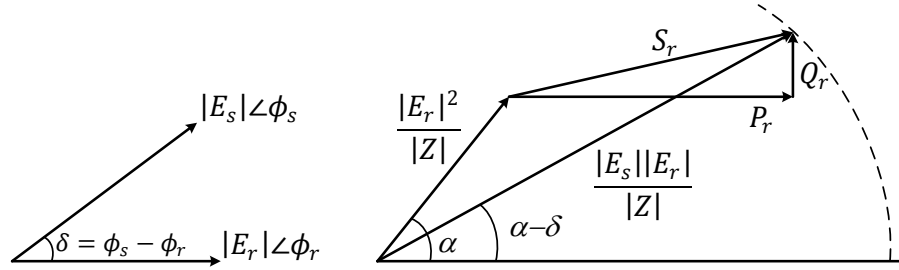


Figure II.15: Phasor diagram concerning the voltage phasor measurements and the complex power components.

For accomplishing this task, the voltage phasor at the load busbar has been settled at $0.995/0^\circ pu$ and performing a simple linear power flow the voltage phasor at the substation busbar can be directly obtained whose value is equal to $1.022/1.314^\circ pu$. Due to the fact that the PMUs are placed at distinct positions, the TVE metrics between them are independent, in other words, the error of a PMU is not correlated with the error of the other device.

In the first analysis, it has been considered that the phase angle estimates are free from errors, and 1% TVE is only related to the magnitude estimates provided by each PMU. In this way, the magnitude estimates of the voltage phasors may vary within the range of $1.022 \pm (0.01 \times 1.022) pu$ and $0.995 \pm (0.01 \times 0.995) pu$ at the substation- and load busbar, respectively. Fig. II.16 depicts the variations of the active power flow concerning 1% TVE.

Clearly, one can observe a wide variation range comprising the interval from $0.17 pu$ to $0.36 pu$ around the true active power equal to $0.265 pu$. The errors for computing the active power is around $\pm 35.85\%$. Fig. II.17 displays the variations of the reactive power flow. For this case, one can notice that a very large error margin is found whose values are within the interval of $\pm 300\%$ demonstrating a high sensitivity of the reactive power flow regarding the TVE excursions.

A negative value of reactive power has been reported that could be characterized as a power flow inversion, a load with capacitive features or the presence of voltage regulator using shunt capacitor, however, neither of these assumptions represent the actual operation status of the feeder. For both analyzes, the highest errors have been found when the phasor

magnitude estimate of a busbar undergoes a variation of +1% and the magnitude estimate of the other busbar varies of -1%.

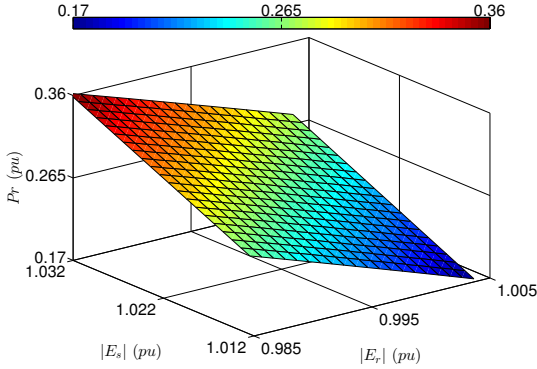


Figure II.16: Active power flow computation concerning $\pm 1\%$ TVE over the phasor magnitude estimates of each PMU (feeder's length of 2 km).

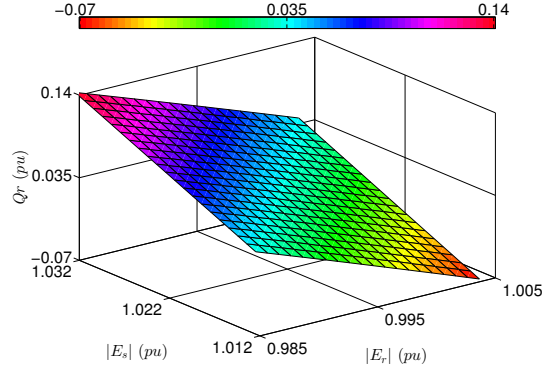


Figure II.17: Reactive power flow computation concerning 1% TVE over the phasor magnitude estimates of each PMU (feeder's length of 2 km).

A similar analysis has been accomplished taking into account 1% TVE over the phase angle estimates. For this analysis, the magnitude estimates are considered free from errors. Phase angle excursions concerning the substation- and the load busbar are within the intervals of $(1.314^\circ \pm 0.573^\circ)$ and $(0^\circ \pm 0.573^\circ)$, respectively. Figs. II.18-II.19 show the active and reactive power flow computation, once again severe errors are reported around $\pm 41.13\%$ and $\pm 291.42\%$, respectively. Once more, the highest errors have been found when the phasor phase angle estimate of a busbar is close to +1% and the other estimate varies close to -1%.

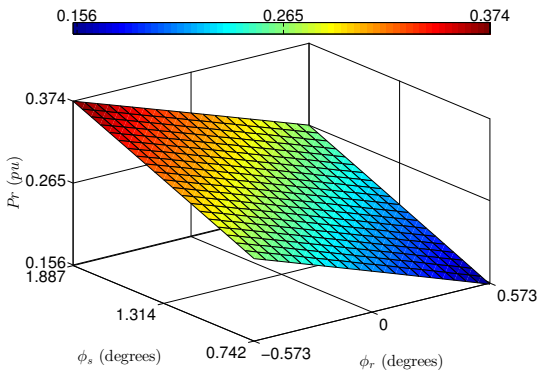


Figure II.18: Active power flow computation concerning 1% TVE over the phasor phase angle estimates of each PMU (feeder's length of 2 km).

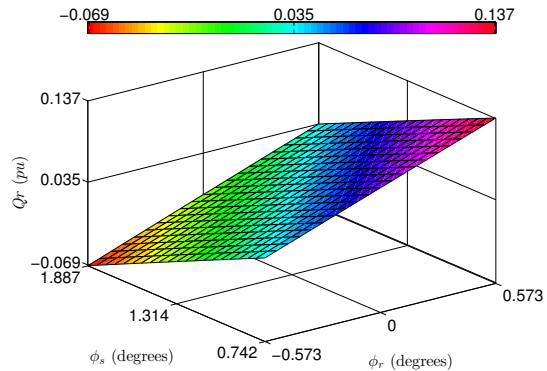


Figure II.19: Reactive power flow computation concerning 1% TVE over the phasor phase angle estimates of each PMU (feeder's length of 2 km).

One can state that the results regarding 1% TVE over the phase angle estimates are similar for those reported to magnitude estimates, in other words, for both 1% TVE produces large errors on the power flow computation whose values are far from representing the actual operating status of the grid. Figs. II.20-II.21 depict the errors for the reactive

power flow regarding the reduction of the feeder's length from 2 km to 1 km.

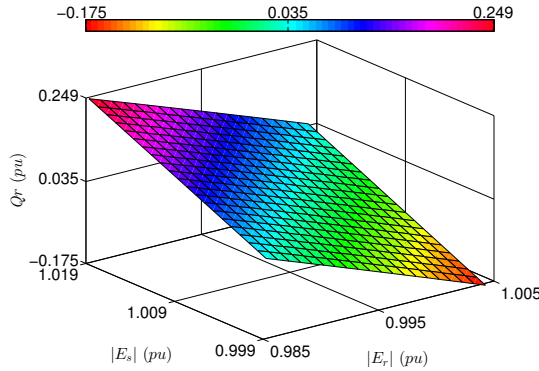


Figure II.20: Reactive power flow computation concerning 1% TVE over the phasor magnitude estimates of each PMU (feeder's length of 1 km).

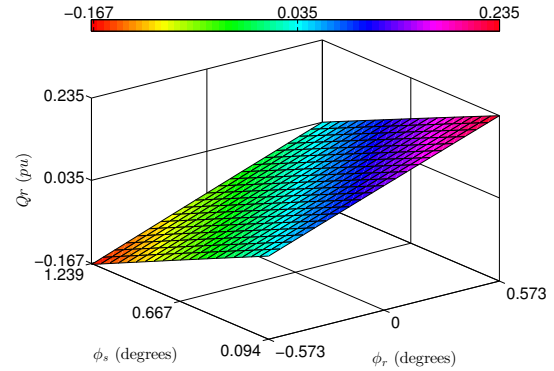


Figure II.21: Reactive power flow computation concerning 1% TVE over the phasor phase angle estimates of each PMU (feeder's length of 1 km).

This makes clear that the shorter the feeder's length, the higher the errors on the power flow computation regarding 1% TVE, therefore, this corroborates the fact that the current TVE value required by [6] is not envisaged to meet the operational requirements of the distribution grids due to the large errors that can be found for computing active and reactive power flows in primary distribution networks.

Other interesting analysis may also be carried out, for instance, the impact of 1% TVE over the residual complex power ΔS_{sr} . To carry out this analysis, let us consider the following equation

$$\Delta S_{sr} = (\underline{E}_s - \underline{E}_r) \underline{I}_r^* \quad (\text{II.8})$$

recall Eq. (II.4) and the relationship $\delta = \phi_s - \phi_r$, Eq. (II.8) can be rewritten as

$$\Delta S_{sr} = (|E_s| \angle \phi_s - |E_r| \angle \phi_r) \left(\frac{|E_s|}{|Z|} \angle \alpha - \phi_s - \frac{|E_r|}{|Z|} \angle \alpha - \phi_r \right) \quad (\text{II.9})$$

yielding,

$$\Delta S_{sr} = \frac{|E_s|^2}{|Z|} \angle \alpha - \frac{|E_s||E_r|}{|Z|} \angle \alpha + \delta - \frac{|E_s||E_r|}{|Z|} \angle \alpha - \delta + \frac{|E_r|^2}{|Z|} \angle \alpha \quad (\text{II.10})$$

rewritten Eq. (II.10) in a more compact form gives

$$\Delta S_{sr} = \frac{|E_s|^2 + |E_r|^2}{|Z|} \angle \alpha - \left(\frac{|E_s||E_r|}{|Z|} \angle \alpha + \delta + \frac{|E_s||E_r|}{|Z|} \angle \alpha - \delta \right) \quad (\text{II.11})$$

calculating the resulting term within the brackets yields

$$\Delta S_{sr} = \frac{|E_s|^2 + |E_r|^2}{|Z|} \angle \alpha - \left(\sqrt{2 \left(\frac{|E_s||E_r|}{|Z|} \right)^2 (1 + \cos(2\delta))} \right) \angle \alpha \quad (\text{II.12})$$

hence, the residual complex power is also represented by

$$\Delta S_{sr} = \left(\frac{|E_s|^2 + |E_r|^2}{|Z|} - \sqrt{2 \left(\frac{|E_s||E_r|}{|Z|} \right)^2 (1 + \cos(2\delta))} \right) \angle \alpha. \quad (\text{II.13})$$

where its phasor diagram representation is show in Fig. II.22.

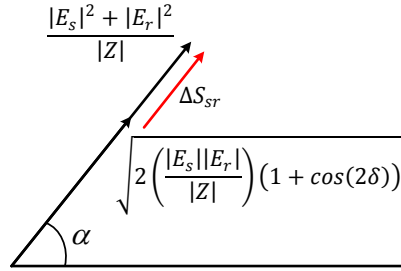


Figure II.22: Phasor diagram of the residual complex power.

Figs. II.23-II.24 illustrate the magnitude variation of the residual complex power concerning 1% TVE over the phasor magnitude and phase angle estimates. Fig. II.23 depicts an error of -54.08% when the magnitude estimates at the substation- and load busbar are -1% and +1%, respectively. However, performing the reverse, a reported error around +111.22% has been found being close to twice the previous result. Likewise, Fig. II.24 shows an error of -40.81% when the phase angle estimation errors related to the substation and load busbars are -1% and +1%, respectively. Once again, performing the reverse, the error is close to +100%.

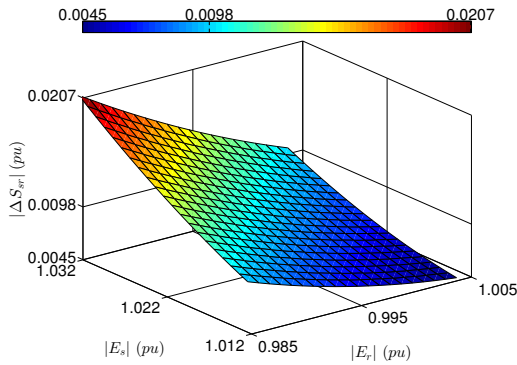


Figure II.23: Magnitude of the residual complex power concerning 1% TVE over the phasor magnitude estimates (feeder's length of 2 km).

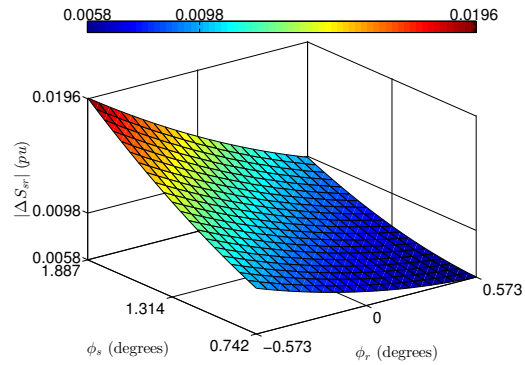


Figure II.24: Magnitude of the residual complex power concerning 1% TVE over the phasor phase angle estimates (feeder's length of 2 km).

Figs. II.25-II.26 depict the vector field of the complex power function. Clearly, one can observe that the gradient indicates that the direction to find the largest errors is decreasing the TVE over the magnitude and phase angle estimates of the load busbar and increasing the TVE over the estimates related to the substation busbar.

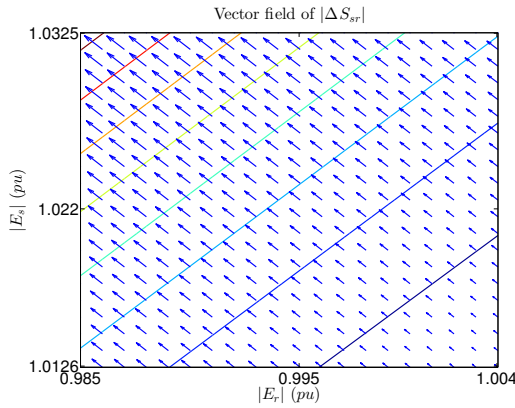


Figure II.25: Vector field of $|\Delta S_{sr}|$ concerning 1% TVE over the phasor magnitude estimates.

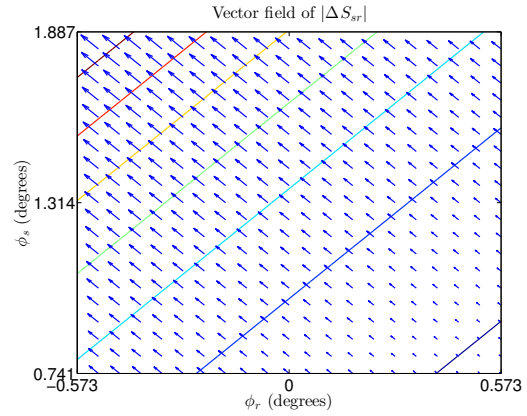


Figure II.26: Vector field of $|\Delta S_{sr}|$ concerning 1% TVE over the phasor phase angle estimates.

Performing several simulations for other primary distribution topologies considering 1% TVE over the phasor measurements taken at many points of a feeder, the reported errors are likewise extremely high, in this way, for reaching an effective deployment of PMUs in distribution environment is imperative that the TVE value be as small as possible. Analyzing the obtained results a TVE value must be less than or close to 0.1% for providing estimates that fulfill several operational requirements in electric distribution grids.

II.3 Frequency deviation

Phasor representation provides a powerful manner to analyze power systems in steady state condition. This assumption is necessary for inferring the operation status of the network. In reality, however, the power system has a dynamic feature because, among other things, the relationship between energy generation and consumption may constantly varies over time yielding imbalances, the interactions between real power demand on the grid also vary over time, operation of automatic speed control of large generators are frequently performed, several types of control are carried out, faults and other switching events may take place, and so forth [3].

In this way, electric quantities as voltage and current signals may also change their fundamental frequency (50-Hz or 60-Hz) due to dynamic conditions that may be found in power systems. In general, the frequency varies only within a relatively narrow range around the fundamental, however, to cover extreme scenarios a more large frequency range may be considered.

Concerning the requirements of the *european network of transmission system operators for electricity* (ENTSO-E), the frequency setting threshold is within 47.5 Hz - 53 Hz [67]. In [22], one can find that the U.K. and Québec power grid requirements allow a temporary frequency deviation of 7.5 Hz during islanding. For the Brazilian interconnected power system the frequency threshold is within the interval of 56.5 Hz - 66 Hz (fundamental frequency at 60-Hz) [68], and the USA power system presents a frequency threshold within the range of 56 Hz - 64 Hz [69].

One can note that each country has a different frequency threshold, however, for all of them, the time interval in which the off-nominal frequency may operate is very small (few minutes or seconds). High frequency excursions are usually controlled by means of available control actions in order to bring it back to normal values.

It is important to mention that frequency deviation in high-voltage power systems can also be ‘felt’ by the active distribution grids due to the interconnected nature of the whole power system, thereby, frequency dynamics is one of the most important measures for inferring the operation status of the electric power system.

The high integration of DERs in active distribution grids may also impose frequency deviation. For instance, during a fault yielding islands, a micro-grid with higher rate of renewable energy or with a system backup with higher storage capacity may operate within a large range of frequency around the fundamental when poor control capabilities are performed for balancing the generation and load.

In Section I.13, it has been shown some projects using PMUs and GPS-based frequency disturbance recorders placed at low-voltage side for measuring system frequency dynamics with high degree of accuracy in order to evaluate the status of the high-voltage power system. In this way, frequency excursions in distribution grid is also a reality and the PMUs and PMU-enabled IEDs specifically developed to monitor the distribution environment must be able to track accurately the frequency deviation for overcoming its undesired effects.

Concerning the IEEE Standard [6], another important issue is outlined. The Table II.1 shows the frequency range for P- and M-class PMUs related to 1% TVE. Based on these data, it is clear that accurate frequency tracking is required in order to use this information for attempting to exceed the TVE metric aiming to fulfill the operational requirements of distribution grids. Independently of the outcome frequency within the deviation range, the synchronized devices must provide very low TVE value.

All the aforementioned statements related to frequency deviation are great challenges that must be circumvent to allow the deployment of phasor measurements in active distribution systems, therefore, the development of frequency-adaptive algorithms, such as those that are proposed in Chapter III, are especially welcome.

Table II.1: Steady-state requirements at off-nominal frequency

Reference condition (nominal frequency)	P-class		M-class	
f_o	Range (Hz)	TVE (%)	Range (Hz)	TVE (%)
	± 2	1	± 5	1

II.4 Harmonic content issues

Fourier series approach that has been properly presented in Section I.3 provides the basis for evaluating the signal harmonic content in electric grids. In *harmonic analysis*, we have shown that any periodic signal can be expressed by a linear combination (superposition principle) of its harmonic content. Determining the harmonic components of the

signals (voltage or current) their effects over the active distribution grids must be carefully evaluated in order to mitigate potential problems related to power quality issues.

It is well known that harmonics can cause excessive heating on the feeder wiring, reduced torque in small-scale motors and generators, increased heating producing dielectric stress in capacitor banks applied to voltage regulation, electronics devices misoperation (relays and switchgear), equipments life-cycle reduction, and interference with communication circuits and other types of equipment [70].

According to [71], harmonics are generated by nonlinear loads connected to the electric grid such as solid state converters, arc furnaces, saturated magnetic devices, and even rotating machines (to a lesser degree). Static powers converters are the largest nonlinear loads employed in industry for several purposes including: electrochemical power supplies, adjustable speed drives, and uninterruptible power supplies. It is important to mention that DERs, such as wind turbines, can also be responsible for harmonic and flicker generation into the distribution grid.

In [72], one can find valuable informations concerning the interharmonics (frequencies that are not integer multiple of the fundamental). The main source of these components is the cycloconverter. These reliable units are used in several applications concerning rolling-mill and linear motor drives to static-var generators. The interharmonics can appear as discrete frequencies or as a wide-band spectrum.

Nonlinear loads change the sinusoidal feature of the AC signals. In short, when a distribution system is designed without regard to harmonic effects caused by nonlinear loads, it may operates under hazardous conditions. Harmonics impose variations on the RMS value of voltage and current signals producing variations on the active, reactive, and apparent powers, as well as on the power factor, as will be seen in Chapter IV.

Voltage and current phasor estimates (fundamental and harmonics) are also more susceptible to errors when the signals are distorted by high harmonic content. Therefore, potential PMUs and PMU-enabled IEDs used to monitor power quality in active distribution systems must require data processing techniques with the following features: very low TVE metric, adaptive in frequency, and accurate estimation of harmonic components.

II.5 Measurement points

The service territory of a distribution system (urban and rural area) is generally very small when compared to the service territory covered by a high-voltage power system (country area), however, performing the comparison of the number of busbars between them (in special, load and transition busbars), in general, the distribution grid has a higher amount. It is a truly difficult to monitor the overall primary and secondary distribution networks, thus, only some points in the grid are monitored. For the primary distribution, the most common measurement points are placed at substations. Normally, few points on the feeders are measured, monitored, and controlled, in which current measurements are often recorded.

In most cases, power measurements are available only at the terminals of power transformers in the substation. The usual remedy to overcome the lack of data has been the applicability of pseudo-measurements yielded by historical load data. Most utilities perform load surveys based on load aggregation (joining power transformers) to characterize

the loads along the primary feeder, in addition, customer billing data have also been applied as another source of historical data [73].

The development of new applications dedicated to active distribution grids will demand an optimized performance of the grid. New requirements for monitoring, control and protection will be created to support the grid operation under the environment introduced by the widespread adoption of DERs connected to the grid. Advances in the architecture and functionality of distribution management and automation must be performed, in this way, Distribution Management Systems (DMSs) - set of analysis functions applied to help the operator to process the data and perform several system analysis studies - and Distribution Automation Systems (DASs) - for monitoring and control of various devices at the substation and on the feeder - have to meet these new challenges in order to ensure an optimized operation [74].

Due to the above referred statements, the amount of measurement points in active distribution grids must increase in order to allow advanced real-time monitoring and control functions. In addition, new measurement capabilities, such as synchronized measurements, are especially welcome to improve the overall framework capabilities. The optimal placement of PMUs and PMU-enabled IEDs at the primary active distribution grid must be directly linked to the desired application. In short, it is not required to place synchronized devices in a widespread manner, however, they must be placed in key points in order to improve the observability of the electric grid (the loads must be known).

II.6 Overview of the deployment cost-benefit ratio

PMUs and PMU-enabled IEDs placement on the electric grid has an associated cost. Several mathematical optimization techniques for optimal placement of these devices in high-voltage power system have been proposed to ensure system observability with reduced cost of installation and maintenance. In [75], this assumption is evaluated with special regard to the PMU instrumentation channel availability (IV.6). According to the amount of busbar in the electric grid the observability cost is intrinsically related to the deployment cost of the measurement devices. It is important to mention that, due to the radial topology of many active distribution networks, the observability cost of these grids is too expensive and several measurement points are demanded.

The cost-benefit ratio is an important metric because it provides the means to assess how much the utilities are willing to pay in order to improve their monitoring, control and protection capabilities. In this way, for a coherent and economically viable deployment of synchronized measurements dedicated to monitor active distribution grid it is imperative that the implementation cost of new PMUs and PMU-enabled IEDs be reduced. In Section I.13, some low-cost synchronized devices have been presented in order to circumvent this challenge.

II.7 Conclusion

The current chapter has treated the main challenges of the synchronized phasor measurements deployment in active power distribution environment. The problematic concerning

the precision requirements demanded by the IEEE Std. C37.118 versus the active distribution system operational requirements has been presented, discussed and evaluated. The admissible TVE metric of 1% stated by the current standard is not conceivable for distribution grids and it is of paramount importance to reduce the TVE in order to achieve valuable phasor estimates in electric distribution grids.

According to the IEEE Std. C37.118, 1% TVE produces phase angle errors close to $\pm 0.573^\circ$. However, the topology of the distribution grid is composed of busbars separated by shorter distances producing smaller angular apertures between adjacent busbars. A practical case concerning an express feeder section comprised between a substation busbar and a load concentration busbar has been evaluated. PMUs with 1% TVE provide no valuable measurements concerning active- and reactive power flow as well as the power losses due to the large error margin obtained.

Additional analyses and simulations were performed and a maximum TVE value less than or close to 0.1% could provide phasor estimates that fulfill several expectations for enabling advanced distribution applications. Other challenges regarding frequency deviation, out-of-band disturbances (DC offset, harmonic, interharmonic and subharmonic), measurement points, and cost-benefit ratio related to the synchronized devices deployment are also reported.

In Chapter III, three accurate frequency-adaptive algorithms are proposed in order to overcome the main operational requirements of active distribution grids. The algorithms are analytically formulated and extensively tested and their digital designs tailored to allow a feasible deployment on low-cost DSP-based or FPGA-based M-class (monitoring) PMU model.

Chapter III

Propositions of frequency-adaptive algorithms to estimate synchronized phasor measurements in active power distribution systems

Education makes a people easy to lead, but difficult to drive; easy to govern but impossible to enslave.

Henry P. Brougham

CONTENTS

III.1	INTRODUCTION	82
III.2	ANTI-ALIASING LOWPASS FILTER DESIGN	85
III.3	FREQUENCY-ADAPTIVE MODIFIED PARK'S TRANSFORMATION-BASED ALGORITHM	88
III.3.a	Park's transformation mathematical basis	89
III.3.b	Park's transformation for estimating fundamental positive-sequence phasor	91
III.3.c	Filtering harmonic and interharmonic components before estimating fundamental positive-sequence phasor	94
III.3.d	Frequency estimation and ROCOF based on Park's transformation	103
III.3.e	Overcoming undefined frequency estimates	105
III.3.f	Frequency estimation error analysis and calibration factor	108
III.4	AN ENHANCED SYNERGISTIC FREQUENCY-ADAPTIVE ALGORITHM (4F-ALGORITHM)	112
III.4.a	Characteristics of the FIR bandpass filter bank	113
III.4.b	Half-cycle Radix-2 DIT FFT for computing selective phasor measurements	116
III.5	FREQUENCY-ADAPTIVE ALGORITHM BASED ON WEIGHTED LEAST SQUARES (WLS) APPROACH (AWLS-ALGORITHM)	118
III.5.a	Weighted Least Squares estimation overview	119
III.5.b	AWLS-algorithm for computing phasor measurements	121
III.6	IEEE STD. C37.118.1-2011 REQUIREMENTS AND COMPLIANCE VERIFICATION FOR MONITORING APPLICATIONS	124
III.6.a	Performance of the algorithms under static and/or dynamic conditions	128
III.7	CONCLUSION	138

Abstract

Accurate phasor measurements is directly related to the algorithms employed during the estimation process. For ensuring an efficient treatment and valuable phasor estimates regarding the signals found particularly in active distribution grids, new algorithms

capable of dealing with the main phenomena that may degrade these signals are highly envisaged. We have seen that the frequency deviation is a pernicious phenomenon that may affect the overall power system, furthermore, it can dramatically reduce the quality of the phasor estimates. Due to this fact, PMUs and PMU-enabled IEDs dedicated to monitor active distribution grids must also be endowed with accurate frequency-adaptive algorithms in order to provide measurements with very-low TVE value. In this chapter, three frequency-adaptive algorithms are proposed aiming to afford accurate phasor estimates under dynamic and/or static conditions of the active distribution grid. The algorithms employ a decoupled stage to track local system frequency and rate of change of frequency (ROCOF) based on classical finite derivative approximation of the fundamental positive-sequence voltage phasor phase angle displacement. However, the Park's transformation have been applied due to its high sensibility and quickly response under frequency deviation. After performing accurate frequency tracking, the algorithms use this information to properly perform the phasor estimation. The overall framework of the proposed frequency-adaptive algorithms are addressed as follow: the first is based on a modified adaptive Park's transformation able to compute fundamental positive-sequence voltage phasor estimates for ensuring an enhanced speed and accuracy in both balanced and unbalanced conditions. In the second algorithm, four steps are performed in a synergistic manner - frequency estimation, digital FIR (Finite Impulse Response) bandpass filtering, fast linear interpolation, and Radix-2 DIT FFT approach - to compute fundamental and selective harmonic phasors of a single-phase input signal. A practical algorithm based on the Weighted Least Squares approach has also been proposed for a complete phasor representation (DC offset, fundamental and harmonics) of a single-phase input signal using full or fractional-cycle data window. The performance evaluation of the proposed algorithms have been carried out under several test cases employing input signals very distorted by DC offset, out-of-band disturbance (harmonics and interharmonics), frequency deviation, and Gaussian white noise.

III.1 Introduction

The performance and accuracy of the data processing techniques used to compute phasors are directly related to the manner in which they are able to process the incoming data. It has been shown that the state of the art concerning algorithms dedicated to phasor estimation are based on the Fourier theory (recursive DFT, FFT or their slight variations) regarding a fixed nominal clock or using frequency tracking methods to overcome the leakage phenomenon whose goal is to give back for the Fourier transform its inherent robustness for estimating the parameters of interest. Non-Fourier-based algorithms have also been proposed in the technical literature, however, one can conclude that, independently of the algorithm employed, it must provide accurate estimates under several dynamic and/or static scenarios combined with a low computational cost.

Due to the vast amount of methods, the IEEE Standard [6] do not specify, require or impose a specific type of algorithm to be applied for estimating phasors. For instance, in Annex C of the aforementioned standard, some recommendations and a reference benchmark, illustrated in Fig. III.1, intended to verify the ability to implement the required performance metrics (see I.11.d) have been presented. This model applies orthogonal FIR filters to estimate phasors. In essence, Eq. (I.66) is used taking into account the coefficients of the low-pass filter (LP) designed by a triangular window function for P-class

model (concerning protection applications) or Hamming window function for M-class (concerning monitoring applications). It is important to mention that the standard itself states that many real implementation algorithms may provide estimates that surpass the referred model. In short, this appealing research field is opened for new propositions.

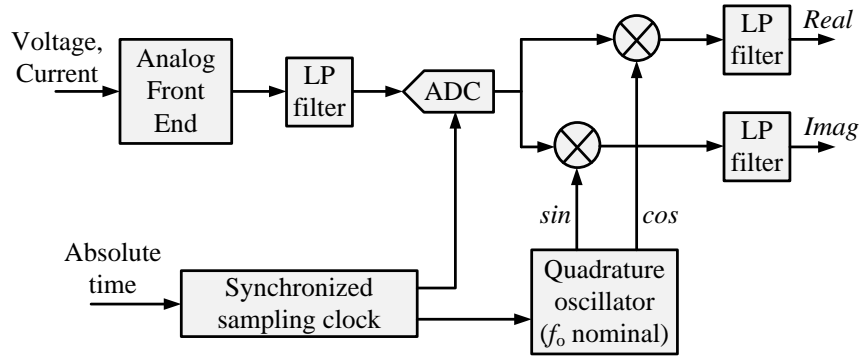


Figure III.1: Single-phase signal processing model for PMU (adapted of [6]).

Concerning the active distribution systems, the accuracy of PMUs and PMU-enabled IEDs must be led beyond the levels stipulated by [6], because the dynamic and static operational requirements of these electric grids claim for a very-low TVE metric even when pernicious phenomenon, such as frequency deviation, harmonic content and out-of-band distortions are present. Aiming to overcome the underlying problem, in this chapter three frequency-adaptive algorithms are proposed seeking to afford accurate phasor estimates under dynamic and/or static scenarios. The main general features of the proposed algorithms are: fixed sampling rate (Digital Phase-Locked Loop (DPLL) is not demanded), decoupling between local system frequency tracking and phasor estimation, and faithful mathematical modeling in time-domain.

The technique used to estimate local system frequency and rate of change of frequency (ROCOF) is based on the classical method concerning the finite derivative approximation of the fundamental positive-sequence voltage phasor phase angle displacement [25], however, Park's transformation has been applied due to its high sensitivity and quickly response under frequency deviation. Park's transformation may provide inaccurate estimates due to noise, out-of-band components and unbalances. In this way, an FIR bandpass filter centered around the nominal frequency is applied to the input signal for removing DC-offset, harmonic and interharmonic components.

The dq -components are filtered by two 3-point moving average filter (MAF) in cascaded mode for reducing the effect of a 2th order harmonic component caused by unbalanced input signals. The output data of the latter MAF is used for estimating the system frequency by finite derivative. Afterward, a short length FIR post-processing averaging filter is properly applied to further alleviate and put the frequency estimates within a very narrow error margin.

It has been commented in Section I.9 that the frequency tracking based on DPLL hardware could face difficulties with clock resolution and noise rejection, thus, to avoid it, the proposed algorithms use the estimated system frequency to change their inner features during the phasor estimation process. In other words, the algorithms employ software-

based frequency-adaptive capability. With the development of high-performance DSPs and FPGAs with powerful routines of floating-point representation this task may be adequately accomplished.

The overall framework of the proposed frequency-adaptive algorithms are addressed as follows: the first is based on a modified adaptive Park's transformation able to compute fundamental positive-sequence voltage phasor estimates aiming at enhancing speed and accuracy in both balanced and unbalanced conditions. The main goal of this algorithm concerns an improved traceability of steady-state and dynamic conditions in active distribution grids.

In the second algorithm four steps are performed in a synergistic manner - frequency estimation, digital FIR bandpass filtering, fast linear interpolation, and half-cycle Radix-2 DIT FFT approach - for computing fundamental and selective harmonic phasors of a single-phase input signal (voltage or current waveforms). This algorithm is capable of interpolating harmonic components individually according to the envisaged application, for instance, identification of typically odd harmonics on current waveforms caused by nonlinear loads for monitoring purposes of micro-grids.

A practical algorithm based on the Weighted Least Squares approach has also been proposed for a complete phasor representation (DC offset, fundamental and harmonics) of single-phase voltage or current waveforms using full or fractional-cycle data window whose goal is to improve the power quality issue on active power distribution systems.

The performance evaluation of the proposed algorithms have been carried out under several static and/or dynamic test cases based on [6]. It is of paramount importance to comment that the 1% TVE will not be used as a performance criterion, however, 0.1% TVE is used as reference in order to comply with the operational requirements of many active distribution grids, as has been shown in II.2.b. The simulations are performed taking into account signal models given by [6], in which, the input signals are very distorted by DC

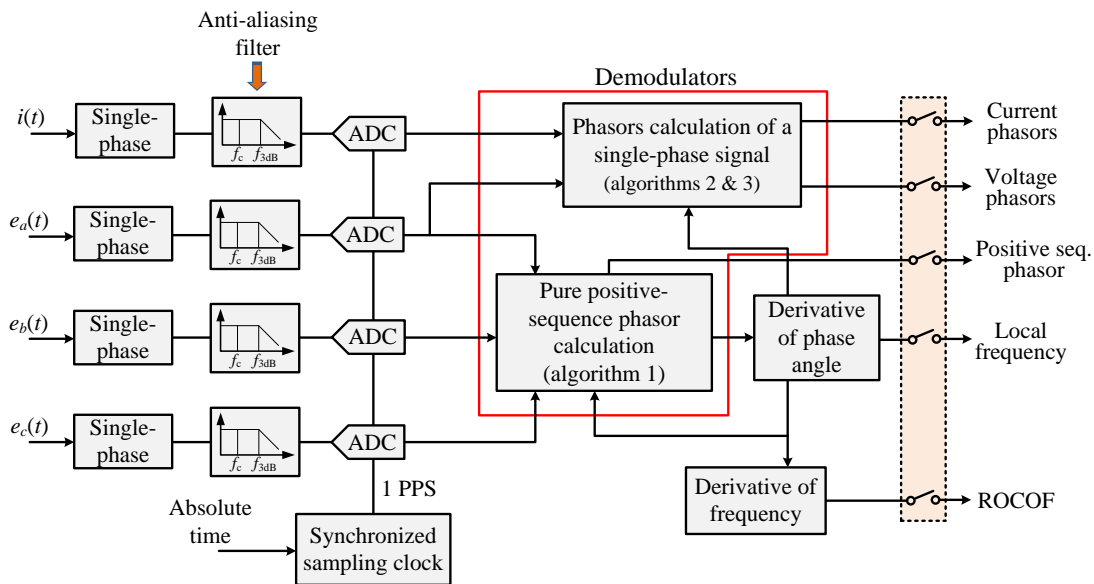


Figure III.2: Simplified signal processing model of the proposed algorithms.

offset, out-of-band disturbance (harmonics and interharmonics), frequency deviation, and Gaussian white noise. Fig. III.2 depicts a simplified signal processing model concerning the three proposed algorithms.

This model aims at displaying an overview of how the algorithms work because detailed informations regarding each of them will be further considered in later sections. In short, the three-phase voltage input signals (or a single-phase current waveform) are filtered by analog anti-aliasing low-pass filters to minimize the effect of aliasing, by removing the frequency components above the useful frequency band of analog signals (see Section I.5). Each algorithm emulates data from a technically feasible sampling process with one individual Analog-to-Digital Converter (ADC) for each input channel.

Despite it being more expensive, this sampling process may ensure true simultaneous samples, that is, samples taken at the same instants. In this way, no calculation is required to perform sample compensations. This is particularly envisaged to reduce the computational effort because the calculations will be performed only in order to compute the parameters of interest (phasors, frequency, and ROCOF). If multiplexed inputs are employed, an interpolation stage is demanded for yielding adjusted samples matched with the 1 PPS.

The sampled voltage signals are used for estimating the fundamental positive-sequence voltage phasor whose estimates are employed to track the local system frequency. Once estimated, the local frequency is used by the algorithms to perform software-based frequency-adaptive in order to calculate the true fundamental positive-sequence voltage phasor (algorithm 1), or the true fundamental and harmonic phasors related to a single-phase voltage or current waveforms (algorithms 2 & 3). Even under frequency deviation and very distorted input signals the phasors remain stationary (or quasi-stationary). In addition, the ROCOF may also be calculated based on the frequency variation over time.

The algorithms presented in the current chapter are dedicated to M-class PMU model. Longer data window (slow response) *versus* accurate estimates are the main features of the M-class, being contrary to the features related to P-class that claim for a quickly response rather than accuracy. The analysis is initiated regarding the design of the analog anti-aliasing lowpass filter whose frequency response must be evaluated in order to perform magnitude and phase angle compensation in the algorithms.

III.2 Anti-aliasing lowpass filter design

Anti-aliasing filter must be applied to a signal prior to the processing of any algorithm. The need for anti-aliasing filter has been established in Section I.5 concerning the sampling theorem, in which, it ensures that the frequency spectrum of the continuous signal is not above the Nyquist frequency. According to the criterion of selectivity, anti-aliasing filter is classified as a lowpass filter being required four parameters to specify its selectivity features: the passband gain (a_{pg}), the stopband gain (a_{sg}), the passband edge frequency or cut-off edge (p_{ef}), and the stopband edge frequency (e_{ef}).

The frequency range of a lowpass filter covers three regions (or bands) called *passband*, *transition band* and *stopband*. The first extends from zero frequency (DC) to the passband edge p_{ef} , the second extends from p_{ef} to the stopband edge frequency e_{ef} , and the third extends from e_{ef} to ‘infinity’. The gain value gives the maximum allowed ripples within

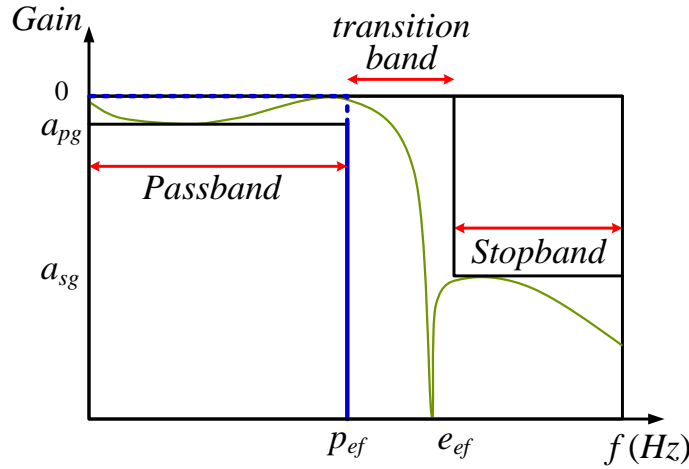


Figure III.3: Lowpass filter response. Ideal and practical filter response in blue and green lines, respectively.

the passband and stopband regions, in other words, the filter response within the passband may vary between 0 dB (unitary gain) and the passband gain a_{pg} , nevertheless the gain in the stopband may vary between the stopband gain a_{sg} and negative infinity. In essence, an ideal anti-aliasing filter presents frequencies from 0 to p_{ef} with a attenuation equal to 1, and all frequencies above p_{ef} are completely attenuated, however, in real life, the ideal filter response is physically unattainable and practical filters can only approximate this ‘brick-wall’ shape, as shown by the green line in Fig. III.3 [19].

Anti-aliasing filters may be implemented using passive components (such as resistors, capacitor and inductors) or by means of active electronic devices as operational amplifiers. Regardless of the type of implementation, in general, a buffer amplifier is employed between the filters and the ADC for protection purposes, thus, active filter design may take advantage of this feature. In addition, the size of the components is much smaller. Monolithic integrated circuits, providing compact packaging, may also be used to implement active filters. The main drawback concerning the active design is related to a more sensitivity to uncertainty of component values and temperature variations, however, selecting precise components such as metal film resistors and polystyrene or polycarbonate capacitors the effect of component’s uncertainty may be meaningfully reduced [76].

The transfer function for the anti-aliasing filter is determined according to the above-mentioned parameters (a_{pg} , a_{sg} , p_{ef} and e_{ef}) taking into account the sharpness of cut-off, the transient response, and the filter order. Several approximation methods have been used to infer the filter’s transfer function. Elliptic approximation produces one of the fastest transitions between passband and stopband, however it may yield a high phase distortion. The inverse Chebyshev response is an usual approximation method that presents a smooth response in the passband, on the other hand, variations in the stopband may be generated. The normal Chebyshev response may have ripples in the passband, but ever-decreasing gain in the stopband. An important feature of these filters is that their phase distortion is not as severe as for the elliptic filter, moreover their designs are quite simple [19].

The Butterworth response is a classical filter approximation that presents good features

related to a smooth response (flat response) in both passband and stopband regions, and a most linear phase response compared to the other approximations, which is important when distortion is considered. The drawback of Butterworth filter is that it may require a much higher order to get similar features regarding the transition band of a Chebyshev or elliptic filter [19]. Looking closely at these aforementioned statements, one can state that the Butterworth presents a more attractive approximation to be used for anti-aliasing filter design because its most linear phase response may be compensated without difficulties in the phasor estimation process.

In this way, an analog anti-aliasing lowpass Butterworth filter has been chosen and implemented to work in a synergistic manner with the proposed algorithms. A nominal frequency of $f_o = 50$ -Hz is considered, however the procedures could also be applied to 60-Hz signals. A fixed sampling rate f_s corresponding to $N = 36$ samples/cycle of the nominal frequency is used, resulting a Nyquist frequency of 18 samples/cycle (that is, 900 Hz for a 50-Hz system). The passband gain a_{pg} and the stopband gain a_{sg} have been stipulated at -0.2 dB and -20 dB, respectively, in order to comply with the reference filter frequency response specification for M-class given by [6]. The passband edge frequency p_{ef} and the stopband edge frequency e_{ef} have been fixed at 450 Hz ($\frac{f_s}{4}$) and 900 Hz ($\frac{f_s}{2}$).

Due to the non-ideality of the filter a cut-off frequency related to a gain of -3 dB is close to 580 Hz. In other words, the signals are bandlimited in 580 Hz, which is much less than the required value for complying with the Nyquist criterion. Based on these parameters, a 6th-order transfer function given by III.1 has been obtained. One can state that the reported order is slightly larger than the order found in the technical literature, for instance 4th-order in [22], however the implemented filter has an overall gain close to 1. In short, it facilitates the transition from filter design down to a physical implementation

$$H(s) = \frac{A}{Bs^6 + Cs^5 + Ds^4 + Es^3 + Fs^2 + Gs + A} \quad (\text{III.1})$$

where $A=2.353e^{21}$; $B=1$; $C=1.409e^4$; $D=9.928e^7$; $E=4.435e^{11}$; $F=1.321e^{15}$; $G=2.493e^{18}$; and $s = j\omega$.

Fig. III.4 depicts the frequency response of the filter. One can observe that the mag-

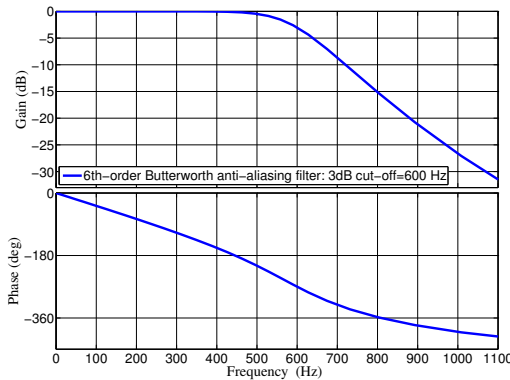


Figure III.4: Frequency response of the Butterworth filter. Magnitude response (up) and phase response (down).

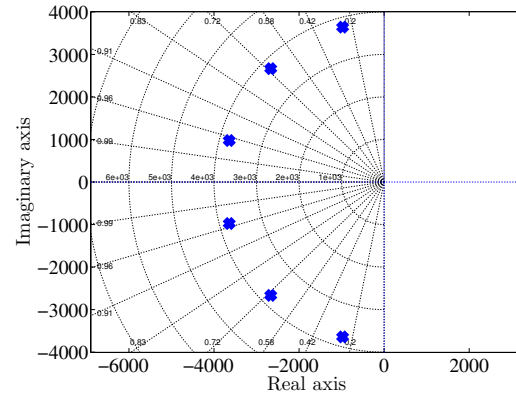


Figure III.5: Zero-pole information of the filter's transfer function. One can note 6 poles with no finite zeros present.

nitude response for the components above the Nyquist frequency (900 Hz) are greatly reduced (more than 22 dB, that fulfills the requirements of [6]). In addition, the phase response is almost linear from 0 Hz to the cut-off frequency of 580 Hz. It is noteworthy to point out that the magnitude and phase shifts introduced by this filter related to the estimated frequency and their harmonics must be compensated in the proposed algorithms. For instance, let us consider an input signal at 50.5 Hz distorted by a second and third order harmonic components, for this case, the phase shift compensation over the phasor estimates will be -19.3° , -38.7° , and -58.3° , respectively.

The main way for computing the phase shifts is using the transfer function III.1, however, a second-order polynomial approach may also be used for fast computation of the phase shifts in the range from 0 to 580 Hz due to the slight curvature. Fig. III.5 shows the zero-pole information of the transfer function, in which one can note 6 poles with no finite zeros present. Once the anti-aliasing filter is properly implemented for compensation of phasor estimates, in Sections III.3-III.5, the fundamentals of the proposed algorithms are presented in detail.

III.3 Frequency-adaptive modified Park's transformation-based algorithm

This section introduces and provides the fundamentals of the proposed data processing technique for computing fundamental positive-sequence voltage and current phasors based on a modified Park's transformation algorithm. A review of the mathematical basis regarding the Park's transformation, often called dq -transformation, is firstly addressed in order to bring the necessary knowledge to properly assess the proposed algorithm. The procedure for estimating phasors taking into account balanced and unbalanced inputs signals corrupted by Gaussian white noise and out-of-band disturbances (harmonics and interharmonics) at nominal and off-nominal frequency is also presented.

Due to its high sensibility and quickly response concerning dynamic variations in the electric grid, Park's transformation is also applied to track the local system frequency based on the fundamental positive-sequence voltage phasor phase angle displacement whose information is used to provide true phasor estimates under several scenarios. In addition, a ROCOF computation is presented aiming to detect frequency variation over time whose information could be used to improve islanding detection methods.

It has been shown that the direct application of the classical Park's transformation to estimate phasors is not advised because signal variations may severely degrade the estimates yielding a chaotic estimation process. However, by combining Park's transformation with other techniques, such as FIR filtering (bandpass and moving average filters), it is possible to take advantage of its well known features - sample-by-sample evaluation, recursivity by nature, direct representation of the real and imaginary parts of a phasor, and fast detection of dynamic variations - to boost an accurate and harmonious phasor estimation process. In essence, the proposed algorithm uses Park's transformation for both system frequency tracking and phasor estimation, however each of them is modeled differently in order to provide the parameters of interest.

III.3.a Park's transformation mathematical basis

Park's transformation is a powerful mathematical approach based on the extension of the work of Blondel, Dreyfus, and Doherty and Nickle. It was originally developed for analysis of electric machines [77] (the second most important paper of the last century concerning electrical engineering [78]). Prior to its development, the calculation of both transient and steady state load condition performance of AC motors (and generators) were based on differential equations with complex and laborious solutions. Park's transformation applies the concept of reference frame transformation to simplify the analysis by converting three-phase sinusoidal instantaneous abc -signals into two equivalent stationary dq -signals (d direct and q quadrature components).

For performing the reference frame transformation, the space vector decomposition theory must be outlined. In essence, three-phase electrical signals s_a , s_b and s_c (voltage, current or flux linkage) can be represented by means of the projections of a space vector \underline{S} over a three-phase (abc) stationary reference frame that are 120° apart in space [79]. Once the abc axes are stationary, the signals s_a , s_b and s_c vary one-cycle when the space vector perform one revolution in space (counterclockwise direction). Considering that the magnitude and rotating speed of the space vector are constants, three-phase sinusoidal waveforms related to s_a , s_b and s_c are produced with an angular aperture of 120° between them.

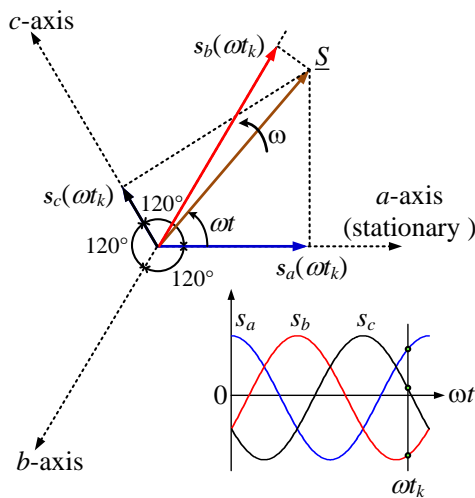


Figure III.6: Space vector diagram of the projections of \underline{S} over the abc -frame. Note the sinusoidal signals yielded by the motion of \underline{S} (adapted of [79]).

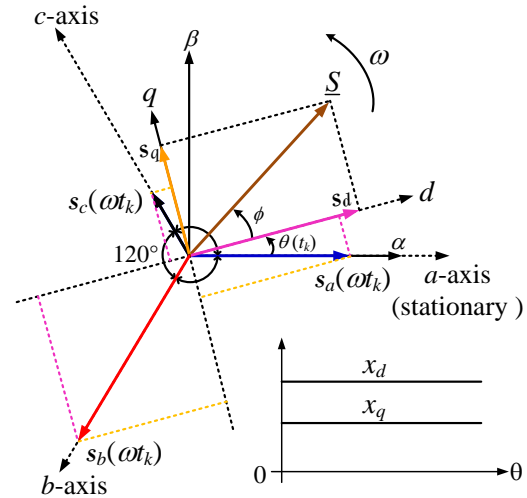


Figure III.7: Space vector diagram concerning the projections of the abc - over the dq -axes. Note that the dq variables are constant values for balanced signals (adapted of [79]).

Fig. III.6 shows the space vector diagram of the projections of a space vector \underline{S} on the abc stationary reference axes at a given instant t_k , being ω an arbitrarily angular velocity. One can observe that the instantaneous values of the three-phase signals are equal $s_a(\omega t_k)$, $s_b(\omega t_k)$, and $s_c(\omega t_k)$ whose values in the corresponding waveform depict a $s_a(\omega t_k)$ greater than $s_c(\omega t_k)$, and $s_b(\omega t_k)$ is negative. Based on this assumption, for transforming three-phase signals from the stationary abc -frame to the synchronous dq -frame, it is required to

consider two orthogonal axes d and q rotating at angular velocity ω , in which the projections of the abc -axes over the dq -axes are taken at each instant of time related to an angle $\theta(t)$ between the a -axis and the d -axis [79].

In this way, the dq -frame rotates at an arbitrary speed given by $\omega = \frac{d\theta}{dt}$, that is, the angular velocity ω is unspecified and it may rotate at any velocity or it may remain stationary [80]. Fig. III.7 illustrates the synchronous dq -frame, thereby, taking into account trigonometric identities, the sum of all projections of the abc -axes on the d - and q -axis provide a transformed s_d and s_q components given by

$$s_d = \kappa (s_a \cos(\theta) + s_b \cos(\theta - 120^\circ) + s_c \cos(\theta + 120^\circ)) \quad (\text{III.2})$$

$$s_q = -\kappa (s_a \sin(\theta) + s_b \sin(\theta - 120^\circ) + s_c \sin(\theta + 120^\circ)). \quad (\text{III.3})$$

It is possible to note that Eqs. (III.2)-(III.3) may uniquely transform s_a , s_b , and s_c to s_d and s_q , however, the converse can not be uniquely transformed. For this reason, a third component must be considered to provide a generalized transformation. In this way, the real zero-component must be used to allow a direct transformation between the reference frames without the need of pseudo-inverse matrix. The generalized transformation, also called $dq0$, covers balanced and unbalanced three-phase input signals and it can be written in matrix notation according to

$$\begin{bmatrix} s_d \\ s_q \\ s_0 \end{bmatrix} = \kappa \begin{bmatrix} \cos(\theta) & \cos(\theta - 120^\circ) & \cos(\theta + 120^\circ) \\ -\sin(\theta) & -\sin(\theta - 120^\circ) & -\sin(\theta + 120^\circ) \\ \xi & \xi & \xi \end{bmatrix} \times \begin{bmatrix} s_a \\ s_b \\ s_c \end{bmatrix} \quad (\text{III.4})$$

or, in a more compact form

$$s_{dq0} = \kappa T(\theta) s_{abc} \quad (\text{III.5})$$

being $T(\theta)$ a rotating matrix. This representation allows a straightforward manner to return from $dq0$ - to abc -reference frame, as given by

$$s_{abc} = \kappa T(\theta)^{-1} s_{dq0}. \quad (\text{III.6})$$

The κ coefficient is arbitrarily chosen according to the result envisaged. For instance, $\frac{2}{3}$, $\sqrt{\frac{2}{3}}$, and $\frac{\sqrt{2}}{3}$ transfer the associated information related to the peak value, phase-to-phase RMS value, and phase-neutral RMS value of the three-phase input signals to the dq representation, respectively. One can notice that the latter is the coefficient used to estimate phasors, as will be shown later. The ξ coefficient is linked to the chosen value of the κ coefficient, for example, if $\kappa = \sqrt{\frac{2}{3}}$ or $\kappa = \frac{\sqrt{2}}{3}$, the ξ coefficient is equal to $\frac{1}{\sqrt{2}}$. Stipulating $\kappa = \frac{2}{3}$, the ξ coefficient will be equal to $\frac{1}{2}$.

Looking closely at Eqs. (III.2)-(III.3), it is clear that the dq -components are constants for each $\theta(t)$ revolution step *if, and only if*, the s_a , s_b , and s_c signals are balanced ($s_a + s_b + s_c = 0$). If this condition is satisfied the resulting space vector \underline{S} is unchanged during the dq -frame revolution and the angular aperture ϕ between the space vector \underline{S} and the d -axis also remains constant. However, for any variation in at least one of these signals the

dynamic of the dq -transformation will be affected by pernicious effects such as harmonics on the d - and q -axis causing a non-stationary space vector \underline{S} . Due to this intrinsically feature, Park's transformation has been often applied to power system harmonic and transient identification [81], [82].

Merely for information purposes, the $\alpha\beta$ -axes appear in Fig. III.7 because the Park's transformation may be linked to the Clarke's transformation ($\alpha\beta$ -transformation), in which the angle between the α and d (β and q) axes also rotates with an angular velocity ω for converting a stationary reference frame ($\alpha\beta$ -frame aligned with the abc -frame) to a synchronous rotating frame. In order to exemplify this statement, let us consider $\kappa = \frac{2}{3}$ and balanced abc -signals, thus the correlation between the transformations is given by

$$\begin{bmatrix} s_\alpha \\ s_\beta \end{bmatrix} = \frac{2}{3} \begin{bmatrix} 1 & -\frac{1}{2} & -\frac{1}{2} \\ 0 & \frac{\sqrt{3}}{2} & -\frac{\sqrt{3}}{2} \end{bmatrix} \times \begin{bmatrix} s_a \\ s_b \\ s_c \end{bmatrix} \quad (\text{III.7})$$

hence,

$$\begin{bmatrix} s_d \\ s_q \end{bmatrix} = \begin{bmatrix} \cos(\theta) & \sin(\theta) \\ -\sin(\theta) & \cos(\theta) \end{bmatrix} \times \begin{bmatrix} s_\alpha \\ s_\beta \end{bmatrix}. \quad (\text{III.8})$$

In [83], a historical overview and the mathematical basis concerning the time-dependent symmetrical-component transformation as well as the application of unitary and orthogonal transformations are properly presented. This reference shows how to derive from general transformations logic choices for base quantities employed in per unit calculations. In addition, an interesting overview between real and complex transformations is reported.

III.3.b Park's transformation for estimating fundamental positive-sequence phasor

It has been seen in the previous section that the space vector \underline{S} may rotate at the same angular velocity of the dq -frame. Satisfying this assumption, the space vector presents constant values of magnitude ($|S|$) and phase angle (ϕ) regarding the dq -frame at any instant t . Looking closely at Fig. III.7, one can obtain $|S|$ and ϕ taking into account the projections of \underline{S} on the dq -axes, hence

$$\vec{S} = |S| \angle \phi = \sqrt{(s_d)^2 + (s_q)^2} \angle \tan^{-1} \frac{s_q}{s_d}. \quad (\text{III.9})$$

Keeping in mind the sampling process, it is possible to note that the dq -frame may rotate according to the sampling period T_s . In other words, it could rotate over time in discrete steps related to the sampling angle $\theta = \frac{2\pi}{N}$ or $\theta = \omega_o T_s$ (being N the number of samples inside a data window, and $\omega_o = 2\pi f_o$ rad/s). Therefore, one revolution of the dq -frame concerns the samples taken at one period of the three-phase abc -signals. Due to this fact, a correlation between the sampling clock, locked to the nominal power frequency, and the dq -frame rotation tends to result a stationary space vector that may represent a \underline{S}_1 voltage phasor.

One can note that the obtained phasor \underline{S}_1 computed from simultaneous three-phase sampled data represents a positive-sequence phasor. We recall that the state-vector of a

electric system concerns the collection of all positive-sequence voltage phasors in the electric grid. According to [25], measurement systems capable of measuring accurate positive-sequence phasors has the potential to simplify real-time analysis programs.

Eq. (III.9) shows that the space vector may be obtained based on its projections on the dq -axes, however, taking into account the sampling process, it is required to perform the space vector estimation using the sampled data of the three-phase input signals. For this, one can observe that the s_d and s_q components given by Eq. (III.9) are the same components found in Eqs. (III.2)-(III.3), thereby, it is possible to obtain the real and imaginary parts of \underline{S}_1 concerning the abc/dq transformation concatenated with the sampling process.

Aiming to avoid misunderstanding, from now, space vector and positive-sequence phasor will be considered as equal quantities. For a comprehensive understanding of the foregoing statements, let us consider a balanced three-phase voltage signal sampled with a T_s interval locked to the fundamental frequency

$$e_a(rT_s) = E_m \cos(\omega_o r T_s + \phi) \quad (\text{III.10})$$

$$e_b(rT_s) = E_m \cos(\omega_o r T_s + \phi - 120^\circ) \quad (\text{III.11})$$

$$e_c(rT_s) = E_m \cos(\omega_o r T_s + \phi + 120^\circ) \quad (\text{III.12})$$

being r the sample number or recursion index. Replacing these signals in Eqs. (III.2)-(III.3) yields

$$s_{d_r} = \kappa(E_m \cos(\omega_o r T_s + \phi) \cos(r\theta) + E_m \cos(\omega_o r T_s + \phi - 120^\circ) \cos(r\theta - 120^\circ) + E_m \cos(\omega_o r T_s + \phi + 120^\circ) \cos(r\theta + 120^\circ)) \quad (\text{III.13})$$

$$s_{q_r} = -\kappa(E_m \cos(\omega_o r T_s + \phi) \sin(r\theta) + E_m \cos(\omega_o r T_s + \phi + 120^\circ) \sin(r\theta - 120^\circ) + E_m \cos(\omega_o r T_s + \phi - 120^\circ) \sin(r\theta + 120^\circ)). \quad (\text{III.14})$$

Using the following trigonometric identities

$$\cos(a) \cos(b) = \frac{1}{2} (\cos(a - b) + \cos(a + b)) \quad (\text{III.15})$$

$$\sin(a) \cos(b) = \frac{1}{2} (\sin(a + b) + \sin(a - b)) \quad (\text{III.16})$$

and performing algebraic manipulations (see Appendix D for a complete deduction), it can be found

$$s_{d_r} = \frac{3\kappa E_m}{2} \cos(\omega_o r T_s + \phi - r\theta) \quad (\text{III.17})$$

$$s_{q_r} = \frac{3\kappa E_m}{2} \sin(\omega_o r T_s + \phi - r\theta). \quad (\text{III.18})$$

Interesting conclusions may be carried out regarding Eqs. (III.17)-(III.18). The first concerns the coefficient κ whose value must be equal to $\frac{\sqrt{2}}{3}$ for transferring the RMS value of the three-phase input signals to the s_{d_r} and s_{q_r} components, as has been noticed in the previous section. Clearly, one can observe that using $\frac{\sqrt{2}}{3}$ the multiplicative factor of the aforementioned equations becomes $\frac{E_m}{\sqrt{2}}$ that corroborates with the definition of phasor magnitude presented in Section I.2.

The second conclusion that may be drawn portrays the equality between the variables $\omega_o r T_s$ and $r\theta$. It has been stated that for a proper sampling process the angular velocity of the dq -frame must be matched with the sampling angle, thereby, $\omega_o r T_s$ and $r\theta$ are equal during each revolution step of the dq -frame. Looking back Eqs. (III.17)-(III.18), one can note that $\omega_o r T_s$ and $r\theta$ are being subtracted remaining only the ϕ angle, for this reason, it is possible to rewrite these equations as follows, in which the s_{d_r} - and s_{q_r} -component represent the real and imaginary parts of \underline{S}_1

$$s_{d_r} = \frac{E_m}{\sqrt{2}} \cos(\phi) \quad (\text{III.19})$$

$$s_{q_r} = \frac{E_m}{\sqrt{2}} \sin(\phi). \quad (\text{III.20})$$

therefore,

$$\underline{S}_{1_r} = s_{d_r} + js_{q_r} \quad \forall r : \underline{S}_{1_r} = \underline{S}_{1_{r-1}}. \quad (\text{III.21})$$

It can be seen that only one set of three simultaneous samples of the three-phase signal is required to estimate \underline{S}_{1_r} during each dq revolution step, that is, the phasor estimation process based on Park's transformation is recursive in nature given that the previous phasor estimate will be equal to the current estimate.

Another intuitive manner to interpret the positive-sequence phasor estimation based on the Park's transformation is combining Fortescue's theorem and DFT (or FFT). According to [84] (the most important paper of the last century concerning electrical engineering [78]) a positive-sequence voltage phasor (analogous to current) can be determined from three-phase phasors according to

$$\underline{S}_1 = \frac{1}{3} (\underline{V}_a + \alpha \underline{V}_b + \alpha^2 \underline{V}_c) \quad (\text{III.22})$$

where α and α^2 are phase shifts of e^{j120° and e^{j240° , respectively. Replacing each phasor on the right side of (III.22) by their respective DFT or FFT from a data window, as given by Eq. (III.23), one can observe that from balanced signals at nominal frequency the positive-sequence phasor estimation may be directly obtained because Eq. (III.23) becomes Eq. (III.4), that is, it has no need to perform the summation.

For balanced signals at off-nominal frequency, it is only required to change θ to rotate matched with a new sampling angle related to the nominal power system frequency. However, for unbalanced signals at nominal or off-nominal frequency interesting relationship may be carried out if the analysis is performed over data windows taking into account recursive estimation and interpolation techniques

$$\begin{aligned} \underline{S}_1 &= \frac{\sqrt{2}}{3N} \sum_{n=0}^{N-1} \left[\begin{array}{c} e^{-jn\theta} \\ e^{j(120^\circ - n\theta)} \\ e^{j(240^\circ - n\theta)} \end{array} \right]^T \left[\begin{array}{c} s_a(n) \\ s_b(n) \\ s_c(n) \end{array} \right] \\ &= d + jq. \end{aligned} \quad (\text{III.23})$$

III.3.c Filtering harmonic and interharmonic components before estimating fundamental positive-sequence phasor

In the previous section, it has been stated that the Park's transformation changes its dynamic according to the variations on the three-phase input signals. In Section II.4, it has been presented that the active distribution grids may be sensitive to harmonic and interharmonic contents, in this way, it is not advised to endow PMU and PMU-enabled IEDs dedicated to monitor these grids with classical Park's transformation-based algorithm because the accuracy of the estimates may be severely compromised. Depending upon the nature of the harmonics (balanced or unbalanced) present on the three-phase signals other new harmonic components will appear on the dq -components.

Even or odd balanced harmonics distorting the abc -signals introduce a harmonic immediately below (for instance, balanced 3th-order harmonic component distorting the abc -signals introduces a 2th harmonic on the dq -components). Unbalanced harmonics present on the abc -signals introduce a harmonic immediately below and other immediately above (for instance, unbalanced 7th-order harmonic distorting the abc -signals introduces a 6th and 8th harmonics on the dq -components) [85].

In [85], one can find an interesting method to estimate fundamental positive-sequence phasor using Park's transformation from a three-phase voltage or current signal distorted by harmonic components. The method consists in delaying samples aiming to create symmetric harmonic components 'to annul' the effect of the original harmonics. Even for high order harmonics, the author claims that the method may be properly applied. However, it should be considered that out-of-band disturbances such as DC-offset and interharmonics may also be found in active distribution grids due to nonlinear loads, but, generally, they are not always considered.

Aiming to avoid the pitfall imposed by these frequency components, in the proposed algorithm a digital FIR bandpass filter centered at the fundamental frequency attenuates harmonics, interharmonics and DC-offset outside of this band. According to [19], digital FIR filters have a finite number of terms in their impulse response, moreover they are stable, realizable, and their phase response is linear under specific conditions. It is worthy to emphasize that digital filters with linear phase response are especially welcome for data processing techniques targeted to PMU and PMU-enabled IEDs due to the ease magnitude and phase angle compensations. The implemented passband filter is based on the *Type 1 FIR filters model* (symmetric coefficients and even order). It has a passband gain (a_{pg}) and stopband gain (a_{sg}) equal to -1 dB and -21 dB, respectively. In the filter design a lower cut-off edge (Lp_{ef}) of 45 Hz and an upper cut-off edge (Ue_{ef}) of 63 Hz have been used, therefore, the signals are bandlimited around the interval of 36 Hz and 74 Hz related to a gain of -3 dB (see section III.4 for more informations regarding FIR filter design).

This asymmetry in the vicinity of the fundamental frequency aims to avoid a large amount of filter's coefficients (n_c) that will impact the filtering latency. Concerning the presented parameters, the filter's order (M) equal to 36 ($n_c = M + 1$) has been obtained, in other words, a convolution process matched with one cycle of the fundamental frequency must be performed to attenuate the undesired frequency components. Once again, magnitude and phase angle compensations related to the incoming power frequency within the bandpass region must be carried out during the phasor estimation process.

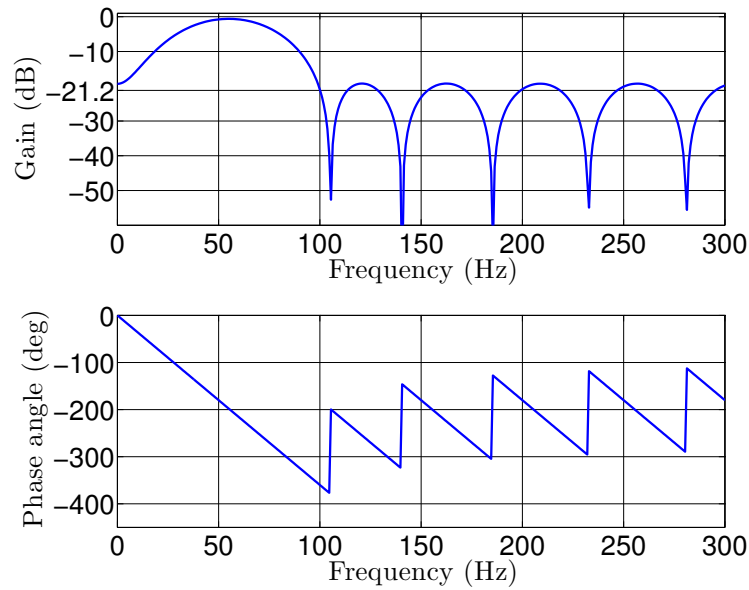


Figure III.8: Frequency response of the bandpass filter.

Fig. III.8 illustrates the frequency response of the implemented filter. For instance, let us assume a local frequency at 50.1 Hz on a distribution feeder busbar, for this case, the magnitude and phase angle compensations are equal to $0.962 pu$ and -180.4° . After removing undesired frequencies several pernicious effects that may degrade the phasor estimation process and, by consequence, the system frequency tracking can be disregarded. The obtained filtered samples are used in both frequency tracking and true positive-sequence phasor computation.

III.3.c.i Phasor estimates of balanced input signals at nominal frequency

The performance analysis of the Park's transformation under scenarios particularly found in active distribution grids such as balanced and unbalanced signals at nominal and off-nominal frequency must be evaluated. In this way, the current section presents analyzes and propositions to boost the performance of the Park's transformation for estimating phasors.

Electric systems operating at nominal frequency combined with balanced input signals represent a 'perfect' operation status. The phasor estimates would not have errors (neglecting frequency estimation error, instrumentation transformers inaccuracy, out-of-band noise, and GPS unavailability) and, in theory, the Park's transformation could be applied in a straightforward manner.

Before moving forward, it is important to mention that the analyzes performed in the current subsection as well as in the following subsections III.3.c.ii, III.3.c.iii, and III.3.c.iv consider that there are no errors in the frequency estimation process and the input signals are free from noise. These assumptions have been considered merely for mathematical formulation purposes. From the Subsection III.3.f, frequency deviation, frequency estimation errors and noise will be considered for computing phasors based on the modified Park's transformation.

In subsection III.3.b, it has been shown the fundamentals of the Park's transformation for estimating phasor, in which all equations have been carried out taking into account

balanced signals at nominal frequency, therefore, we recall that, for this scenario, the phasor estimates are obtained recursively (see Appendix D). A very small computational effort is required when compared to traditional methods such as DFT or FFT that generally require 1 cycle to track the first estimate.

For demonstrating the elegance and simplicity of the Park’s transformation under this scenario, let us consider a numerical example where a balanced voltage three-phase signal (*in pu*) at 50-Hz, given by Eqs. (III.24)-(III.26), is sampled at a rate of 1800 Hz (36 samples per period of the nominal frequency). Merely to simplify the analysis, let us assume that the power frequency is already known and let us disregard the convolution process with the FIR bandpass filter

$$e_a(t) = 1 \cos(\omega_o t + 30^\circ) \tag{III.24}$$

$$e_b(t) = 1 \cos(\omega_o t + 30^\circ - 120^\circ) \tag{III.25}$$

$$e_c(t) = 1 \cos(\omega_o t + 30^\circ + 120^\circ). \tag{III.26}$$

Since the *dq*-frame rotates according to the sampling angle, the *d*- and *q*-signal are constant values representing the real and imaginary parts of the positive-sequence voltage phasor, respectively. Fig. III.9 depicts the three-phase input signals and Fig. III.10 shows the resulting *dq*-components. One can observe that for this scenario the Park’s transformation properly estimates the real *d*-component equal to 0.6123 and the imaginary *q*-component equal to 0.3535 that represent the true phasor in polar form given by $\underline{E} = 0.7071/30^\circ$. Figs. III.11-III.12 show the phasor magnitude and phase angle estimates. One can notice that without leakage phenomenon or unbalances the resulting phasor components remain stationary.

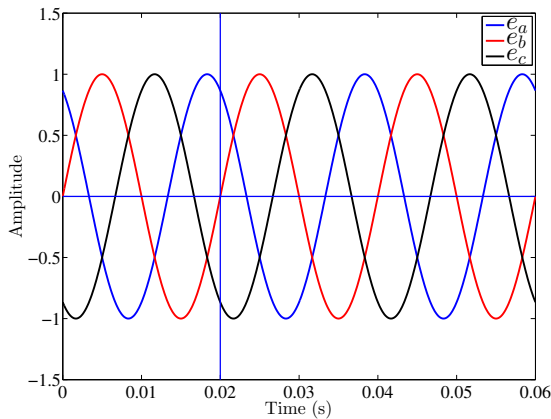


Figure III.9: Balanced three-phase voltage signal at 50-Hz nominal frequency. Sampling clock locked to the power frequency.

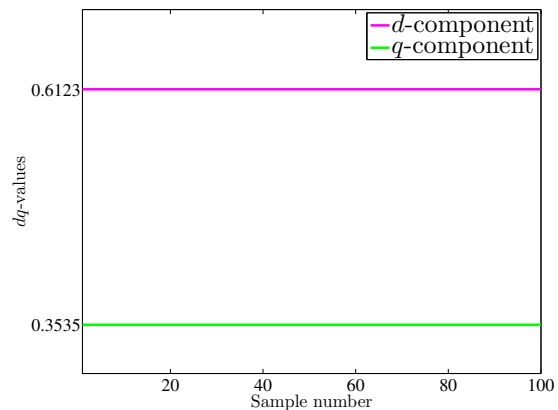


Figure III.10: Resulting *dq*-signal concerning the balanced three-phase input signal at nominal.

III.3.c.ii Phasor estimates of unbalanced input signals at nominal frequency

The real and imaginary parts of a fundamental positive-sequence phasor considering the scenario of unbalanced input signals at nominal frequency are given by Eqs. (III.27)-(III.28), respectively (see Appendix D)

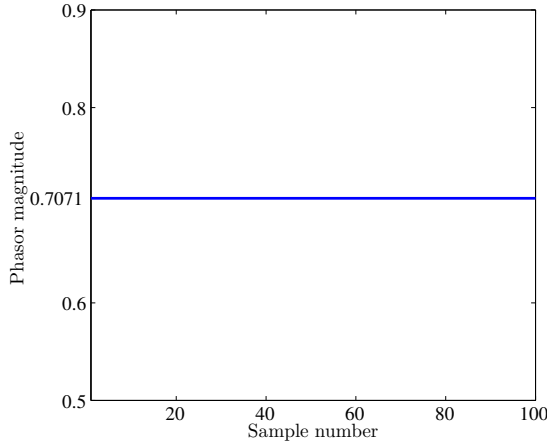


Figure III.11: Stationary positive-sequence phasor magnitude estimate of the three-phase input signal.

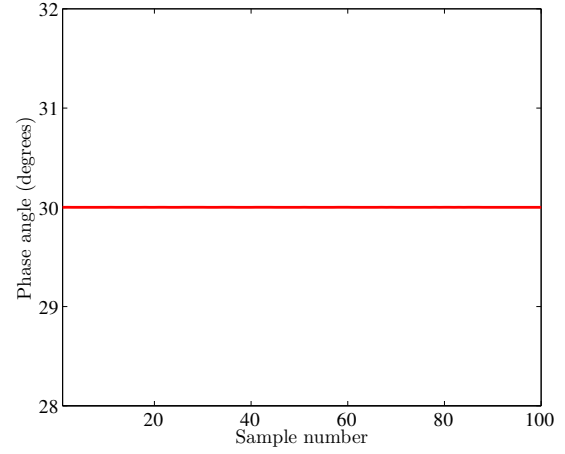


Figure III.12: Stationary positive-sequence phasor phase angle estimate of the three-phase input signal.

$$\begin{aligned}
 s_{d_r} = & \frac{\sqrt{2}}{6} (E_{m_a} [\cos(\phi_a) + \cos(2\omega_o r T_s + \phi_a)] \\
 & + E_{m_b} [\cos(\phi_b) + \cos(2\omega_o r T_s + \phi_b - 240^\circ)] \\
 & + E_{m_c} [\cos(\phi_c) + \cos(2\omega_o r T_s + \phi_c + 240^\circ)])
 \end{aligned} \tag{III.27}$$

$$\begin{aligned}
 s_{q_r} = & \frac{\sqrt{2}}{6} (E_{m_a} [\sin(\phi_a) - \sin(2\omega_o r T_s + \phi_a)] \\
 & + E_{m_b} [\sin(\phi_b) - \sin(2\omega_o r T_s + \phi_b - 240^\circ)] \\
 & + E_{m_c} [\sin(\phi_c) - \sin(2\omega_o r T_s + \phi_c + 240^\circ)]) .
 \end{aligned} \tag{III.28}$$

where $\omega_o = 2\pi f_0$ is the nominal angular frequency; ϕ is the phase angle; $T_s = \frac{1}{N \times f_o}$ is the sampling period (being N the number of samples inside a data window); and r represents the recursion index.

One can observe that the dq -components are distorted by a 2th harmonic component, in other words, they will oscillate locked to this harmonic. Due to this fact, the phasor magnitude and the phase angle estimates will also be distorted by this component. Regardless of the type of unbalance (magnitude, phase angle, or both), it can be seen that the effect of the 2th harmonic will always be present over the real and imaginary parts of the phasor. This is clear evidence that beyond the leakage phenomenon the negative-sequence component also contributes to errors in the positive-sequence phasor estimation when unbalanced signals are employed.

It is essential to remove or alleviate the oscillating over the dq -components caused by this pernicious harmonic in order to provide valuable phasor estimates. This task can be accomplished by means of a post-processing averaging digital filter (MAF) to average three delayed successive values (length equal to $l=3$). Assuming a sampling frequency of 1800 Hz a simple filter, as specified in [3], is modeled as follows

$$y(n) = \frac{1}{3} (u(k) + u(k - 6) + u(k - 12)) . \tag{III.29}$$

where $y(n)$ is the current filtered value obtained by the current and delayed $u()$ input values.

In essence, the filter averages samples with relative phase angles at 0° , 60° and 120° of the nominal frequency. Looking behind this angles taking into account the Fourier Series approach presented in Section I.3, it can be found 0° , 120° and 240° for the second harmonic whose sum of the sampled data at this relative phase angle position will be null. In this way, the undesired component may be properly removed with small computational effort. The present analysis corroborates with the Fourier-based theory shown in [3].

For the current scenario, magnitude unbalances on the three-phase signals given by Eqs. (III.24)-(III.26) have been considered. The magnitude of the e_a -signal increases by 10%, the e_b -signal remains unchanged and the magnitude of e_c -signal increases by 15%. The real and imaginary parts of the positive-sequence phasor are close to $0.6634 pu$ and $0.3830 pu$, respectively, being its representation in polar form given by $\underline{E} = 0.766/30^\circ$.

Fig. III.13 shows the unbalanced three-phase signal. In Fig. III.14, one can see that the dq -components are distorted by a 2th-order harmonic. Figs. III.15-III.16 depict the magnitude and phase angle estimates before and after performing the MAF. It is clear that

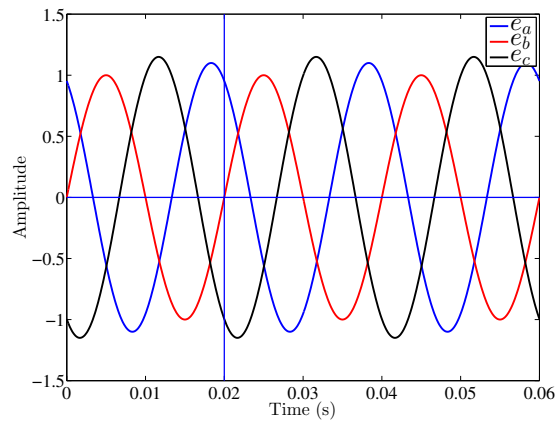


Figure III.13: Three-phase input signals with unbalanced magnitude.

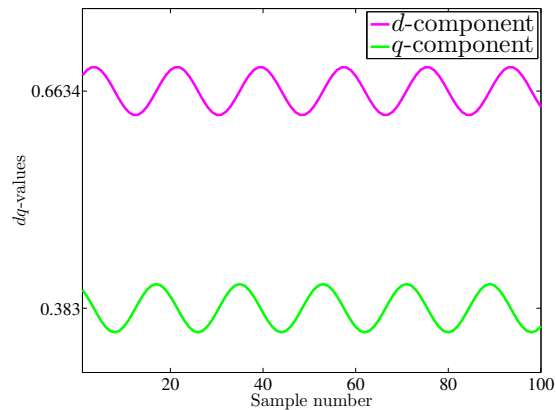


Figure III.14: Resulting dq -signal distorted by a 2th-order harmonic component.

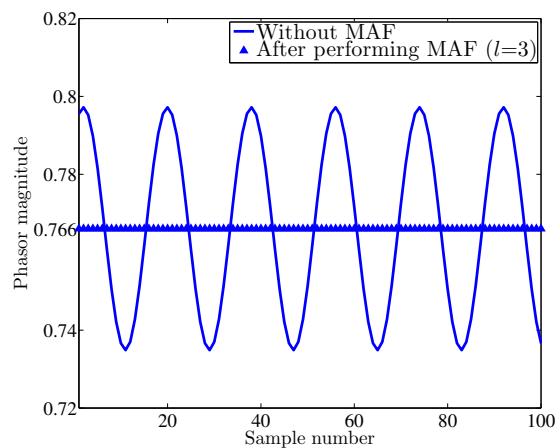


Figure III.15: Phasor magnitude before and after performing the MAF.

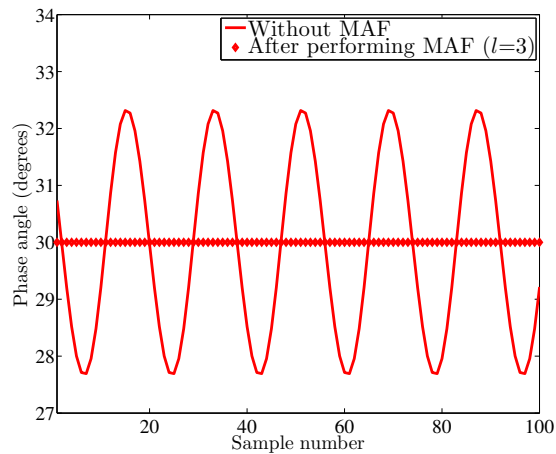


Figure III.16: Phasor phase angle before and after performing the MAF.

the filter remove adequately the undesired harmonic component and the phasor estimates will be corrected.

III.3.c.iii Phasor estimates of balanced input signals at off-nominal frequency

In Appendix D, one can find that the positive-sequence phasor components taking into account balanced input signals at off-nominal frequency are given by

$$s_{d_r} = \frac{E_m}{\sqrt{2}} \cos(\Delta\omega r T_s + \phi) \quad (\text{III.30})$$

$$s_{q_r} = \frac{E_m}{\sqrt{2}} \sin(\Delta\omega r T_s + \phi). \quad (\text{III.31})$$

being $\Delta\omega$ the angular velocity related to the frequency deviation.

It is clear that the real and imaginary components are distorted by the frequency deviation that will impose severe variations. This phenomenon corroborates with the theory presented in I.8.b concerning the leakage phenomenon under Fourier-based algorithms. It is possible to circumvent this problem keeping in mind that the θ angle represents both the angular displacement of dq -frame and the fixed sampling angle locked to the power frequency. Therefore, from balanced signals at off-nominal frequency ($f_m = f_o + \Delta f$) the required solution concerns the computation of a new dq -frame angular displacement locked to the incoming f_m frequency according to

$$\theta_{new} = \frac{2\pi f_m}{N f_o}. \quad (\text{III.32})$$

For exemplification, let us consider the balanced three-phase voltage signals given by Eqs. (III.24)-(III.26) at 51 Hz. Regardless of the frequency, the corrected phasor representation of this signal is $\underline{E} = 0.7071/30^\circ$. Figs. III.17 depicts a balanced three-phase signals at off-nominal frequency (intersection point between crossed blue lines is not matched with e_b -signal) and Fig. III.18 shows the resulting dq -components. One can observe that the dynamic of the dq -components is affected and they vary over time.

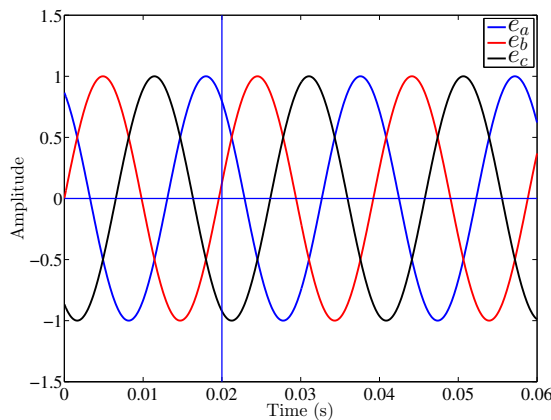


Figure III.17: Balanced three-phase signals at 51 Hz. Recall that the sampling clock is locked to the nominal frequency.

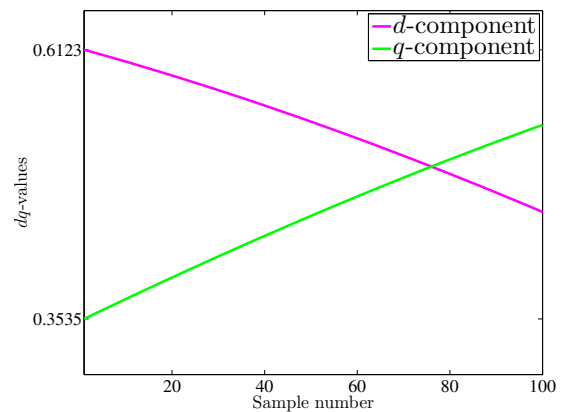


Figure III.18: Resulting dq -components of the balanced three-phase signals at off-nominal frequency.

We could be led to believe that the magnitude and the phase angle estimates are severely affected, however, Fig. III.19 depicts that the magnitude is constant. Fig. III.20 shows a wide variation of the phase angle estimates over time when the dq -frame is non-locked to the system frequency f_m . Performing corrections on the phase angle displacement according to Eq.(III.32) constant estimates are obtained.

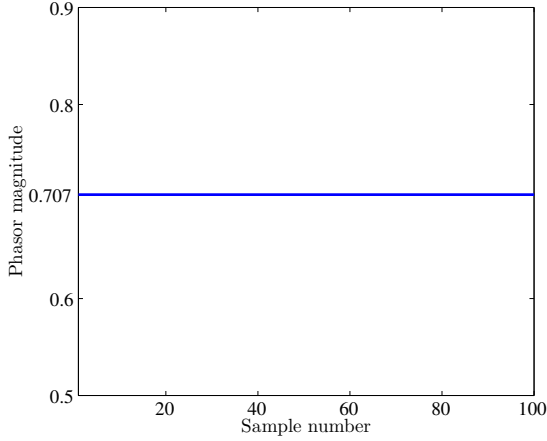


Figure III.19: Positive-sequence voltage magnitude estimate for a balanced signal at off-nominal frequency.

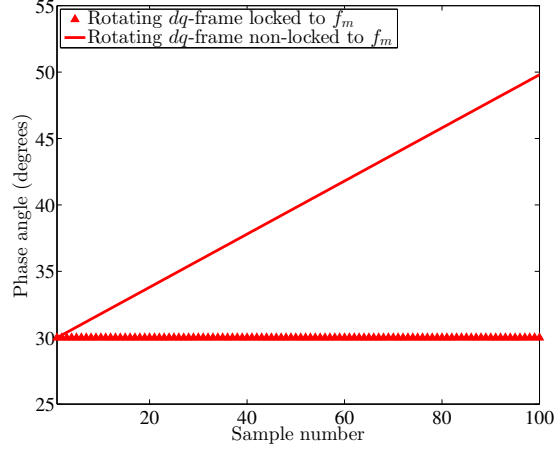


Figure III.20: Phase angle estimates before and after the corrections on the dq -frame phase angle displacement.

III.3.c.iv Phasor estimates of unbalanced input signals at off-nominal frequency

The generalized equations for the real and imaginary parts of a positive-sequence phasor based on Park's transformation are show below (see Appendix D)

$$s_{dr} = \frac{\sqrt{2}}{6} (E_{m_a} [\cos(\Delta\omega r T_s + \phi_a) + \cos(2\omega_o r T_s + \Delta\omega r T_s + \phi_a)] \quad (III.33)$$

$$+ E_{m_b} [\cos(\Delta\omega r T_s + \phi_b) + \cos(2\omega_o r T_s + \Delta\omega r T_s + \phi_b - 240^\circ)]$$

$$+ E_{m_c} [\cos(\Delta\omega r T_s + \phi_c) + \cos(2\omega_o r T_s + \Delta\omega r T_s + \phi_c + 240^\circ)])$$

$$s_{qr} = \frac{\sqrt{2}}{6} (E_{m_a} [\sin(\Delta\omega r T_s + \phi_a) - \sin(2\omega_o r T_s + \Delta\omega r T_s + \phi_a)] \quad (III.34)$$

$$+ E_{m_b} [\sin(\Delta\omega r T_s + \phi_b) - \sin(2\omega_o r T_s + \Delta\omega r T_s + \phi_b - 240^\circ)]$$

$$+ E_{m_c} [\sin(\Delta\omega T_s + \phi_c) - \sin(2\omega_o r T_s + \Delta\omega r T_s + \phi_c + 240^\circ)]) .$$

The scenario concerning unbalanced input signals at off-nominal frequency represents the worst case because the real and imaginary phasor components will be distorted by a 2th harmonic component combined with an angular velocity related to the frequency deviation. For evaluating this scenario, let us consider the same magnitude unbalances shown in the previous section combined with a high frequency deviation of +5 Hz around the fundamental. Fig. III.21 depicts the three-phase input signals and Fig. III.22 illustrates the chaotic environment of the dq -components caused by the joint action of the leakage phenomenon and the negative-sequence component.

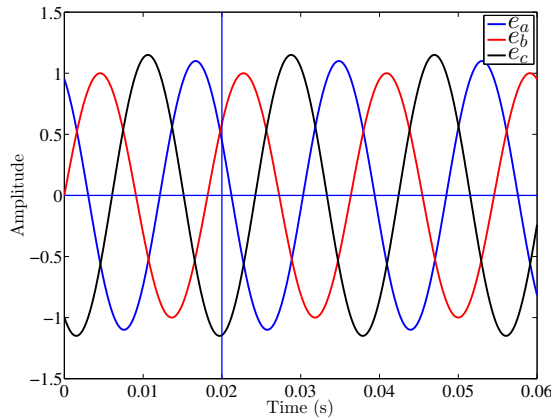


Figure III.21: Magnitude unbalances on the three-phase input signals at system frequency of 55 Hz.

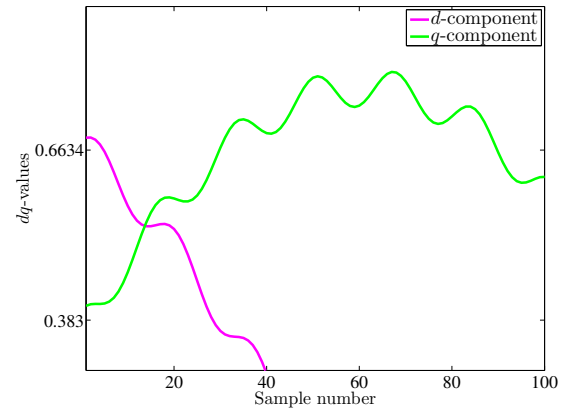


Figure III.22: Resulting dq -components for magnitude unbalances and off-nominal frequency at 55 Hz.

The goal is to determine how to extract valuable phasor estimates from the chaos. Looking closely at Eqs. (III.33)-(III.34), the analysis is initiated recalling that the leakage phenomenon may be circumvented when the phase angle of the dq -frame displacement is locked to the system frequency. Therefore, the first step consists in computing a new phase angle according to the incoming frequency. After performing this step, it can be seen in Fig. III.23 that the dq -components vary in parallel over time. In the same figure, one can note the distortion of the components provoked by the 2th harmonic component.

Filtering the estimates with the post-processing MAF1 filter the results are alleviated, but small fluctuations persist due to the frequency deviation. When computing the magnitude and phase angle estimates, it can be noted that the results maintain an oscillatory feature, as illustrated in Fig. III.24 and III.25, respectively. It can be stated that the smaller the frequency deviation produces smaller fluctuations on the filtered estimates.

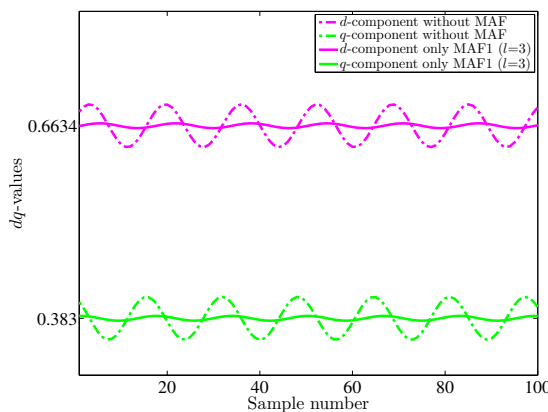


Figure III.23: Resulting dq -components locked to the off-nominal frequency.

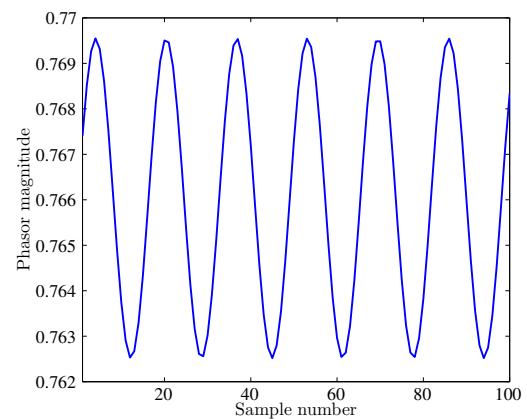


Figure III.24: Magnitude estimates computed from the MAF1 output data.

Calculating the TVE value, it can be found a maximum error around 0.641% that could be high for applications in distribution grids. In this way, it is demanded to reduce the fluctuations caused by the frequency deviation. Looking closely at Eq. (III.33)-(III.34), the

angle associated with the frequency deviation is added to the angle of the second harmonic at each instant of time. In short, some traces of the second harmonic remains on the frequency deviation, in this way, a second MAF2 post-processing filter is used to alleviate the output of the MAF1.

Fig. III.26 displays the estimates provided by the second filter MAF2. It is clear that the dq -components are even more attenuated. Now, computing the magnitude and phase angle estimates, as illustrated in Figs. III.27-III.28, one can observe the magnitude and phase angle estimates continue to vary because it is almost non feasible to remove all undesired components, however, the oscillations are within very narrow margin providing a maximum TVE value close to 0.071%. To further improve the performance of the estimates a post-processing moving average filter with length equal to $l=12$ has been applied. Besides improving the results, this filter ensures a concatenation between the phasor estimation process and the system frequency tracking with respect to a small latency for providing the envisaged estimates. Fig. III.29 illustrates the phasor estimation configuration.

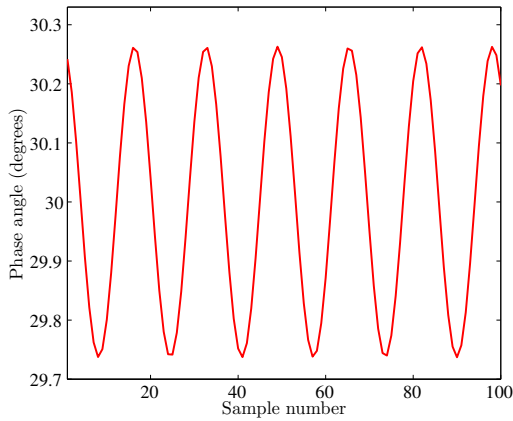


Figure III.25: Phase angle estimates computed from the MAF1 output data.

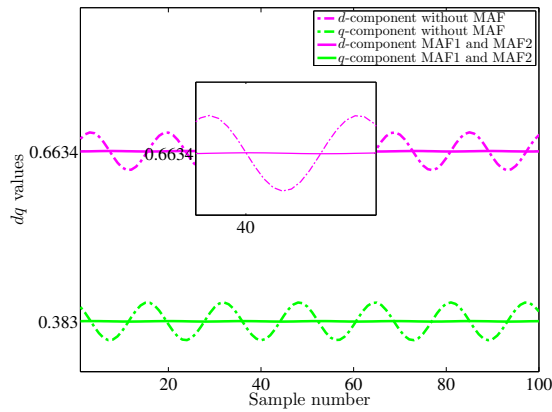


Figure III.26: Resulting dq -components computed from the MAF2 output data.

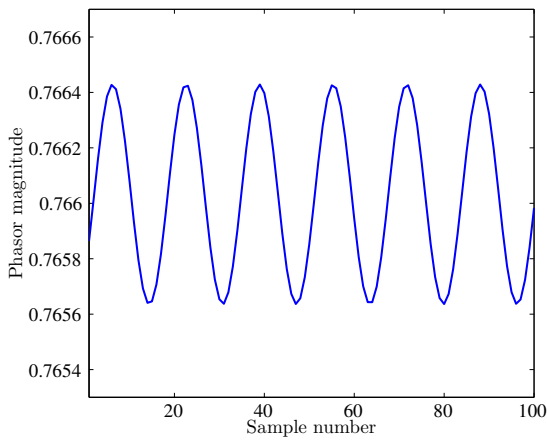


Figure III.27: Magnitude estimates computed from the MAF2 output data. The results oscillate within the range of ± 0.0004 .

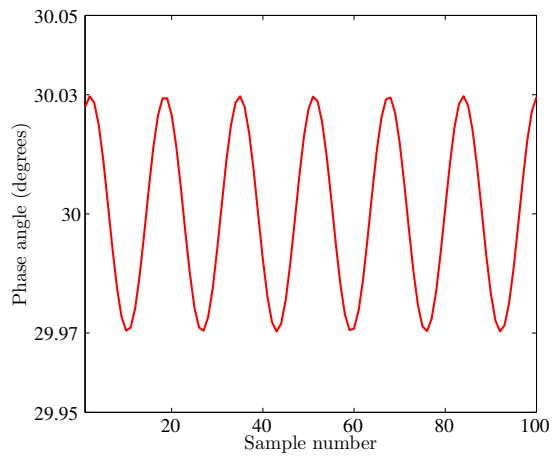


Figure III.28: Phase angle estimates computed from the MAF2 output data. The results oscillate within the range of $\pm 0.03^\circ$

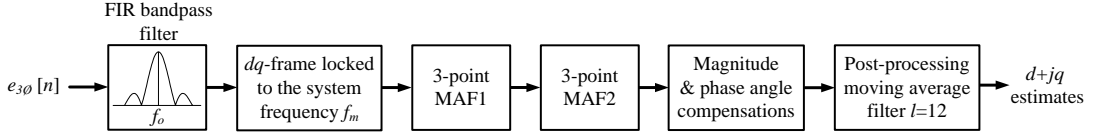


Figure III.29: Configuration to estimate fundamental positive-sequence phasor.

III.3.d Frequency estimation and ROCOF based on Park's transformation

The frequency estimation technique reported in this section is based on the theory proposed in [25], however, the Park's transformation has been applied due to its high sensitivity under signal variations. In I.8.a, it has been demonstrated that the leakage effect caused by the asynchronous sampling condition tends to rotate the phasor estimates according to the frequency deviation. In Appendix B, one can see that the impact of the leakage phenomenon over the phasor magnitude is very small when compared with the impact over the phasor phase angle.

Due to this fact, an effective manner for estimating local system frequency consists in evaluating the phase angle displacement degree over time of the positive-sequence voltage phasor estimates. Therefore, assuming that the dq -frame angular displacement rotates precisely locked to the nominal frequency, then for any voltage signal frequency variation around the nominal the resulting dq -components will vary uniformly according to the frequency deviation. The rate of change of the phasor phase angle can be defined by:

$$\frac{\Delta\phi}{\Delta t} = \frac{\phi_r - \phi_{r-1}}{\Delta t} \quad (\text{III.35})$$

being r the sample number or recursion index.

The time interval Δt (in seconds) represents the sampling period $T_s = \frac{1}{Nf_o}$, since the phase angle estimates are computed sample-by-sample. It is possible to note that Eq. (III.35) also represents the angular velocity of the frequency deviation Δf (in Hz), hence

$$2\pi\Delta f = \frac{\phi_r - \phi_{r-1}}{\frac{1}{Nf_o}} \quad (\text{III.36})$$

therefore, the frequency deviation estimate can be obtained as follows

$$\Delta f = \frac{\phi_r - \phi_{r-1}}{2\pi \frac{1}{Nf_o}} = \frac{Nf_o}{2\pi} (\phi_r - \phi_{r-1}). \quad (\text{III.37})$$

It is clear that Eq. (III.37) can also be derived from the sensitivity analysis of the dq -components through the forward finite difference approximation between the computed angles given by Eq. (III.9), thus the local system frequency can be determined according to

$$f_{m_r} = f_o + \frac{Nf_o}{2\pi} \left(\tan^{-1} \left(\frac{q_r}{d_r} \right) - \tan^{-1} \left(\frac{q_{r-1}}{d_{r-1}} \right) \right). \quad (\text{III.38})$$

Performing a similar analysis, the rate of change of frequency (ROCOF) can also be

$$ROCOF = \frac{df_m}{dt} = \frac{\Delta f}{\Delta t} \quad (\text{III.39})$$

thus, the Frequency Error (FE) and ROCOF Error (RFE) performance metrics concerning dynamic conditions of the electric grid are estimated with small computational burden.

In practice, when the classical Park's transformation is directly applied the results provided by Eqs. (III.38)-(III.39) could lead to very noisy estimates caused by meter errors, inaccuracy of metering equipment or Gaussian white noise. In addition, as shown in the previous section, the dq -components will be distorted by a 2th harmonic component when an unbalanced three-phase input signal is employed. In this way, frequency estimation based on the Park's transformation sensitivity must be carefully implemented to provide accurate estimates.

The first step consists in filtering the input signal using the FIR bandpass filter shown in III.3.c, whose goal is to remove out-of-band components (harmonics and interharmonics). Afterwards, the angular displacement of the dq -frame must be locked to the sampling nominal clock because the goal is to evaluate the offset from the nominal frequency.

The third step claims for the application of the 3-point moving average filter (MAF1) given by Eq. (III.29) in order to remove the 2th harmonic produced by the negative-sequence component. It has been shown in III.3.c.iv that the dq -components computed from unbalanced three-phase signal present the combined effect between the frequency deviation and the 2th harmonic to each recursive computation step, in this way, the MAF1 can remove the 2th harmonic but some traces of this undesired component remains on the frequency deviation. Therefore, another 3-point moving average filter (MAF2) is used for filtering the outputs of the first filter (MAF1). In other words, the filters are applied in a cascaded mode. After performing these steps the local system frequency may be computed according to Eq. (III.38).

It is important to mention that white noise may reduce the accuracy of the estimates, therefore, if a low Signal-to-Noise Ratio (SNR) in dB is present (signal very disturbed by noise) a post-processing moving average filter with length $\ell = 12$ must be applied to alleviate and put the results within a narrow error margin. One can observe that the overall filtering process uses short length filters, thereby, a very low computational burden is required and a short latency response may be achieved.

The proposed frequency tracking technique, depicted in Fig. III.30, is able to provide valuable and accurate frequency estimates even in presence of unbalanced signals. For the best case, only $1\frac{2}{3}$ cycle is required to provide the frequency estimates. Considering the post-processing filter, 2 cycles are demanded. One can note slight variations between the procedures of frequency tracking and the phasor estimation.

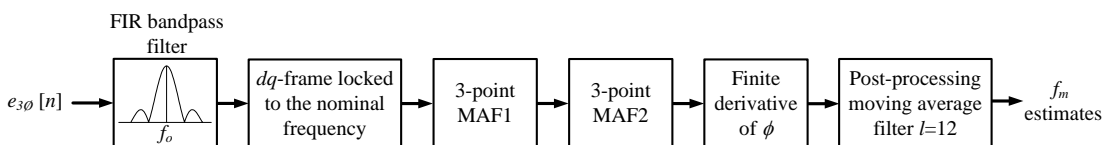


Figure III.30: Configuration to track accurate local system frequency.

III.3.e Overcoming undefined frequency estimates

Looking closely at Eq. (III.38), a special regard to the ratio between the q - and d -component must be carried out. The frequency deviation imposes variations over these components, therefore under a specific sample number the frequency estimate may be undefined. For a comprehensive understanding, let us consider the three-phase signal given by Eqs. (III.24)-(III.26) sampled at 1800 Hz (36 samples per period of the system nominal frequency at 50-Hz). Now, let us assume hypothetically that the active distribution grid has balanced three-phase signal at 55 Hz caused by a high integration of DERs.

Due to the fact that the dq -frame is matched with the nominal frequency, the phase angle variation caused by a deviation of $\Delta f = +5$ Hz is equal to is 1° ($2\pi\Delta fT_s$) between samples. In addition, independent white noise with SNR=60 dB has been added for each single-phase input signal. Fig. III.31 (a) shows the frequency estimates. One can observe that at sample number 48 and 228 the frequency estimate is undefined. Fig. III.31 (b) provides the answer for this phenomenon, in which it is caused by d -component values close to zero making unsolved Eq. (III.38) or due to the zero-crossing of the d -component yielding corrupted frequency estimates that do not match with the actual system frequency.

Another point to note is related to the interval in which the frequency estimate is undefined. For instance, for the first interval one can notice that it begins at a sample number 48 and ends at 61, that is, the interval comprises 13 samples. In this way, one can state that the width of the interval is related to the convolution process between the post-processing averaging filter (length $\ell = 12$) with the undefined estimate. The same analysis may be performed for other intervals.

For overcoming this phenomenon, the frequency estimation process uses a routine to monitor the d -component. In essence, this routine performs the product between the current d -component estimate and the immediately previous estimate. The obtained result

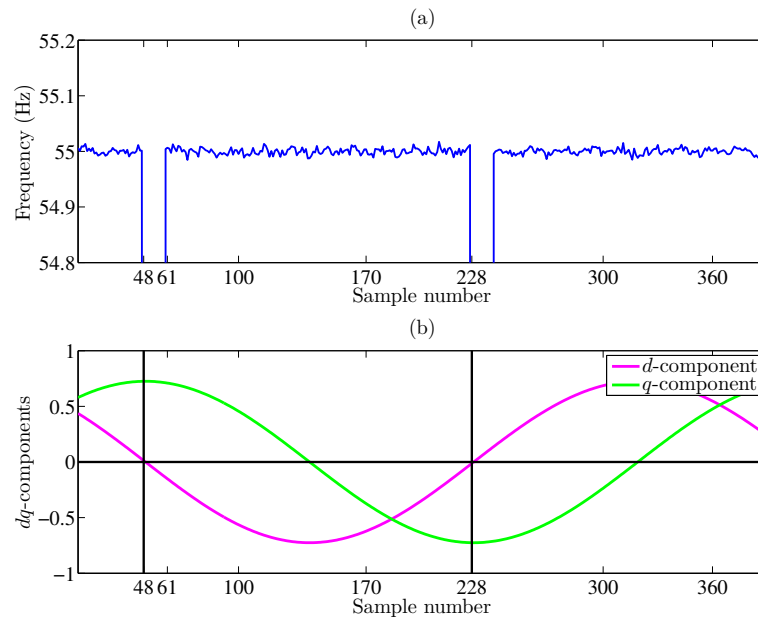


Figure III.31: (a) Frequency estimates, (b) dq -components variation. Note the undefined frequencies beginning at sample numbers 48 and 228 caused by d -components close to zero.

is compared with a very low threshold and for results above it the frequency estimate is computed by Eq. (III.38). For results below the threshold, the estimate is assigned with the value of the immediately previous estimate. This procedure is performed for avoiding the convolution between the post-processing filter output and this undesirable estimate.

For evaluating the performance of the frequency tracking technique under several scenarios, Figs. III.32-III.39 show the estimates considering variations on the three-phase signals given by Eqs. (III.24)-(III.26). We would like to point out that the reported results concern the worst estimates. In Fig. III.32 the frequency estimates have been obtained taking into account balanced signals at 50.05 Hz. A SNR=87.95 dB has been considered representing a measurement process with small noise disturbance.

For this scenario the estimates are very accurate providing a maximum estimation error around 0.64 mHz. Fig. III.33 depicts the estimates computed from a small degree of unbalanced magnitudes at system frequency of 50.1 Hz. The unbalance degree of the e_a -, e_b -, and e_c -signal increased by 1%, 2%, and 1.5%, respectively. Once again a measurement process with small noise is considered regarding a SNR=88.63 dB. A maximum estimation error around 0.57 mHz has been reported.

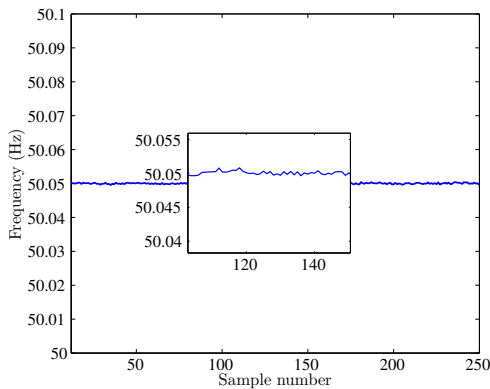


Figure III.32: Frequency estimates obtained from balanced three-phase signals at 50.05 Hz. For this scenario a SNR=87.95 dB has been considered.

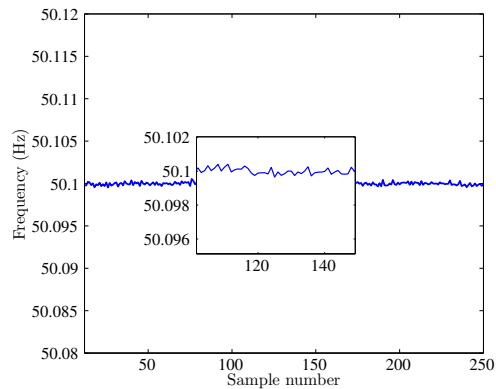


Figure III.33: Frequency estimates obtained from small degree of unbalanced magnitude of three-phase signals at 50.1 Hz. SNR=88.63 dB.

Now, for further evaluation of the frequency estimates let us assume pernicious signal scenarios such as high frequency deviation and/or high noise content. It is important to mention that white noise models are applied independently for each single-phase. In Fig. III.34, the frequency estimates have been obtained concerning unbalanced magnitudes and a local system frequency at 45 Hz. The magnitude of the e_a -signal increased by 10%, the magnitude of the e_b -signal remains constant, and the magnitude of the e_c -signal increased by 15%. For this scenario a SNR=60 dB has been considered. For this noisy scenario, a maximum frequency estimation error around 0.02 Hz has been obtained.

Fig III.35 shows the frequency estimates computed from unbalanced magnitudes at 49.72 Hz. The magnitude of the e_a -signal reduced by 10%, the magnitude of the e_b -signal increased by 10%, and the magnitude of the e_c -signal increased by 25%. For simulation puprposes, a SNR=66.02 dB has been considered. For this scenario, a maximum frequency estimation error around 7.2 mHz has been found.

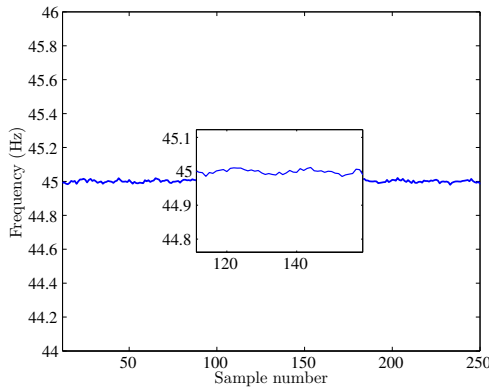


Figure III.34: Frequency estimates obtained from unbalanced magnitude of three-phase signals at 45 Hz. SNR=60 dB.

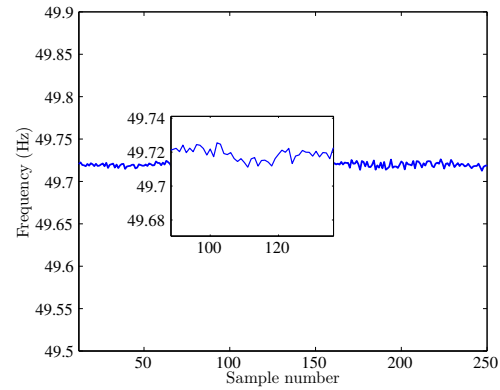


Figure III.35: Frequency estimates obtained from unbalanced magnitude of three-phase signals at 49.72 Hz. SNR=66.02 dB.

Another scenario concerning frequency estimates under unbalanced magnitude is shown in Fig. III.36. Now, the magnitude of the e_a -signal reduced by 5%, the magnitude of the e_b -signal increased by 15%, and the magnitude of the e_c -signal increased by 30%. Assuming a system frequency of 50.15 Hz and a SNR=67.95 dB, a maximum error around 5.7 mHz has been reported. Fig. III.37 illustrates the frequency estimates regarding unbalanced phase angles at system frequency of 49.95 Hz. The phase angles of the e_a -, e_b -, and e_c -signal are equal to 30° , 90° , and 45° , respectively. A SNR=72.04 dB is employed. The maximum frequency estimation error is close to 4.4 mHz.

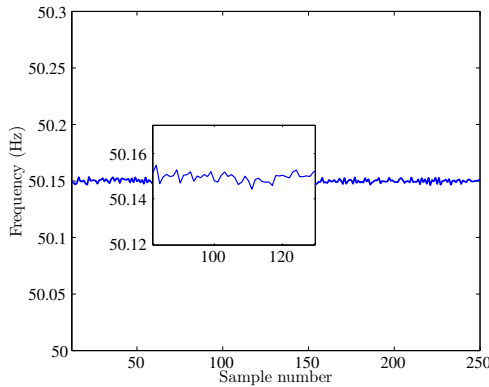


Figure III.36: Frequency estimates obtained from unbalanced magnitude of a three-phase signal at 50.15. SNR=67.95 dB.

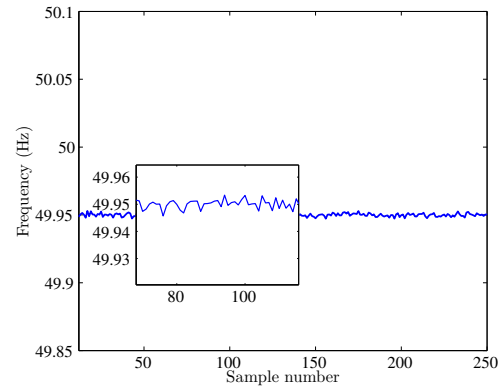


Figure III.37: Frequency estimates obtained from unbalanced magnitude of a three-phase signal at 49.95 Hz. SNR=72.04 dB.

Figs. III.38-III.39 display the frequency estimates regarding unbalance in both magnitude and phase angle. For estimating the frequency in Fig. III.38, the magnitudes of e_a -, e_b -, and e_c -signal increased by 10%, 20%, and 30%, in addition, the phase angle of e_a -, e_b -, and e_c -signal are equal to 36° , 25.7° , and 6.2° , respectively. A system frequency at 51 Hz and a SNR=66.93 dB have been considered. For this scenario a maximum error around 7.1 mHz has been obtained. In Fig. III.39, the frequency estimates have been car-

ried out taking into account magnitude unbalances of 10%, 30%, and 25% over the signals e_a , e_b , and e_c , and their phase angles are equal to 60° , 20° , and 10.58° , respectively. A system frequency at 55 Hz and a SNR=60 dB have been deemed. The maximum frequency estimation error obtained for this scenario is around 0.048 Hz.

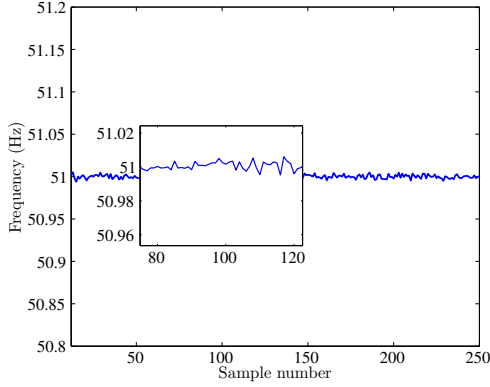


Figure III.38: Frequency estimates obtained from unbalance in both magnitude and phase angle a three-phase signal at 51 Hz. SNR=66.93 dB.

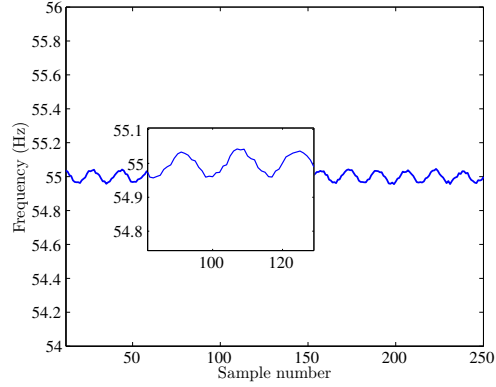


Figure III.39: Frequency estimates obtained from unbalance in both magnitude and phase angle a three-phase signal at 55 Hz. SNR=60 dB.

One can observe that high degree of unbalances combined with high frequency deviation and very noisy data tend to reduce the performance of the frequency estimation process due to the difficulty of removing all the unwanted components. This is depicted especially in the last scenario presented where one can note a small effect of the 2th harmonic component caused by the negative-sequence component over the dq -components. However, it can be noted that even under very distorted scenarios the frequency estimates remain within an acceptable margin of accuracy for practical applications. We recall that the reported results concern the worst estimates with a small probability of occurrence. Performing several simulations under various types of scenarios accurate frequency estimates with errors within ± 0.5 mHz have been obtained.

III.3.f Frequency estimation error analysis and calibration factor

From a very intuitive point of view, the only way to get constant phase angle estimates without slope is ensuring a frequency estimation free from errors, however, it is almost unattainable. Even a small error in the frequency estimate will change the dynamic of the Park's transformation. In this way, a frequency estimation error analysis is essential for assessing the effect of the frequency estimation error over the phasor estimates. For instance, consider the three-phase signals given by Eqs.(III.24)-(III.26) with an actual system frequency at 50.05 Hz and a SNR=70 dB.

For this analysis, it has been assumed that the frequency estimate is equal to the incoming system frequency. Fig. III.40 depicts the frequency distribution of the phase angle. One can observe that the estimates are accurate and a very small phase angle error margin is provoked by the noise. Fig. III.41 illustrates the phase angle estimates around the true value of 30° . Assuming an estimation error of -5 mHz, that is, an estimate of 50.045 Hz, the frequency distribution changes completely its shape, as shown in Fig. III.42.

It is a clear evidence that the phase angle continues to vary slowly over time. The analyzed time interval to plot the frequency distribution is 1 second, that is, the interval between two successive 1 PPS or the time required to the dq -frame rotate 1800 samples. In this way, after 1 second the phase angle increases around 1.812° , as can be seen in Fig. III.43.

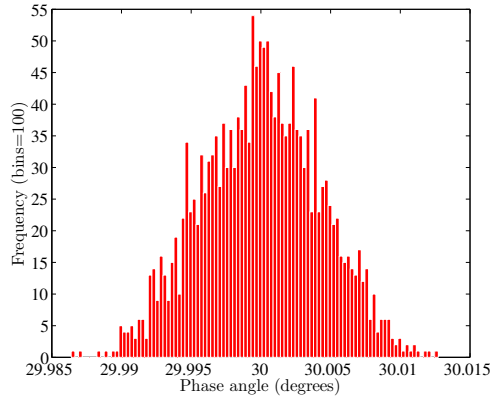


Figure III.40: Frequency distribution of the phase angle estimates when the estimated and the actual system frequency are identical. A SNR=70 dB has been considered.

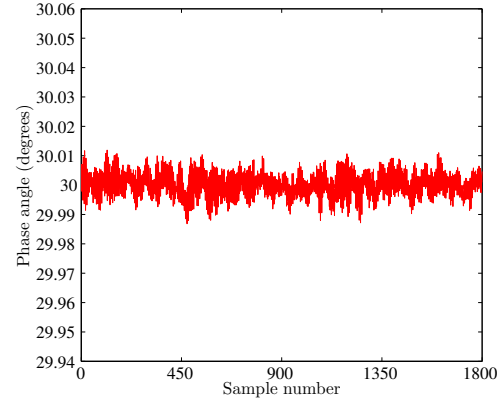


Figure III.41: Phase angle estimates without slope when the estimated and the actual system frequency are identical. Note the small variations caused by the noise.

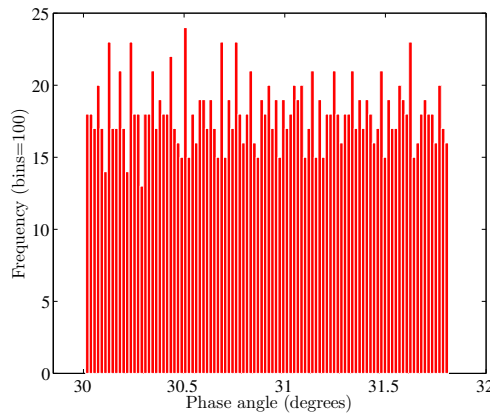


Figure III.42: Frequency distribution of the phase angle estimates considering a system frequency estimation error of -5 mHz.

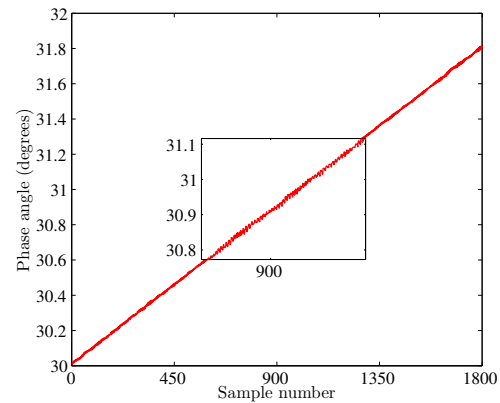


Figure III.43: Phase angle estimates with slope caused by the frequency estimation error. After 1 s, the phase angle varies 1.812° .

Due to this fact, a calibration factor (CF) may be required for compensating the phasor phase angle estimates. One can observe that during 1 second the frequency estimation error imposes a variation with linear feature, therefore, an ordinary least square regression model, given by Eq. (III.40), has been applied to infer the CF . The goal is to determine the parameter concerning the angular coefficient (A_c), given by Eq. (III.41), that represents the slope's angle. It is important to mention that the linear coefficient (A_l), Eq. (III.42), could be computed for providing an approach of the initial phase angle

$$y_i = A_c x_i + A_l \quad (\text{III.40})$$

being,

$$A_c = \frac{\sum_{i=1}^h x_i y_i - \frac{1}{h} \sum_{i=1}^h x_i \sum_{i=1}^h y_i}{\sum_{i=1}^h x_i^2 - \frac{1}{h} \left(\sum_{i=1}^h x_i \right)^2} \quad (\text{III.41})$$

and

$$A_l = \bar{Y} - A_c \bar{X} \quad (\text{III.42})$$

where x_i is the sample number and y_i represents the phase angle estimate; A_c and A_l are the angular and linear coefficients, respectively; and \bar{Y} and \bar{X} represent the average values of the desired amount of phase angle estimates and sample number, respectively.

The greater the amount of data, the more the accuracy of the model is obtained. Once the parameter A_c is defined, the calibration factor may be computed for any desired sample number. In order to accomplish this task, we recall the concept of PMU reporting rate that represents the amount of synchronized measurements by second, as has been shown in I.11.c. Choosing a reporting rate equal to 50, it is required to perform the phase angle compensation of the 50 output measurements. In this way, the CF approach can be computed at sample numbers $N_{sn}=36, 72, 108, \dots, 1800$ (each period of the nominal frequency) according to

$$CF = 1/A_c N_{sn} \quad (\text{III.43})$$

hence, the corrected phasors can be computed as given below

$$\underline{Y}_{corrected} = \frac{\underline{Y}}{CF}. \quad (\text{III.44})$$

The calibration factor must be performed when the frequency estimation error is above a predefined value yielding phase angle estimates that may affect an envisaged application. In the previous section, it has been stated that the estimation error under several scenarios is within the range of ± 0.5 mHz. In this way, Fig. III.44 depicts the phase angle variation related to this frequency error. One can note that after 1800 samples the phase angle varies 0.18° . This variation provides a maximum TVE value close to 0.314%. It is to be noted that the calibration factor must be carried in such a way that TVE value for all phasor estimates be lower than 0.1%. For frequency estimates below ± 0.2 mHz the CF could be omitted because very low TVE values are obtained.

Fig. III.45 illustrates a flowchart of the proposed frequency-adaptive modified Park's transformation-based algorithm for fast estimating fundamental positive-sequence voltage phasor, local system frequency, and Rate of Change of Frequency (ROCOF). Recapitulating the entire process, the first step consists in filtering the three-phase input signals using an analog anti-aliasing lowpass filter, as shown in III.2. Afterwards, the filtered signals are sampled at a rate of 36 samples per period of the system nominal frequency of 50-Hz.

Merely for illustration purposes, a digital decimation filter has been included to ensure a concatenation with the anti-aliasing lowpass filter for a high sampling rate condition

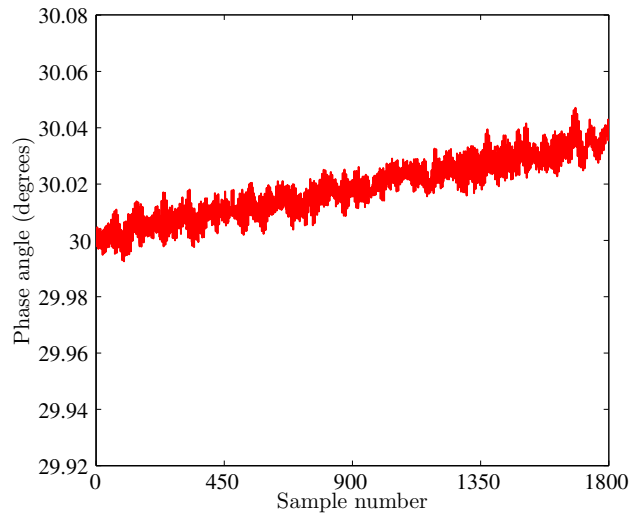


Figure III.44: Phase angle estimates of the positive-sequence voltage phasor considering a frequency estimation error of ± 0.5 mHz. After 1800 samples the phase angle estimate varies 0.18° .

of the ADC. The sampled data are filtered by FIR bandpass filters centered around the nominal frequency whose goal is to remove harmonic and interharmonic components that may degrade the dynamic of the Park's transformation. The output of the bandpass filters are used simultaneously in the decoupled stages related to the incoming system frequency tracking and the fundamental positive-sequence phasor estimation.

The technique employed to track the system frequency takes into consideration the

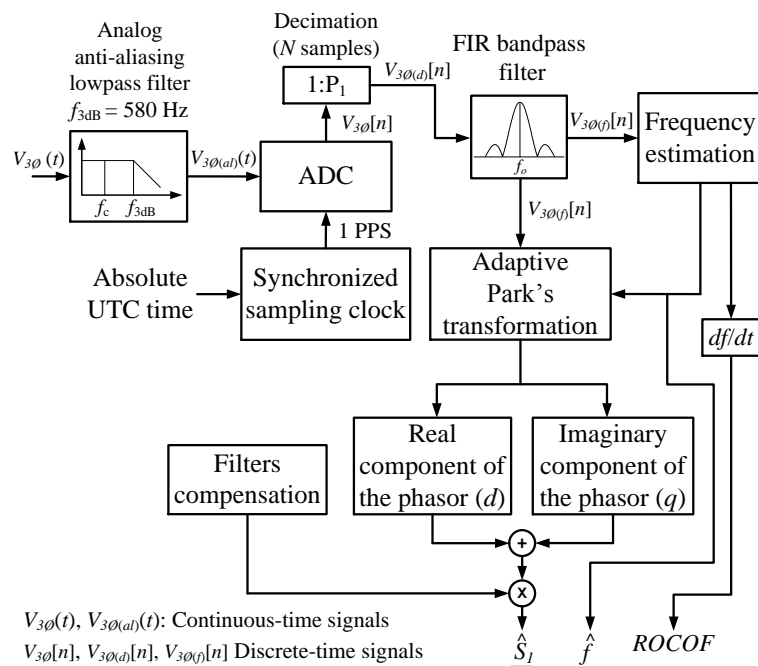


Figure III.45: Flowchart of the proposed frequency-adaptive modified Park's transformation-based algorithm.

high sensitivity of the Park's transformation concerning frequency deviation. In essence, positive-sequence voltage phasors are computed locked to the nominal frequency and for any frequency deviation the phase angle of the phasor tends to rotate. Thus taking the finite derivative approximation of the phasor phase angle displacement one can infer the frequency drift from the nominal.

After performing this step, the estimated system frequency is used to compute a new phase angle displacement of the dq -frame in order to provide valuable phasor estimates. Depending on the incoming system frequency estimation error the estimated phasors must be corrected by the calibration factor.

III.4 An enhanced synergistic frequency-adaptive algorithm (4F-algorithm)

In the current section, an enhanced frequency-adaptive algorithm based on the Fourier theory is proposed. The algorithm titled '4F-algorithm' performs four steps in a synergistic manner - frequency estimation, FIR bandpass filtering, fast linear interpolation, and half-cycle Radix-2 DIT FFT approach - for estimating fundamental and selective harmonic phasors of a single-phase input signal. Once again the system frequency tracking and the phasor estimation process are decoupled.

It is important to comment that a classical method based on adaptive bandpass filter bank is often found in the technical literature, in which the incoming system frequency is used to re-tune the center frequency of each bandpass filter. The proposed algorithm also applies a bandpass filter bank, however the procedure differs from the aforementioned technique because the filter bank is used only to 'separate' the components of the input signal.

It is known that a digital filter is a discrete-time system that transforms an input sequence into an output sequence univocally [8], in other words, the superposition principle can be applied. In this way, when an interpolation process for a full-cycle FFT is performed over an input signal corrupted by harmonics the phasor estimates will be identical to the results given by the interpolation performed over the bandpass filters output data taking into account the filter magnitude and phase compensation. Nevertheless, a half-cycle FFT approach has not a good property to estimate phasors when the input signal is corrupted by harmonics.

In order to circumvent the underlying problem the proposed algorithm applies a linear interpolation on the filter's output data using the estimated off-nominal frequency to calculate adaptive angles for each component, in which the adjusted samples are used by a fast half-cycle Radix-2 DIT FFT for computing the phasors. This algorithm aims to evaluate the individual impact of the frequency deviation over each component of the input signal and it may be applied to retain only the components of interest according to the envisaged application.

In the analyzes that will be presented later, a frequency deviation range of ± 2 Hz is used for evaluating the performance of the 4F-algorithm, whose goal is to estimate the fundamental and the selective 3th, 5th, 7th odd harmonic components because they are particularly found in power distribution systems [70].

III.4.a Characteristics of the FIR bandpass filter bank

The design of the FIR bandpass filter bank is based on the Parks-McClellan optimization technique for providing a stable performance and a linear phase response. The *Type 1 FIR filters* have been chosen because symmetric coefficients, odd length, and frequency response that has even symmetry about both digital frequencies $\Omega = 0$ and $\Omega = \pi$ can be obtained. This even symmetry allows the frequency response to take on any value within the interval of these two critical frequencies. In this way, the bandpass filters used to separate the input signal components can be properly implemented using this filter type [19].

Global parameters as passband gain of -1 dB (a_{pg}) and a stopband gain of -60 dB (a_{sg}) are used in the design of all filters. High attenuation is required in order to reduce the effects of undesired components over the analyzed component. The errors within the passband and stopband regions are specified as Δ_p and Δ_s , respectively, whose values provide the maximum allowable ripples inside these regions [19]

$$\Delta_p = 1 - 10^{0.05 \times a_p} \quad (\text{III.45})$$

$$\Delta_s = 10^{0.05 \times a_s}. \quad (\text{III.46})$$

The filter bank's size is concatenated with the analog anti-aliasing lowpass filter, thereby the maximum allowed size is 11 filters due to the cut-off frequency of 580 Hz (III.2). Due to this fact, the center frequencies could be allocated from 50 Hz to 550 Hz, respectively. It is necessary to keep in mind that the bandpass regions must involve the drift of ± 2 Hz from nominal, thus an enlargement of the bandpass region associated with the order of the harmonic component must be taken into account. Therefore, a bank's size equal to 7 has been considered (from fundamental to the 7th order component). The enlargement of the bandpass region may impact on the quantity of coefficients for each FIR filter, thus the constraint used to limit the filter's order concerns the group delay (τ).

The indices of the coefficients are limited within the range $-M/2 \leq n_c \leq +M/2$, where n_c is the number of coefficients or the length of the FIR filter and M is its order. A constant group delay ($\tau = (n_c - 1)/2$), for any frequency, can be understood as the delay of samples that will give for the FIR filter a *causal* characteristic, which will imply the existence of a linear phase shift response. The overall response delay of a FIR filter is matched with its order, because the M initial samples must be disregarded due to the transient behavior of the convolution process between the input sampled signal and the filter's coefficients.

The overall delay has been determined assuming that the order of the filters can not be greater than the number of samples in a span of 4 cycles of the nominal frequency. This assumption has been considered for ensuring a proper performance of the filtering. Besides, 4 cycles are more than enough to meet the requirements of the system frequency estimation process. Fig. III.46 illustrates the frequency response (magnitude and phase) for each FIR filter whose outcomes are used during the final calculation of the phasor measurements.

Table III.1 summarizes the individual parameters of the filters. A sampling process of 1800 Hz has been considered and one can observe that the order of all filters is matched with 4 cycles of the nominal frequency. In this way, the processes for estimating phasors using the filters output data are concatenated among them. Using 4 cycles for filtering purposes a reporting rate of 10 phasor measurements per second may be chosen.

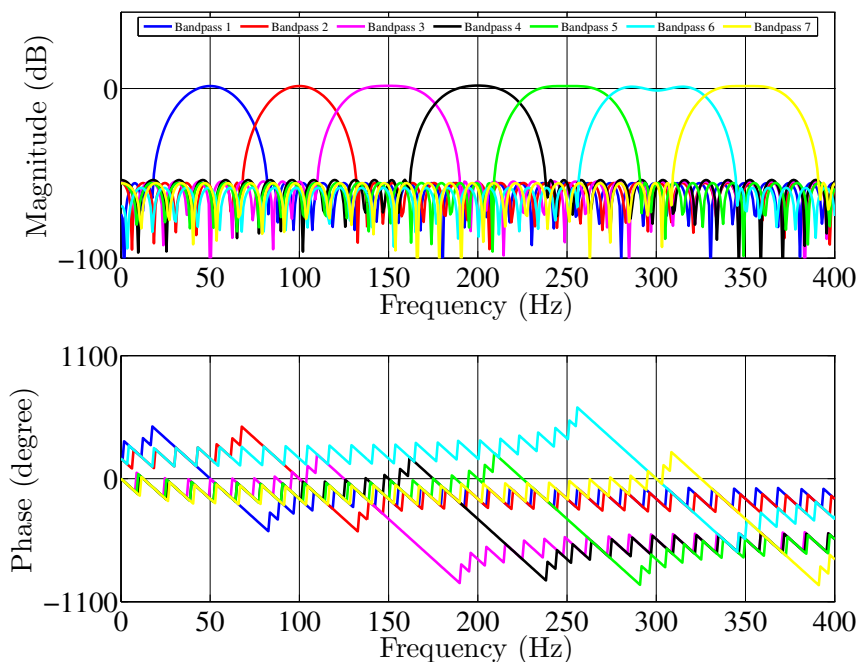


Figure III.46: Frequency response of the FIR filter bank.

Table III.1: Filter bank parameters

FIR Filter	Parameters			
	Order	Length	Group delay	Transition bands (Hz)
Bandpass 1	144	145	72	[18-40] [60-82]
Bandpass 2	144	145	72	[68-90] [110-132]
Bandpass 3	144	145	72	[110-132] [168-190]
Bandpass 4	144	145	72	[162-184] [216-238]
Bandpass 5	144	145	72	[209-231] [269-291]
Bandpass 6	144	145	72	[255-279] [323-345]
Bandpass 7	144	145	72	[309-331] [369-391]

III.4.a.i Classical linear trigonometric interpolation technique and its extended version

The interpolation technique that has been used is based on the theory proposed in [3]. A linear interpolation using trigonometric identities is applied on the output data of each filter. An extended version of the classical method have been implemented for evaluating directly the effect of frequency deviation over the harmonic components. Off-nominal sampling condition will drift the magnitude of the output samples with proportional variation to time, thus the goal is to modify the filter output sequence such that a new sequence matched to the estimated frequency can be obtained.

It is a well-know fact that the linear interpolation is a regression line that adjusts two points, given by Eq. (III.47)

$$g(x) = \frac{b-x}{b-a} \times f(a) + \frac{x-a}{b-a} \times f(b) \quad (\text{III.47})$$

where $f(a)$ and $f(b)$ are the corresponding values of a generic function $f(x)$ at $x = a$ and $x = b$, respectively. The idea depicted in Fig. III.47 is to calculate the adjusted output sequence of each bandpass filter taking projections of the samples obtained by the off-nominal sampling condition over the trigonometric circle imaginary axis. Assuming that at instant k and $k+1$ the off-nominal magnitude y_k and y_{k+1} are available the adjusted magnitude y_{x_1} can be determined using the following identities

$$\rho_1 = \Phi - \theta \quad (\text{III.48})$$

$$f(a) = y_k, \quad f(b) = y_{k+1} \quad (\text{III.49})$$

$$b-x = y_{k+1} - y_{x_1} = \sin(\rho_1) \times X_M \quad (\text{III.50})$$

$$b-a = y_{k+1} - y_k = \sin(\Phi) \times X_M \quad (\text{III.51})$$

$$x-a = y_{x_1} - y_k = \sin(\theta) \times X_M \quad (\text{III.52})$$

thus,

$$y_{x_1} = \frac{\sin(\rho_1)}{\sin(\Phi)} y_k + \frac{\sin(\theta)}{\sin(\Phi)} y_{k+1} \quad (\text{III.53})$$

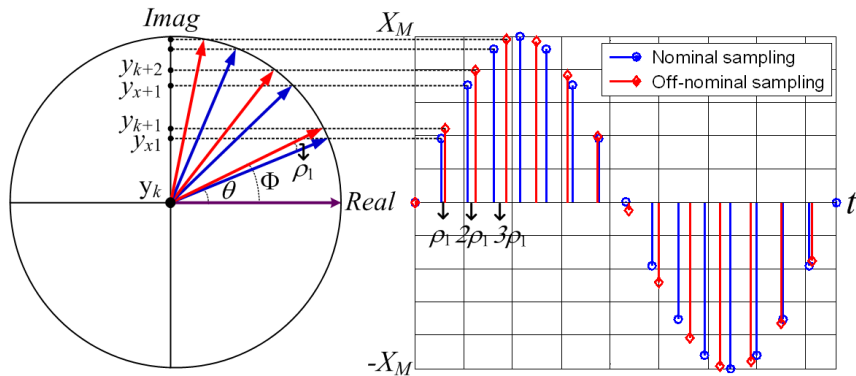


Figure III.47: Linear interpolation based on trigonometric identities.

being $\Phi = 2\pi(f_o + \Delta_f)/Nf_o$ radians the off-nominal sampling interval expressed according to the estimated frequency; $\theta = 2\pi/N$ radians is the nominal sampling interval; and ρ_1 is the adaptive angle related to the estimated frequency given by the relative position difference between the nominal and off-nominal samples. The ρ_1 angle varies linearly to time, as illustrated in Fig. III.47, therefore to compute the subsequent adjustable samples ρ_1 needs to be subtracted from the θ angle in Eq. (III.53).

The first sample of the adjusted set will be numerically equal to the first sample of the filter output. One can notice that only two output samples of the filter are required to compute the adjusted sample being suitable for online implementation. An interesting feature is that all trigonometric identities are valid independent of the phasor initial angle. An extended version of this method have been implemented to allow directly the interpolation of the bandpass filter output samples concerning the harmonic components. The

basic idea is the same, however, special care must be taken to determine the variables of interest. The angular frequency of the harmonic component will require adaptive angles proportional to the harmonic order, thus

$$\begin{aligned}\rho_2 &= 2\Phi - 2\theta; \rho_3 = 3\Phi - 3\theta; \rho_4 = 4\Phi - 4\theta; \\ \rho_5 &= 5\Phi - 5\theta; \rho_6 = 6\Phi - 6\theta; \rho_7 = 7\Phi - 7\theta\end{aligned}\tag{III.54}$$

furthermore, for performing a correct linear interpolation the nominal and off-nominal sampling intervals must also be based on the harmonic order. Therefore, the generalized equation concerning the extended version of the classical interpolation technique for computing adjusted samples for any bandpass FIR filter is given by

$$y_{x_n} = \frac{\sin(\rho_n)}{\sin(n\Phi)} y_{k_n} + \frac{\sin(n\theta - \rho_n)}{\sin(n\Phi)} y_{(k+1)_n}\tag{III.55}$$

where ρ_n is the adaptive angle according to Eq. (III.54); n is an integer number representing the harmonic order (from 1th to 7th); $n\Phi = 2\pi n(f_o + \Delta_f)/Nf_o$ radians is the off-nominal sampling interval for the respective harmonic component expressed according to the estimated frequency; $n\theta = 2n\pi/N$ radians is the nominal sampling interval of the harmonic; y_{k_n} and $y_{(k+1)_n}$ is the pair of samples taken at instant k for each harmonic whose goal is to compute the adjusted samples y_{x_n} .

III.4.b Half-cycle Radix-2 DIT FFT for computing selective phasor measurements

A half-cycle Radix-2 DIT FFT approach have been employed for computing raw phasor measurements using the adjusted output samples of the filters. It has been shown in Section I.7 that FFT splits the time domain sequence into even and odd samples in order to decompose discrete Fourier transform (DFT) into smaller DFTs whose calculation requires less computational effort. Based on the theory reported in I.7.ii, let us assume the following identity $W_N^{nk} = e^{-j2n\pi k/N}$, thus, half-cycle DFT can be rewritten as follows

$$Y(k) = \sum_{n=0}^{\frac{N}{2}-1} y[n] W_N^{nk}.\tag{III.56}$$

By splitting the $y[n]$ samples into even and odd samples, Eq. (III.56) can be rewritten as

$$Y(k) = \sum_{n=0}^{\frac{N}{4}-1} y[2n] W_N^{2nk} + W_N^k \sum_{n=0}^{\frac{N}{4}-1} y[2n+1] W_N^{2nk}.\tag{III.57}$$

Using the fact that $W_{N/2}^{nk} = W_N^{2nk}$, Eq. (III.57) can be reformulated as (III.58). Where $A(k)$ and $B(k)W_N^k$ are the DFT of even- and odd-numbered adjusted samples, respectively

$$\begin{aligned}
Y(k) &= \sum_{n=0}^{\frac{N}{4}-1} y[2n]W_{N/2}^{nk} + W_N^k \sum_{n=0}^{\frac{N}{4}-1} y[2n+1]W_{N/2}^{nk} \\
&= A(k) + B(k)W_N^k.
\end{aligned} \tag{III.58}$$

Using the periodicity and symmetry properties, the following relations can be found: $A(k + N/2) = A(k)$ and $B(k + N/2) = B(k)$; $W_N^{k+(N/2)} = -W_N^k$, respectively. Thus, Eq. (III.58) can be rewritten for phasor representation as given below

$$Y_s(k) = \frac{2\sqrt{2}}{N} \left(A(k) + B(k)e^{-j\frac{2\pi k}{N}} \right) \tag{III.59}$$

where k varies from 1 to 7.

The advantages of the half-cycle Radix-2 DIT FFT are remarkable because it uses a fractional data window, that is, only half of the number of adjusted samples of each filter could be employed for fast computing of the raw phasor measurements. In addition, the parameter $e^{-j2\pi k/N}$ could be pre-calculated and stored for use in real-time.

Using the frequency response of the FIR bank for each filter, in the form of a complex valued function of frequency, the magnitude and phase compensations can be performed for any particular frequency in the range of ± 2 Hz offset-nominal. The complex value for the frequency response is determined and converted to polar form, as

$$H_k(e^{j\Omega}) = V_k(\Omega)\angle\Psi_k(\Omega). \tag{III.60}$$

In Eq. (III.60), $V_k(\Omega)$ and $\Psi_k(\Omega)$ represent the magnitude and phase compensations, respectively, that the raw phasor estimates will experience due to the flow of the samples through each filter. Therefore, the corrected phasor estimates will be computed by

$$Y_s(k)_{corrected} = \frac{Y_s(k)}{H_k(e^{j\Omega})}. \tag{III.61}$$

Fig. III.48 shows the flowchart of the proposed frequency-adaptive 4F-algorithm. Recapitulating the steps concerning the algorithm, the first step consists in filtering the three-phase input signal using the analog anti-aliasing lowpass filter shown in Section III.2. Then, the signals are sampled at a sampling rate of 1800 Hz. The three-phase samples are used in the system frequency estimation process and ROCOF computation based on the Park's transformation, as has been shown in III.3.d.

For computing the phasors, the sampled data concerning a single phase pass through the bandpass filter bank for separating the 1th, 3th, 5th, and 7th order harmonic components. We recall that these components have been chosen because they are particularly found in power distribution system.

Once the harmonics are separated a fast linear trigonometric interpolation is applied on the output data of each filter in order to adjust the samples regarding the estimated system frequency. The interpolated data of each filter is treated by a half-cycle Radix-2 DIT FFT for computing raw phasors. Afterward, the magnitude and phase angle compensations related to the entire filtering process are performed to provide corrected phasors. In short,

the 4F-algorithm takes advantage of the superposition principle to separate and analyze individually each component of a single-phase input signal under frequency deviation. In subsection III.6.a, the performance evaluation of the 4F-algorithm has been presented.

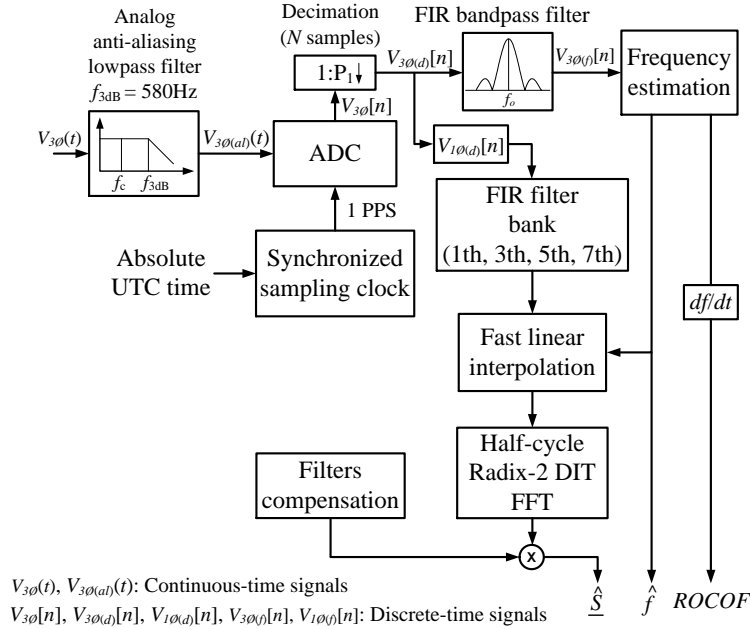


Figure III.48: Flowchart of the frequency-adaptive 4F-algorithm.

III.5 Frequency-adaptive algorithm based on Weighted Least Squares (WLS) approach (AWLS-algorithm)

Electric signals are not free from noise and spurious out-of-band frequency components may be considered to be noise. In addition, electromagnetic interference may also induce electrical noise picked up in the wiring of the instrumentation channel of a measured signal [3]. Noise tends to distort the sampled data in the digital domain, however, it is necessary to keep in mind that we can indeed get some information from less reliable samples.

A powerful mathematical approach often used to provide the best estimate of an unknown variable when errors are present is the WLS approach. As will be seen further in III.5.a, this approach has important statistical representations being frequently applied to provide optimal solutions for overdetermined systems of linear equations. Instead of solving the linear system, the WLS seeks to minimize an *objective function* (also called *cost function* or *return function*) [86].

Taking into account classical methods for estimating phasors (DFT or FFT), one may observe that several samples inside a data window are used to compute two parameters: the real and imaginary parts of a phasor. In this way, it is clear that this problem can be modeled in the least square sense. Due to this fact, a practical frequency-adaptive algorithm titled ‘AWLS-algorithm’ is proposed in the current section. Its mathematical formulation is based on the WLS approach for accurate identification and estimation of

phasor measurements (DC offset, fundamental and harmonics) under frequency deviation in active power distribution grids.

For accomplishing this task, an intuitive mathematical formulation is carried out, in which the real and imaginary parts of all components of a single-phase voltage or current waveform are linearly combined with the sampled data taking into account the frequency deviation within the range of ± 5 Hz. In essence, the algorithm uses the system frequency estimate, obtained from the technique shown in III.3.d, for computing a new sampling angle to be used during the computation of the real and imaginary parts of all phasors.

III.5.a Weighted Least Squares estimation overview

WLS approach is a class of state estimators and its mathematical formulation claims for an extensive and rigorous statistical background, however, in this section, it will be presented only the key points which are of direct interest for phasor estimation. In [86] an excellent and complete description of the optimal state estimation theory can be found.

The development of the least square approach has been credited to the renowned mathematician Carl Friedrich Gauss (although there is opposition from Adrien-Marie Legendre's advocates). This mathematical approach may be understood according to the quote said by Gauss [86]:

"The most probable value of the unknown quantities will be that in which the sum of the squares of the differences between the actually observed and the computed values multiplied by numbers that measure the degree of precision is a minimum."

For a comprehensive understanding of the aforementioned quote, let us assume that each element of a measured sample vector x is a linear combination of the real (s_r) and imaginary (s_i) parts of a phasor with the addition of some noise, hence

$$\begin{aligned} x_1 &= H_{11}s_r + H_{12}s_i + \varepsilon_1 \\ x_2 &= H_{21}s_r + H_{22}s_i + \varepsilon_2 \\ &\vdots \\ x_k &= H_{k1}s_r + H_{k2}s_i + \varepsilon_k \end{aligned} \tag{III.62}$$

in matrix notation this set of equations can be rewritten as follows

$$x = Hs + \varepsilon \tag{III.63}$$

being H the coefficient matrix. In this way, taking the difference between the noisy samples vector x and the vector $H\hat{s}$ (being \hat{s} the vector of estimates) provides

$$\varepsilon_x = x - H\hat{s} \tag{III.64}$$

ε_x is called the *residue*. Thereby, taking into account the Gauss's quote the best estimate of the vector s is given by the vector \hat{s} that minimizes the sum of squares of the residues. In short, the vector \hat{s} seeks to minimize the following objective function J

$$J = \varepsilon_{x_1}^2 + \varepsilon_{x_2}^2 + \dots + \varepsilon_{x_k}^2. \quad (\text{III.65})$$

Looking closely at Eq. (III.65), one can observe that the objective function J can be obtained by dot product between the vectors ε_x^T and ε_x that satisfy the definition of the L_2 -norm, hence

$$J = \varepsilon_x^T \varepsilon_x. \quad (\text{III.66})$$

Now, let us assume that the noise for each sample is a zero-mean Gaussian process and independent, thus, the measurement covariance matrix W is given by

$$[W] = \begin{bmatrix} \sigma_1^2 & \dots & 0 \\ \vdots & \dots & \vdots \\ 0 & \dots & \sigma_k^2 \end{bmatrix} \quad (\text{III.67})$$

hence, each element of the objective function J must be weighted by its respective covariance, therefore, Eq. (III.65) can be rewritten as follows

$$J_1 = \frac{\varepsilon_{x_1}^2}{\sigma_1^2} + \frac{\varepsilon_{x_2}^2}{\sigma_2^2} + \dots + \frac{\varepsilon_{x_k}^2}{\sigma_k^2} = \varepsilon_x^T W^{-1} \varepsilon_x. \quad (\text{III.68})$$

It is clear that the objective function to be minimized concerns the weighted sum of squares. In other words, independent variance may be used to give for more confidence measurements a greater contribution on the calculation of the estimates. Likewise, a small contribution for noise measurements may also be considered. Based on [86], for evaluating the vector of estimates \hat{s} , Eq. (III.64) must be replaced into Eq. (III.68), hence

$$\begin{aligned} J_1 &= (x - H\hat{s})^T W^{-1} (x - H\hat{s}) \\ J_1 &= x^T W^{-1} x - \hat{s}^T H^T W^{-1} x - x^T W^{-1} H \hat{s} + \hat{s}^T H^T W^{-1} H \hat{s}. \end{aligned} \quad (\text{III.69})$$

The best estimate of \hat{s} may be computed taking the partial derivative of J with respect to \hat{s} and set it equal to zero as shown below

$$\frac{\partial J_1}{\partial \hat{s}} = -x^T W^{-1} H + \hat{s}^T H^T W^{-1} H = 0 \quad (\text{III.70})$$

in this way, the following identity is obtained

$$H^T W^{-1} H \hat{s} = H^T W^{-1} x \quad (\text{III.71})$$

hence,

$$\hat{s} = (H^T W^{-1} H)^{-1} H^T W^{-1} x. \quad (\text{III.72})$$

It is possible to note that the WLS approach can not be performed if the covariance matrix is singular (a square matrix that does not have a matrix inverse). This happens when at least one of the diagonal elements of W is close to zero. In other words, each of the samples x_i must be corrupted by noise so that the method can work.

III.5.b AWLS-algorithm for computing phasor measurements

The proposed algorithm provides a practical, intuitive and accurate manner to compute DC-offset, fundamental and harmonics phasors under frequency deviation of a single-phase voltage or current input signal. Based on the theory presented in [3], the phasor estimation process is modeled in the weighted least square sense and it has the ability to modify its parameters according to the frequency estimate given by the technique presented in III.3.d. Like the other two proposed algorithms in this chapter, once again the decoupling between system frequency tracking and phasor estimation process is performed.

From a practical point of view concerning phasor estimation, it is possible to ensure a linear combination between the measurement vector (composed by the samples), and the state vector (formed by DC-offset, and the real and imaginary parts of the phasors), through a coefficient matrix H recognized for having the sampling angle as its main parameter. In general, H matrix has constant elements, therefore, for any frequency deviation the linear model given by III.63 will not be properly correlated and the state vector will be affected by errors.

In order to circumvent this problematic, the proposed algorithm computes a new sampling angle θ_{new} , as given by Eq. (III.32), locked to the estimated system frequency and this new angle is used for updating the coefficient matrix H to maintain the correct correlation between the measurement- and the state vector. In this way, the matrix H does not have constant elements because they are updated according to the incoming system frequency. The mathematical formulation of the AWLS-algorithm is shown as follows: let a single-phase current signal (*in pu*) under frequency deviation be given by

$$i(t) = I_{DC} + I_{m_1} \cos(2\pi f_m t + \phi_{i_1}) + \sum_{v=2}^D I_{m_v} \cos(2\pi v f_m t + \phi_{i_v}) \quad (\text{III.73})$$

where I_{DC} is the DC-offset; I_{m_1} and I_{m_v} being the peak magnitude of fundamental and harmonic components, respectively; ϕ_{i_1} and ϕ_{i_v} being the phase angle of the fundamental and the harmonics during the observation interval, respectively; D is the highest harmonic present in the input signal; and f_m is the off-nominal frequency.

Evaluating Eq. (III.73) at each fixed sampling time nT_s matched to the nominal system frequency and considering the influence of Gaussian white noise, provides

$$I[n] = I_{DC} + I_{m_1} \cos(2\pi n f_m T_s + \phi_{i_1}) + \sum_{v=2}^D I_{m_v} \cos(2\pi n v f_m T_s + \phi_{i_v}) + \varepsilon_n \quad (\text{III.74})$$

that is,

$$I[n] = I_{DC} + I_{m_1} \cos(n\theta_{new} + \phi_{i_1}) + \sum_{v=2}^D I_{m_v} \cos(nv\theta_{new} + \phi_{i_v}) + \varepsilon_n. \quad (\text{III.75})$$

Eq. (III.75) may be rewritten as follows

$$I[n] = I_{DC} + \sqrt{2} \text{Re} \left(\frac{I_{m_1}}{\sqrt{2}} e^{j\phi_{i_1}} e^{jn\theta_{new}} \right) + \sum_{v=2}^D \sqrt{2} \text{Re} \left(\frac{I_{m_v}}{\sqrt{2}} e^{j\phi_{i_v}} e^{jn v \theta_{new}} \right) + \varepsilon_n \quad (\text{III.76})$$

in a more compact form we have

$$I[n] = I_{DC} + \sqrt{2}Re\left(\underline{I}_1 e^{jn\theta_{new}}\right) + \sum_{v=2}^D \sqrt{2}Re\left(\underline{I}_v e^{jnv\theta_{new}}\right) + \varepsilon_n \quad (\text{III.77})$$

being \underline{I}_1 and \underline{I}_v the correct value of the fundamental and the harmonic phasors at the off-nominal frequency and Re represents a real value function.

Recalling that any real value may be expressed as the average of a phasor and its complex conjugate according to

$$y(t) = \frac{\underline{I}e^{j\omega t} + \underline{I}^*e^{-j\omega t}}{2} \quad (\text{III.78})$$

Eq. (III.77) can be rewritten as follows

$$\begin{aligned} I[n] = & I_{DC} + \frac{\sqrt{2}}{2}(\underline{I}_1 e^{jn\phi_{new}} + \underline{I}_1^* e^{-jn\phi_{new}}) \\ & + \frac{\sqrt{2}}{2} \sum_{v=2}^D (\underline{I}_v e^{jnv\phi_{new}} + \underline{I}_v^* e^{-jnv\phi_{new}}) + \varepsilon_n. \end{aligned} \quad (\text{III.79})$$

Performing the sum and subtraction properties of complex conjugate yields

$$\begin{aligned} I[n] = & I_{DC} + \sqrt{2}|I_1|(\cos(n\phi_{new}) - j\sin(n\phi_{new})) \\ & + \sqrt{2} \sum_{v=2}^D |I_v|(\cos(nv\phi_{new}) - j\sin(nv\phi_{new})) + \varepsilon_n. \end{aligned} \quad (\text{III.80})$$

Clearly from Eq. (III.80), it is possible to note that the phasor estimation problem can be reformulated to find the unknown state vector using the off-nominal samples through a set of h overdetermined linear equations according to the linear system (III.81). A simple mathematical modification is performed for a correct correlation of the DC-offset component. In practice, the length of the measurement vector is equal to N samples within the data window, however the formulation can also be applied for fractional-cycle data window provided that the number of samples be greater than the amount of variables to be determined.

The maximum amount of state variables is equal to $2D+1$, in which D represents the maximum number of harmonic components in the input signal, in other words, this parameter is related to the 3-dB cut-off frequency of the analog anti-aliasing lowpass filter (580 Hz). Therefore, the maximum number of harmonics that may be present in the input signal is 11 yielding an amount of state variables equal to 23 (DC-offset and real and imaginary parts of all phasor components). Eq. (III.81) can be rewritten in a more compact form according to Eq. (III.82)

$$x = H(\theta_{new})\hat{s} + \varepsilon \quad (\text{III.82})$$

being x the measurement vector of the samples corrupted by Gaussian white noise ε ; and $H(\theta_{new})$ represents the coefficient matrix whose elements may change related to the incoming system frequency.

$$\begin{aligned}
 \begin{bmatrix} x_0 \\ x_1 \\ x_2 \\ \vdots \\ x_h \end{bmatrix} &= \sqrt{2} \begin{bmatrix} \frac{1}{\sqrt{2}} \cos(0) & \cdots & \cos(D0) & -\sin(0) & \cdots & -\sin(D0) \\ \frac{1}{\sqrt{2}} \cos(\theta_{new}) & \cdots & \cos(D\theta_{new}) & -\sin(\theta_{new}) & \cdots & -\sin(D\theta_{new}) \\ \frac{1}{\sqrt{2}} \cos(2\theta_{new}) & \cdots & \cos(2D\theta_{new}) & -\sin(2\theta_{new}) & \cdots & -\sin(2D\theta_{new}) \\ \vdots & \vdots & \vdots & \vdots & \vdots & \vdots \\ \frac{1}{\sqrt{2}} \cos(h\theta_{new}) & \cdots & \cos(hD\theta_{new}) & -\sin(h\theta_{new}) & \cdots & -\sin(hD\theta_{new}) \end{bmatrix} \\
 &\times \begin{bmatrix} I_{DC} \\ |I_1| \cos(\phi_1) \\ |I_2| \cos(\phi_2) \\ \vdots \\ |I_D| \cos(\phi_D) \\ |I_1| \sin(\phi_1) \\ |I_2| \sin(\phi_2) \\ \vdots \\ |I_D| \sin(\phi_D) \end{bmatrix} + \begin{bmatrix} \varepsilon_0 \\ \varepsilon_1 \\ \varepsilon_2 \\ \vdots \\ \varepsilon_h \end{bmatrix} \quad (III.81)
 \end{aligned}$$

In the weighted least squares sense the solution of Eq. (III.82) is given by

$$\hat{s} = [H(\theta_{new})^T W^{-1} H(\theta_{new})]^{-1} H(\theta_{new})^T W^{-1} x. \quad (III.83)$$

The elements of the covariance matrix W are intrinsically associated with the accuracy of the synchronized device. Several elements of the coefficient matrix H are numerically identical, therefore a formation law concerning constant elements and symmetric sub-matrix of H have been performed to significantly reduce the calculation effort. For instance, assuming that the length of the measurement vector x is equal to $h=36$, one can note that the elements of the column vector $H_c(i, 1)_{1 \leq i \leq 36}$ is a constant value equal to $\frac{1}{\sqrt{2}}$, therefore, it is only required to storage this value.

Similarly, the elements of the row vectors $H_{r1}(1, j)_{2 \leq i \leq 12}$ and $H_{r2}(1, j)_{13 \leq i \leq 23}$ are numerically equal to 1 and 0, respectively. In addition, one can notice that the sub-matrices $H_1 = (a_{i,j})_{2 \leq i \leq 12, 2 \leq j \leq 12}$ and $H_2 = (a_{i,j})_{2 \leq i \leq 12, 13 \leq j \leq 23}$ are symmetric. Taking into account these relationships a reduction around 20.28% over the full calculation of the H matrix may be obtained. It is important to mention that for practical applications, a recursive WLS estimation must be performed [86]. Fig. III.49 depicts the diagram of the AWLS-algorithm.

The steps concerning the AWLS-algorithm are presented as follows: after filtering the three-phase input signal using the analog anti-aliasing lowpass filter shown in Section III.2, the signals are sampled at a sampling rate of 1800 Hz (36 samples/cycle of the 50-Hz nominal frequency). The sampled data are used for estimating the system frequency and ROCOF computation based on the technique shown in III.3.d. The estimated frequency is used to compute a new sampling angle (θ_{new}) matched to the off-nominal frequency for updating the coefficient matrix H of the AWLS-algorithm.

The maximum number of estimated phasor is matched with the highest frequency component imposed by the analog anti-aliasing lowpass filter. Once estimated all components of the input signal the magnitude and phase compensation of the filter is performed in order to provide corrected phasor estimates. In subsection III.6.a, the performance evaluation of the AWLS is presented.

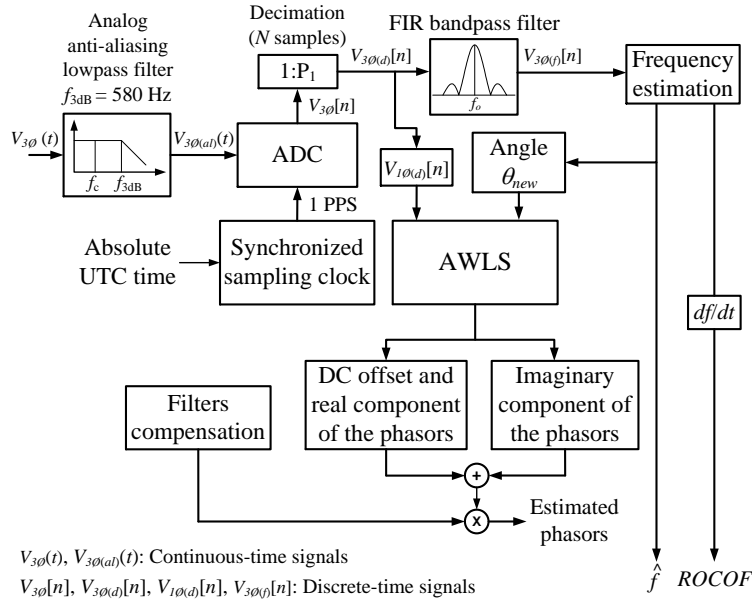


Figure III.49: Practical frequency-adaptive Weighted Least Squares-based algorithm for estimating DC-offset, fundamental and harmonic phasors of a single-phase input signal.

III.6 IEEE Std. C37.118.1-2011 requirements and compliance verification for monitoring applications

In order to be compliant with the IEEE Std. C37.118.1-2011 [6], a PMU or a PMU-enabled IED must provide synchronized phasors, frequency, and ROCOF measurements that fulfill all requirements stated by this standard. The evaluation of the M-class synchronized devices (for monitoring purposes) is based on steady-state and dynamic test conditions. Steady-state compliance must be confirmed taking into account the comparison between the synchronized phasor, frequency, and ROCOF estimates obtained under steady-state conditions to the corresponding theoretical values, as it has been shown in I.11.d.

For steady-state tests, the magnitude and the frequency (nominal or off-nominal) of the input signal remain constant during the test. In short, the steady-state tests aim to confirm that the accuracy of the synchronized devices is within the specified limits regarding steady-state operating conditions. Dynamic compliance also takes into consideration the comparison between the estimated and the theoretical values, however, the input signal must be swept over time. Tables III.2 and III.3 depict the steady-state synchrophasor measurement requirements and the steady-state frequency and ROCOF measurement requirements, respectively.

The parameter F_s represents the PMU reporting rate (see I.11.c). One can notice that the standard claims for a limit of 1% TVE, however, this value is not conceivable for electric distribution grids, as it has been show in II.2. Due to this fact, a reference TVE of 0.1% has been considered for evaluating the performance of the proposed algorithms.

Magnitude and phase angle step tests represent an abrupt transition between two steady states. The step tests aim to simulate various scenarios concerning switching events on the network. The goal of these tests is to evaluate the response time, delay time, and overshoot

Table III.2: Steady-state synchrophasor measurement requirements [6]

Influence quantity	Reference condition	Minimum range of influence quantity over which PMU shall be within given TVE limit	
		M-class	
		Range	Max TVE (%)
Signal frequency range (test applied nominal + deviation: $f_o \pm \Delta f$)	$F_{nominal}$ (f_o)	± 2.0 Hz for $F_s < 10$ $\pm F_s/5$ for $10 \leq F_s < 25$ ± 5.0 Hz for $F_s \geq 25$	1
Signal magnitude - voltage	100% rated	10% to 120% rated	1
Signal magnitude - current	100% rated	10% to 200% rated	1
Phase angle with $ f_{in} - f_o < 0.25$ Hz	Constant or slowly varying angle	$\pm \pi$ radians	1
Harmonic distortion (single harmonic)	<0.2% (THD)	10%, each harmonic up to 50th	1
Out-of-band interference	<0.2% of input signal magnitude	10% of input signal magnitude for $F_s \geq 10$. No requirements for $F_s < 10$	1.3

Table III.3: Steady-state frequency and ROCOF measurement requirements [6]

Influence quantity	Reference condition	Error requirements for compliance	
		M-class	
Signal frequency	Frequency = f_o Phase angle constant	Range: $f_o \pm 2.0$ Hz for $F_s \leq 10$ $\pm F_s/5$ for $10 \leq F_s < 25$ ± 5.0 Hz for $F_s \geq 25$	
		Max FE	Max RFE
		0.005 Hz	0.01 Hz/s
Harmonic distortion	<0.2% THD	10% each harmonic up to 50th	
		Max FE	Max RFE
	$F_s > 20$	0.025 Hz	6 Hz/s
	$F_s \leq 20$	0.005 Hz	2 Hz/s
Out-of-band interference	<0.2% of input signal magnitude	Interfering signal 10% signal magnitude	
		Max FE	Max RFE
		0.01 Hz	0.1 Hz/s

of the measurements provided by synchronized devices. According to [6], measurement response time may be understood as the difference between the time that the measurement leaves a specified accuracy limit and the time in which the measurement stays within that limit after applying a negative or positive step change to the PMU input. *Measurement delay time is defined as the time interval between the instant that a step change is applied to the input of a PMU and the measurement time that the stepped parameters achieves a value that is halfway between the initial and the final steady-state values* [6]. Overshoot is the output exceeding before to achieve the final steady-state value.

The steps can be evaluated assuming the mathematical model given by

$$Y_a = Y_m(1 + k_x f_1(t)) \times \cos(\omega_o t + k_a f_1(t)) \quad (\text{III.84})$$

$$Y_b = Y_m(1 + k_x f_1(t)) \times \cos(\omega_o t - 120^\circ + k_a f_1(t)) \quad (\text{III.85})$$

$$Y_c = Y_m(1 + k_x f_1(t)) \times \cos(\omega_o t + 120^\circ + k_a f_1(t)) \quad (\text{III.86})$$

hence, the positive-sequence signal that represents the above three-phase input signals can be expressed by

$$Y_1 = Y_m [1 + k_x f_1(t)] \times \cos(\omega_o t + k_a f_1(t)) \quad (\text{III.87})$$

where Y_m is the amplitude of the input signal; ω_o represents the nominal power system frequency; $f_1(t)$ is a unit step function; k_x and k_a are the magnitude and phase step size, respectively. It is important to mention that frequency step tests are not reported in [6], however, these tests are will also be considered for performance evaluation purposes.

Table III.4 shows the phasor performance requirements for input magnitude and phase step changes. One can observe that the response time to obtain the parameters of interest (TVE, FE, and RFE) depends of the user selectable reporting rate. Concerning dynamic tests, measurement performance during system frequency change is accomplished by linear frequency ramp of the system frequency. Once again, taking into account balanced three-phase input signals the following signal model may be used

$$Y_a = Y_m \cos(\omega_o t + \pi R_f t^2) \quad (\text{III.88})$$

$$Y_b = Y_m \cos(\omega_o t - 120^\circ + \pi R_f t^2) \quad (\text{III.89})$$

$$Y_c = Y_m \cos(\omega_o t + 120^\circ + \pi R_f t^2) \quad (\text{III.90})$$

where $R_f = \frac{df}{dt}$ is the frequency ramp rate in Hz/s. For simulation purposes, these parameter remains constant during the analysis.

In this way, the positive-sequence signal corresponding to the above three-phase input signals is given by

$$Y_1 = Y_m \cos(\omega_o t + \pi R_f t^2). \quad (\text{III.91})$$

At reporting time tags $t = nT$, being T the phasor reporting interval (see I.11.c), the synchronized device produces a positive-sequence measurement as given by Eq. (III.92)

$$Y(nT) = \frac{Y_m}{\sqrt{2}} / \pi R_f (nT)^2. \quad (\text{III.92})$$

In a similar manner, the true values of frequency, frequency deviation, and ROCOF can be obtained by Eqs.(III.93)-(III.95), respectively

$$f(nT) = \omega_o/2\pi + (R_f)(nT) \tag{III.93}$$

$$\Delta f(nT) = (R_f)(nT) \tag{III.94}$$

$$\frac{d[f(nT)]}{dt} = R_f. \tag{III.95}$$

The measurement error limits under frequency ramp tests are illustrated in Table III.6. In subsection III.6.a, the performance evaluation of the proposed algorithms is carried out taking into account these compliance tests. Steady-state and dynamic tests presented in the current section will be used for evaluating the frequency-adaptive modified Park’s transformation-based algorithm. For the 4-F and AWLS algorithms the evaluation will be performed concerning steady-state scenarios. All tests aim to demonstrate the capabilities of the proposed algorithms in dealing efficiently with spurious and distorted signals particularly found in power distribution systems even under frequency deviation.

Table III.4: Phasor performance requirements for input step change [6]

Step change specification	Reference condition	Maximum response time, delay time, and overshoot		
		M-Class		
		Response time (s)	Delay time (s)	Max overshoot/undershoot
Magnitude= $\pm 10\%$ $k_x = \pm 0.1$ $k_a = 0$	All test conditions nominal at start or end of step	see Table III.5	$1/(4 \times F_s)$	10% of step magnitude
Angle= $\pm 10^\circ$ $k_x = 0$ $k_a = \pm \pi/18$	All test conditions nominal at start or end of step	see Table III.5	$1/(4 \times F_s)$	10% of step magnitude

Table III.5: Response time for M-class phasor, frequency and ROCOF for input step change [6]

Maximum response time in step change test for M-class, in seconds								
Reporting rate (F_s)	10	12	15	20	25	30	50	60
Phasor (TVE)	0.595	0.493	0.394	0.282	0.231	0.182	0.199	0.079
Frequency (FE)	0.869	0.737	0.629	0.478	0.328	0.305	0.130	0.120
ROCOF (RFE)	1.038	0.863	0.691	0.520	0.369	0.314	0.134	0.129

Table III.6: Frequency and ROCOF performance requirements under frequency ramp tests [6]

Signal specification	Reference condition	Error requirements for compliance	
Linear frequency ramp	100% rated signal magnitude and 0 radian base angle	M-class	
		Max FE	Max RFE
		0.005 Hz	0.1 Hz/s

III.6.a Performance of the algorithms under static and/or dynamic conditions

In this section, the simulations and the performance evaluation of the proposed algorithms are presented. They have been developed in MATLAB 2014a environment. An extensive range of signal models have been used to cover static and dynamic conditions particularly found in active power distribution systems.

Test cases are performed in three parts: the starting point is the evaluation of the frequency-adaptive modified Park’s transformation-based algorithm using off-nominal three-phase input signals within a range of ± 5 Hz. The input signals are corrupted by DC-offset, high harmonic content, out-of-band disturbances, and Gaussian noise. The analyzed scenarios include the positive-sequence voltage phasor estimation under magnitude and phase angle steps using balanced and unbalanced input signals.

Furthermore, tests related to frequency transient conditions are performed for evaluating the ability of the proposed algorithm to track the local system frequency with a fast time response in the presence of sudden changes in power system frequency (frequency step). In addition, tests related to linear frequency ramp and ROCOF computation have also been performed.

In the second base case, the 4F-algorithm is evaluated using off-nominal single-phase signals, over a range of ± 2 Hz around the nominal. Once again the input signals are corrupted by DC offset, high harmonic content, out-of-band disturbances, and Gaussian noise. The goal of the algorithm is to estimate with accuracy the fundamental, 3th, 5th, and 7th harmonic phasors because these odd components can often be found in active distribution environment.

For the third base case, the AWLS-algorithm is evaluated in order to provide a complete estimation of all components of a single-phase input signal upto 11th harmonic order component (DC-offset, fundamental and harmonic phasors). A frequency range within ± 5 Hz around the fundamental has been considered. In the latest two base cases, a static off-nominal frequency has been considered.

For all test cases, it has been considered a sampling rate corresponding to $N = 36$ samples/cycle of the 50-Hz nominal frequency. The input signals are corrupted by harmonics upto 11th order component (not above the 3-dB cut-off frequency) and interharmonics are also deemed. For three-phase signals, independent Gaussian white noise is applied in each phase aiming to provide a stochastic feature for each sampled signal. The signal-to-noise ratio (SNR) varies within the range from 40 dB to 85 dB.

III.6.a.i Test cases concerning the modified Park's transformation-based algorithm

Let the sampled balanced three-phase input signals be given by

$$e_a(n) = 15 \cos(n\theta + 30^\circ) + \varepsilon_1(n) + \varepsilon_2(n) \tag{III.96}$$

$$e_b(n) = 15 \cos(n\theta - 120^\circ + 30^\circ) + \varepsilon_1(n) + \varepsilon_3(n) \tag{III.97}$$

$$e_c(n) = 15 \cos(n\theta + 120^\circ + 30^\circ) + \varepsilon_1(n) + \varepsilon_4(n) \tag{III.98}$$

where $\theta = \frac{2\pi}{N}$ is the sampling angle locked to the nominal frequency; ε_1 represents the disturbances of harmonics and DC-offset; and $\varepsilon_2, \varepsilon_3, \varepsilon_4$ represent disturbances due to Gaussian white noise for each phase.

Table III.7 shows the magnitude and phase angle of the non-fundamental components present in the input signal. Note that the magnitudes of them are given by the percentage of the fundamental component magnitude. Recalling that the proposed algorithm uses a bandpass filter to remove the undesirable ε_1 terms, it is possible to note that it will still have a sensitivity related to the Gaussian noise, however, the moving average filters tend to reduce the effect of noise.

For the tests concerning magnitude and phase steps, a rising step sustained during a short time interval followed by a falling step are employed to evaluate the dynamic response of the algorithm.

Table III.7: Components of the input signal

Harmonic component	Amplitude (nominal reference)	Phase angle (degrees)
0	1.5%	0
2	3%	22.5°
3	6%	15°
4	1.5%	60°
5	8%	20°
6	1%	90°
7	7%	-12°
8	1%	90°
9	5%	20°
10	1%	10.58°
11	2.5%	-10°

Fig. III.50 depicts the results for a magnitude step test equivalent to +10% of the nominal magnitude taking into account a static off-nominal frequency at 51.5 Hz. The steps occur at sample numbers 300 and 551. It can be observed that the estimates provided by the algorithm track the step very fast with a smooth variation due to the filtering process, in addition, a very small overshoot is produced. A maximum time response of 0.04 s has been obtained due to the latency of the filtering process. This measurement response time meets and exceeds the requirements shown in Table III.5.

Neglecting the magnitude step, the positive-sequence voltage phasor estimate (making the compensation of all filters) in rectangular form is close to $9.185 + j5.303 (d + jq)$. In

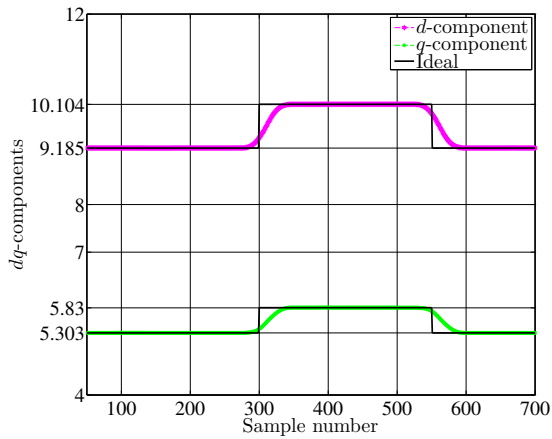


Figure III.50: Response of the algorithm under balanced magnitude step.

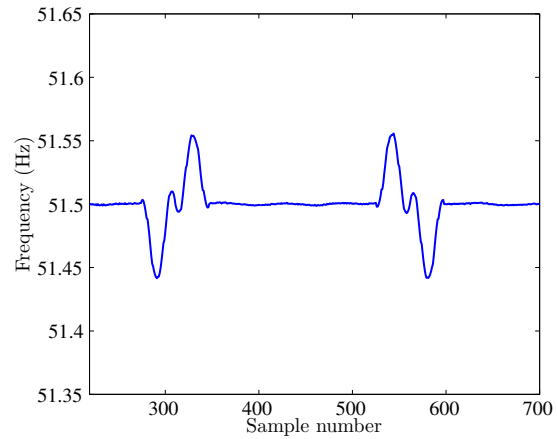


Figure III.51: Frequency estimates under balanced magnitude step

this way, a maximum TVE value of 0.035% has been obtained before the step and a TVE value around 0.056% has been achieved after the step. During the steady-state of the step the phasor estimates change to $10.104 + j5.833$ yielding a maximum TVE value close to 0.0452%. Fig. III.51 illustrates the frequency estimates under magnitude step. Note the transient response of the frequency estimates during the step. Considering steady-state conditions the frequency estimation error is around 0.143 mHz. The test is evaluated using a SNR=63.52 dB.

Now, let us consider an unbalanced magnitude step. Fig. III.52 depicts the results for a test case where the magnitude of e_a -signal is suddenly reduced by -3%, and the magnitudes of e_b - and e_c -signal are suddenly increased by +5% and +6.5%, respectively. A SNR=60 dB and a static off-nominal frequency at 49.85 Hz have been considered. The steps occur at sample numbers 364 and 591. Fig. III.53 shows the dynamic response of the algorithm for unbalanced signals operating at 49.85 Hz. Before and after the step, the true value of the positive-sequence voltage phasor remains close to $9.185 + j5.303$ ($d + jq$).

A maximum TVE value of 0.100% has been obtained before the step and a maximum

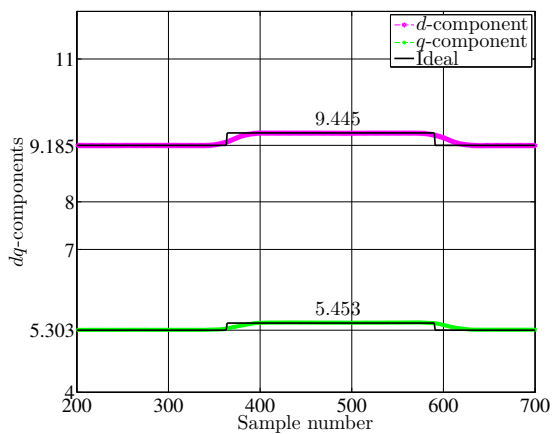


Figure III.52: Response of the algorithm under unbalanced magnitude step.

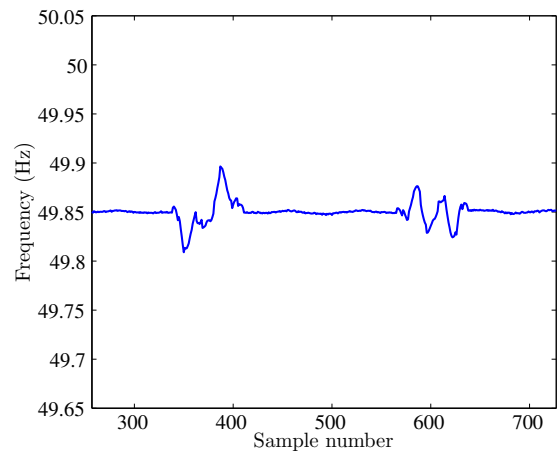


Figure III.53: Frequency estimates under unbalanced magnitude step

TVE value around 0.129% has been achieved after the step. In the steady-state of the step the phasor estimates change to $9.445+j5.453$ and a maximum TVE value close to 0.129% has been reported. A frequency estimation error of 0.2 mHz has been obtained. One can notice that the reported results are far lower than the reference values shown in Tables III.2 and III.3. Fig III.53 illustrates the transient condition of the frequency estimates during the step.

At this point, let us consider step tests concerning the phasor phase angle. Table III.4 depicts a step within $\pm 10^\circ$ for evaluating purposes. The test cases are divided into two parts: the first concerns balanced change of the phase angle, in other words, the same sudden variation of the phase angle is performed for each phase, and the second test regards unbalanced change, that is, different phase angle step for each phase is carried out.

Fig III.54 illustrates the performance of the proposed algorithm when a balanced phase angle step equal to -9° is performed over the three-phase input signals. The step takes place at sample numbers 300 and 551. The system frequency is equal to 50.15 Hz and a SNR=55.56 dB have been deemed. Once again the true positive-sequence voltage phasor before and after the step is close to $9.185+j5.303$.

During the steady-state of the step the value changes to $9.902+j3.801$. Before the step the maximum TVE value is close to 0.1254% and after the step the obtained value is around 0.1405%. When the step is in steady-state a TVE value around 0.1232% has been obtained. Fig. III.55 depicts the frequency estimates under this scenario. A frequency estimation error around 0.22 mHz has been obtained.

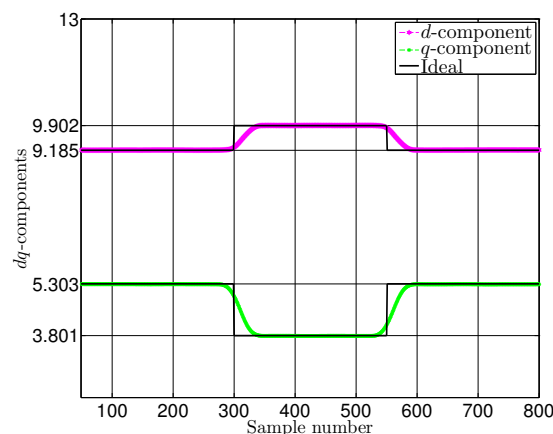


Figure III.54: Response of the algorithm under balanced phase angle step.

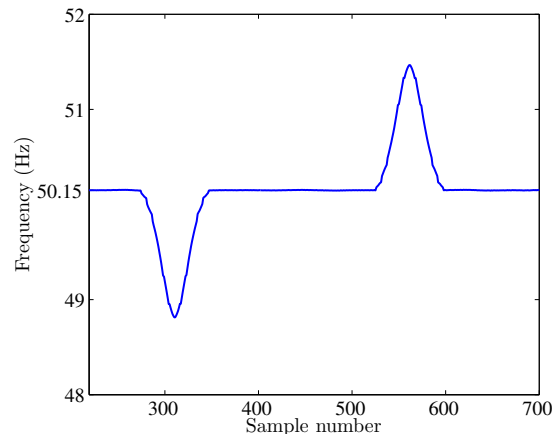


Figure III.55: Frequency estimates under balanced phase angle step

Fig. III.56 depicts the results concerning an unbalanced phase angle step. The step occurs at sample numbers 364 and 591. The phase angle of e_a -, e_b -, and e_c -signal has been increased by $+5^\circ$, $+2^\circ$, and $+8^\circ$, respectively. The system frequency is 49.5 Hz. Due to the rising step the value of positive-sequence phasor changes from $9.185+j5.303$ to $8.68+j6.078$. Before, after and during the steady-state of the step the TVE value is close to 0.1209%, 0.2324%, and 0.1755%, respectively. Fig. III.57 illustrates the environment of the frequency estimates. For this case, a estimation error around 0.9 mHz has been found.

For frequency step tests, sudden frequency variations have been performed. For evaluating the dynamic response of the algorithm a rising frequency step is performed during

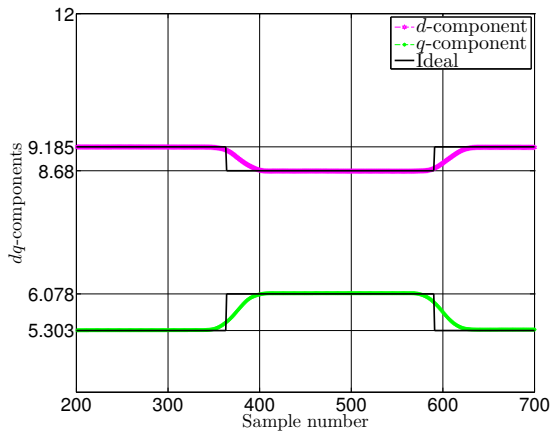


Figure III.56: Response of the algorithm under unbalanced phase angle step.

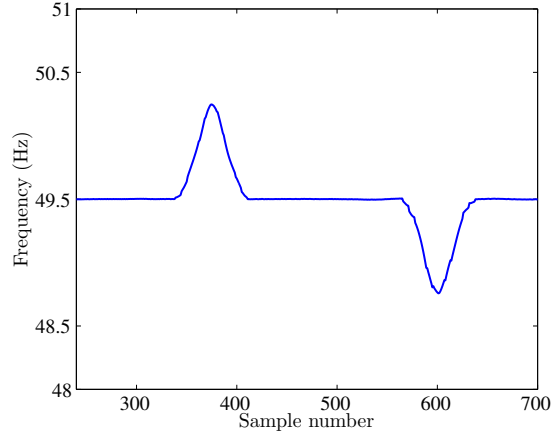


Figure III.57: Frequency estimates under unbalanced phase angle step

a short time interval followed by a falling frequency step (or opposite). Fig. III.58 shows a frequency step of -2.5 Hz. At the sample numbers 251 and 601 the steps are performed. In addition, unbalanced magnitudes are considered on the three-phase input signals.

The e_a -signal magnitude is reduced by 3%, for e_b -, and e_c -signal the magnitudes increase by 3.33% and 5.66%, respectively. A subharmonic of 4 Hz has also been added to the noisy input signal. For this test case a SNR=60 dB is deemed. In the steady-state of the step a frequency error around 0.0462 mHz has been observed. It can be seen that the algorithm presents a maximum time response locked to the filtering latency impose by the FIR filters.

Similarly, Fig. III.59 depicts the results regarding a step of +1.5 Hz. The three-phase input signals are balanced. An interharmonic of 125 Hz is added to the input and a SNR=63.52 dB has been considered. For this test case a frequency error around 0.0746 mHz has been observed during the steady-state of the step. In Fig. III.60 a step of +1.85 Hz is simulated. In this test case, balanced three-phase input signals, an interharmonic of 95 Hz and a SNR=65.46 dB have been considered. During the step, a frequency error close to 0.0771 mHz has been observed.

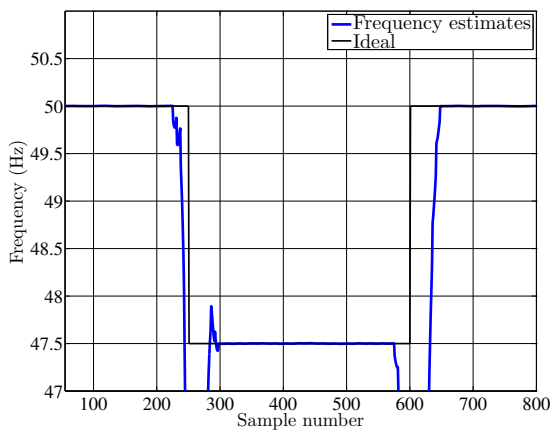


Figure III.58: Response of the algorithm considering a frequency step of -2.5 Hz.

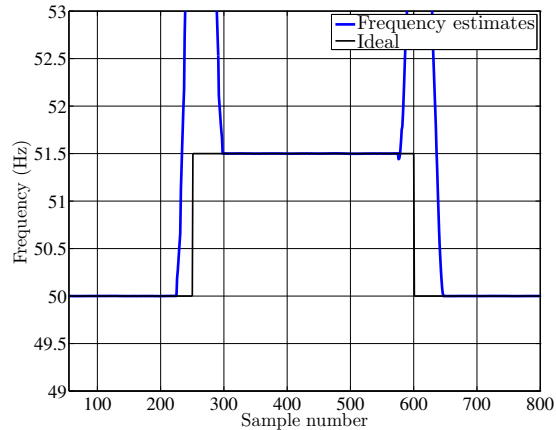


Figure III.59: Response of the algorithm considering a frequency step of +1.5 Hz.

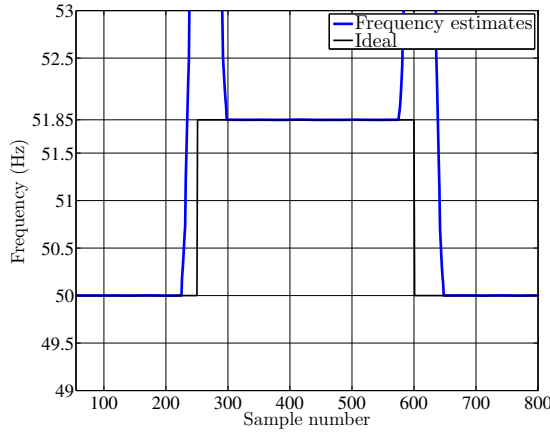


Figure III.60: Response of the algorithm considering a frequency step of +1.85 Hz.

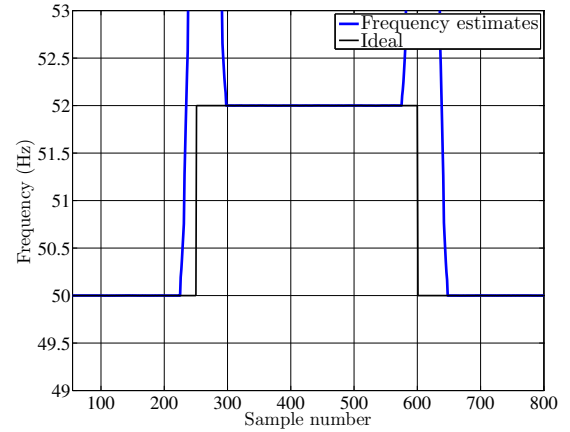


Figure III.61: Response of the algorithm considering a frequency step of +2.0 Hz.

Fig. III.61 displays the results for a step of +2 Hz. Amplitude unbalances of the three-phase input signals are used. The magnitude of e_a -signal is reduced by 1.66% and for the e_b -, and e_c -signal the magnitudes have been increased by 1.33% and 3%, respectively. An interharmonic of 115 Hz and a SNR=69.54 dB are deemed. For this test case a frequency error around 0.0302 mHz has been achieved. It is possible to note that the proposed algorithm provides estimates with high degree of accuracy even under sudden frequency variations.

For frequency ramp tests, input signals have been applied over each phase to enable a linear frequency variation. Eq. (III.99) shows the employed signal model based on Eq. (III.87)

$$x(n) = 15\cos(\omega_o n \Delta T_o + \pi\nu(n\Delta T_o)^2) \quad (\text{III.99})$$

ν being the frequency ramp rate.

During the test the local system frequency starts from 50-Hz followed by a positive ramp +15 Hz/s starting at sample number 201 and ending at 560, followed by a static frequency of 53 Hz. Fig. III.62 displays the response of the proposed algorithm under this scenario. It can be note that the dynamic variation of the signal is shifted from the ideal response due to the latency of the FIR filtering process, moreover, a transient feature on the discontinues points will be present. Using these data for computing the ROCOF metric the accuracy of the results is impaired. The algorithm circumvents this problem by means of a ROCOF monitor that uses the nominal frequency to allow a normalized representation.

For clarifying the foregoing, let us analyze Fig. III.63. In essence, the ROCOF metric is computed taking into account a triangle that represents the frequency variation over time, as it has been shown in Eq. (III.39). The true and estimated ROCOF triangle are represented by red and black lines, respectively. Looking closely at the triangles, one can observe that for both the catheti regarding the frequency axis are equal. However, the catheti related to the time variation are not equal due to the filtering latency. In this way, it is necessary to estimate the time interval Δt_1 and Δt_2 whose values are subtracted from the total time interval Δt_e in order to obtain the true time interval Δt . The value of Δt_1

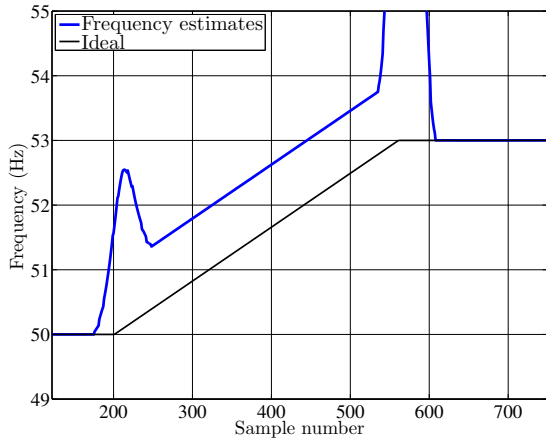


Figure III.62: Response of the algorithm under linear frequency ramp of +15 Hz/s

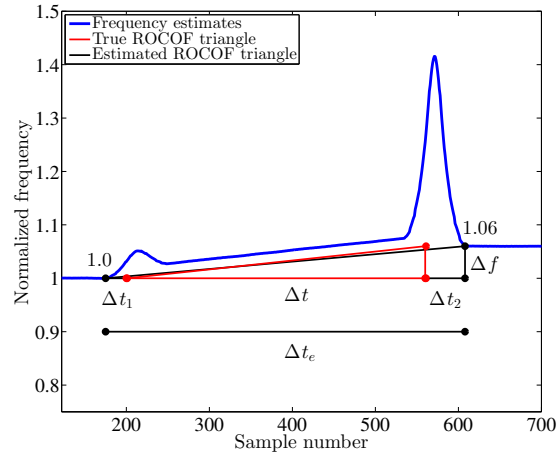


Figure III.63: ROCOF monitor based on the normalized frequency estimates.

is computed by the product between the first 25 samples inside of the transient region of the first discontinuity point and the fixed sampling interval.

The value of Δt_2 is computed taking into account the product between the last 49 samples inside of the second transient region and the sampling interval. Clearly, the cascaded mode of the filters must be evaluated in order to provide the amount of samples to be multiplied by the sampling time in order to estimate the envisaged time intervals. This method for computing the ROCOF metric may provide very accurate results yielding errors below 0.01 Hz/s. It is of paramount importance to mention that Table III.3 depicts the error requirements taking into account individual influence quantity, however, in the analyzed test these quantities are combined together.

III.6.a.ii Test cases concerning the 4F-algorithm

Let a sampled single-phase input signal (*in pu*) be given by

$$y(t) = Y_{DC} + Y_1 \cos(2\pi f_m t + \phi_1) + \sum_{m=2}^D Y_m \cos(2\pi m f_m t + \phi_m). \quad (\text{III.100})$$

Let us assume that this signal is distorted by high order harmonics components as shown in Table III.8.

For the first analysis, let us consider a fundamental signal having a magnitude of 1.0 pu and a phase equal of 60° , so that the correct phasor representation of this signal is $\underline{Y} = 1/60^\circ$. Considering only the fundamental phasor estimates under several frequency deviation the obtained results are very accurate, as it can be seen in Table III.9. The frequency error is within ± 0.2 mHz. Clearly, using accurate frequency estimates based on the Park's transformation sensitivity combined with trigonometric interpolation [3] applied over the FIR bandpass filter output data one can obtain accurate adjusted samples.

The second analysis is performed for estimating simultaneously the selective phasor components (1th, 3th, 5th, and 7th) under frequency variation. Fig. III.64 depicts the

Table III.8: Components of the input signal

Harmonic component	Amplitude (nominal reference)	Phase angle (degrees)
0	2%	0
2	3%	20°
3	7.5%	15°
4	2%	13.84°
5	8%	20°
6	1%	8.18°
7	7%	-12°
8	1.2%	15°
9	5.5%	30°
10	1%	12°
11	2%	-22.5°

Table III.9: Fundamental phasor estimates

Signal frequency	Parameters		
	TVE (%)	Magnitude (pu)	Angle (degrees)
50.75 Hz	0.0212	1.00021	60.00180°
50.67 Hz	0.0246	1.00024	60.00188°
50.40 Hz	0.0248	1.00024	60.00207°
50.18 Hz	0.0126	1.00012	60.00202°
50.03 Hz	0.0095	1.00009	60.00183°
49.95 Hz	0.0174	1.00017	60.00164°
49.68 Hz	0.0276	1.00027	60.00224°
49.55 Hz	0.0252	1.00025	60.00138°
49.18 Hz	0.0106	1.00009	60.00277°
49.00 Hz	0.0238	1.00023	60.00174°
Ref. IEEE C37.118	0.0	1.0	60°

results for these components taking into account static off-nominal frequencies at 49.3 Hz and 49.8 Hz. For this scenario a SNR=74 dB has been considered. Performing several simulations a maximum TVE value of 0.218% has been found for the 3th harmonic at 49.3 Hz. One can note the accuracy of the results in which most values are below or close to 0.1%. Similarly, Fig. III.65 shows the results regarding static off-nominal frequencies at 50.5 Hz and 52 Hz.

Once again accurate harmonic phasor estimates have been obtained being the maximum TVE among all results equal to 0.202% related to the 7th harmonic component at 52 Hz. One can observe that the TVE value present a slight increase concerning the harmonic phasors. This is expected due to the small magnitude of the harmonics components. Concerning the fundamental component, one can note very accurate estimates that fulfills the constraints imposed by the active distribution grids.

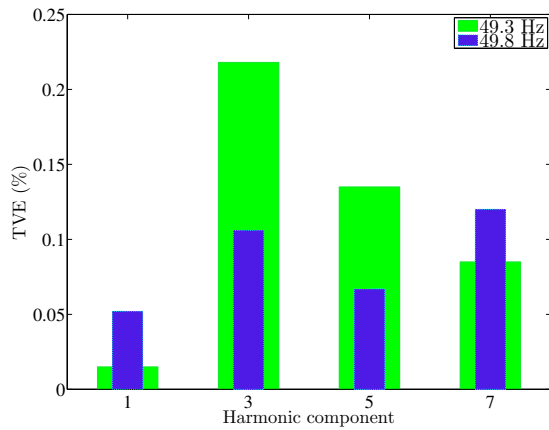


Figure III.64: Harmonic phasor estimates at system frequency of 49.3 Hz and 49.8 Hz.

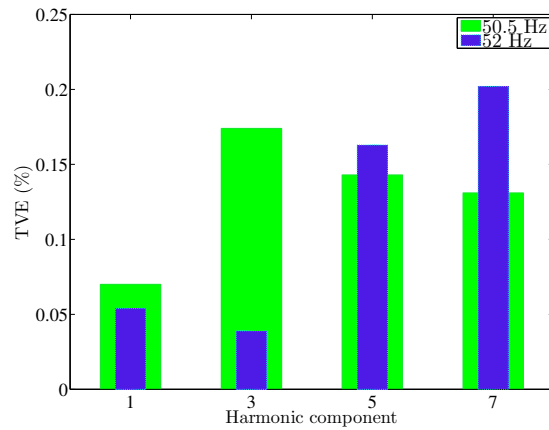


Figure III.65: Harmonic phasor estimates at system frequency of 50.5 Hz and 52 Hz.

III.6.a.iii Test cases concerning the AWLS-algorithm

The AWLS-algorithm has been evaluated for providing accurate estimates of all components of a single-phase input signal (DC-offset, fundamental and harmonic phasors) over a frequency range of ± 5 Hz. The tests are performed taking also into account the number of cycles used for estimating the envisaged components.

Let us consider the single-phase input signal given by Eq. (III.100) being distorted by the components shown below

Table III.10: Harmonic components of the input signal

Harmonic component	Amplitude (nominal reference)	Phase angle (degrees)
0	1%	0°
2	3%	-22.5°
3	6%	-10.58°
4	1.5%	-45.71°
5	8%	9.47°
6	1%	123.15°
7	7%	36°
8	1%	30°
9	2.5%	29.5°
10	1%	8.18°
11	5%	3.27°

The fundamental component phasor is equal to $\underline{Y} = 1/\underline{-45^\circ}$ and the frequency estimation error for all test cases is within the range of ± 0.5 mHz being computed by three-phase balanced input signals. In addition, the simulations have been performed taking into account 1000 Monte Carlo trials. Fig. III.66 shows the TVE value for all components of the single-phase input signal considering a SNR = 46 dB at system frequency of 49.9 Hz. The obtained estimates providing maximum TVE below 0.25%.

Fig. III.67 illustrates the results considering a system frequency at 50.1 Hz and a SNR=49.1 dB. Once again, the maximum TVE is below 0.25% , however a slight improve-

ment on the results have been obtained. Fig. III.68 depicts the TVE value concerning a system frequency at 50.25 Hz with a SNR=60 dB. The maximum TVE achieved is below 0.14%. One can note that most of the estimates are below 0.1%.

Fig. III.69 shows the estimates regarding a system frequency at 51 Hz with a SNR=69.1 dB. Note that several of the estimates are below 0.08%. Now, let us consider the boundaries of the frequency range. Fig. III.70 illustrates the TVE values taking into account a system frequency at 45 Hz with a SNR =77 dB. One can observe that the maximum TVE value achieved is close to 0.18% and several estimates are below 0.12%. Similarly, Fig. III.71 depicts the estimates regarding a system frequency at 55 Hz with a SNR=80 dB. The maximum reported TVE value is close to 0.12% and most estimates are below 0.07%.

It is important to mention that the standard deviation of the estimates tends to increase when the SNR decreases. One can notice a satisfactory overall performance in terms of TVE accuracy regarding the three frequency-adaptive algorithms. Phasor estimates with very low TVE will open the doors to the deployment of PMU and PMU-enabled IED to increase the situational awareness in active power distribution systems.

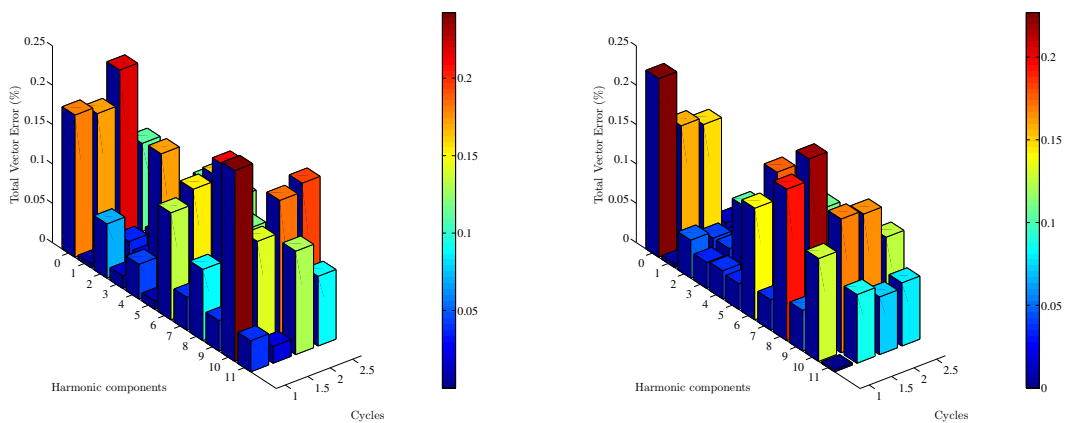


Figure III.66: Estimates at 49.9 Hz with a SNR = 46 dB.

Figure III.67: Estimates at 50.1 Hz with a SNR = 49.1 dB.

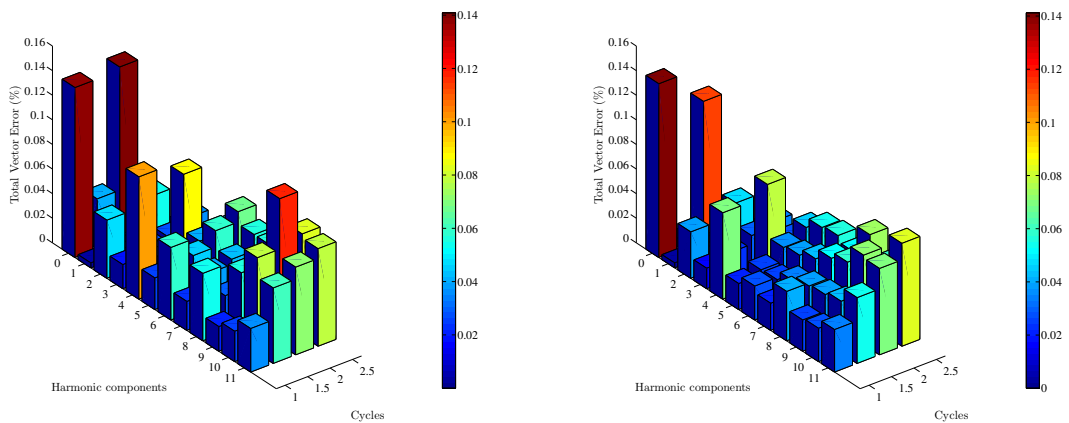


Figure III.68: Estimates at 50.25 Hz with a SNR = 60 dB.

Figure III.69: Estimates at 51 Hz with a SNR = 69.1 dB.

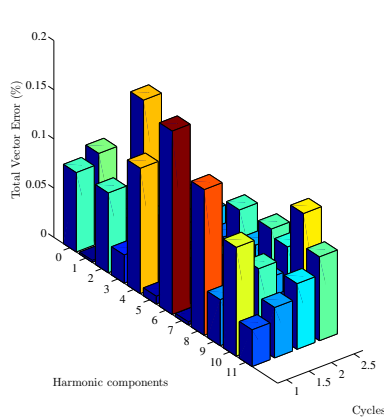


Figure III.70: Estimates at 45 Hz with a SNR = 77 dB.

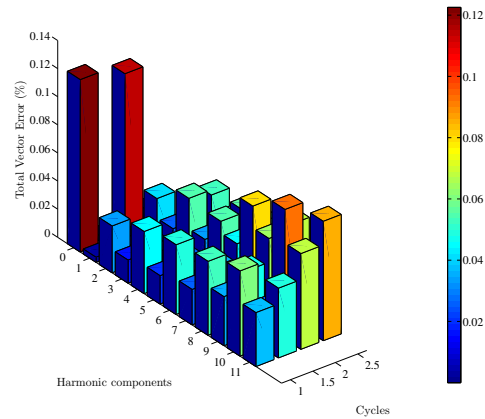


Figure III.71: Estimates at 55 Hz with a SNR = 80 dB.

III.7 Conclusion

In the present chapter three frequency-adaptive algorithms have been presented aiming to boost synchronized phasor measurements estimation in electric distribution environment under dynamic and/or static conditions. The algorithms employ a decoupled stage to track local system frequency based on the classical finite derivative approximation of the fundamental positive-sequence voltage phasor phase angle displacement. However, the Park's transformation has been applied due to its high sensitivity and quick response under frequency deviation. Using the system frequency estimates the rate of change of frequency (ROCOF) has been also computed.

It is well-known that the Park's transformation changes its dynamic according to the variations on the three-phase input signals (Gaussian white noise, harmonics, and so on) leading to very noisy estimates. For overcoming these effects, FIR filters (bandpass and moving average) have been applied to substantially alleviate the undesirable effects and, consequently, to give back to the Park's transformation its inherent robustness. After performing accurate frequency tracking, the algorithms use this information to properly perform software-based adaptive-frequency. With the development of high-performance DSPs and FPGAs with powerful routines of floating-point representation this task may be adequately accomplished.

The first frequency-adaptive algorithm is based on a modified adaptive Park's transformation able to compute fundamental positive-sequence voltage phasor estimates for ensuring an enhanced speed and accuracy in both balanced and unbalanced conditions. The main goal of the proposed algorithm concerns an improved traceability of steady-state and dynamic conditions in active distribution grids. The obtained results show that the algorithm has good performance for estimating the fundamental positive-sequence voltage phasor estimates within the range of ± 5 Hz around the nominal frequency.

The second one called 4F-algorithm performs four steps in a synergistic manner - frequency estimation, digital FIR bandpass filtering, fast linear interpolation, and Radix-2 DIT FFT approach - to compute fundamental and selective harmonic phasors of a single-phase input signal. The envisaged components to be estimated are the fundamental and

the selective 3th, 5th, 7th odd harmonic components because they are particularly found in power distribution systems. This algorithm applies the technique ‘divide and conquer’ because the components of a very distorted input signal are separated from each other by a FIR filter bank and thereafter interpolation is individually performed at the filters output data. This process allows a direct application of the half-cycle FFT approach when the input signal is distorted by harmonics. The obtained results show that the algorithm has good performance within the range of ± 2 Hz around the nominal frequency.

The third algorithm titled ‘AWLS algorithm’ provides a practical, intuitive and accurate manner for computing DC offset, fundamental and harmonics phasors under frequency deviation of a single-phase voltage or current input signal using full or fractional-cycle data window. A range within ± 5 Hz around the nominal frequency has been used for evaluation purposes. The phasor estimation process is modeled in the weighted least squares sense and the algorithm modifies its inner parameters according to the estimated system frequency.

Input signals very distorted by out-of-band disturbances (DC offset harmonics and interharmonics), frequency deviation, and Gaussian white noise have been used for the evaluation of the proposed algorithms. Test cases related to magnitude- and phase step, frequency step, and frequency ramp have been performed. Considering the accuracy of the phasor estimates the reported results have a very low TVE value. Therefore, the tests demonstrate the capability of the proposed algorithms in dealing efficiently with very corrupted signals under frequency deviations that can be particularly found in active distribution grids.

Chapter IV

Applications of synchronized phasor measurements to increase the situational awareness in active power distribution systems

Phasor is the nature's evidence of the harmony between real and imaginary worlds.

The author

CONTENTS

IV.1	INTRODUCTION	142
IV.2	CONTRIBUTIONS FOR REAL-TIME ESTIMATION OF THÉVENIN'S EQUIVALENT USING ACCURATE PMU DATA	144
IV.2.a	Classical method for evaluating the Thévenin's equivalent using PMU data	146
IV.2.b	Evaluation of the TE circuit based on accurate PMU data for steady- or <i>quasi</i> -steady state conditions	151
IV.2.c	Main objective: Online tracking of the grid model based on the Thévenin's equivalent and enhanced operating point assessment on generation capability curves	154
IV.3	PRACTICAL ONLINE EXTERNAL EQUIVALENTS IN RADIAL ACTIVE DISTRIBUTION GRIDS USING PMU DATA	160
IV.3.a	Ward linear equivalent overview	162
IV.3.b	Practical on-line external equivalent based on PMU data	163
IV.3.c	Main objective: Reduction of the grid size and online evaluation of the external network	166
IV.4	ASSESSMENT OF THREE-PHASE VOLTAGE DROP IN PRIMARY RADIAL DISTRIBUTION GRIDS USING PMU DATA	169
IV.4.a	Overall voltage drop of a radial feeder calculated from PMU data taken at the feeder ends	171
IV.4.b	Main objective: Online three-phase voltage drop assessment	173
IV.5	ASSESSMENT OF HARMONIC ISSUES USING PMU DATA	175
IV.5.a	Main objective: Enhanced detection of both harmonic power flow direction and main source of harmonic pollution under frequency deviation	178
IV.6	CONCLUSION	184

Abstract

Deployment of accurate PMUs and PMU-enabled IEDs in active distribution systems may boost the development of advanced online monitoring applications. In this chapter, four potential applications are presented aiming to increase the situational awareness

in distribution environment. The first one brings contributions for online estimation of Thévenin's equivalent (TE) circuit using accurate PMU data for steady- or quasi-steady state conditions. This application aims to overcome the problematic related to the Thévenin's impedance locus method when equal or very close consecutive measurements are used. The proposed application is applied to determine the reduced grid model seen by the PCC between aggregated DERs (wind turbines) and the active distribution grid. In this way, online power flow exchanges between both sides and updated capability curve of synchronous generators can be properly carried out. The second one is a practical application to track dynamic external equivalents in radial active distribution grids using PMU data. This application uses the voltage and current phasor measurements recorded at a given boundary busbars to replace the external network (EN) by a dynamic impedance or a dynamic power injection (simplified Norton's theorem). Besides the external equivalent evaluation, this application also reduces the electric grid size. The third one is related to the online three-phase voltage drop assessment in primary radial distribution grids. This application takes into consideration accurate synchronized voltage measurements recorded at the feeder ends. The goal is to improve the voltage regulation along the feeder even for conditions related to heavy current combined with leading power factor caused by the integration of DERs. The last one concerns the assessment of harmonic issues. This application brings contributions for improving the classical P_H method (harmonic active power) using synchronized measurements. The goal is to improve both detection of the main source of harmonic pollution and actual power flow direction. The aforementioned applications use accurate phasor measurements, in this way, each of them is related to one of the frequency-adaptive algorithms proposed in Chapter III.

IV.1 Introduction

Applications of PMUs in wide-area management systems (WAMSs) are already consolidated. Angular separation, islanding and resynchronization, oscillatory stability, linear state estimation, and disturbance location identification have been one of the flagship applications of PMUs in high-voltage power systems. Using synchronized measurements, it is possible to extract valuable informations of the electric system without full knowledge of its characteristics.

In order to bring the well-known benefits of the synchronized measurements towards electric distribution grids the PMUs and PMU-enabled IEDs must have different features from those dedicated to the high-voltage system. In other words, the accuracy of the measurements must be taken beyond current standards for overcoming the main challenges cited in Chapter II.

The effective advent of advanced monitoring applications dedicated to distribution grids has the measurement accuracy as the primary goal to be achieved. However, the PMU placement issue can not be passed up. Several methods have been proposed for optimal PMU placement in high-voltage electric power systems [87]-[88]-[89]. In general, a multi-objective optimization problem must be solved in order to fulfill the observability of the grid in a cost-effective manner.

In short, these techniques take advantage of the meshed grid topology to place PMUs in some busbars so that the overall observability of the grid may be ensured. We could be led to believe that these optimization techniques can also be applied in a straightforward

manner to active distribution grids because the service area of these systems are very small when compared to the coverage area of the high-voltage electric systems, however, this is not necessarily true.

For a practical exemplification, let us cite a very interesting information found in [90]. A network distribution associated to a CEMAR (Electricity Utility of Maranhão) substation, called Renascença has approximately 3924 busbars, while the Brazilian interconnected transmission system has 3538 busbars. If the number of busbars is the point compared, one can note that the network supplied by the substation of Renascença has a dimension greater than the Brazilian interconnected power system. It is important to mention that the substation of Renascença is not an exception and other large substations are found in the CEMAR's service area.

Now, we can note the challenges for monitoring the distribution grids so that the overall grid be observable. In this way, even if an optimization technique provides the best location to place PMUs in the distribution environment, the total cost of installation is unattainable. Thereby, an important issue may be raised: Where to place PMUs for increasing the situational awareness in active distribution systems? The author advocates the idea of PMU placement at specific busbars according to the envisaged application, that is, optimal solution based on mathematical approach is not demanded.

Being clear about it, if the application aims a reliable integration of multiple high-rate DERs at the grid, an accurate PMU must be placed at each Point of Common Coupling (*PCC*). Furthermore, it has been shown in II.2.b the problematic of the angular aperture between busbars connected by short lines, however, if the envisaged application aims to evaluate the synchronized measurements taken at the feeder ends so that the angular aperture be more expressive, the placement of only two PMUs will be required.

Keeping in mind the aforementioned statements concerning the synchronized measurements accuracy and PMU placement considerations, four potential applications are presented in the current chapter. The first one brings contributions for online tracking of Thévenin's equivalent circuit taking into account steady- or *quasi*-steady state conditions. This application aims to overcome the problematic related to the Thévenin's impedance locus method when equal or very close consecutive measurements are used.

The proposed application is applied to determine the reduced grid model seen by the *PCC* between aggregated DERs (wind turbines) and the active distribution grid. Based on the positive-sequence voltage and current phasors computed from the frequency-adaptive Park's transformation algorithm, online power flow exchanges between both sides may be properly accomplished. In addition, updated capability curve of synchronous generators can also be evaluated.

The second one is a practical application to track dynamic external equivalents in radial active distribution grids using accurate PMU data. Once again, the frequency-adaptive Park's transformation algorithm has been employed to perform this application. The voltage and current phasor measurements recorded at a given boundary busbars are used to replace the external network (EN) by a variable impedance or, additionally, by a variable power injection (simplified Norton's theorem). Besides the external equivalent evaluation, this application also reduces the electric grid size allowing advanced monitoring on the area of interest (internal network).

The third one is related to the online three-phase voltage drop assessment in primary

radial distribution grids. This application takes into consideration accurate synchronized voltage measurements recorded at the feeder ends. The goal is to improve the voltage regulation along the feeder even for conditions related to heavy currents combined with leading power factor caused by the integration of DERs. This application uses the frequency-adaptive 4F-algorithm to compute the fundamental phasor of each phase recorded at the feeder ends.

The last one concerns the assessment of harmonic issues. This application brings contributions for improving the classical P_H method (harmonic active power) using accurate harmonic measurements. The goal is to improve both detection of the main source of harmonic pollution and actual power flow direction. This application takes advantage of the frequency-adaptive AWLS-algorithm to track harmonic components upto 11th order. Accurate results have been employed for sharing the harmonic responsibility. The complete presentation of the aforementioned applications will be addressed in Sections [IV.2-IV.5](#).

IV.2 Contributions for real-time estimation of Thévenin's equivalent using accurate PMU data

When Léon Charles Thévenin, illustrious son of the beautiful town of Meaux, published his paper titled '*Sur un nouveau théoreme d'électricité dynamique*', he was about to change the manner for analyzing electric circuits through a description of an elegant and powerful theorem. He proved that an electric circuit can be analyzed between two nodes without the need of a rigorous knowledge and modeling of the rest of the circuit. The theorem brings its great importance when dealing with electrical circuits with multiple elements because a direct simplification may be performed. In essence, the rest of the circuit seen from the two nodes can be modeled as a voltage source in series with an impedance, in which they are known as Thévenin's voltage and impedance (E_{Th} and Z_{Th} , respectively).

The ability of reproducing the behavior of the rest of a system based on local measurements makes the Thévenin's theorem a powerful method for analyzes concerning the reliable integration of DERs in active distribution grids. A PMU or PMU-enabled IED placed at *PCC* can be used to provide real-time tracking of Thévenin equivalent parameters using the synchronized measurements taken at that node. Within this context, the theory presented in [91], [92], and [93] deals properly with this subject.

In [91], three consecutive voltage and current measurements one at a time have been used to determine the Thévenin's equivalent. Using these measurements, two equations concerning the Thévenin's impedance locus are determined for inferring the most probable value. The equation of the circles are determined from the voltage and current magnitudes as well as the active and reactive powers. The method provides two solutions for Z_{Th} and, by consequence, two corresponding values of E_{Th} may be reported. The higher one that is near to the system voltage is chosen as the true E_{Th} .

In addition, the author claims that the proposed method recognizes and considers the phase angle drift caused by frequency deviation. The angle difference between E_{Th1} and E_{Th2} calculated at different time instants determines the drift that took place between the synchronized measurements. In this way, corrected Thévenin's voltage and impedance could be obtained.

In [92], the problematic of the TE estimation taking into account the frequency deviation is treated in more details. Once again, three consecutive voltage and current phasor measurements, taken at *PCC*, are employed. The phase drifts caused by frequency deviation are first determined and after the phasors phase angle have been synchronized to the same reference. The synchronization process is performed by triangulation.

The phase angle of a phasor tends to rotate according to the frequency deviation (see Section I.9), therefore, once determined the shifted phase angles the necessary adjustments are performed so that the subsequent pairs of measurements can then be corrected to the same reference. The method uses the first recorded measurement pair as the reference.

In [93], a method for estimating TE taking into account the measurement errors and the changes in the system side is presented. Similarly to [91], the proposed method uses circle equations concerning the Thévenin's impedance locus calculated from voltage and current magnitudes as well as active and reactive powers. Due to this fact, the authors claim that the proposed method avoids the need to synchronize measurements at different instances to the same reference. In short, it could be immune to frequency deviations.

For computing the Thévenin's impedance, a linear relationship may be outlined between R_{Th} and X_{Th} ($Z_{Th} = R_{Th} + jX_{Th}$) using different straight-line equations that involve the intersection points between the locus. The procedure to solve this problem is based on the calculation of the determinant of three measurement matrices formed by the measurements under consideration. The estimates of R_{Th} and X_{Th} are achieved using probability distributions for any desired confidence interval.

The aforementioned methods have good performances when consecutive synchronized measurements are not equal or when they have not very close values. If this assumption is not retained, the coefficients of the equations will be zero and no solution can be obtained. This can be clearly observed on the methods based on the Thévenin impedance locus, in which different consecutive measurements must be achieved in order to ensure a displacement among the circles for inferring the Thévenin parameters. Due to this fact, when variations on the system or load side are recorded by a PMU, powerful techniques for voltage stability may be carried out.

Meanwhile, a new issue has emerged concerning the TE estimation using accurate measurements that do not change significantly during the analysis interval, that is, for steady state or *quasi*-steady state conditions. Considering the integration of DERs into the active distribution grid, one can assume that the DER side is more dynamic and changes faster than the system side.

For this case, the assumption of invariant system side during the analysis interval of few cycles has been recognized. In other words, the system side will not experience noticeable variation during the time interval of the reported consecutive measurements. Therefore, the determination of the TE for the grid side seen by the *PCC* considers that the variation of the grid side is stable or slow enough to not affect the calculation.

Aiming to contribute with this issue, a real-time estimation technique for evaluating the TE equivalent using accurate data provided by a PMU or PMU-enabled IED endowed with the frequency-adaptive Park's transformation algorithm is presented. The technique takes into account the simplifying assumption of the infinite busbar concept, in which the system voltage is constant and independent whether the power flow is consumed or supplied by the DER.

Two characteristics of the estimation process may be boosted using this technique: a fast time span of few cycles, because the phasor estimates are recursively recorded sample-by-sample, and an effective immunity against frequency deviation. Concerning the latter, the effectiveness of the proposed algorithm in dealing with frequency drifts has been shown in Section III.3. In this way, it can provide corrected phasors, that is, there is no need to perform, for example, triangulation to adjust the measurements.

Once the Thévenin's voltage is assumed to be equal to the infinite busbar voltage, the Thévenin's impedance may be computed taking into account the voltage and current phasor measurements in rectangular coordinates. A time span matched to the one quarter of the cycle at nominal frequency has been employed resulting in the treatment of 9 phasor estimates. Therefore, a total amount of 18 linear equations are determined and solved by WLS approach, as shown in Eq. (IV.27). Subsequent estimates of Z_{Th} into the analyzed cycle is determined using recursive WLS to provide a real-time updating of the impedance estimates as newer phasors are acquired.

It can be noted that the time between two consecutive phasors is locked to the sampling time, which is so far less than the time constants of OLTC regulating transformer and automatic feeder switching. The obtained TE parameters represent an electric model that fulfills the power flow interaction between the DER- and the grid side.

Another discussion concerning the Thévenin impedance estimation is outlined. In [93], it is stated that the proposed method is immune to frequency deviation because the measurements used are based on voltage and current magnitudes (RMS values) as well as active and reactive powers (average values). However, this statement is true *only, and only if*, the algorithm employed for computing the active power measurement takes into consideration the product sample-by-sample between the voltage and current waveforms divided by the number of samples inside the interval under consideration. Using the RMS values of voltage and current the magnitude of the apparent power may be evaluated and, by consequence, the reactive power is determined.

For the algorithms that compute power measurements by the product between the voltage and current phasors, if no action is taken to overcome the frequency deviation the power measurements will have errors. Using the frequency-adaptive modified Park's transformation algorithm this problem may be circumvented.

In IV.2.a, the classical method based on the circles of the Thévenin's impedance locus using PMU data is shown. We have refurbished the equations reported in [93] in order to put them in a system of linear equations. The goal is to show the difficulties concerning the application of accurate phasor measurements for estimating TE. In IV.2.b the proposed technique to estimate the TE related to the system side is presented.

IV.2.a Classical method for evaluating the Thévenin's equivalent using PMU data

Let us consider the Thévenin's equivalent given by Fig. IV.1. Where \underline{I} and \underline{V} are the recorded current and voltage phasor measurements of a PMU placed at PCC ; P and Q represent respectively the active and reactive power injections into the grid; $\bar{Z}_{Th} = R_{Th} + jX_{Th}$ and \underline{E}_{Th} represent the Thévenin's impedance and voltage phasor for a given system condition.

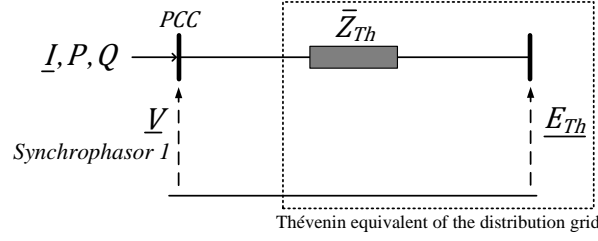


Figure IV.1: PCC monitored by a PMU and the rest of the distribution grid is treated as a TE circuit.

The phasor diagram shown in Fig. IV.2 provides the relationship between the synchronized measurements and the Thévenin parameters based on the assumed power flow direction. Therefore, the equality given by Eq. (IV.1) can be obtained

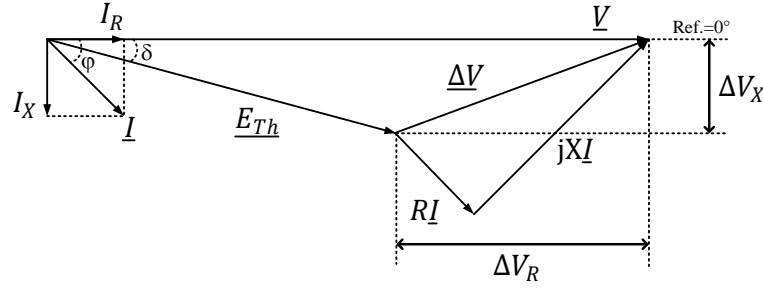


Figure IV.2: Phasor diagram relating the synchronized measurements and the Thévenin parameters. Power flow from the distributed resource to the grid (lagging power factor).

$$\underline{V} = \underline{E}_{Th} + \underline{\Delta V} \Rightarrow \underline{V} = \underline{E}_{Th} + \bar{Z}_{Th}\underline{I}. \quad (IV.1)$$

One can note that the components of $\underline{\Delta V}$ can be obtained by the product between the \bar{Z}_{Th} and \underline{I} , as given by Eq. (IV.2)

$$\underline{\Delta V} = \bar{Z}_{Th}\underline{I} = (R_{Th} + jX_{Th})(I_R - jI_X) \quad (IV.2)$$

being I_R and I_X equal to

$$I_R = |I| \cos(\varphi) \quad (IV.3)$$

$$I_X = |I| \sin(\varphi). \quad (IV.4)$$

Replacing Eqs. (IV.3)-(IV.4) into Eq. (IV.2) one can obtain the following equation

$$\begin{aligned} \underline{\Delta V} &= R_{Th}I_R - jR_{Th}I_X + jX_{Th}I_R + X_{Th}I_X \\ &= (R_{Th}I_R + X_{Th}I_X) + j(X_{Th}I_R - R_{Th}I_X) = \Delta V_R + j\Delta V_X. \end{aligned} \quad (IV.5)$$

Looking closely at Fig. IV.2, it can be seen that the Thévenin's voltage magnitude can be computed taking into account the magnitude of \underline{V} and the components ΔV_R and ΔV_X , hence

$$|E_{Th}|^2 = (|V| - \Delta V_R)^2 + \Delta V_X^2. \quad (IV.6)$$

Replacing Eqs. (IV.3)-(IV.5) into Eq. (IV.6) yields

$$\begin{aligned} |E_{Th}|^2 &= (|V| - (R_{Th} |I| \cos(\varphi) + X_{Th} |I| \sin(\varphi)))^2 \\ &+ (X_{Th} |I| \cos(\varphi) - R_{Th} |I| \sin(\varphi))^2. \end{aligned} \quad (IV.7)$$

Recalling that

$$P = |V||I|\cos(\varphi) \quad (IV.8)$$

$$Q = |V||I|\sin(\varphi) \quad (IV.9)$$

and replacing the above equations into Eq. (IV.7) provides

$$|E_{Th}|^2 = \left(|V| - \left(\frac{R_{Th}P}{|V|} + \frac{X_{Th}Q}{|V|} \right) \right)^2 + \left(\frac{X_{Th}P}{|V|} - \frac{R_{Th}Q}{|V|} \right)^2. \quad (IV.10)$$

Expanding Eq. (IV.10) a reduced equation for the Thévenin voltage magnitude can be founded, hence

$$|E_{Th}|^2 = |V|^2 + \left(\frac{R_{Th}^2 P^2 + X_{Th}^2 Q^2 + X_{Th}^2 P^2 + R_{Th}^2 Q^2}{|V|^2} \right) - 2R_{Th}P - 2X_{Th}Q \quad (IV.11)$$

or in a more compact form given by Eq. (IV.12)

$$|E_{Th}|^2 = |V|^2 + |Z_{Th}|^2 |I|^2 - 2R_{Th}P - 2X_{Th}Q. \quad (IV.12)$$

Taking into account that the Thévenin's voltage magnitude between the first pair of measurements (V_1, I_1) and its subsequent pair are to be close within the analysis time interval [93], the following approximate relationship to the second pair (V_2, I_2) is carried out

$$|E_{Th1}| \approx |E_{Th2}| \quad (IV.13)$$

or alternatively,

$$|V_1|^2 + |Z_{Th}|^2 |I_1|^2 - 2R_{Th}P_1 - 2X_{Th}Q_1 \approx |V_2|^2 + |Z_{Th}|^2 |I_2|^2 - 2R_{Th}P_2 - 2X_{Th}Q_2. \quad (IV.14)$$

In order to reach a generalized equation related to the parameters R_{Th} and X_{Th} the following manipulations on Eq. (IV.14) must be performed. The first step consists of regrouping the terms, hence

$$(|I_1|^2 - |I_2|^2) |Z_{Th}|^2 \approx |V_2|^2 - |V_1|^2 + 2R_{Th}P_1 + 2X_{Th}Q_1 - 2R_{Th}P_2 - 2X_{Th}Q_2 \quad (IV.15)$$

therefore,

$$(R_{Th}^2 + X_{Th}^2) \approx \left(\frac{|V_2|^2 - |V_1|^2}{|I_1|^2 - |I_2|^2} \right) + 2R_{Th} \left(\frac{P_1 - P_2}{|I_1|^2 - |I_2|^2} \right) + 2X_{Th} \left(\frac{Q_1 - Q_2}{|I_1|^2 - |I_2|^2} \right). \quad (IV.16)$$

Arranging the parameters R_{Th} and X_{Th} gives

$$R_{Th}^2 - 2R_{Th} \left(\frac{P_1 - P_2}{|I_1|^2 - |I_2|^2} \right) + X_{Th}^2 - 2X_{Th} \left(\frac{Q_1 - Q_2}{|I_1|^2 - |I_2|^2} \right) \approx \left(\frac{|V_2|^2 - |V_1|^2}{|I_1|^2 - |I_2|^2} \right). \quad (\text{IV.17})$$

It is possible to note that Eq. (IV.17) can be rewritten in terms of quadratic polynomials regarding R_{Th} and X_{Th} , as shown in Eq. (IV.18)

$$\begin{aligned} \left(R_{Th} - \left(\frac{P_1 - P_2}{|I_1|^2 - |I_2|^2} \right) \right)^2 + \left(X_{Th} - \left(\frac{Q_1 - Q_2}{|I_1|^2 - |I_2|^2} \right) \right)^2 &\approx \left(\frac{|V_2|^2 - |V_1|^2}{|I_1|^2 - |I_2|^2} \right)^2 \\ &+ \left(\frac{P_1 - P_2}{|I_1|^2 - |I_2|^2} \right)^2 + \left(\frac{Q_1 - Q_2}{|I_1|^2 - |I_2|^2} \right)^2. \end{aligned} \quad (\text{IV.18})$$

It can be noticed that Eq. (IV.18) represents a circle of the Thévenin impedance locus. Special attention must be paid to the two latest terms on the right side of Eq. (IV.18). They have been written as a matter of formality because expanding the quadratic polynomials on left side these two members will appear and they must be disregarded. Due to the equation's features, two solutions can be found. Due to this fact, others circles must be taken for inferring a single Thévenin's impedance.

This procedure may be performed using the first pair of measurement $(\underline{V}_1, \underline{I}_1)$ as reference and for each new pair another locus is computed. For instance, let us consider two new measurement pairs $(\underline{V}_3, \underline{I}_3)$ and $(\underline{V}_4, \underline{I}_4)$. In this way, the new two impedance locus are computed according to Eqs. (IV.19)-(IV.20)

$$\begin{aligned} \left(R_{Th} - \left(\frac{P_1 - P_3}{|I_1|^2 - |I_3|^2} \right) \right)^2 + \left(X_{Th} - \left(\frac{Q_1 - Q_3}{|I_1|^2 - |I_3|^2} \right) \right)^2 &\approx \left(\frac{|V_3|^2 - |V_1|^2}{|I_1|^2 - |I_3|^2} \right)^2 \\ &+ \left(\frac{P_1 - P_3}{|I_1|^2 - |I_3|^2} \right)^2 + \left(\frac{Q_1 - Q_3}{|I_1|^2 - |I_3|^2} \right)^2 \end{aligned} \quad (\text{IV.19})$$

$$\begin{aligned} \left(R_{Th} - \left(\frac{P_1 - P_4}{|I_1|^2 - |I_4|^2} \right) \right)^2 + \left(X_{Th} - \left(\frac{Q_1 - Q_4}{|I_1|^2 - |I_4|^2} \right) \right)^2 &\approx \left(\frac{|V_4|^2 - |V_1|^2}{|I_1|^2 - |I_4|^2} \right)^2 \\ &+ \left(\frac{P_1 - P_4}{|I_1|^2 - |I_4|^2} \right)^2 + \left(\frac{Q_1 - Q_4}{|I_1|^2 - |I_4|^2} \right)^2. \end{aligned} \quad (\text{IV.20})$$

Based on the three circle of Thévenin's impedance locus computed from four synchronized measurements taking into account the first pair of measurement as reference, it is possible to estimate the resulting impedance. Theoretically, the envisaged impedance is matched with the intersection point of the three circles, however, the relative positions of the circles may change and they may not intersect at exactly the same single point. Fig. IV.3 illustrates the foregoing statement. Note that the relative position of the circles has been exaggerated in order to illustrate the behavior of the parameters estimation.

One can observe that different values of R_{Th} and X_{Th} may be reported falling within the red region. A potential solution for this problem may be performed by solving the three

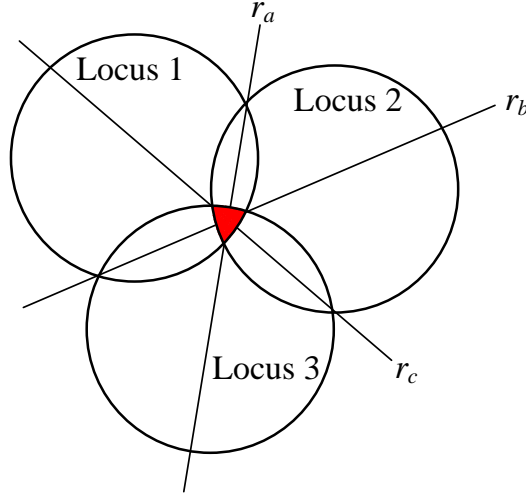


Figure IV.3: Circles of Thévenin impedance and common straight lines among them used to estimate R_{Th} and X_{Th} .

equations for the two unknowns parameters R_{Th} and X_{Th} using 2D-trilateration technique. However, another method to solve this problem is based on the intersection point regarding the straight lines r_a , r_b , and r_c that cross the common point between the circles.

These lines bring the information regarding the relationship between R_{Th} and X_{Th} . For accomplish this task, let us consider the system formed by the equations concerning the Locus 1 (Eq. (IV.18)) and the Locus 2 (Eq.(IV.19)). Solving the system we can find the r_a line equation given by

$$r_a : \left[\frac{P_1 - P_3}{|I_1|^2 - |I_3|^2} - \frac{P_1 - P_2}{|I_1|^2 - |I_2|^2} \right] R_{Th} + \left[\frac{Q_1 - Q_3}{|I_1|^2 - |I_3|^2} - \frac{Q_1 - Q_2}{|I_1|^2 - |I_2|^2} \right] X_{Th} = \quad (IV.21)$$

$$\frac{1}{2} \left[\frac{|V_2|^2 - |V_1|^2}{|I_1|^2 - |I_2|^2} - \frac{|V_3|^2 - |V_1|^2}{|I_1|^2 - |I_3|^2} \right].$$

In a similar manner, the equations concerning the lines r_b and r_c can be obtained according to

$$r_b : \left[\frac{P_1 - P_4}{|I_1|^2 - |I_4|^2} - \frac{P_1 - P_2}{|I_1|^2 - |I_2|^2} \right] R_{Th} + \left[\frac{Q_1 - Q_4}{|I_1|^2 - |I_4|^2} - \frac{Q_1 - Q_2}{|I_1|^2 - |I_2|^2} \right] X_{Th} = \quad (IV.22)$$

$$\frac{1}{2} \left[\frac{|V_2|^2 - |V_1|^2}{|I_1|^2 - |I_2|^2} - \frac{|V_4|^2 - |V_1|^2}{|I_1|^2 - |I_4|^2} \right]$$

$$r_c : \left[\frac{P_1 - P_4}{|I_1|^2 - |I_4|^2} - \frac{P_1 - P_3}{|I_1|^2 - |I_3|^2} \right] R_{Th} + \left[\frac{Q_1 - Q_4}{|I_1|^2 - |I_4|^2} - \frac{Q_1 - Q_3}{|I_1|^2 - |I_3|^2} \right] X_{Th} = \quad (IV.23)$$

$$\frac{1}{2} \left[\frac{|V_3|^2 - |V_1|^2}{|I_1|^2 - |I_3|^2} - \frac{|V_4|^2 - |V_1|^2}{|I_1|^2 - |I_4|^2} \right].$$

Looking closely at Eqs. (IV.21)-(IV.23), it is clear that an algebraic linear system can be performed for estimating the parameters R_{Th} and X_{Th} given by

$$\begin{bmatrix} |V_2|^2 - |V_1|^2 & |V_3|^2 - |V_1|^2 \\ |I_1|^2 - |I_2|^2 & |I_1|^2 - |I_3|^2 \\ |V_2|^2 - |V_1|^2 & |V_4|^2 - |V_1|^2 \\ |I_1|^2 - |I_2|^2 & |I_1|^2 - |I_4|^2 \\ |V_3|^2 - |V_1|^2 & |V_4|^2 - |V_1|^2 \\ |I_1|^2 - |I_3|^2 & |I_1|^2 - |I_4|^2 \end{bmatrix} = 2 \begin{bmatrix} \frac{P_1 - P_3}{|I_1|^2 - |I_3|^2} - \frac{P_1 - P_2}{|I_1|^2 - |I_2|^2} & \frac{Q_1 - Q_3}{|I_1|^2 - |I_3|^2} - \frac{Q_1 - Q_2}{|I_1|^2 - |I_2|^2} \\ \frac{P_1 - P_4}{|I_1|^2 - |I_4|^2} - \frac{P_1 - P_2}{|I_1|^2 - |I_2|^2} & \frac{Q_1 - Q_4}{|I_1|^2 - |I_4|^2} - \frac{Q_1 - Q_2}{|I_1|^2 - |I_2|^2} \\ \frac{P_1 - P_4}{|I_1|^2 - |I_4|^2} - \frac{P_1 - P_3}{|I_1|^2 - |I_3|^2} & \frac{Q_1 - Q_4}{|I_1|^2 - |I_4|^2} - \frac{Q_1 - Q_3}{|I_1|^2 - |I_3|^2} \end{bmatrix} \times \begin{bmatrix} R_{Th} \\ X_{Th} \end{bmatrix}. \quad (IV.24)$$

Interesting conclusions may be carried out regarding the linear system (IV.24). Clearly, one can note that the problematic involved concerns equal or very close consecutive measurements, because they will produce null values for the parameters R_{Th} and X_{Th} . That is, no solution will be achieved. Due to this fact, it is of paramount importance to evaluate the TE circuit when accurate measurements that do not change significantly during the analysis interval are employed.

IV.2.b Evaluation of the TE circuit based on accurate PMU data for steady- or quasi-steady state conditions

The TE circuit for the active distribution system side is depicted in Fig. IV.4. A PMU placed at PCC measures the positive-sequence voltage and current phasors, the complex power ($S = P + jQ$) injected into the grid, and the power factor. As depicted in Fig. IV.4, the following representation are applied:

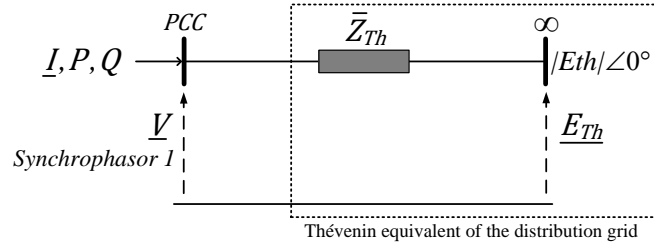


Figure IV.4: TE circuit of the system side considering the assumption of infinite busbar.

- $\underline{E}_{Th} = E_{Th_R} + jE_{Th_X}$: Thévenin's voltage at infinite busbar seen by the PCC .
- $\bar{Z}_{Th} = R_{Th} + jX_{Th}$: Thévenin's impedance seen by the PCC .
- $\underline{V} = V_R + jV_X$: The voltage phasor measurement recorded by the PMU.
- $\underline{I} = I_R + jI_X$: the current phasor measurement recorded by the PMU.
- $\bar{S} = P + jQ$: Complex power injected to the grid measured by the PMU.

As it has been commented, the infinite busbar assumption states that the system voltage is constant and independent of the power flow direction, that is, supplied or consumed by

the DER. In this way, it has been assumed that the infinite busbar voltage phasor is equal to $1\angle 0^\circ$ pu. The unitary magnitude represents the equality between the true voltage of the grid and base voltage. In addition, the phase angle has been considered as the reference for enabling the power flow interaction. Looking closely at Fig. IV.4, the following relationship can be drawn assuming the power flows from the DER to the distribution grid

$$\underline{V} = \bar{Z}_{Th}\underline{I} + 1\angle 0^\circ \quad (\text{IV.25})$$

in this way, Eq. (IV.25) can be rewritten in rectangular form for the first pair $(\underline{V}_1, \underline{I}_1)$ as follows

$$V_{R_1} + jV_{X_1} = (R_{Th} + jX_{Th})(I_{R_1} + jI_{X_1}) + E_{ThR}. \quad (\text{IV.26})$$

Performing the same procedure for the subsequent phasor measurements matched to one quarter of the cycle at nominal frequency, the following overdetermined linear system can be achieved

$$\begin{bmatrix} V_{R_1} - E_{ThR} \\ V_{X_1} \\ V_{R_2} - E_{ThR} \\ V_{X_2} \\ V_{R_3} - E_{ThR} \\ V_{X_3} \\ \vdots \\ V_{R_9} - E_{ThR} \\ V_{X_9} \end{bmatrix} = \begin{bmatrix} I_{R_1} & -I_{X_1} \\ I_{X_1} & I_{R_1} \\ I_{R_2} & -I_{X_2} \\ I_{X_2} & I_{R_2} \\ I_{R_3} & -I_{X_3} \\ I_{X_3} & I_{R_3} \\ \vdots & \vdots \\ I_{R_9} & -I_{X_9} \\ I_{X_9} & I_{R_9} \end{bmatrix} \times \begin{bmatrix} R_{Th} \\ X_{Th} \end{bmatrix}. \quad (\text{IV.27})$$

The above linear system is valid for any PCC on the active distribution system. It can be rewritten in a more compact form according to Eq. (IV.28)

$$v = H\hat{s} + \varepsilon \quad (\text{IV.28})$$

being v the voltage phasor measurement vector in rectangular coordinates; H represents the coefficient matrix formed by the current phasor measurements in rectangular coordinates; \hat{s} is the state vector to be estimated concerning the parameters of the Thévenin's impedance; and the vector error ε has been added to represent the Gaussian white noise.

It is clear that the Thévenin's impedance estimation attempts to minimize the error in a least-squares sense. In this manner, the following section presents the optimal solution overview based on recursive WLS approach.

IV.2.b.i Optimal solution of the Thévenin's impedance based on Recursive Weighted Least Squares (RLS) estimation

A powerful technique to solve an overdetermined system of linear equations is based on the least squares estimation (LES). Recalling the mathematical formulation presented in III.5.a, the first Thévenin's impedance estimate is computed by

$$\hat{s} = (H^T W^{-1} H)^{-1} H^T W^{-1} v \quad (\text{IV.29})$$

where W is the covariance matrix of the error vector.

When measurements are obtained sequentially and we want to update the envisaged estimate with each new measurement, it is required to increase the H matrix and completely recompute the estimate \hat{s} using Eq. (IV.29). However, for large amount of measurements, the computational effort could become prohibitive.

For overcoming this problem, a recursive least square estimation (RLS) must be performed. In [86], it can be found the background concerning optimal estimation. For a comprehensive understanding it will be present in this section only the key points which are of direct interest for the Thévenin's impedance estimation.

Let us consider a linear recursive estimator written in the form

$$\begin{aligned} v_k &= H_k s + \varepsilon_k \\ \hat{s}_k &= \hat{s}_{k-1} + K_k (v_k - H_k \hat{s}_{k-1}). \end{aligned} \quad (\text{IV.30})$$

It is clear that \hat{s}_k can be computed on the basis of the previous estimate \hat{s}_{k-1} and the new measurement v_k . K_k is called the estimator gain matrix and it must be determined. The quantity inside the brackets is called the correction term. Looking closely at Eq. (IV.30), one can note that the current estimate will be equal to the previous estimate when the correction term is zero, or if the gain matrix is zero. The RLS employs the optimality criterion for minimizing the sum of the variances of the estimation errors, thus the following objective function is generally used

$$J_k = E [(s_1 - \hat{s}_1)^2] + \dots + E [(s_n - \hat{s}_n)^2]. \quad (\text{IV.31})$$

For determining K_k the objective function given by Eq. (IV.31) must be minimized. Thereby, taking the derivative of this function and set it equal to zero the K_k matrix can be determined, hence

$$K_k = P_{k-1} H_k^T (H_k P_{k-1} H_k^T + W_k)^{-1}. \quad (\text{IV.32})$$

One can note that the square matrix P_k arises from the formulation of Eq. (IV.32). It is called estimation-error covariance matrix. It is required to compute P_k recursively according to

$$P_k = (I - K_k H_k) P_{k-1} (I - K_k H_k)^T + K_k W_k K_k^T \quad (\text{IV.33})$$

therefore, Eq. (IV.33) represents the recursive formula for the covariance of the least squares estimation error.

Eqs. (IV.30), (IV.32), and (IV.33) represent the recursive weighted least squares estimator. Now, for each new pair of synchronized measurements these equations are performed in order to estimate recursively the Thévenin's impedance during a short time interval.

IV.2.c Main objective: Online tracking of the grid model based on the Thévenin’s equivalent and enhanced operating point assessment on generation capability curves

The main goal of an aggregated distributed resource is to send the necessary power to the electric grid in order to contribute to supply regular demand. However, distributed resources based on synchronous generators can also absorb power from the grid. In essence, they can only absorb a small amount of reactive power (kVAr) because they are physically unable to absorb more than a predefined power setpoint (it depends on each type of generator). When the absorbed power surpasses this setpoint the generator could be lead to misoperation.

Aiming to assess the grid model based on the Thévenin’s equivalent as well as the operating point of aggregated generators into a capability curve, let us assume a bidirectional reactive power exchange between the DER side and the grid side, as shown in Fig. IV.5. The integration of battery energy storage systems (BESSs) has been considered in order to ensure fluctuations reduction on the power generation provoked by the dynamic and intermittent nature of the wind. In other words, the power flow could not have noticeable variations during a reasonable time interval due to the BESS support. For this scenario, a steady state condition (or *quasi-steady state*) may be assumed.

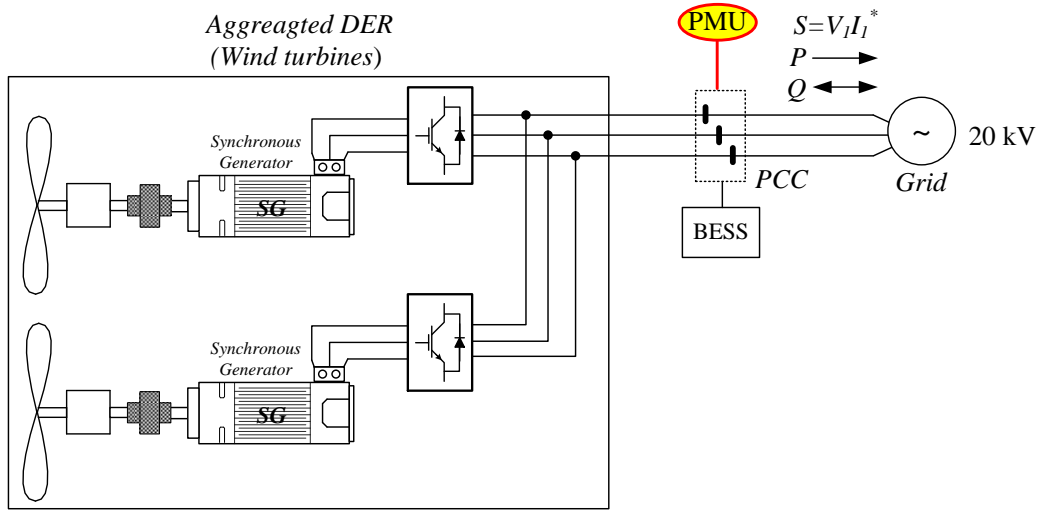


Figure IV.5: Integration of a high-rate aggregated DER with the distribution grid. Note the bidirectional reactive power flow between the DER- and the grid side.

For the first scenario, an aggregated DER with a rated capacity of 1 MVA is connected to a 20 kV primary distribution network (these values have been used as reference base). Assuming that a given instant in time the local frequency recorded at *PCC* is equal to 49.995 Hz and three-phase voltage and current signals (*in pu*) have a slight unbalance in both amplitude and phase angle, as depicted in Table IV.1

Performing the frequency-adaptive Park’s transformation algorithm, a frequency error close to 0.1 mHz has been observed. The complex power estimated is computed from the product between the positive-sequence voltage and current phasors. The three-phase input

Table IV.1: Three-phase voltage and current input signals (1° scenario)

	<i>a</i> -phase		<i>b</i> -phase		<i>c</i> -phase		Freq. (Hz)
	Amplitude (<i>pu</i>)	Angle (deg.)	Amplitude (<i>pu</i>)	Angle (deg.)	Amplitude (<i>pu</i>)	Angle (deg.)	
Voltage	1.4099	150.945	1.4160	30.362	1.4176	-89.106	49.995
Current	1.1343	147.945	1.1204	28.549	1.1448	-93.645	

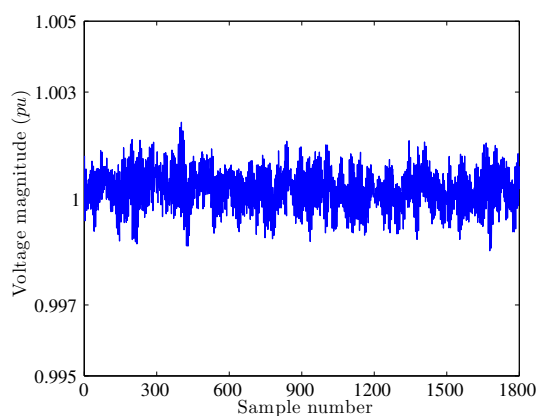


Figure IV.6: Positive-sequence voltage phasor magnitude estimates. Note the very narrow range of variation.

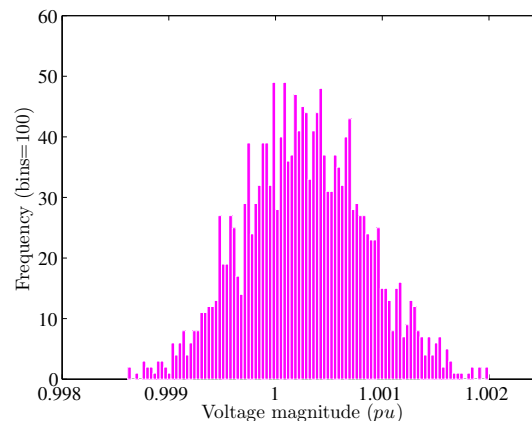


Figure IV.7: Frequency distribution of the positive-sequence voltage phasor magnitude estimates.

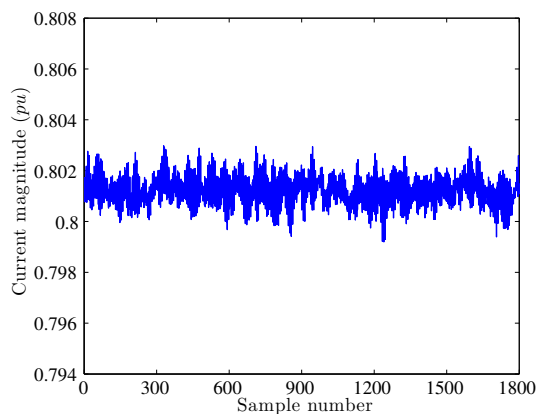


Figure IV.8: Positive-sequence current magnitude estimates. Once again the estimates are within a narrow range.

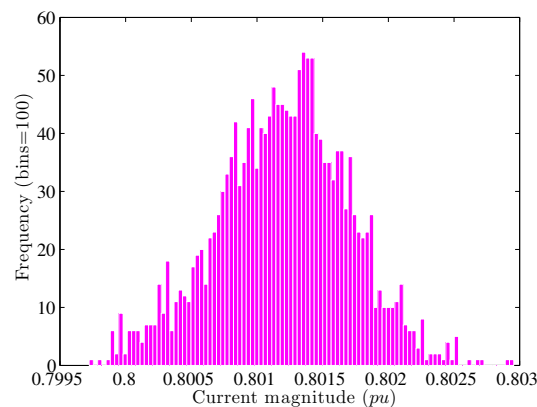


Figure IV.9: Frequency distribution of the positive-sequence current phasor magnitude estimates.

signals are sampled at a rate of 1800 Hz (36 samples obtained over one period of the 50-Hz signal). For all simulations a SNR=60 dB has been used.

Assuming a *quasi*-steady state condition with time interval of 1 second, that is, the grid side does not have noticeable variation during the analysis, one can observe in Figs. IV.6 and IV.8 the magnitude estimates of the voltage and current phasors taken at *PCC*. Figs. IV.7 and IV.9 illustrate the frequency distribution of the magnitude estimates.

One can note that the results have a high frequency of occurrence around the true magnitude value of 1.0002 for the voltage and 0.8015 regarding the current. Figs. IV.10

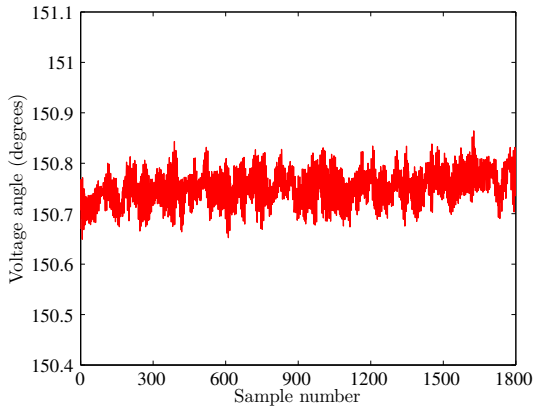


Figure IV.10: Positive-sequence voltage phasor phase angle estimates. Note the *quasi*-steady state condition.

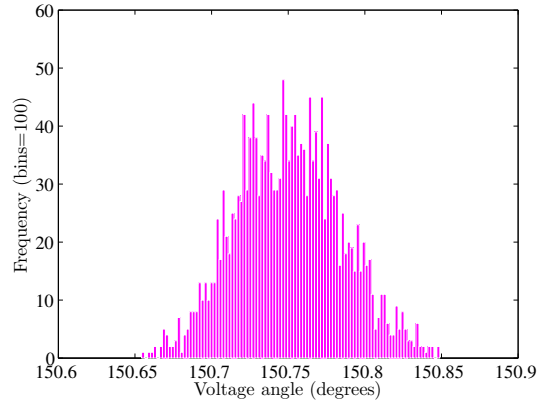


Figure IV.11: Frequency distribution of the positive-sequence voltage phasor phase angle estimates.

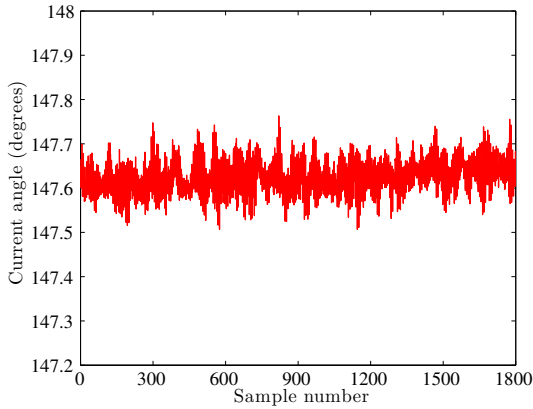


Figure IV.12: Positive-sequence current phasor phase angle estimates.

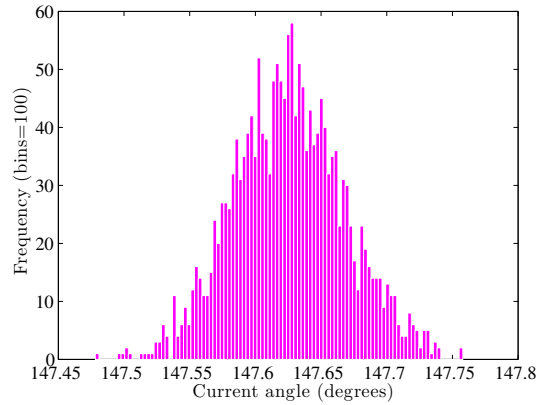


Figure IV.13: Frequency distribution of the current phasor phase angle estimates.

and IV.12 depict the phase angle estimates concerning the voltage and current phasors. Figs. IV.13 and IV.11 show a high frequency of occurrence around the true values of 150.73° and 147.64° concerning the voltage and current phasors, respectively.

Taking into account the positive-sequence voltage and current phasor estimates, the computation of the complex power has been performed. Fig. IV.14 illustrates the active *vs* reactive power estimates. It can be seen that the results are scattered within a small cluster. Positive values of active and reactive power indicate a lagging power factor, that is, the power flow is sent from the DER side to the grid side. For this scenario, the reported value of power factor is close to 0.998.

Fig. IV.15 depicts the resulting Thévenin's impedance of the grid side. The recursive WLS provides resistance and reactance estimates close to $2.337 pu$ and $0.683 pu$, respectively. One can notice that constant values have been achieved corroborating with the assumption of invariant grid side during the analysis interval. In addition, one can also state that the Thévenin's impedance components have not noticeable variation due to the high accuracy system frequency estimation yielding *quasi*-steady state positive-sequence phasors.

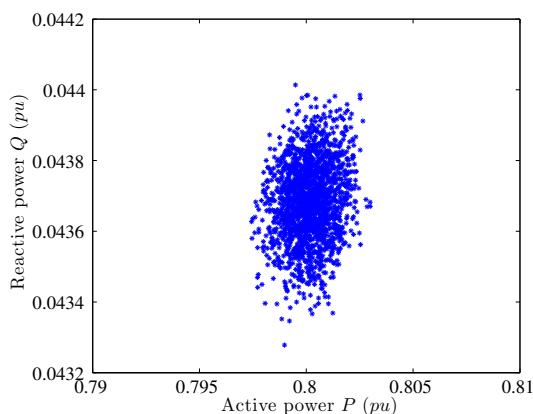


Figure IV.14: Active *vs* reactive power estimates scattered within a narrow cluster.

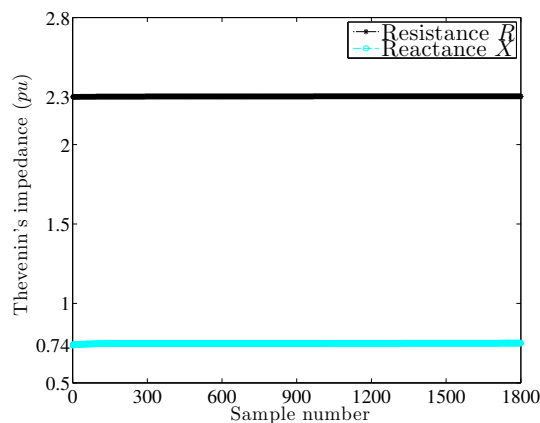


Figure IV.15: Resulting Thévenin's impedance of the grid side.

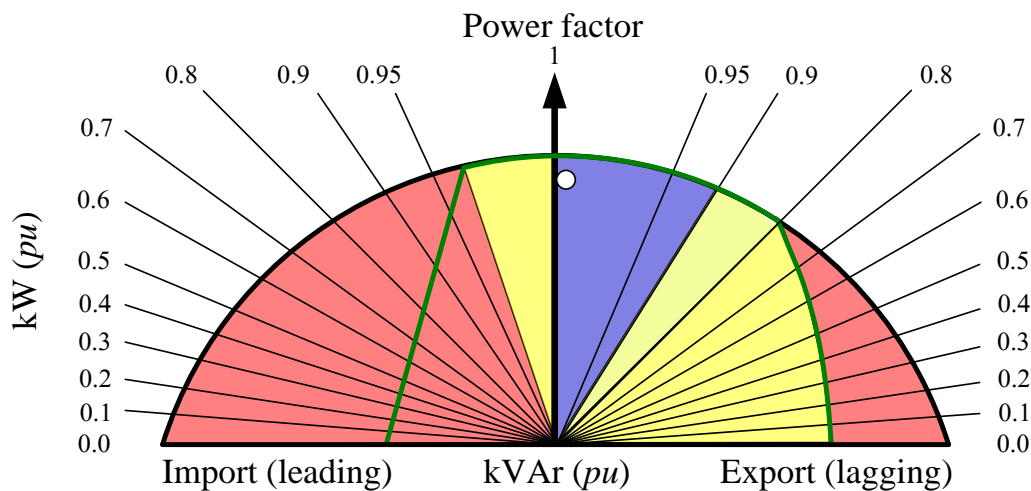


Figure IV.16: Classical capability curve of synchronous generators. Note that the white circle representing the power factor of the first analyzed scenario falls into the normal operating area.

Let a classical composite capability diagram of aggregated synchronous generators be given by the curve depicted in Fig. IV.16. It is possible to see that the power factor (white circle) of the analyzed scenario falls into the blue area. This area provides a steady state operating condition. The yellow area represents a near-normal operating point, however it is strongly advised to take control actions to bring the power factor to the blue region. Red area can provoke synchronous generator based DER misoperation. Looking closely at the aforementioned figure, one can notice that the aggregated DER sends power to the grid and it is operating in a normal condition. Fig. IV.17 illustrates the Thévenin equivalent of the grid side that fulfills the power flow exchanges between the DER side and the grid side seen from the *PCC*.

In the second scenario, the Thévenin's equivalent of the grid side is evaluated taking into account the inversion of the reactive power flow, that is, from the grid side to the DER

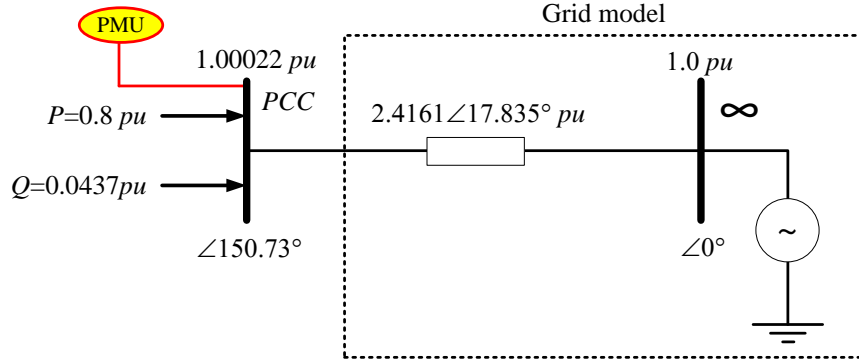


Figure IV.17: Thévenin's equivalent circuit of the grid side (1° scenario: lagging power factor).

side. A special regard must be given to this statement, because, in essence, the DER will be seen as a load that consumes reactive power. Considering that a given instant in time the local frequency recorded at *PCC* is equal to 50.05 Hz and once again the three-phase voltage and current input signals (*in pu*) have a slight unbalance in both amplitude and phase angle, as depicted in Table IV.2

Table IV.2: Three-phase voltage and current input signals (2° scenario)

	<i>a</i> -phase		<i>b</i> -phase		<i>c</i> -phase		Freq. (Hz)
	Amplitude (<i>pu</i>)	Angle (deg.)	Amplitude (<i>pu</i>)	Angle (deg.)	Amplitude (<i>pu</i>)	Angle (deg.)	
Voltage	1.3876	-25.443	1.3843	-145.548	1.4021	94.668	50.05
Current	1.1234	-20.567	1.1204	-140.222	1.1448	99.587	

For this scenario, a frequency estimation error around 0.15 mHz has been obtained. The reported positive-sequence voltage and current phasor are close to $0.9838/-25.44^\circ pu$ and $0.7986/-20.40^\circ pu$. Computing the complex power over the analysis interval, Fig. IV.18 depicts the reactive *vs* active power estimates. Once again the results are scattered into a small cluster. One can note that the reactive power is negative, that is, the DER side absorbs power from the grid because a leading power factor close to 0.996 has been achieved.

An interesting analysis may be accomplished for understanding this phenomenon. The effect of the reactive power flow inversion will impose variations on the grid side model. Once the Thévenin's voltage is assumed to be equal to the infinite busbar voltage whose value is invariant during the observation interval, a capacitive effect will appear on the Thévenin's impedance, as depicted in Fig. IV.19. It can be seen that the reactance has a negative value, furthermore it has a much larger contribution on the Thévenin impedance computation whose reported value is close to $0.547/-84.44^\circ pu$.

Fig. IV.20 illustrates the operating point of the aggregated DER concerning the scenario analyzed. One can observe that the power factor falls into the yellow area of the left side. In other words, the DER absorbs power near-normal operating point, however, actions must be taken in order to lead the power factor to the right side of the capability

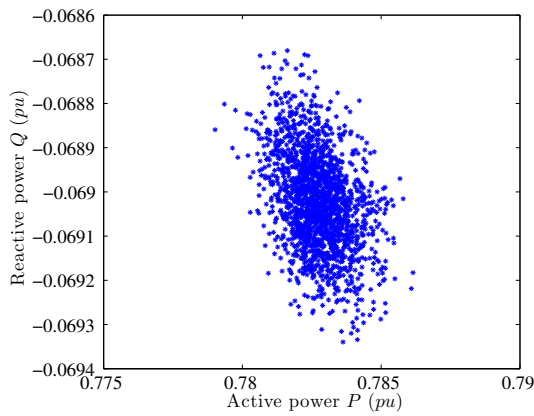


Figure IV.18: Active *vs* reactive power estimates scattered within a narrow cluster. Note the negative value of the reactive power

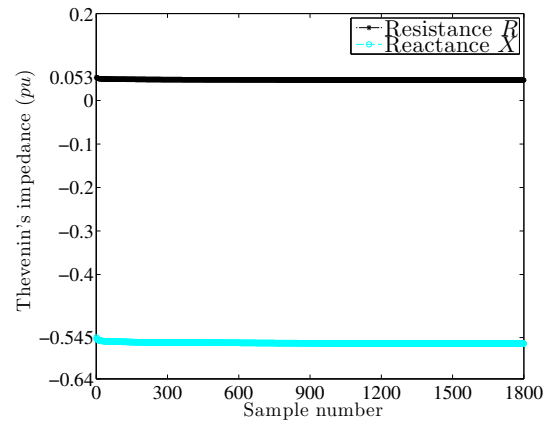


Figure IV.19: Resulting Thévenin's impedance of the grid side. Negative reactance value provides a fictitious capacitive effect on the grid model's impedance.

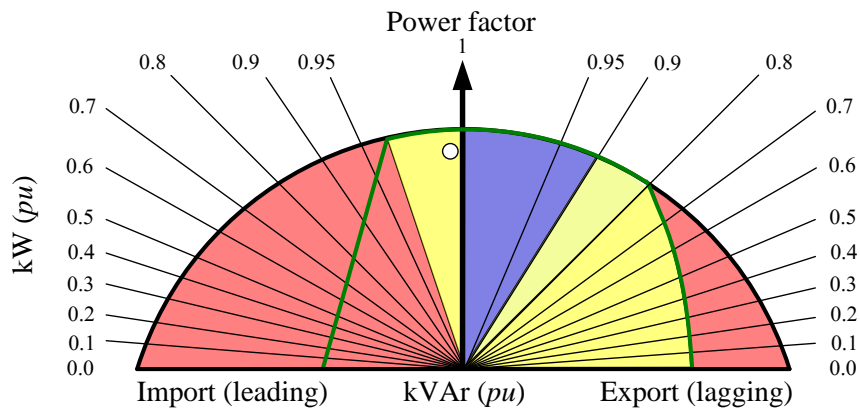


Figure IV.20: Relative position of the power factor (white circle) into the capability curve.

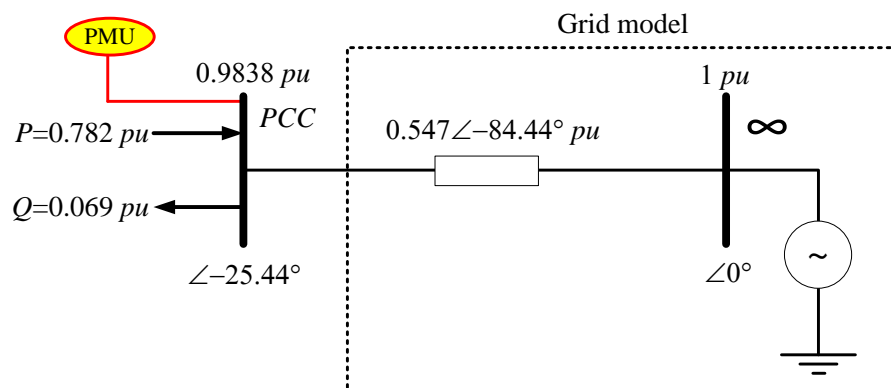


Figure IV.21: Thévenin's equivalent circuit of the grid side (2° scenario: leading power factor).

curve, more precisely, into the blue area. Fig. IV.21 shows the equivalent grid model that fulfills the power flow exchanges between the DER- and grid side.

Now, let us evaluate the impact of the frequency deviation on the Thévenin's impedance estimates. The previous scenarios presented on this section take into account accurate local frequency measurement in order to provide phasor measurements with high degree of accuracy. However, when the frequency tracking process does not have a satisfactory performance the computation of the Thévenin's impedance will be completely jeopardized. In I.9, it has been presented the pernicious effect of the frequency deviation over the synchronized phasor measurements, in this way, variations over time on the Thévenin's impedance estimates are also expected.

For simulation purposes, let us consider the second scenario. Assuming that the three-phase input signals are sampled at a sampling rate of 1800 Hz locked to the fundamental frequency. However, a true local system frequency at 50.3 Hz has been applied. If no action is taken to track the system frequency the impedance estimates will not have valuable informations. In Figs. IV.22-IV.23, one can see clearly that both the magnitude and phase angle vary in time. In this way, the assumption of invariant grid side during the analysis interval is not fulfilled. The estimates start from the true values, however they quickly change according to the frequency deviation.

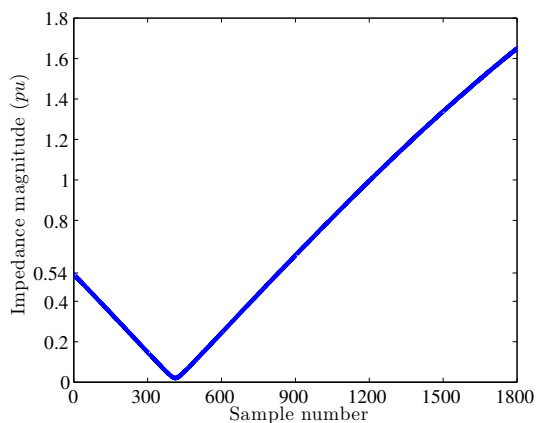


Figure IV.22: Impedance magnitude variation caused by the frequency deviation.

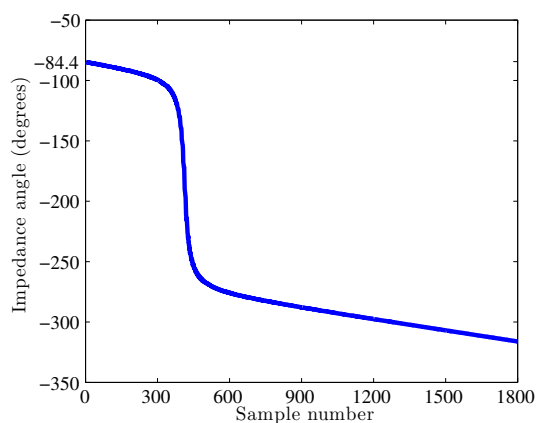


Figure IV.23: Impedance phase angle variation caused by the frequency deviation.

IV.3 Practical online external equivalents in radial active distribution grids using PMU data

In several studies concerning the expansion planning and operation of the electrical power systems, the external equivalents have been employed for reducing the dimensions of the analysis aiming mainly to improve the computational efficiency. Many control and monitoring functions require external equivalents due to the lack of updated and complete system informations. Generally, a grid control center receives updated data only of the grid's observable zones and outside them monitoring capabilities may not be found [94].

According to [94], for a comprehensive understanding of the external equivalent theory three networks must be evaluated, as illustrated in Fig. IV.24. The internal network

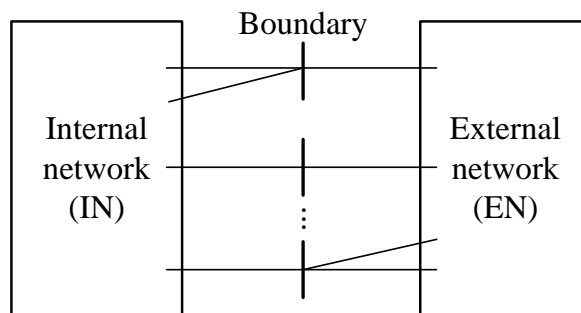


Figure IV.24: Representation of the internal network, boundaries, and external network (adapted of [94]).

(IN) combined with the boundaries represent the area of interest. For practical real-time monitoring applications, the area of interest can be considered as the observable zone.

The goal of the external equivalent is to simulate the reactions of the external network (EN) when variations are provoked in the IN. It is of paramount importance to mention that for several internal variations the external reactions may be not noticeable, however, when the variations take place in the vicinity of the boundaries, the reactions on the EN could be meaningful.

The trivial solution that has been employed concerning external equivalents is disregard and replace the EN by additional power injections in the boundaries busbars. The *constant* power injections are equal to the power flow among the boundaries busbars and the external network. However, this type of equivalent is not advised due to the fact that the power injection is constant, that is, even if a variation occurs in the vicinity of the boundary the equivalent will not react.

In other words, for variations into the area of interest that change the power flow between the boundary and the external network, when the EN is replaced by a constant power injection the model imposes that the power exchanging between the boundary and the EN is constant, which does not always correspond to the reality.

External equivalents have been sufficiently studied in the scope of generation and transmission systems [95], however its application for distribution grids needs to be stepped up. The main problematic is related to the large number of sections and branches of the primary feeders that may yield topologies having thousands of busbars. In [90], it is possible to find a work that describes properly a method for evaluating external equivalents in electric distribution networks.

The proposed method has been developed based on the principle of the mesh of the REI equivalent. However, modifications have been performed in the REI mesh to allow its applicability in the distribution network [94]. The method has been applied to reconfiguration problem and the results show significant reduction regarding the computational burden. The method has been modeled taking into account classical measurements (non-synchronized) and multiple power flows.

PMUs may change the manner for evaluating external equivalents in active distribution grid. Synchronized voltage and current phasors taken at the boundary busbars may provide the necessary sensitivity to detect variations in the IN that change the operating status of

the EN. In addition, synchronized phasors simplify the equivalent model providing a linear representation. In this way, according to the envisaged application, the external equivalent may be modeled as a variable impedance that changes its values regarding the operating point of the system or it may be modeled as a variable power injection in the boundary busbars.

One can note that the power injections are not constant because the PMU will track the internal network variations seen from the boundaries. In essence, for each boundary busbar a simplified Norton equivalent is obtained. In the following section the Ward linear equivalent is introduced in which it will be the basis for a comprehensive understanding of the equivalent provided by PMU measurements.

IV.3.a Ward linear equivalent overview

This section has been written based on the theory presented in the references [94] and [96]. The Ward linear equivalent can be interpreted as the generalized Norton theorem. For this model the generators/loads can be represented by constant current, constant admittance, or both. The currents appear in vector \underline{I} and the admittances are allocated in the main diagonal of the matrix Y . For exemplification, let us consider the linear system give by

$$\bar{Y} \times \underline{E} = \underline{I} \quad (\text{IV.34})$$

where Y is the nodal admittance matrix; \underline{E} is the voltage phasor vector of the busbars; and \underline{I} represents the current phasor vector of nodal injections.

Looking closely at Fig. IV.24, Eq. (IV.34) can be put according to the following linear system

$$\begin{bmatrix} Y_{EE} & Y_{EB} & 0 \\ Y_{BE} & Y_{BB} & Y_{BI} \\ 0 & Y_{IB} & Y_{II} \end{bmatrix} \times \begin{bmatrix} \underline{E}_E \\ \underline{E}_B \\ \underline{E}_I \end{bmatrix} = \begin{bmatrix} \underline{I}_E \\ \underline{I}_B \\ \underline{I}_I \end{bmatrix} \quad (\text{IV.35})$$

being Y_{EE} all admittances connected among the EN busbars; Y_{EB} is formed by the admittances that connect the EN and the boundary busbars (equal to and Y_{BE}); Y_{BB} is formed by all admittances connected to the boundary busbars; Y_{BI} represents all admittances connected among the IN and the boundary busbars (equal to and Y_{IB}); and Y_{II} covers all admittances connected among the IN busbars.

Arranging \underline{E}_E in the first equation of (IV.35) yields

$$\underline{E}_E = Y_{EE}^{-1}(\underline{I}_E - Y_{EB}\underline{E}_B). \quad (\text{IV.36})$$

Replacing Eq. (IV.36) into the second equation of (IV.35) provides the reduced linear system given by

$$\begin{bmatrix} Y_{BB}^{eq} & Y_{BI} \\ Y_{IB} & Y_{II} \end{bmatrix} = \begin{bmatrix} \underline{E}_B \\ \underline{E}_I \end{bmatrix} \times \begin{bmatrix} \underline{I}_B^{eq} \\ \underline{I}_I \end{bmatrix} \quad (\text{IV.37})$$

hence,

$$Y_{BB}^{eq} = Y_{BB} - Y_{BE}Y_{EE}^{-1}Y_{BE} \quad (IV.38)$$

$$\underline{I}_B^{eq} = \underline{I}_B - Y_{BE}Y_{EE}^{-1}\underline{I}_E \quad (IV.39)$$

one can note that the reduced system given by Eq. (IV.37) involves only the state variables regarding the area of interest (\underline{E}_B and \underline{E}_I). In the same way that the linear system (IV.35) is associated with the Fig. IV.24, the reduced system (IV.37) can be associated with the Fig. IV.25.

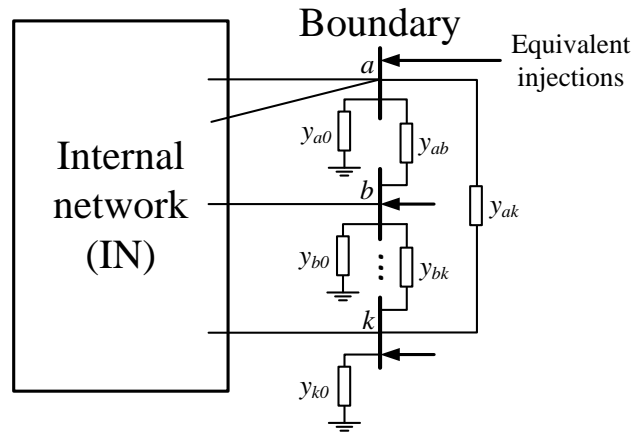


Figure IV.25: Reduction of the external network.

One can note that the matrix Y_{BB}^{eq} contains the admittances connected among the boundary busbars as well as the *shunt* admittances. Y_{BB} corresponds to the existent elements of the original network and the matrix $-Y_{BE}Y_{EE}^{-1}Y_{BE}$ appears due to the reduction process. The vector \underline{I}_B^{eq} contains the equivalent current injections formed by two components: the vector \underline{I}_B formed by the injections previously existent and the vector formed by the distribution of the currents into the boundary busbars caused by the external injections ($-Y_{BE}Y_{EE}^{-1}\underline{I}_E$).

It is clear that the external network can be replaced by a set of admittances (series and *shunts*) connected to the boundary busbars and by a set of current injections at these busbars. In essence, the Ward linear equivalent may be interpreted as the generalized Norton's equivalent.

IV.3.b Practical on-line external equivalent based on PMU data

The first step of the external equivalent based on PMU measurements for active distribution systems consists in determine the zones of the grid concerning the IN, boundaries, and EN. This step is primordial because the PMUs must be placed at the boundary busbars, as illustrated in Fig. IV.26. For accomplishing this task, it has been considered that the area of interest involves the main feeder. The lateral *taps* (or other feeder's sections) may be represented as the EN.

Fig. IV.27 shows the three subdivisions for a radial distribution feeder. In this figure,

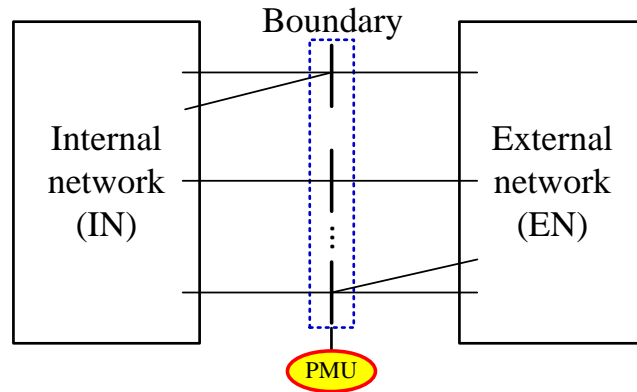


Figure IV.26: PMU placement at the boundary busbars.

one can see that the area of interest involves the main feeder (blue line) and the boundary (green circle). For identifying the components of the internal network an upstream search of the network data must be performed. One can note that the boundary represents the connection point between the main feeder and the external area. Once the boundary identification is accomplished, the EN represents the components upstream from the boundary busbars (red lines).

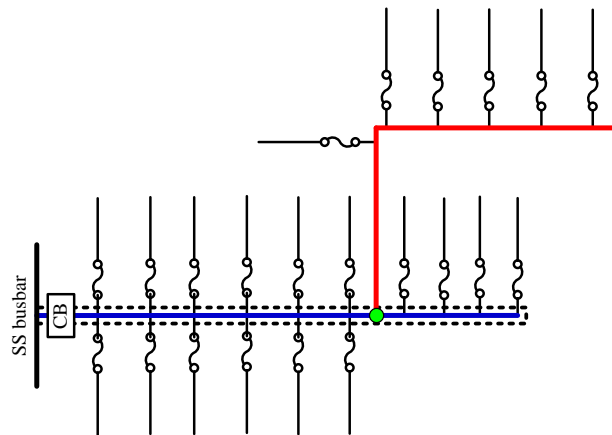


Figure IV.27: Subdivision of the grid into three areas. Internal network (blue line), boundary (green circle), and external network (red line).

As already mentioned, a PMU has the capability to compute the overall information of the busbar in which it has been placed (voltage phasor, input and output current phasors, power factor, frequency, and complex power measurement). In this way, the first manner for evaluating the EN, seen from the boundary, is to take into account the local voltage phasor and the current phasor that flows from the boundary to the EN. For this case, the EN can be interpreted as an impedance that may vary its value according to the operating point of the overall distribution system.

In this way, the variable impedance seen from the boundary busbar can be computed according to

$$\bar{Z}_{EN} = \frac{|E_k|}{S_{EN}^*} \quad (IV.40)$$

being $|E_k|$ the phasor magnitude at the boundary busbar and \bar{S}_{EN} is the complex power that flows from the boundary to the EN.

If more boundary busbars are considered, Eq. (IV.40) must be computed for each of them. In this way, the EN is modeled as a variable impedance that change its value due to the sensitivity of the PMU measurements regarding the variations into the IN. From the original network shown in Fig. IV.27, the equivalent network is displayed in Fig. IV.28.

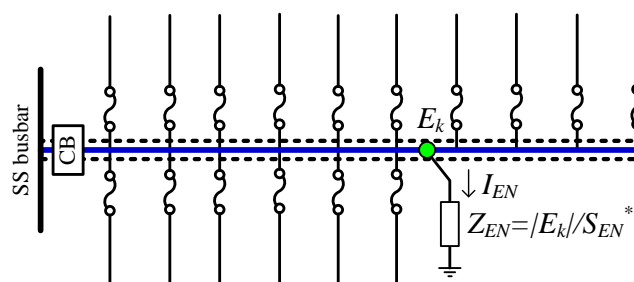


Figure IV.28: Equivalent network.

This type of equivalent may be applied for studies concerning, for example, reactive compensation using capacitor banks or allocation assessment of DERs into the internal network. The aforementioned studies for active distribution grids must be carefully evaluated in order to ensure voltage level within specified operational limits. Therefore, a PMU placed at the boundary busbar may provide an evaluation of the external network when variations are introduced in the IN.

Another type of equivalent that may be employed is based on the Ward linear model. It is of paramount importance to mention that the direct application of the theory presented IV.3.a could have a poor performance due to the radiality of the network. As it has been shown in II.2.a, *loops* in electric distribution grids have been often applied for increasing the reliability of critical areas, however radial design is already the main topology. Taking into account Eq. (IV.38) and looking closely at Fig. IV.25, one can see that the admittances among the boundary busbars appear due to the reduction process.

For this reason, it must be avoided the application of techniques based on the network matrices for solving problems in distribution grids because a high dimension matricial formulation can be achieved whose consequence is a high computational burden. Thereby, the external equivalent to be used is based on the simplified Norton's theorem applied at each boundary busbar, as illustrated in Fig. IV.29. One can see that for each predefined boundary busbar in which a PMU is placed the EN can be replaced by a variable power injection. This type of equivalent may be applied for studies related to enhanced power flow in which the power balance must be properly fulfilled.

The two practical methods for evaluating the external equivalent in active distribution systems (variable impedance and power injection) take into consideration the synchronized measurements associated with the EN recorded at the boundary busbar. The EN is replaced

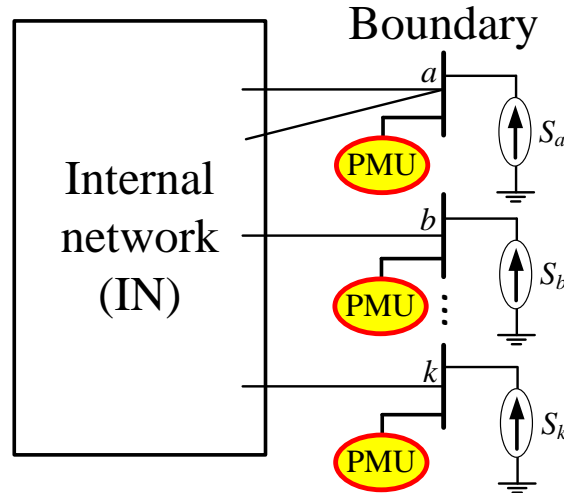


Figure IV.29: Equivalent network based on the simplified Norton's theorem.

by these measurements, that is, one can imagine that it is disconnected of the area of interest. This is particularly envisaged because even if there are topological errors in the EN they will not compromise the performance of the equivalent based on synchronized measurements. It is to be noted that the performance of classical methods is reduced due to these errors.

IV.3.c Main objective: Reduction of the grid size and online evaluation of the external network

The proposed technique for determining online external equivalent of zones of the electric distribution grid has been tested in a radial feeder with eighteen busbars, as illustrated in the one line diagram of Fig. IV.30. The following characteristics of the substation (SS) have been considered: operating voltage of 20 kV, transformer size of 4 MVA and power factor of 0.92 lagging. In Appendix E, one can find the full details of the feeder's data.

Considering the base case, that is, the original grid depicted in Fig. IV.30, the results obtained using a load flow solution (Power System Analysis Toolbox - PSAT [97]) are shown in Figs. IV.31-IV.32. The power flow solution has been used as the source of PMU measurements. Clearly, one can observe a voltage magnitude drop along the feeder and a maximum angular aperture of 1.2454° between the slack-bus (substation busbar) and the busbar 18. As it has been commented in II.2.b, when 1% TVE is considered for any phasor measurement taken at this grid, the actual grid operating status could not be valid. Due to this fact, the modeling of the external network is severely jeopardized regarding this error margin.

It has been shown that the accuracy of the phasor estimates provided by the frequency-adaptive Park's transformation-based algorithm may be close to 0.1% TVE, thus, let us consider this error margin in order to evaluate its impact on the external equivalent computation. Assuming that the IN comprises the busbars {1, 2, 3, 4, 5, 6, 7, 8} and the other busbars are into the EN. According to IV.3.b, the busbar 5 will be the boundary. In this

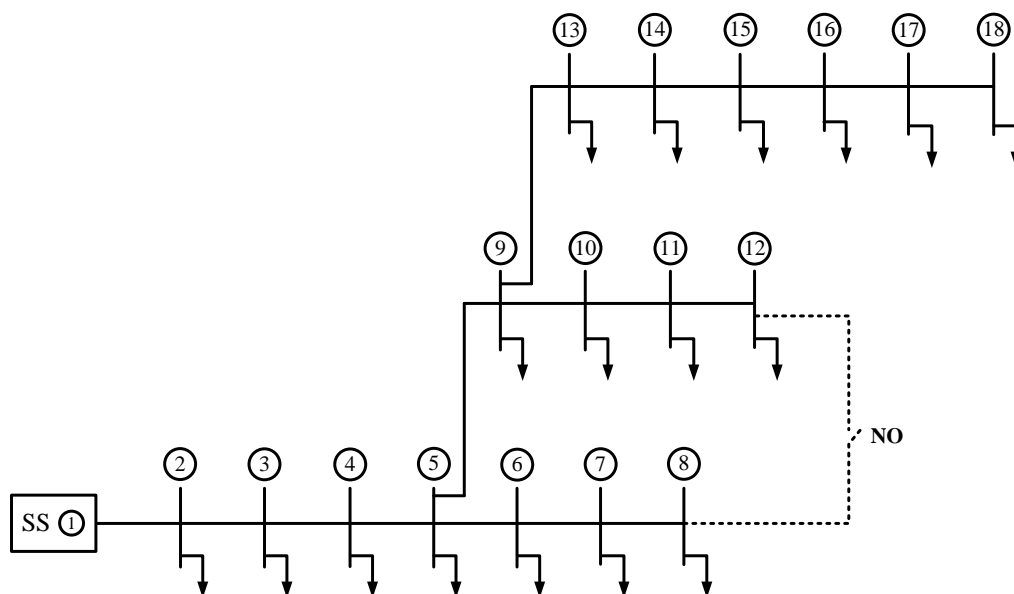


Figure IV.30: Feeder model with 18 busbars (Appendix E).

manner, it is required to place an accurate PMU at this busbar. Fig. IV.33 illustrates the equivalent network, in which the grid size is reduced from 18 to 8 busbars. The proposed technique has reduced the original network by a factor of two approximately.

Considering 0.1% TVE over the phase angle measurements taken at the busbar 5, one can see in Figs. IV.34-IV.35 the comparison between the original and reduced network from the base case. Values of voltage magnitude and phase of the each IN busbar have been considered for evaluation purposes. It can be noted that the results obtained for the reduced network are close to the values reported for the original network. This error margin provides a variable impedance (\bar{Z}_{EN}) equal to $0.8940/18.693^\circ pu$.

In this way, accurate PMUs providing measurements with a very small TVE value may properly evaluate the external equivalent of electric distribution grids. It is important to

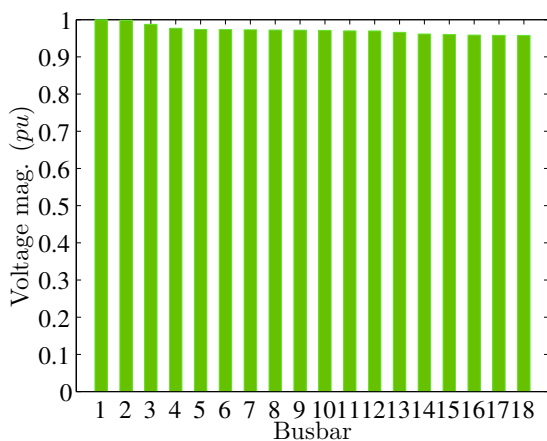


Figure IV.31: Voltage magnitude profile (base case).

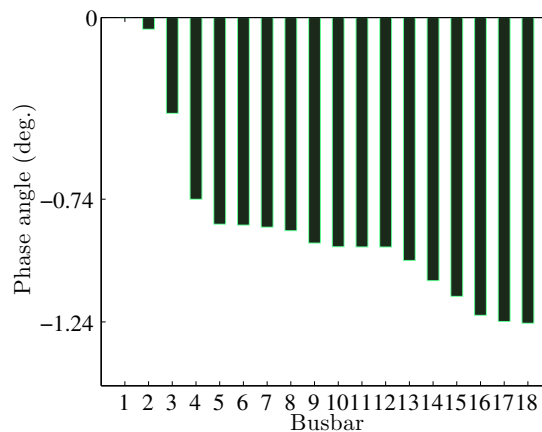


Figure IV.32: Voltage phase profile (base case).

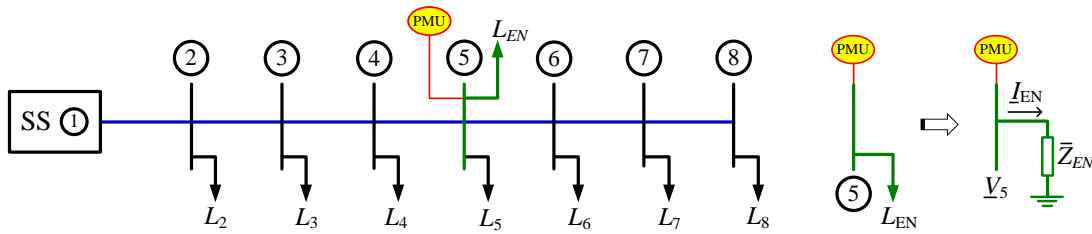


Figure IV.33: Equivalent network.

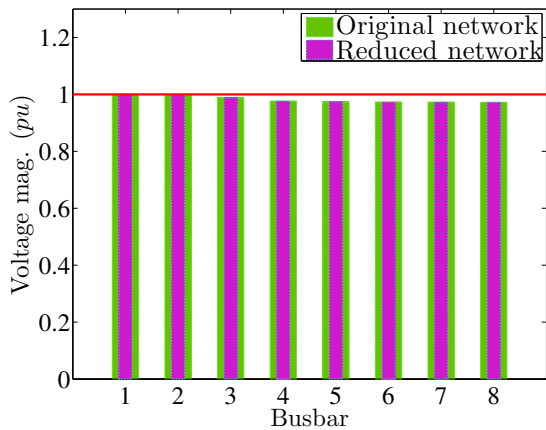


Figure IV.34: Voltage magnitude profile of the IN busbars.

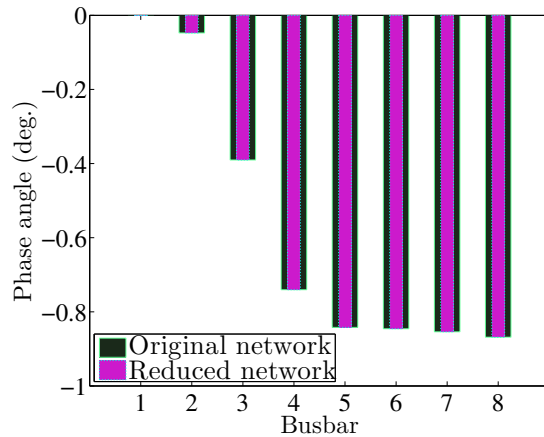


Figure IV.35: Voltage phase profile of the IN busbars.

mention that for evaluating the external equivalent, it is only required the positive-sequence voltage phasor measurement at the boundary busbar and the current phasor measurement that flows toward the EN.

For the next scenario, let us assume the integration of a DER (photovoltaic site) at the busbar 4 with an installed capacity of 1 MVA and a power factor of 0.98 lagging. The goal is to evaluate the external equivalent taking into account variations at the vicinity of the boundary from the base case. The power injection into the grid arising from the DER tends to reduce the power delivered by the substation, due to this fact the net generation is given by the difference over time between the power supplied for both substation and DER.

This new generation setpoint changes the overall characteristics of the power flow into the grid. Fig. IV.36-IV.37 illustrate the voltage magnitude and phase profiles after the integration of the DER. One can note a slight improvement on the voltage magnitude level and a smaller angular aperture between the busbars.

Considering 0.1% TVE over the phase angle measurements taken at the boundary busbar 5, it can be seen in Figs. IV.38-IV.39 that the results for the reduced network are very close to the reported values regarding the original network. It is important to mention that the integration of the DER imposes a new distribution of the power flows, therefore, the variable impedance related to the EN for this new operation status has been changed to $0.8852/18.688^\circ pu$.

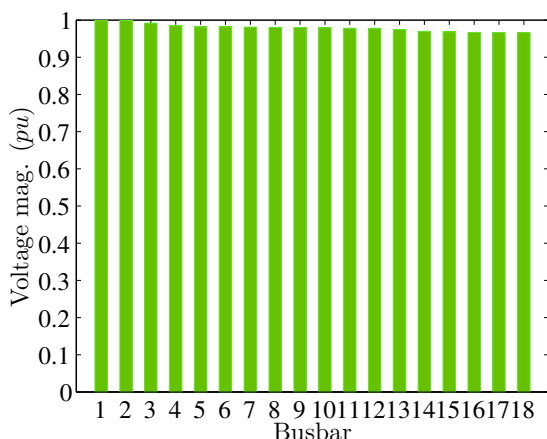


Figure IV.36: Voltage magnitude profile after the integration of the DER.

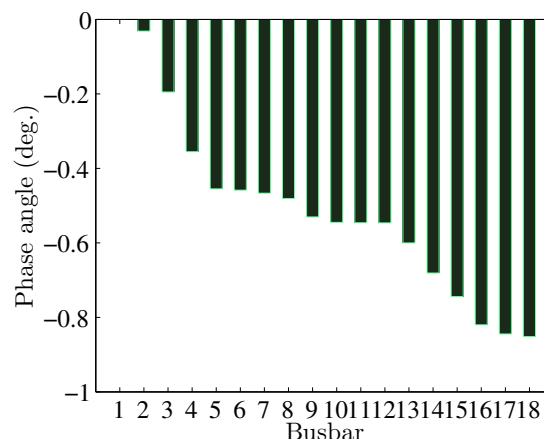


Figure IV.37: Voltage phase profile after the integration of the DER.

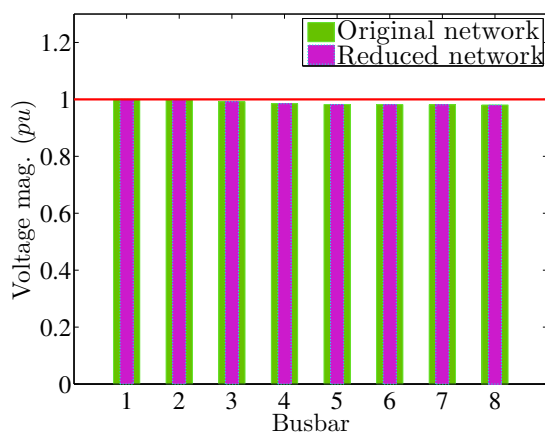


Figure IV.38: Voltage magnitude profile of the IN busbars considering the integration of the DER.

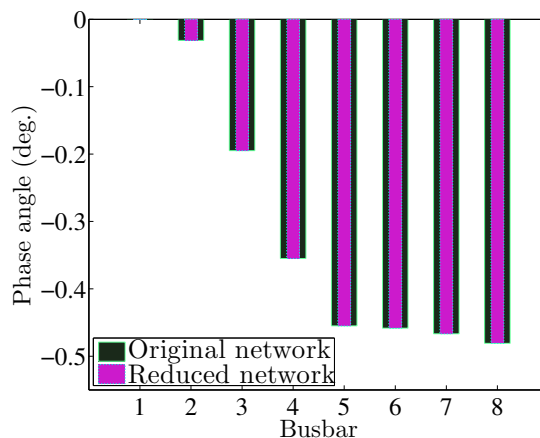


Figure IV.39: Voltage phase profile of the IN busbars considering the integration of the DER.

IV.4 Assessment of three-phase voltage drop in primary radial distribution grids using PMU data

On distribution circuits, voltage drops are caused by current flowing through the line impedances. The impact of voltage drop is more apparent over the customers located at the end of the feeder, in which the voltage level may be lower than the limits imposed by the standards (for example, ANSI C84.1-1995 [98]). One of the main responsibilities of the electric distribution utilities is to deliver voltage to customers within a suitable range, thereby voltage regulation is often required to enhance the primary voltage level along the feeders. Voltage regulators placed in the substation or on the feeders are employed to enhance the voltage limits. Several methods to control primary voltage have been used by distribution utilities such as [64]:

- Substation power transformers endowed with on-load tap-changing (OLTCs)
- Substation feeder or bus voltage regulators.

- Line voltage regulators.
- Fixed and switched capacitor banks.

Until nowadays, classical voltage drop calculation is performed taking into account the feeder's segmentation, that is, the feeder is divided into a given number of segments. For simplification, the segments have the same wire size and the loading on a segment is calculated using a given current (presumed to be known) at a predetermined power factor (for example, 0.92 lagging). The computation is performed segment-by-segment and the overall voltage drop of a feeder is given from the summation of all segment voltage drops. Knowing the busbar voltage at the sending end, the voltage profile may be obtained [99].

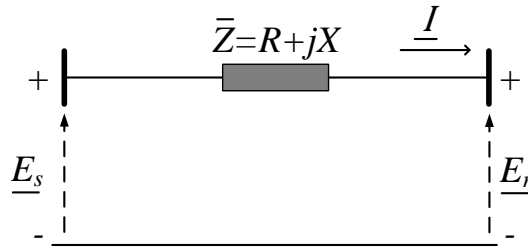


Figure IV.40: Distribution feeder segment model.

A segment of a distribution feeder is depicted in Fig. IV.40. \underline{E}_s and \underline{E}_r represent the phasor at the sending and receiving ends. $\bar{Z} = R + jX$ is the segment's impedance, and \underline{I} is the current phasor flowing through the segment. The linear relationship among the quantities can be obtained as follows

$$\underline{E}_s = \underline{E}_r + \underline{\Delta E} = \underline{E}_r + \bar{Z}\underline{I}. \quad (\text{IV.41})$$

being,

$$\underline{\Delta E} = \bar{Z}\underline{I} = (R + jX)(I_R - jI_X). \quad (\text{IV.42})$$

The phasor diagram for the segment line is depicted in Fig. IV.41. Note that this representation has been modeled using a lagging power factor.

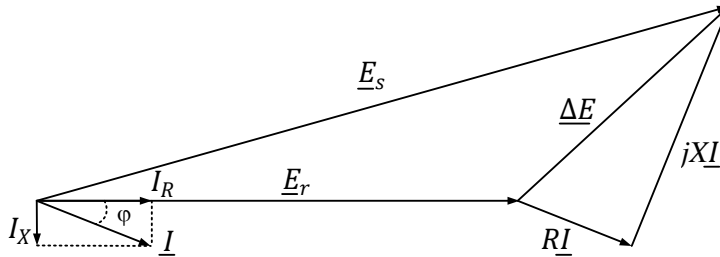


Figure IV.41: Phasor diagram of the feeder segment line.

Replacing Eq. (IV.42) into Eq. (IV.41) and rewritten in rectangular coordinates yields

$$\underline{V}_{drop} = \underline{E}_s - \underline{E}_r = RI_R + XI_X + j(XI_R - RI_X). \quad (IV.43)$$

Eq. (IV.43) represents the exact voltage drop calculation, however its real part is the well-known approximate voltage drop used by several distribution utilities [99]

$$|V_{drop}| = |E_s| - |E_r| \approx RI_R + XI_X. \quad (IV.44)$$

Eq. (IV.44) represent the classical method used for evaluating the voltage drop on a feeder's section. The term $(XI_R - RI_X)$ is often negligible. In [99], it can be found the background concerning the approximate and the exact methods for distribution feeder voltage drop calculation. The error estimate has been properly evaluated and it is shown that, unless the term $(XI_R - RI_X)$ exceeds 10% of the nominal voltage, a very small error of less than 0.5% of nominal voltage is introduced by the approximative method. In this way, this method is normally quite accurate under most conditions.

However, the approximative method may be caught in a trap when heavy currents at a leading power factor occur. This is considered the worst case, however, it is not always taken into consideration because a small probability of occurrence is associated to it. In Section II, we have explained that the integration of the DERs may be considered as one of the main actors on the active power distribution grids and this integration makes this case (heavy current at a leading power factor) somewhat more likely to occurs.

Keeping in mind the quantity $(XI_R - RI_X)$, if I_R and I_X are both negative or positive real values their effects tend to cancel. However, if I_R is negative and I_X is positive (or the reverse), then the quantity $(XI_R - RI_X)$ may have a largest values. Due to this fact, one can note clear evidence that leading power factor will impact on the voltage drop calculation.

When other segments have experienced heavy current at a leading power factor, one can observe that the errors will accumulate and the overall result of the voltage drop may be severely compromised. In this way, accurate methods must be proposed in order to circumvent this problematic. PMUs endowed with accurate frequency-adaptive algorithms may change the manner for evaluating the overall voltage drop in radial distribution feeders aiming to provide results close to the exact calculation.

IV.4.a Overall voltage drop of a radial feeder calculated from PMU data taken at the feeder ends

Let us consider the feeder with k segments depicted in Fig. IV.42

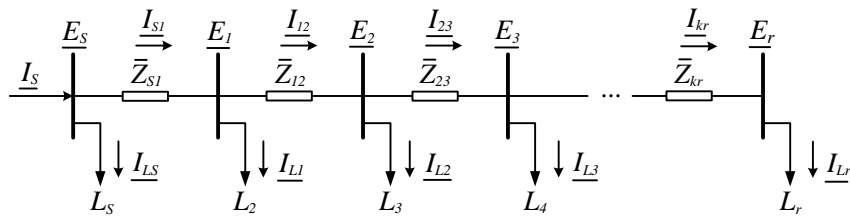


Figure IV.42: Radial distribution network with k segments.

where \underline{E}_s and \underline{I}_s represent the voltage and current phasors at the sending end of the feeder; from \bar{Z}_{s1} to \bar{Z}_{kr} , we have the impedance of the segments; from \underline{I}_{s1} to \underline{I}_{kr} , we have the complex currents flowing through the impedance of the segments; from \underline{I}_{Ls} to \underline{I}_{Lr} , we have the complex currents flowing toward the loads; and \underline{E}_r is the voltage phasor at the feeder end.

Taking into account the nodal analysis, the following relationship concerning the first segment can be obtained

$$\underline{E}_s = \bar{Z}_{s1}\underline{I}_{s1} + \underline{E}_1 \quad (\text{IV.45})$$

in a similar manner, Eq. (IV.46) shows the relationship for the second segment

$$\underline{E}_1 = \bar{Z}_{12}\underline{I}_{12} + \underline{E}_2 \quad (\text{IV.46})$$

looking closely at Eqs. (IV.45)-(IV.46), one can note that the phasor \underline{E}_1 appears in both. Thereby, replacing Eq. (IV.46) into Eq. (IV.45) yields

$$\underline{E}_s = \bar{Z}_{s1}\underline{I}_{s1} + \bar{Z}_{12}\underline{I}_{12} + \underline{E}_2. \quad (\text{IV.47})$$

One can remark that the terms $\bar{Z}_{s1}\underline{I}_{s1}$ and $\bar{Z}_{12}\underline{I}_{12}$ represent the voltage drop (\underline{V}_{drop}) in the respective segments. Performing the same procedure for all segments of the feeder a generalized equation can be obtained according to

$$\underline{E}_s = \bar{Z}_{s1}\underline{I}_{s1} + \bar{Z}_{12}\underline{I}_{12} + \bar{Z}_{23}\underline{I}_{23} + \dots + \bar{Z}_{kr}\underline{I}_{kr} + \underline{E}_r. \quad (\text{IV.48})$$

Clearly, one can see that Eq. (IV.48) provides the overall voltage drop (\underline{V}_{dropT}) on the feeder. Taking into account Eq. (IV.43) related to the exact model of the voltage drop, Eq. (IV.48) can be rewritten in rectangular form according to Eq. (IV.49). It can be noted that the overall voltage drop of a feeder may be obtained simply using accurate voltage phasor measurements at the feeder ends

$$\begin{aligned} \underline{V}_{dropT} &= \underline{E}_s - \underline{E}_r = \left(\sum_{i=1}^k R_i I_{R_i} \right) + \left(\sum_{i=1}^k X_i I_{X_i} \right) + j \left(\left(\sum_{i=1}^k X_i I_{R_i} \right) - \left(\sum_{i=1}^k R_i I_{X_i} \right) \right) \\ &= E_{sr} - E_{rr} + j(E_{sx} - E_{rx}) = \sum_{i=1}^k \mathbf{R}(V_{drop_i}) + j \left(\sum_{i=1}^k \mathbf{Imag}(V_{drop_i}) \right). \end{aligned} \quad (\text{IV.49})$$

where $\underline{E}_s = E_{sr} + jE_{sx}$ and $\underline{E}_r = E_{rr} + jE_{rx}$.

It can be seen that Eq. (IV.49) can be applied to each phase of a three-phase primary distribution feeder, as given by the reduced Eq. (IV.50). That is, individual analyzes may be carried out. Assessment of three-phase voltage drop is strongly advisable for improving the percentage voltage regulation to each phase.

$$\underline{V}_{dropT_{abc}} = \underline{E}_{s_{abc}} - \underline{E}_{r_{abc}}. \quad (\text{IV.50})$$

One can notice that PMU measurements may change the way for monitoring radial feeders. When heavy currents with leading power factor are present on the segments the

voltage drop along the feeder tends to increase, thus, the impact will appear at the end of the feeder. In this way, taking the measurements at the feeder ends the overall voltage drop can be computed regardless of the current level or the power factor present in each segment. However, it is necessary to keep in mind that the accuracy of the voltage drop computation is directly related to the accuracy of the estimated phasors $\underline{E}_{s_{abc}}$ and $\underline{E}_{r_{abc}}$.

In II.2.b, it has been presented the challenges concerning the voltage angle difference between adjacent busbars in distribution feeders. By placing PMUs at the feeder ends, the angular aperture between them could have the highest value, however, depending of the feeder's features, this aperture may be small. Within this context, the algorithm used by the PMUs will play an imperative role.

The 4F-algorithm has the qualities demanded to satisfactorily fulfill the present application. We recall that this algorithm compute phasors of a single-phase input signal. Therefore, considering the fundamental phasor of each phase recorded at the feeder ends, advanced monitoring functions for radial feeder in active distribution grids may be properly performed.

IV.4.b Main objective: Online three-phase voltage drop assessment

The IEEE 34 node test feeder has been considered for three-phase voltage drop assessment using PMU data. Fig. IV.43 illustrates the feeder topology, in which the busbars were renumbered from 1 to 34 for ease of reference. The substation transformer has an installed capacity of 2.5 MVA with operating voltage of 24.9 kV. Delta and Wye 3-phase spot and distributed loads are connected along the feeder, however single- and two-phase loads are also considered for giving to the grid an unbalanced characteristic.

In addition, shunt capacitors and regulators have also been considered (see [100] to find the complete data of the grid). Based on [100], three-phase power flow results from the base case are depicted in Figs. IV.44-IV.45. Considering the *abc*-sequence and the *a*-phase as angular reference, a maximum angular aperture of 5.18° , 6.78° , and 6.02° have been reported for the *a*-, *b*-, and *c*-phase, respectively.

The approximate voltage drop may be calculated according to the difference between the voltage magnitude at the feeder ends. A special regard must be taken to this statement, because, in essence, the approximative voltage drop may be determined using conventional measurement devices (non-synchronized).

Now, assuming that two accurate PMUs are allocated in the grid. The first one is placed at the substation busbar and the second one is placed at the busbar 9. The feeder length between the PMUs is approximately equal to 31.726 Km. Considering that the PMUs are endowed with the 4F-algorithm whose fundamental phasor estimates may be close to 0.1% TVE under several scenarios (III.6.a.ii), this error margin has been considered over the phasor measurements taken at the aforementioned busbars.

Table IV.3 shows the voltage drop comparison between the calculation performed by the approximate technique and accurate PMUs. Concerning the power flow data, the approximate voltage magnitude drop for the *abc*-phases are 0.0328, 0.0247, 0.0300 (*in pu*), respectively. Thereby, the approximate voltage drops *in volts* are equal to 816.72 V, 615.03 V, and 747 V.

However, considering the angular aperture between the busbars where the PMUs have

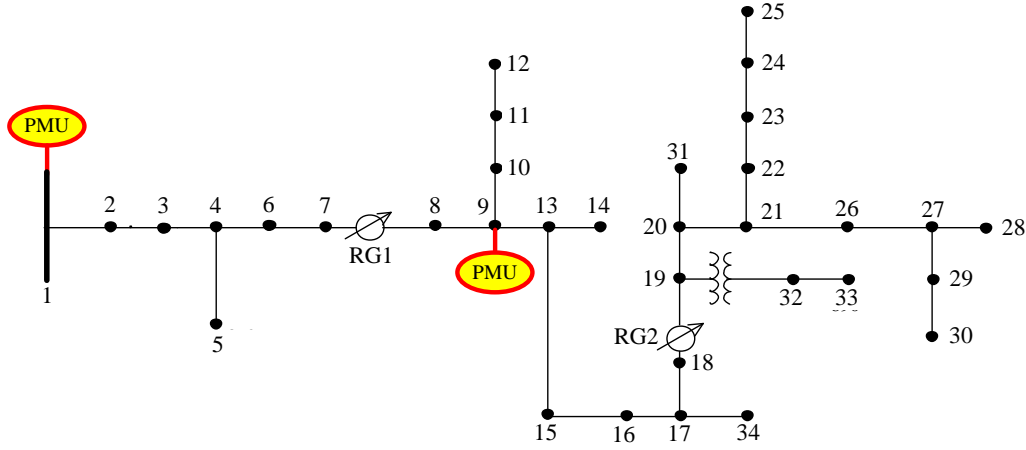


Figure IV.43: IEEE 34 node test feeder [100].

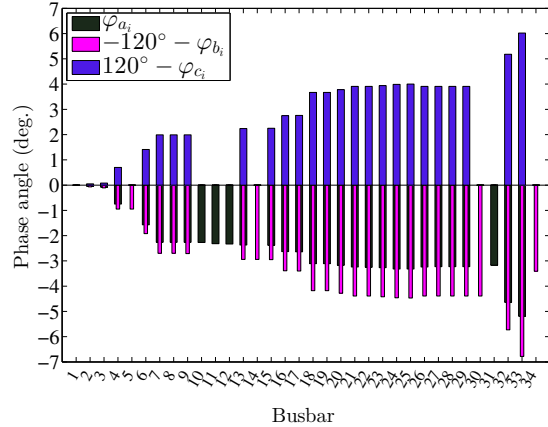
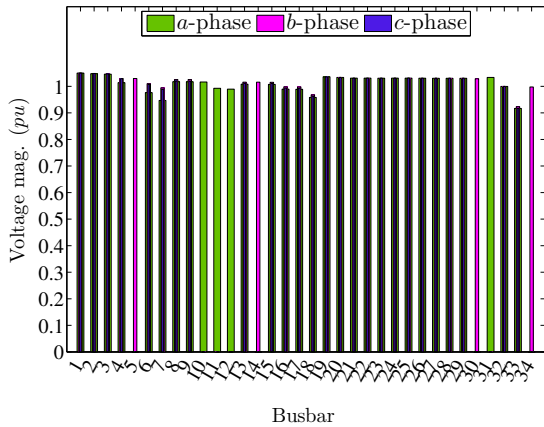


Figure IV.44: Voltage magnitude profile of the *abc*-phases from the base case.

Figure IV.45: Voltage phase profile of the *abc*-phases from the base case.

been placed, one can note an increasing of the voltage drop. For the *a*-phase an angular aperture close to 2.26° has been reported. For the *b*- and *c*-phase the angular apertures are close to 2.70° and 1.9° , respectively. Assuming $+0.1\%$ TVE, one can notice that the reported voltage drop for the *abc*-phases are equal to 0.0531, 0.0557, and 0.0476 (*in pu*), respectively. In this way, the voltage drop *in volts* to be corrected for the *abc*-phases are close to 1.322 kV, 1.386 kV, and 1.185 kV.

Clearly, the obtained estimates show a significant deviation between the techniques whose impact will be on the percentage voltage regulation (*VR*) given by Eq. (IV.51)

$$VR(\%) = \frac{|V_{SE}| - |V_{RE}|}{|V_{RE}|} \times 100. \quad (IV.51)$$

being $|V_{SE}|$ the sending end voltage at substation busbar and $|V_{RE}|$ the receiving end

voltage at busbar 9.

Fig. IV.46 depicts the reported percentages. The exact calculation provides values close to 5.14%, 5.36%, and 4.59% for the *abs*-phase, respectively. One can see that the corrected voltage adjustments provided by accurate PMUs are of the order of 5.6%, 5.89%, and 5%, whereas the adjustments provided by the approximate calculation are of the order of 3.39%, 2.53%, and 3.1%, respectively. In this way, using accurate PMUs data it is possible to boost the adjustments of the voltage regulator RG1 in order to put the voltage profile along the feeder within reliable limits.

Table IV.3: Comparison between the voltage drop calculation

Calculation	Voltage drop (<i>pu</i>)			Voltage drop (kV)		
	<i>a</i> -phase	<i>b</i> -phase	<i>c</i> -phase	<i>a</i> -phase	<i>b</i> -phase	<i>c</i> -phase
Approximate	0.0328	0.0247	0.0300	0.8167	0.6150	0.7470
Accurate PMU (0.1% TVE)	0.0531	0.0557	0.0476	1.3222	1.3869	1.1852

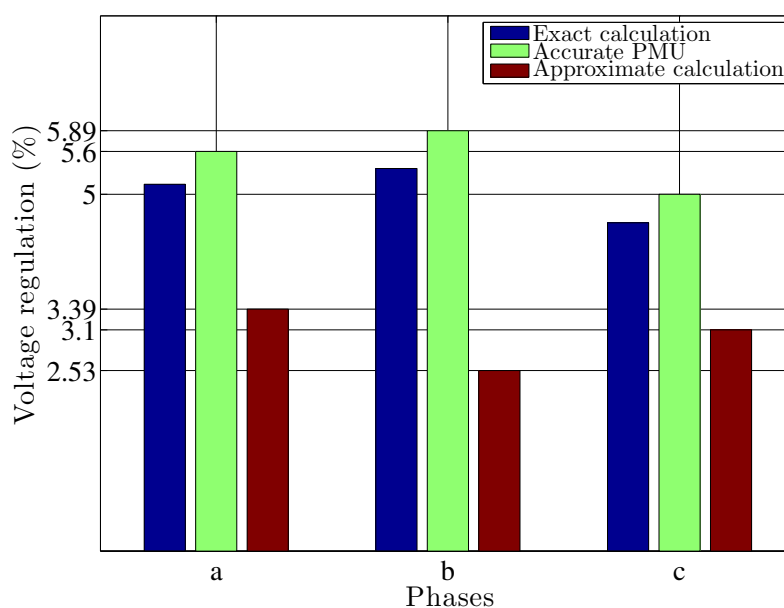


Figure IV.46: Voltage regulation profile.

IV.5 Assessment of harmonic issues using PMU data

Power quality in electric distribution systems is a very delicate issue because it may produce different interpretations from customer and utility perspectives. In [65], one can find a statement that well summarizes this issue: “From a customer perspective, a power quality problem might be defined as any electric supply condition that causes appliances to malfunction or prevents their use. From a utility perspective, a power quality problem might be perceived as noncompliance with various standards such as RMS voltage or harmonics.”

In theory, a perfect power quality can be attained when the sinusoidal signals are free from disturbances (interruption, sag, swell, spike, noise, flicker, harmonic distortion, and

frequency deviation). In the real life, however, this is almost unattainable. Among the aforementioned disturbances that may be found in electric distribution environment, the harmonic distortion has a special attention due to various operational problems that it may produce in primary feeders. In Section II.4, it has been presented some drawbacks caused by harmonics, such as, excessive heating on the feeder wiring, increased heating producing dielectric stress in capacitor banks, misoperation of relays and switchgears, and equipments life-cycle reduction.

Within this context, the identification of the responsible by the origin of harmonics plays a crucial role. When the customers are considered as the main source of harmonics they are penalized with increases in their energy bills, on the other hand, when the utilities are found guilty they must take actions for reducing harmonics (for instance, installing filter banks) in order to meet with the requirements imposed by the standards and also avoid penalties.

The classical method for identifying the main source of harmonics takes into account the harmonic active power flow direction seen at *PCC* between the utility and the customer [101]. Harmonics change the RMS value of voltage and current waveforms producing variations on the active, reactive, and apparent powers as well as on the power factor. In this way, the classical method monitors the sign of the harmonic active power. Based on [10], let us demonstrate these variations in an intuitive manner. Assuming that an instantaneous current waveform be given by

$$i(t) = I_0 + I_{m_1} \sin(\omega t) + I_{m_2} \sin(2\omega t + \phi_{i2}) + \dots + I_{m_k} \sin(k\omega t + \phi_{ik}) \quad (\text{IV.52})$$

being I_0 the DC-offset, I_m the sinusoidal components peak value and k the highest harmonic component present in the signal.

Computing the RMS value for this signal yields

$$I_{RMS} = \sqrt{\frac{1}{T} \int_0^T [i(t)]^2 dt} = \sqrt{I_0^2 + \frac{I_{m_1}^2 + I_{m_2}^2 + \dots + I_{m_k}^2}{2}} \quad (\text{IV.53})$$

or

$$I_{RMS} = \sqrt{I_0^2 + |I_1|^2 + |I_2|^2 + \dots + |I_k|^2} \quad (\text{IV.54})$$

it is clear that the RMS value of a current signal distorted by harmonics must be computed taking into account the peak value of the harmonics or the RMS value to each harmonic component. Similar results may be obtained for voltage signals, as shown below

$$V_{RMS} = \sqrt{V_0^2 + |V_1|^2 + |V_2|^2 + \dots + |V_k|^2}. \quad (\text{IV.55})$$

Now, let us consider voltage and current signals distorted by harmonics in order to evaluate their impacts on the active power flow. Considering the following signals

$$e(t) = E_0 + E_{m_1} \sin(\omega t + \phi_{e1}) + E_{m_2} \sin(2\omega t + \phi_{e2}) + \dots + E_{m_k} \sin(k\omega t + \phi_{ek}) \quad (\text{IV.56})$$

$$i(t) = I_0 + I_{m_1} \sin(\omega t + \phi_{i1}) + I_{m_2} \sin(2\omega t + \phi_{i2}) + \dots + I_{m_k} \sin(k\omega t + \phi_{ik}) \quad (\text{IV.57})$$

the overall active power can be calculated as follows

$$P = \frac{1}{T} \int_0^T [E_0 + E_{m_1} \sin(\omega t + \phi_{e1}) + E_{m_2} \sin(2\omega t + \phi_{e2}) + \dots + E_{m_k} \sin(k\omega t + \phi_{ek})] \times [I_0 + I_{m_1} \sin(\omega t + \phi_{i1}) + I_{m_2} \sin(2\omega t + \phi_{i2}) + \dots + I_{m_k} \sin(k\omega t + \phi_{ik})] dt. \quad (\text{IV.58})$$

Performing the calculations inside the integral of Eq. (IV.58), one can obtain product of terms with same frequencies or product of terms with different frequencies. Thereby, the integral of the product of the terms with different frequencies, regarding the period of the smallest frequency, will be null. By that, only the product of terms with equal frequencies must be considered whose generalized equation is given by

$$P = \frac{1}{T} \int_0^T F \sin(m\omega t + \phi_e) G \sin(m\omega t + \phi_i) dt = \frac{FG}{2} \cos(\phi_e - \phi_i) \quad (\text{IV.59})$$

hence,

$$\begin{aligned} P &= E_0 I_0 + |E_1| |I_1| \cos(\phi_{e1} - \phi_{i1}) + \dots + |E_k| |I_k| \cos(\phi_{ek} - \phi_{ik}) \quad (\text{IV.60}) \\ &= P_1 + \sum_{n \neq 1}^k P_{H_n} = P_1 + P_H \end{aligned}$$

where P_0 represents the active power of the DC component, P_1 is the fundamental active power and P_H is the harmonic active power.

According to [102], when $P_H < 0$ (inversion of the harmonic flow) a customer will be considered as the main source of harmonic pollution. When $P_H > 0$, the harmonics are generated within the distribution grid, that is, the grid is the source of pollution. Fig. IV.47 illustrates the harmonic power flow direction regarding the term P_H .

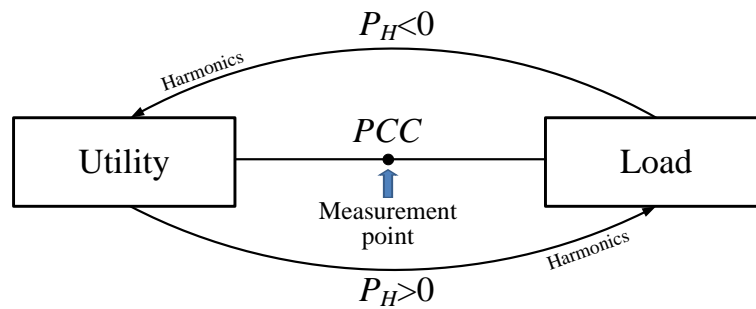


Figure IV.47: Representation of the harmonic active power flow direction.

It can be seen that the average power computed from nonsinusoidal voltage and current signals will be the summation of the harmonic components average power. Based on the aforementioned analysis, the calculation of the overall apparent power (S) might be carried out according to Eq. (IV.61)

$$S = \sqrt{E_0^2 + |E_1|^2 + |E_2|^2 + \dots + |E_k|^2} \times \sqrt{I_0^2 + |I_1|^2 + |I_2|^2 + \dots + |I_k|^2}. \quad (\text{IV.61})$$

According to C.I. Budeanu [103]-[101], the nonactive power could be represented as follows

$$Q = |E_1||I_1| \sin(\phi_{e1} - \phi_{i1}) + \dots + |E_k||I_k| \sin(\phi_{ek} - \phi_{ik}) = Q_1 + \sum_{n=2}^k Q_{H_n} = Q_1 + Q_H \quad (\text{IV.62})$$

where Q_1 and Q_H denote the fundamental reactive power and the harmonic reactive power, respectively.

The effectiveness of Eq. (IV.62) has been questioned because it could not quantify properly the harmonic reactive power flow [104]. Aiming to avoid misunderstanding the standard [102] states that the nonactive power can be calculated using Eq. (IV.63)

$$Q_N = \sqrt{S^2 - P^2}. \quad (\text{IV.63})$$

The identification of the harmonic power flow direction using the P_H method has been applied in existing measurements devices from the major vendors [105]. However, the standard [102] itself states that in most common practical situations, it is difficult to measure correctly the higher order components of P_H using conventional instrumentation. The main reason for this difficulty stems from the fact that the phase angle between the harmonic voltage and current phasors may be close to $\pm 90^\circ$, in this way even small errors in phase angle measurements can cause large errors in P_H . Thus, it is advised to use instrumentation optimized specifically for measurements of P_H components.

One can note clear evidence that accurate PMUs endowed with frequency-adaptive algorithms may overcome this problematic. The AWLS-algorithm has the qualities required to satisfactorily contribute with the P_H method. We recall that this algorithm is able to compute with accuracy harmonic phasors of a single-phase input signal even under frequency deviation. Therefore, advanced monitoring concerning harmonic power flow direction and pollution source identification in active distribution grids could be achieved. In the following section, contributions for improving the P_H method using PMU data are reported.

IV.5.a Main objective: Enhanced detection of both harmonic power flow direction and main source of harmonic pollution under frequency deviation

Let us analyze scenarios in which both the grid- and industry side are experiencing harmonic problems. A steel mill having nonlinear loads such as solid state converters, arc furnaces and saturated magnetic devices is connected to a 20 kV primary distribution feeder. The industry is assumed as a balanced load, thus single phase analysis is performed. The rated current by phase is 40 A. In the grid side nonlinear loads are also presented, in this way, for both sides, random harmonic components up to 11th component can be recorded by a PMU placed at *PCC*, as depicted in Fig. IV.48.

For the first scenario, the even- and odd-harmonic voltage phasors can have a magnitude up to 2% and 5% of the fundamental voltage magnitude, respectively. For all of them, the phase angle can take any value within the range of $\pm 180^\circ$. Concerning the even- and odd-harmonic current phasors the reported magnitudes are 2.5% and 5% of the fundamental

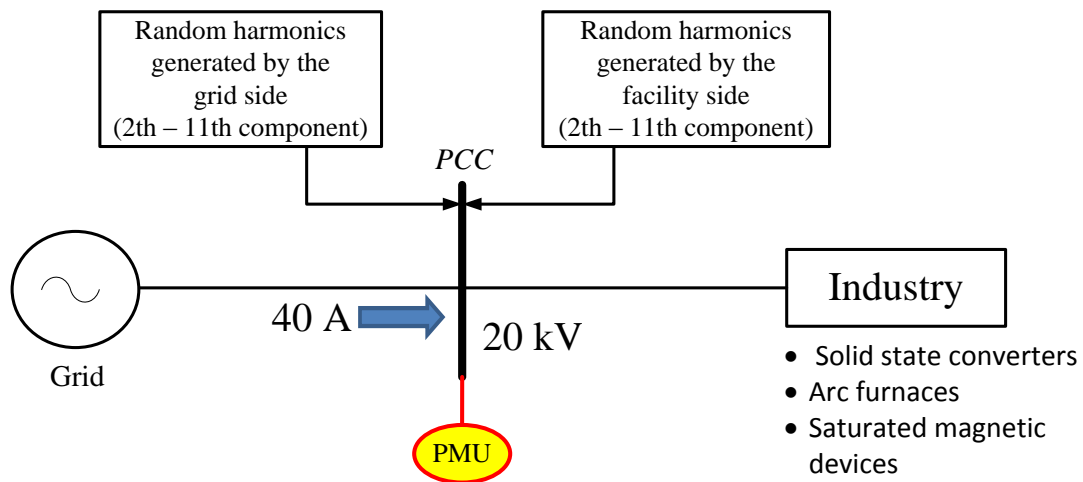


Figure IV.48: Representation of the analyzed system model.

current magnitude, respectively. Likewise, their phase angle can also falls within the range of $\pm 180^\circ$. The phase angle of the fundamental voltage and current phasors are equal to 45° and 22.5° . A system frequency at 50.2 Hz has been considered in order to evaluate the impact of the frequency deviation on the harmonic issues. In Table IV.4 the reported data have been summarized.

Table IV.4: Input signal components range for the first scenario.

Component	Voltage		Current		Freq. (Hz)
	Magnitude	Angle (deg.)	Magnitude	Angle (deg.)	
0 ^a	0.5%	–	0.5%	–	50.2
1 ^a	100 %	45°	100 %	22.5°	
2 ^a , 4 ^a , 6 ^a , 8 ^a , 10 ^a	2%	$\pm 180^\circ$	2.5%	$\pm 180^\circ$	
3 ^a , 5 ^a , 7 ^a , 9 ^a , 11 ^a	5%	$\pm 180^\circ$	5%	$\pm 180^\circ$	

Taking into account the input signal components range, the harmonic phasors have been randomly created to simulate various magnitude and phase angle patterns at PCC. Table IV.5 depicts the obtained phasors for the first scenario. Figs. IV.49-IV.50 illustrate the resulting voltage and current input signals in time domain locked to the fundamental frequency at 50-Hz. It can be seen that the waveforms are very distorted, in this way, it is of paramount importance to determine who is the main source of harmonic pollution as well as the identification of the power flow direction in order to share harmonic responsibility.

Concerning the identification of the main source of harmonics, it has been commented that the term P_H by itself can provide this information, however, knowing that the power flow can be directly related to a given angular aperture, we have used another intuitive term entitled *harmonic power factor* (Pf_H) for accomplishing this task, as shown in Eq. (IV.64). In essence, it provides the information of leading or lagging power factor concerning the harmonics.

When $Pf_H < 0$, a leading power factor is obtained that can be interpreted as a capacitive effect on the industry side. In this way, the non-linear loads at the industry side are the

Table IV.5: Phasors randomly created (first scenario).

Component (th)	Voltage		Current	
	Magnitude (V)	Angle (deg.)	Magnitude (A)	Angle (deg.)
0	100	0°	0.2	0°
2	303	-30°	0.418	97°
3	851	132°	0.620	-105°
4	28	68°	0.887	-112°
5	769	166°	0.485	-73°
6	294	134°	0.957	72°
7	334	-8°	1.448	145°
8	224	-132°	0.867	-97°
9	390	-92°	1.627	140°
10	145	-166°	0.244	102°
11	314	68°	1.253	-21°

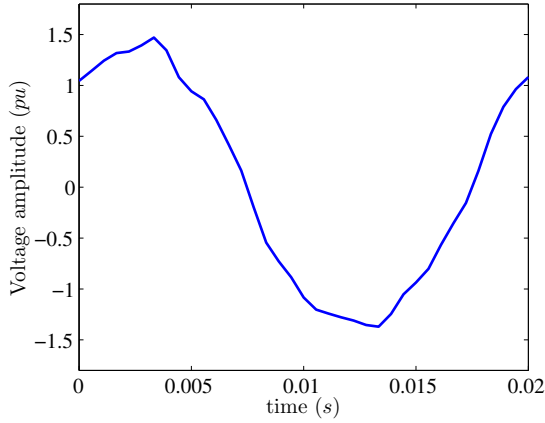


Figure IV.49: Voltage waveform at PCC (first scenario).

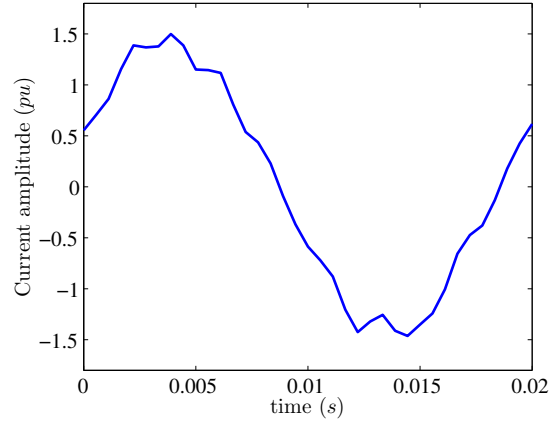


Figure IV.50: Current waveform at PCC (first scenario).

main source of harmonic pollution. Otherwise, a lagging power factor is achieved and the grid side will be the main source of pollution.

Computing the resulting angle from the obtained harmonic power factor a valuable information regarding the zone in the complex unit circle in which it falls can be addressed. Leading power factor yields angles into the range $+90^\circ < \theta < -90^\circ$ and lagging power factor produces angles within $+90^\circ > \theta > -90^\circ$.

$$Pf_H = \cos \theta_H = \frac{P_H}{S_H} = \frac{|E_2||I_2| \cos(\phi_{e2} - \phi_{i2}) + \dots + |E_k||I_k| \cos(\phi_{ek} - \phi_{ik})}{\sqrt{|E_2|^2 + \dots + |E_k|^2} \times \sqrt{|I_2|^2 + \dots + |I_k|^2}} \quad (\text{IV.64})$$

Now, let us evaluate the impact of the system frequency deviation. For this purpose, the voltage and current signals shown in Figs. IV.49-IV.50 are sampled at a rate of 36 samples obtained over one period of the 50-Hz signal. Fig. IV.51 illustrates the comparison between the P_{H_n} value of each harmonic component. The figure on the left side (blue bars) depicts the true P_{H_n} values. The Pf_H is equal to -0.2516 resulting in an angle of 104.57° . The

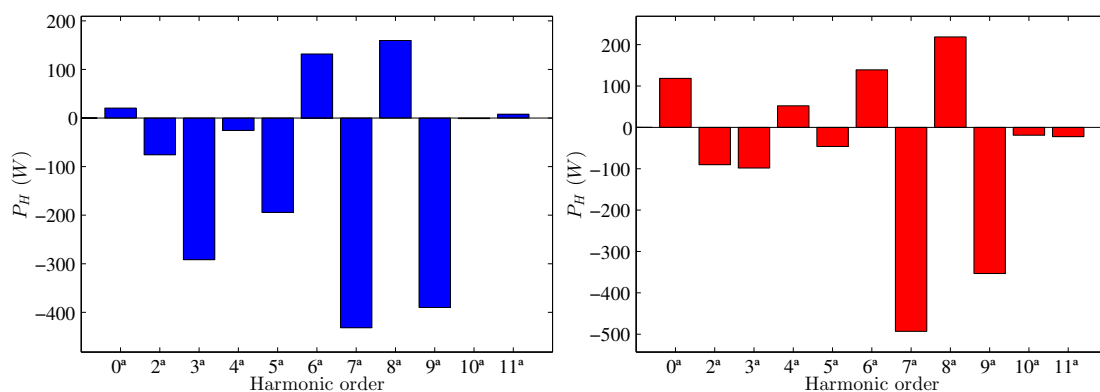


Figure IV.51: Comparison between the P_{H_n} values for the first scenario: on the left, true values - on the right, the reported values taking into account a frequency deviation of +0.2 Hz.

overall P_H is equal to -1090.48 W. In other words, the industry side is the main source of pollution. Recalling that the system frequency is 50.2 Hz, that is, a frequency deviation of +0.2 Hz, the figure on the right side (red bars) shows significant variations on the P_{H_n} estimates.

The DC-offset, 2th, 6th, 7th, 8th, and 10th components have an absolute increase in the order of 483.33%, 19.15%, 5.30%, 14.12%, 36.87%, and 1496.63%, respectively. The 3th, 5th, and 9th components have experienced a reduction in the order of 66.33%, 76.18%, and 9.48%, respectively. One can also observe that the 4th and 11th components are in opposite direction. The first one is a harmonic caused by the non-linear loads at the industry side, however the frequency deviation imposes a change in its direction.

Now, this harmonic becomes erroneously imputed to the grid side. Similarly, the 11th component is caused by the grid side, but it is attributed to the industry side. The Pf_H is equal to -0.1241 resulting in an angle of 97.129° . The overall P_H taking into account the frequency deviation is equal to -594.16 W.

The obtained harmonic power factor indicates that the main source of pollution is the industry side. Despite correctly inferring the main source of pollution, one can note that the overall P_H has not valuable information due to the large margin of error concerning the harmonic active power. Due to this fact, the main goal is to infer precisely both source of pollution and harmonic power flow direction.

Now, let us evaluate the first scenario using the frequency-adaptive AWLS-algorithm. The voltage and current input signals are distorted by Gaussian white noise related to a SNR=66 dB. The reported frequency estimation error is close to -0.5 mHz. Fig. IV.52 shows the comparison between the true P_{H_n} value of each component. The maximum error that has been obtained is close to 0.794% for the 10th component.

The harmonic power factor is close to -0.2515, thus, a resulting angle of 104.56° has been attained. In addition, power flow inversion of individual harmonic components has not been reported. It is clear that the proposed algorithm imputes correctly the industry side as the main source of harmonic pollution and the harmonic power flow direction is properly determined.

In the second scenario, the worst case related to phase angle between the voltage and

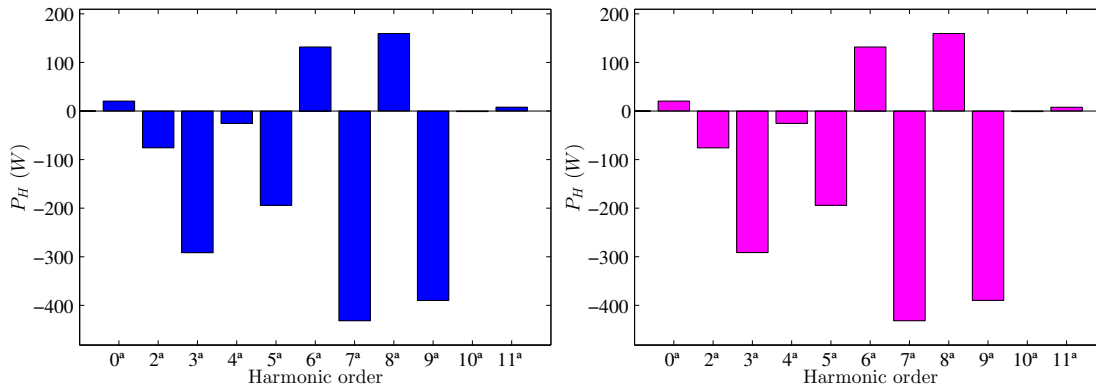


Figure IV.52: Comparison between the P_{H_n} values for the first scenario: on the left, true values - on the right, the reported values using the frequency-adaptive AWLS-algorithm.

current harmonic phasors near $\pm 90^\circ$ is evaluated. In this way, the phase angle of the harmonic voltage and current phasors have been settled to be close to $\pm 90^\circ$ and $\pm 0^\circ$, respectively. A system frequency at 49.85 Hz has been considered.

In Table IV.6, the reported data have been summarized. Based on the input signal components range the obtained phasors randomly created are shown in Table IV.7. We state that the DC component has been omitted in order to evaluate only the sinusoidal harmonics. Figs. IV.53-IV.54 depict the resulting voltage and current input signals in time domain.

Once again, a similar analysis is performed. Fig. IV.55 depicts the comparison between

Table IV.6: Signal input components for the second scenario.

Component	Voltage		Current		Freq. (Hz)
	Magnitude	Angle (deg.)	Magnitude	Angle (deg.)	
0 ^a	0.5%	–	0.5%	–	49.85
1 ^a	100 %	60°	100 %	30°	
2 ^a , 4 ^a , 6 ^a , 8 ^a , 10 ^a	2%	$\approx \pm 90^\circ$	2.5%	$\approx \pm 0^\circ$	
3 ^a , 5 ^a , 7 ^a , 9 ^a , 11 ^a	5%	$\approx \pm 90^\circ$	5%	$\approx \pm 0^\circ$	

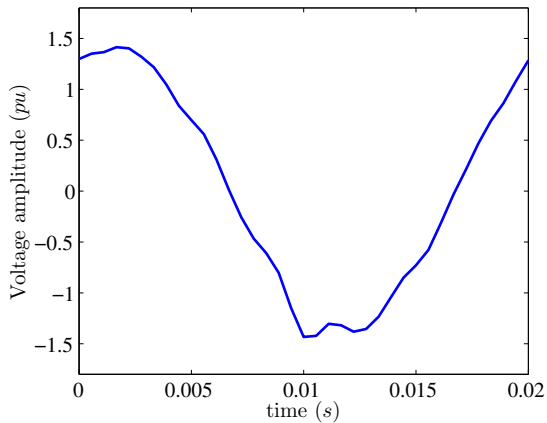


Figure IV.53: Voltage waveform at PCC (second scenario).

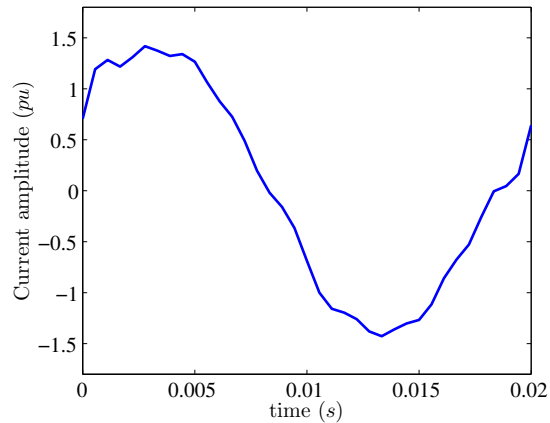


Figure IV.54: Current waveform at PCC (second scenario).

Table IV.7: Phasors randomly created (second scenario)

Component (th)	Voltage		Current	
	Magnitude (V)	Angle (deg.)	Magnitude (A)	Angle (deg.)
0	0	0°	0	0°
2	29	-90.08°	0.550	-0.030°
3	537.5	89.95°	1.178	-0.010°
4	240	-89.94°	0.967	-0.100°
5	149	90.10	1.992	-0.030°
6	375	-90.10°	0.631	-0.040°
7	872	90.07°	1.556	-0.010°
8	349	-90.03°	0.374	-0.040
9	207.5	90.05°	1.844	-0.060°
10	10	-90.10°	0.836	0.020°
11	278	90.02°	0.075	0.020°

the P_{H_n} value of each harmonic component. The figure on the left side (blue bars) shows the true P_{H_n} values. For this scenario, the Pf_H is equal to -0.001228 resulting in an angle of 90.070° . The overall P_H is equal to -5.574 W. Based on the reported data, one can state that the industry side is the main source of pollution. Assuming a frequency deviation of -0.15 Hz, the figure on the right side (red bars) shows large errors on the P_{H_n} estimates.

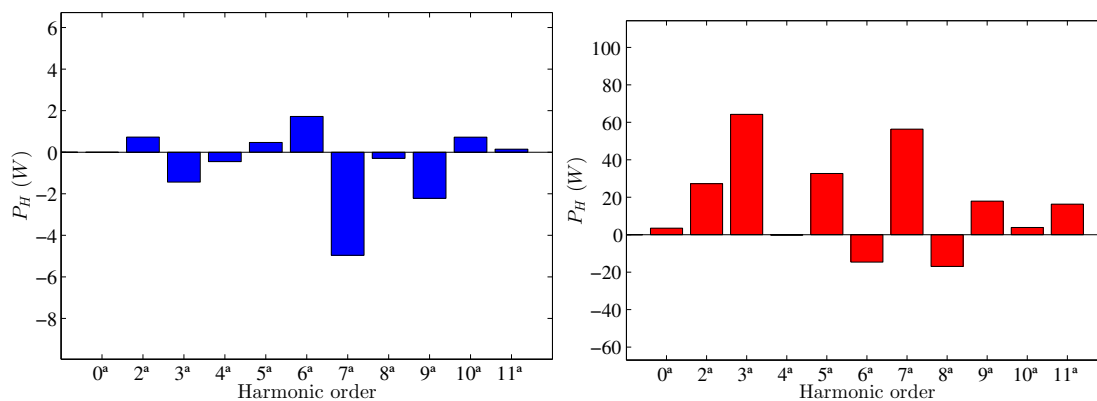


Figure IV.55: Comparison between the P_{H_n} values for the second scenario: on the left, true values - on the right, the reported values taking into account a frequency deviation of -0.15 Hz near $\pm 90^\circ$.

One can notice that the frequency deviation imposes a reverse harmonic flow for the 3th, 6th, 7th, and 9th components. The Pf_H is close to 0.0404 providing an angle of 87.681° . It can be noted that the nonlinear loads at the grid side are imputed as the main source of harmonic pollution, however, this does not reflect the reality. Fig. IV.56 depicts the estimates provided by the AWLS algorithm.

The Pf_H that has been obtained is close to -0.0011 providing an angle of 90.062° . The overall P_H is equal to -4.972 W. It can be seen that even in a critical scenario, in which the angular aperture between voltage and current harmonic phasors is near $\pm 90^\circ$ combined with frequency deviation, the AWLS algorithm presents the capability to track efficiently

the main source of harmonic pollution as well as the corrected power flow direction.

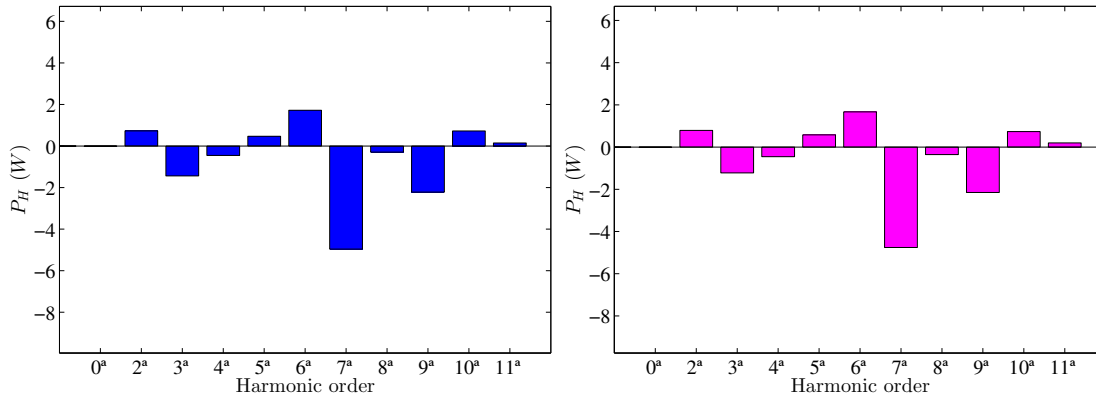


Figure IV.56: Comparison between the P_{H_n} values for the second scenario: on the left, true values - on the right, the reported values using the frequency-adaptive AWLS-algorithm. Note the accuracy of the estimates.

IV.6 Conclusion

In the current chapter, contributions are outlined for improving four potential applications of synchronized phasor measurements in electric distribution grids. The first application brings contributions for online estimation of Thévenin’s equivalent (TE) circuit using accurate PMU data provided by the frequency-adaptive Park’s transformation algorithm assuming steady- or quasi-steady state conditions. This application aims to overcome the problematic related to the Thévenin’s impedance locus method when equal or very close consecutive measurements are used. The proposed application is able to determine the TE circuit of the grid side seen by the *PCC* between aggregated DERs (wind turbines) and the active distribution grid. It has been assumed that the Thévenin’s voltage is equal to the fictitious infinity busbar voltage whose value is $1\angle 0^\circ pu$. In this way, online power flow exchanges between both sides and updated capability curve of synchronous generators can be properly carried out.

The second one is a practical application to track online external equivalents in radial active distribution grids using PMU data. This application uses the voltage and current phasor measurements recorded at a given boundary busbars to replace the external network (EN) by a variable impedance or power injection (simplified Norton’s theorem). The concept ‘*variable*’ has been employed to indicate that the measurements taken at the boundary busbar change according to the operating status of the grid. Besides the external equivalent evaluation, this application also reduces the electric grid size aiming to improve advanced monitoring functions dedicated to the area of interest (internal network) without loss of accuracy. Test cases are performed using a feeder model with 18 busbars and the power flow results for the internal network busbars taking into account the original and equivalent networks have not shown significant differences when accurate PMU data are employed.

The third one is related to the online three-phase voltage drop assessment in primary radial distribution grids. This application takes into consideration accurate synchronized

voltage measurements recorded at the feeder ends. The frequency-adaptive 4F-algorithm has been used to accomplish this task. The goal is to improve the voltage regulation along the feeder even for conditions related to heavy current combined with leading power factor caused by the integration of DERs. A test case has been performed using the IEEE 34 node test system and the obtained results show significant differences between the voltage drop calculation computed from the approximate method and the one using accurate PMU data.

The last one concerns the assessment of harmonic issues. This application brings contributions for improving the classical P_H method (harmonic active power) using accurate synchronized measurements. The goal is to improve both detection of the main source of harmonic pollution and real power flow direction under several scenarios including the worst case when the phase angle between the harmonic voltage and current phasors are near $\pm 90^\circ$. The frequency-adaptive AWLS-algorithm has been employed for estimating randomly harmonic phasor estimates upto the 11th component at PCC to identify the harmonic components that are generated by the grid- and customer side even under frequency deviation.

General Conclusion and Prospects

The work reported in the present thesis covers the subject concerning the applications of phasor measurement units in active power distribution systems to increase the situational awareness. Advanced knowledge regarding phasor estimation process is required in order to allow a comprehensive understanding of the challenges that must be circumvented for ensuring the deployment of PMUs and PMU-enabled IEDs in electric distribution environment. Due to this fact, in Chapter I, the state of the art regarding the estimation of synchronized phasor measurements has been presented.

The powerful Fourier's methods are still the cornerstone of the data processing techniques employed to estimate phasor measurements. In this way, a thorough review of the main key points with respect to Fourier series (FS) approach, Fourier transform (FT) properties, discrete Fourier transform (DFT) and fast Fourier transform (FFT) have been described in details to provide an intuitive mathematical basis for phasor representation in continuous and discrete-time domain. This review has been used as theoretical support for the accurate frequency-adaptive algorithms that have been proposed in the current thesis. Additionally, the main drawbacks concerning phasor estimation in electric power systems are also outlined. A special regard has been given to the system frequency deviation responsible for introducing the pernicious leakage phenomenon whose impact on the phasor estimation accuracy is relentless.

The characteristics and features of the classical PMU used in high-voltage power systems have been described taking into account the overall informations provided by the IEEE Std. C37.118. Concerning the state of art of synchronized measurements in distribution grids, the current conjuncture of the major projects related to the deployment of synchronized devices in the distribution environment are equally carried out. In addition, a survey of some tailored algorithms found in the technical literature for estimating phasors in distribution environment has also been reported.

In Chapter II, the main challenges of the synchronized phasor measurements deployment in active power distribution grids have been presented. A special regard to the problematic concerning the precision requirements demanded by the IEEE Std. C37.118 *versus* the active distribution system operational requirements has been presented and discussed. It has been shown that the admissible TVE metric stated by this standard is not conceivable for distribution grids and it is essential to reduce the TVE in order to obtain valuable phasor estimates in distribution environment.

The standard requires a maximum permissible TVE of 1%, therefore phase angle errors

close to $\pm 0.573^\circ$ are permitted. However, classical distribution grid topology having buses separated by shorter distances can produce smaller angular apertures between adjacent busbars. A practical case concerning an express feeder section comprised between a substation busbar and a load concentration busbar has been analyzed. Assuming PMUs with 1% TVE, the obtained results concerning active- and reactive power flows as well as the power losses have not valuable informations due to the large error margin arisen.

Additional analyses were performed and the reported results suggest a maximum TVE value less than or close to 0.1% in order to provide phasor estimates that fulfill several expectations for enabling advanced distribution applications. Other challenges regarding frequency deviation, out-of-band disturbances (harmonic, interharmonic and subharmonic), measurement points, and cost-benefit ratio of the synchronized devices deployment are also reported. In this way, PMUs and PMU-enabled IEDs especially developed for active distribution grids must fulfill the following prerequisites: high degree of accuracy, adaptive in frequency, and economically viable.

In Chapter III, three frequency-adaptive algorithms for estimating synchronized phasor measurements in active power distribution systems have been proposed. They aim to afford accurate phasor estimates under dynamic and/or static conditions. The algorithms employ a decoupled stage to track local system frequency based on the classical finite derivative approximation of the fundamental positive-sequence voltage phasor phase angle displacement. For accomplishing this task, however, the Park's transformation have been applied due to its high sensitivity and quick response under frequency deviation. Additionally, rate of change of frequency (ROCOF) has been also computed accurately.

In practice, Park's transformation could lead to very noisy estimates caused by several factors that degrade its stability (Gaussian white noise, harmonics, and so on). For overcoming these effects, FIR filters (bandpass and moving average) have been applied to substantially alleviate the undesirable effects and, consequently, to give back to the Park's transformation its inherent robustness. After performing accurate frequency tracking, the algorithms use this information to properly perform software-based adaptive-frequency. With the development of high-performance DSPs and FPGAs with powerful routines of floating-point representation this task may be adequately and easily accomplished.

The first algorithm for estimating phasors is based on a modified Park's transformation that adjusts its inner parameters according to the measured system frequency, thus fundamental positive-sequence voltage phasor estimates can be achieved with an enhanced speed and accuracy in both balanced and unbalanced conditions. The main goal of the proposed algorithm concerns an improved traceability of steady-state and dynamic conditions in active distribution grids.

The second algorithm titled '4F-algorithm' performs four steps in a synergistic manner - frequency estimation, FIR bandpass filtering, fast linear interpolation, and half-cycle Radix-2 DIT FFT approach - for estimating fundamental and selective harmonic phasors of a single-phase input signal. This algorithm applies the technique 'divide and conquer' because the components of a very distorted input signals are separated from each other by a FIR filter bank and thereafter interpolation is individually performed at the filters output data. This process allows a direct application of the half-cycle FFT approach to be obtained when the input signal is distorted by harmonics.

The third algorithm titled 'AWLS algorithm' provides a practical, intuitive and accurate

manner for computing DC-offset, fundamental and harmonics phasors under frequency deviation of a single-phase voltage or current input signal using full or fractional-cycle data window. The phasor estimation process is modelled in the weighted least square sense and the algorithm has also the ability to modify its inner parameters according to the estimated system frequency.

An extensive range of signal models have been used to cover static and/or dynamic conditions particularly found in active power distribution systems. These signals are corrupted by DC-offset, high harmonic content, out-of-band disturbances, and Gaussian white noise. They have been employed for evaluating the algorithms performance. Test cases related to amplitude- and phase step, frequency step, and frequency ramp have been performed. Considering the accuracy of the phasor estimates the reported results have a very low TVE value. Therefore, the tests demonstrate the capability of the proposed algorithms in dealing efficiently with very corrupted signals under frequency deviation.

Once accurate phasor measurement estimates have been obtained, four potential applications for improving monitoring capabilities in active distribution grids have been proposed. The first application brings contributions for online estimation of Thévenin's equivalent circuit using accurate data provided by the frequency-adaptive Park's transformation algorithm assuming steady- or *quasi*-steady state conditions. This application aims to overcome the problematic related to the Thévenin's impedance locus method when equal or very close consecutive measurements are used. The proposed application is applied to determine the reduced grid model seen by the *PCC* between aggregated DERs (wind turbines) and the active distribution grid. In this way, online power flow exchanges between both sides and updated capability curve of synchronous generators have been properly carried out.

The second application is a practical application to track online external equivalents in radial active distribution grids using accurate PMU data. This application reduces the electric grid size replacing the external network (EN) by a variable impedance or a variable power injection (simplified Norton's theorem) related to the voltage and current phasors recorded at a given boundary busbars. Reducing the size of the grid using external equivalents advanced monitoring functions dedicated to the area of interest (internal network) may be achieved without loss of accuracy. Test cases are performed using a feeder model with 18 busbars and the power flow results for the internal network busbars taking into account the original and equivalent network have not shown significant differences when accurate PMU data are employed.

The third application is related to the online three-phase voltage drop assessment in primary radial distribution grids. Knowing that one of the main responsibilities of the electric distribution utilities is to deliver voltage to customers within a suitable range, this application takes into consideration accurate synchronized voltage measurements recorded at the feeder ends to improve voltage regulation even for conditions related to heavy current combined with leading power factor caused by the integration of DERs. The frequency-adaptive 4F-algorithm has been used to provide accurate fundamental phasor estimates at the feeder ends. A test case has been performed using the IEEE 34 node test system and the obtained results show significant differences between the voltage drop calculation computed from the approximate method and from accurate PMU data.

The fourth application concerns the assessment of harmonic issues. It brings contri-

butions for improving the classical P_H method (harmonic active power) using accurate synchronized measurements. The goal is to improve both detection of the main source of harmonic pollution and real power flow direction under several scenarios including the worst case when the phase angle between the harmonic voltage and current phasors are near $\pm 90^\circ$. The frequency-adaptive AWLS-algorithm has been employed for estimating randomly harmonic phasor estimates upto the 11th component at PCC . These harmonics are generated by both grid- and load side. The obtained results shows that the main source of harmonic pollution and the real power flow direction can be properly carried out even under frequency deviation.

The propositions presented in the current thesis - frequency-adaptive algorithms and applications of accurate phasor measurements in active power distribution systems - have been characterized and modelled in simulation environment. Due to this fact, future prospects are related to a feasible deployment of the proposed algorithms on a DSP- or FPGA-based PMU for the development of low cost advanced devices for enabling the envisaged monitoring applications. Prospects concerning new possibilities to use the GPS-UTC to synchronize events in the power distribution grid are also aimed. Prospects related to differential approach for communication framework among advanced PMUs are also envisaged. It is important to mention that other effects capable of degrading phasor measurements accuracy, especially nonideal frequency response of voltage and current transducers, must also be evaluated for ensuring valuable phasor estimates. Additionally, test cases concerning modulated input signals (sags and swells) must also be evaluated. Despite the content of the thesis is based on simulations, it is of paramount importance to mention that they can describe in a consistent manner the behavior of the phasors estimation process as well as their applications. Based on the propositions and results presented in this thesis, it can be stated that significant contributions concerning the state of the art of synchronized phasor measurements in electric power distribution systems have been obtained.

Bibliography

- [1] C. P. Steinmetz, “Symbolic Representation of General Alternating Waves and of Double Frequency Vector Products,” *Transactions of the American Institute of Electrical Engineers*, vol. XVI, Jan. 1899, pp. 269–296. doi: 10.1109/T-AIEE.1899.4764075
- [2] J. Grainger and W. Stevenson, *Power System Analysis*. McGraw-Hill, 1994, p. 784.
- [3] A. G. Phadke and J. S. Thorp, *Synchronized Phasor Measurements and Their Applications*. New York: Springer, 2008, p. 248. ISBN 978-0-387-76535-8
- [4] J. Giri, M. Parashar, J. Trehern, and V. Madani, “The Situation Room: Control Center Analytics for Enhanced Situational Awareness,” *IEEE Power and Energy Magazine*, vol. 10, no. 5, Sep. 2012, pp. 24–39. doi: 10.1109/MPE.2012.2205316
- [5] A. Phadke and R. de Moraes, “The Wide World of Wide-area Measurement,” *IEEE Power and Energy Magazine*, vol. 6, no. 5, 2008, pp. 52–65. doi: 10.1109/MPE.2008.927476
- [6] IEEE, “Std. C37.118.1-2011 for Synchrophasor Measurements for Power Systems (Revision of IEEE Std C37.118-2005),” Tech. Rep. December, 2011.
- [7] —, “Std C37.118.1a-2014 for Synchrophasor Measurements for Power Systems Amendment 1 : Modification of Selected Performance Requirements,” Tech. Rep. March, 2014.
- [8] G. D’Antona and A. Ferrero, *Digital Signal Processing for Measurement Systems Theory and Applications*. Springer, 2006, p. 268. ISBN 978-0-387-24966-7
- [9] G. Bachman, L. Narici, and E. Beckenstein, *Fourier and Wavelet Analysis*. New York: Springer, 1999, p. 507.
- [10] R. Kerchner and G. Corcoran, *Alternating-Current Circuits*, 3rd ed. New York: Wiley, 1951, p. 598.
- [11] H. Davis, *Fourier Series and Orthogonal Functions*. Dover Publications, 2012, p. 416.
- [12] M. Vetterli, J. Kovacevic, and V. Goyal, *Foundations of Signal Processing*. Cambridge University Press, 2014, p. 744.

- [13] O. Brigham, *The Fast Fourier Transform*. Englewood Cliffs: Prentice-Hall, 1974.
- [14] A. Papoulis, *The Fourier Integral and its Applications*. New York: McGraw-Hill, 1962.
- [15] I. Good, "The Interaction Algorithm and Practical Fourier Series," *J. Roy. Stat. Soc.*, vol. 20, 1958, pp. 361–372.
- [16] J. Cooley and J. Tukey, "An Algorithm for the Machine Calculation of Complex Fourier Series," *Mathematics of Computation*, vol. 19, 1965, pp. 297–301.
- [17] J. Stein, *Digital Signal Processing: A Computer Science Perspective*. John-Wiley, 2000.
- [18] M. Akke and J. S. Thorp, "Sample Value Adjustment Improves Phasor Estimation at Off-Nominal Frequencies," *IEEE Transactions on Power Delivery*, vol. 25, no. 4, Oct. 2010, pp. 2255–2263. doi: 10.1109/TPWRD.2010.2052114
- [19] L. Thedes, *Practical Analog and Digital Filter Design*. Artech House, 2004.
- [20] A. J. Roscoe, I. F. Abdulhadi, and G. M. Burt, "P and M Class Phasor Measurement Unit Algorithms Using Adaptive Cascaded Filters," *IEEE Transactions on Power Delivery*, vol. 28, no. 3, Jul. 2013, pp. 1447–1459. doi: 10.1109/TPWRD.2013.2238256
- [21] I. Kamwa, A. K. Pradhan, and G. Joos, "Adaptive Phasor and Frequency-Tracking Schemes for Wide-Area Protection and Control," *IEEE Transactions on Power Delivery*, vol. 26, no. 2, Apr. 2011, pp. 744–753. doi: 10.1109/TPWRD.2009.2039152
- [22] I. Kamwa, S. R. Samantaray, and G. Joos, "Wide Frequency Range Adaptive Phasor and Frequency PMU Algorithms," *IEEE Transactions on Smart Grid*, vol. 5, no. 2, Mar. 2014, pp. 569–579. doi: 10.1109/TSG.2013.2264536
- [23] D. Thomas and M. Woolfson, "Evaluation of Frequency Tracking Methods," *IEEE Transactions on Power Delivery*, vol. 16, no. 3, Jul. 2001, pp. 367–371. doi: 10.1109/61.924812
- [24] R. Lutwak, "The Chip-Scale Atomic Clock - Recent developments," in *2009 IEEE International Frequency Control Symposium Joint with the 22nd European Frequency and Time forum*. IEEE, Apr. 2009, pp. 573–577. doi: 10.1109/FREQ.2009.5168247. ISBN 978-1-4244-3511-1
- [25] A. G. Phadke, J. S. Thorp, and M. G. Adamiak, "A New Measurement Technique for Tracking Voltage Phasors, Local System Frequency, and Rate of Change of Frequency," *IEEE Power Engineering Review*, vol. PER-3, no. 5, May 1983, pp. 23–23. doi: 10.1109/MPER.1983.5519136
- [26] I. Kamwa and R. Grondin, "Fast Adaptive Schemes for Tracking Voltage Phasor and Local Frequency in Power Transmission and Distribution Systems," in

- Proceedings of the 1991 IEEE Power Engineering Society Transmission and Distribution Conference.* IEEE, pp. 930–936. doi: 10.1109/TDC.1991.169614. ISBN 0-7803-0219-2
- [27] M. Kezunovic, S. Meliopoulos, V. Venkatasubramanian, and V. Vittal, *Application of Time-Synchronized Measurements in Power System Transmission Networks.* Springer, 2014.
- [28] A. Phadke, “Synchronized Phasor Measurements-A Historical Overview,” in *IEEE/PES Transmission and Distribution Conference and Exhibition*, vol. 1. IEEE, pp. 476–479. doi: 10.1109/TDC.2002.1178427. ISBN 0-7803-7525-4
- [29] —, “Synchronized Phasor Measurements in Power Systems,” *IEEE Computer Applications in Power*, vol. 6, no. 2, Apr. 1993, pp. 10–15. doi: 10.1109/67.207465
- [30] V. Terzija, G. Valverde, P. Regulski, V. Madani, J. Fitch, S. Skok, M. M. Begovic, and A. Phadke, “Wide-Area Monitoring, Protection, and Control of Future Electric Power Networks,” *Proceedings of the IEEE*, vol. 99, no. 1, Jan. 2011, pp. 80–93. doi: 10.1109/JPROC.2010.2060450
- [31] Z. Dong and P. Zhang, *Emerging Techniques in Power System Analysis.* Springer, 2010.
- [32] IEEE, “Std. 1344-1995 for Synchrophasors for Power Systems,” Tech. Rep. January, 1995.
- [33] —, “Std. C37.118-2005 for Synchrophasors for Power Systems (Revision of IEEE Std 1344-1995),” Tech. Rep. April, 2006.
- [34] —, “Std. C37.118.2-2011 for Synchrophasor Measurements for Power Systems (Revision of IEEE Std C37.118-2005),” Tech. Rep. December, 2011.
- [35] IEC, “Std. 61850 for Communication Network and Systems in Substations,” Tech. Rep., 2003.
- [36] A. Phadke, B. Pickett, M. Adamiak, M. Begovic, G. Benmouyal, R. Burnett, T. Cease, J. Goossens, D. Hansen, M. Kezunovic, L. Mankoff, P. McLaren, G. Michel, R. Murphy, J. Nordstrom, M. Sachdev, H. Smith, J. Thorp, M. Trotignon, T. Wang, and M. Xavier, “Synchronized Sampling and Phasor Measurements for Relaying and Control,” *IEEE Transactions on Power Delivery*, vol. 9, no. 1, 1994, pp. 442–452. doi: 10.1109/61.277716
- [37] W. Lewandowski, J. Azoubib, and W. Klepczynski, “GPS: Primary Tool for Time Transfer,” *Proceedings of the IEEE*, vol. 87, no. 1, 1999, pp. 163–172. doi: 10.1109/5.736348
- [38] S. Nardi and M. Pachter, “GPS Estimation Algorithm Using Stochastic Modeling,” in *Proceedings of the 37th IEEE Conference on Decision and Control (Cat. No.98CH36171)*, vol. 4. IEEE, pp. 4498–4502. doi: 10.1109/CDC.1998.762029. ISBN 0-7803-4394-8

- [39] E. D. Kaplan, *Understanding GPS: Principles and Applications*. Artech House, 1996.
- [40] P. Surveying and P. of GPS, “Available: <http://www.sage.unsw.edu.au/>.”
- [41] A. P. Meliopoulos, V. Madani, D. Novosel, and E. Al., “Synchrophasor Measurement Accuracy Characterization,” Tech. Rep., 2007.
- [42] A. P. Meliopoulos and G. J. Cokkinides, “Visualization and Animation of Instrumentation Channel Effects on DFR Data Accuracy,” in *Georgia Tech Fault and Disturbance Analysis Conference*, 2002.
- [43] IEEE, “Std C37.244-2013 - IEEE Guide for Phasor Data Concentrator Requirements for Power System Protection , Control , and Monitoring,” Tech. Rep. May, 2013.
- [44] P. Romano and M. Paolone, “An Enhanced Interpolated-Modulated Sliding DFT for High Reporting Rate PMUs,” in *2014 IEEE International Workshop on Applied Measurements for Power Systems Proceedings (AMPS)*. IEEE, Sep. 2014, pp. 1–6. doi: 10.1109/AMPS.2014.6947708. ISBN 978-1-4799-5643-2
- [45] D. Belega and D. Petri, “Accuracy of the Synchrophasor Estimator Provided by the Interpolated DFT Algorithm,” in *2012 IEEE International Instrumentation and Measurement Technology Conference Proceedings*. IEEE, May 2012, pp. 2700–2705. doi: 10.1109/I2MTC.2012.6229682. ISBN 978-1-4577-1772-7
- [46] P. Castello, M. Lixia, C. Muscas, and P. A. Pegoraro, “Adaptive Taylor-Fourier Synchrophasor Estimation for Fast Response to Changing Conditions,” in *2012 IEEE International Instrumentation and Measurement Technology Conference Proceedings*. IEEE, May 2012, pp. 294–299. doi: 10.1109/I2MTC.2012.6229532. ISBN 978-1-4577-1772-7
- [47] P. Castello, J. Liu, C. Muscas, P. A. Pegoraro, F. Ponci, and A. Monti, “A Fast and Accurate PMU Algorithm for P+M Class Measurement of Synchrophasor and Frequency,” *IEEE Transactions on Instrumentation and Measurement*, vol. 63, no. 12, Dec. 2014, pp. 2837–2845. doi: 10.1109/TIM.2014.2323137
- [48] D. Belega and D. Petri, “A Real-Valued Taylor Weighted Least Squares Synchrophasor Estimator,” in *2014 IEEE International Workshop on Applied Measurements for Power Systems Proceedings (AMPS)*. IEEE, Sep. 2014, pp. 1–6. doi: 10.1109/AMPS.2014.6947704. ISBN 978-1-4799-5643-2
- [49] A. Roscoe, “Available: <http://desl-pwrs.epfl.ch/workshop>.”
- [50] E. Workshop, “Synchrophasor Estimation Processes for Phasor Measurement Units: Algorithms and Metrological Characterisation (Available <http://desl-pwrs.epfl.ch/workshop>),” Lausanne, Switzerland, 2014.
- [51] I. Decker, D. Dotta, M. Agostini, S. Zimath, and A. Silva, “Performance of a Synchronized Phasor Measurements System in the Brazilian Power System,” in *2006 IEEE PES Power Systems Conference and Exposition*. IEEE, 2006, pp. 150–150. doi: 10.1109/PSCE.2006.296289. ISBN 1-4244-0177-1

- [52] Z. Zhong, C. Xu, B. Billian, L. Zhang, S.-J. Tsai, R. Conners, V. Centeno, A. Phadke, and Y. Liu, "Power System Frequency Monitoring Network (FNET) Implementation," *IEEE Transactions on Power Systems*, vol. 20, no. 4, Nov. 2005, pp. 1914–1921. doi: 10.1109/TPWRS.2005.857386
- [53] Y. Liu, "A US-Wide Power Systems Frequency Monitoring Network," in *2006 IEEE PES Power Systems Conference and Exposition*. IEEE, 2006, pp. 159–166. doi: 10.1109/PSCE.2006.296291. ISBN 1-4244-0177-1
- [54] A. Naumann, P. Komarnicki, M. Powalko, Z. A. Styczynski, J. Blumschein, and M. Kereit, "Experience with PMUs in Industrial Distribution Networks," in *IEEE PES General Meeting*. IEEE, Jul. 2010, pp. 1–6. doi: 10.1109/PES.2010.5589343. ISBN 978-1-4244-6549-1
- [55] M. Gurbiel, P. Komarnicki, Z. A. Styczynski, M. Kereit, J. Blumschein, and B. M. Buchholz, "Usage of Phasor Measurement Units for Industrial Applications," in *2011 IEEE Power and Energy Society General Meeting*. IEEE, Jul. 2011, pp. 1–5. doi: 10.1109/PES.2011.6039249. ISBN 978-1-4577-1000-1
- [56] A. Borghetti, C. Nucci, M. Paolone, G. Ciappi, and A. Solari, "Synchronized Phasors Monitoring During the Islanding Maneuver of an Active Distribution Network," in *2010 Innovative Smart Grid Technologies (ISGT)*. IEEE, Jan. 2010, pp. 1–8. doi: 10.1109/ISGT.2010.5434733. ISBN 978-1-4244-6264-3
- [57] M. Pignati, M. Popovic, and E. Al., "Real-Time State Estimation of the EPFL-Campus Medium-Voltage Grid by using PMUs."
- [58] ARPA-E, "<http://pqubepmu.com/library.php>," 2015.
- [59] P. Barker, T. Short, T. Key, and F. Goodman, "Engineering Guide for Integration of Distributed Generation and Storage into Power Distribution Systems," EPRI, Tech. Rep., 2000.
- [60] R. Carbone, *Energy Storage in the Emerging Era of Smart Grids*. InTech, 2011.
- [61] M. Pierre, G. Per-Olof, H. Per, L. Gunnar, and M. Pavla, "Power to the People!" *IEEE Power and Energy Magazine*, 2014, pp. 51–64.
- [62] P. Castello, C. Muscas, and P. A. Pegoraro, "Performance Comparison of Algorithms for Synchrophasors Measurements under Dynamic Conditions," in *2011 IEEE International Workshop on Applied Measurements for Power Systems (AMPS)*. IEEE, Sep. 2011, pp. 25–30. doi: 10.1109/AMPS.2011.6090351. ISBN 978-1-61284-947-8
- [63] M. Lixia, "IEEE 1588 Synchronization in Distributed Measurement Systems for Electric Power Networks," Ph.D. dissertation, University of Cagliari, 2012.
- [64] T. A. Short, *Electric Power Distribution Handbook*. CRC Press, 2004.
- [65] R. E. Brown, *Electric Power Distribution Reliability*, 2nd ed. CRC Press, 2009.

- [66] N. Kagan, C. C. Barioni, and E. J. Robba, *Introduction to Electric Power Distribution Systems*. Blucher, 2010.
- [67] ENTSO-E, “<https://www.entsoe.eu/Pages/default.aspx>,” 2015.
- [68] ANEEL, “Electricity Distribution Procedures in the National Power System: Module 8 - Power Quality,” Tech. Rep., 2008.
- [69] B. J. Kirby, J. Dyer, C. Martinez, R. A. Shoureshi, R. Guttromson, and J. Dagle, “Frequency Control Concerns In The North American Electric Power System,” Tech. Rep., 2002.
- [70] IEEE, “Std. 519-1992 - IEEE Recommended Practices and Requirements for Harmonic Control in Electrical Power Systems,” Tech. Rep., 1992.
- [71] ———, “Std. 519-2014 Recommended Practice and Requirements for Harmonic Control in Electric Power Systems,” Tech. Rep., 2014.
- [72] I. Harmonics Working Group, “Interharmonic Task Force Working document,” Tech. Rep., 2001.
- [73] M. Baran, “Challenges in State Estimation on Distribution Systems,” in *2001 Power Engineering Society Summer Meeting. Conference Proceedings (Cat. No.01CH37262)*, vol. 1. IEEE, 2001, pp. 429–433. doi: 10.1109/PESS.2001.970062. ISBN 0-7803-7173-9
- [74] S. Borlase, “The Evolution of Distribution,” *IEEE Power and Energy Magazine*, vol. 7, no. 2, Mar. 2009, pp. 63–68. doi: 10.1109/MPE.2008.931392
- [75] R. J. Albuquerque and V. L. Paucar, “Evaluation of the PMUs Measurement Channels Availability for Observability Analysis,” *IEEE Transactions on Power Systems*, vol. 28, no. 3, Aug. 2013, pp. 2536–2544. doi: 10.1109/TPWRS.2013.2244620
- [76] A. Phadke and J. S. Thorp, *Computer Relaying for Power System*, 2nd ed. Wiley, 2009.
- [77] R. H. Park, “Two-Reaction Theory of Synchronous Machines Generalized Method of Analysis—part I,” *Transactions of the American Institute of Electrical Engineers*, vol. 48, no. 3, Jul. 1929, pp. 716–727. doi: 10.1109/T-AIEE.1929.5055275
- [78] S. S. Venkata, G. T. Heydt, and N. Balijepalli, “High Impact Papers in Power Engineering (1900-1999),” *IEEE Power Engineering Review*, 2001, pp. 52–53.
- [79] B. Wu, Y. Lang, N. Zargari, and S. Kouro, *Power Conversion and Control of Wind Energy Systems*. John-Wiley, 2011.
- [80] H. A. Toliyat and S. G. Campbell, *DSP-Based Electromechanical Motion Control*. CRC Press, 2004.

- [81] S. A. Soliman, M. E. Hawary, and A. H. Mantaway, "Parks Transformation Application for Power System Harmonics Identification and Measurements," *Electric Power Components and Systems*, vol. 31, no. 8, Aug. 2003, pp. 777–789. doi: 10.1080/15325000390219767
- [82] R. G. Ferraz, L. U. Iurinic, A. D. Filomena, and A. S. Bretas, "Parks Transformation Based Formulation for Power Systems Transients Detection," Institute of Electrical Power Engineering of the Wroclaw University of Technology, Tech. Rep., 2013.
- [83] G. Paap, "Symmetrical Components in the Time Domain and Their Application to Power Network Calculations," *IEEE Transactions on Power Systems*, vol. 15, no. 2, May 2000, pp. 522–528. doi: 10.1109/59.867135
- [84] C. L. Fortescue, "Method of Symmetrical Co-ordinates Applied to the Solution of Polyphase Networks," *Proceedings of the American Institute of Electrical Engineers*, vol. 37, no. 6, Jun. 1918, pp. 629–716. doi: 10.1109/PAIEE.1918.6594104
- [85] Z. Yao, "Fundamental Phasor Calculation With Short Delay," *IEEE Transactions on Power Delivery*, vol. 23, no. 3, Jul. 2008, pp. 1280–1287. doi: 10.1109/TPWRD.2008.916734
- [86] D. Simon, *Optimal State Estimation*. New Jersey: Wiley, 2006.
- [87] B. Gou, "Generalized Integer Linear Programming Formulation for Optimal PMU Placement," *IEEE Transactions on Power Systems*, vol. 23, no. 3, Aug. 2008, pp. 1099–1104. doi: 10.1109/TPWRS.2008.926475
- [88] F. Aminifar, M. Fotuhi-Firuzabad, and A. Safdarian, "Optimal PMU Placement Based on Probabilistic Cost/Benefit Analysis," *IEEE Transactions on Power Systems*, vol. 28, no. 1, Feb. 2013, pp. 566–567. doi: 10.1109/TPWRS.2012.2198312
- [89] N. M. Manousakis, "A Weighted Least Squares Algorithm for Optimal PMU Placement," *IEEE Transactions on Power Systems*, vol. 28, no. 3, Aug. 2013, pp. 3499–3500. doi: 10.1109/TPWRS.2013.2242698
- [90] A. Neto, A. Rodrigues, R. Prada, and M. da Guia da Silva, "External Equivalent for Electric Power Distribution Networks With Radial Topology," *IEEE Transactions on Power Systems*, vol. 23, no. 3, Aug. 2008, pp. 889–895. doi: 10.1109/TPWRS.2008.922250
- [91] S. M. Abdelkader, "Online Thevenin's Equivalent Using Local PMU Measurements," in *International Conference on Renewable Energies and Power Quality (ICREPQ)*, 2010.
- [92] S. M. Abdelkader and D. J. Morrow, "Online Tracking of Thévenin Equivalent Parameters Using PMU Measurements," *IEEE Transactions on Power Systems*, vol. 27, no. 2, May 2012, pp. 975–983. doi: 10.1109/TPWRS.2011.2178868
- [93] —, "Online Thévenin Equivalent Determination Considering System Side Changes and Measurement Errors," *IEEE Transactions on Power Systems*, 2014, pp. 1–10. doi: 10.1109/TPWRS.2014.2365114

- [94] A. J. Monticelli, *Power Flow in Electric Power Networks*. Edgard Blücher, 1983.
- [95] A. Monticelli, S. Deckmann, A. Garcia, and B. Stott, "Real-Time External Equivalents for Static Security Analysis," *IEEE Transactions on Power Apparatus and Systems*, vol. PAS-98, no. 2, Mar. 1979, pp. 498–508. doi: 10.1109/TPAS.1979.319387
- [96] J. B. Ward, "Equivalent Circuits for Power-Flow Studies," *Transactions of the American Institute of Electrical Engineers*, vol. 68, no. 1, Jul. 1949, pp. 373–382. doi: 10.1109/T-AIEE.1949.5059947
- [97] F. Milano, "<http://faraday1.ucd.ie/index.html>," 2014.
- [98] ANSI, "Standard C84.1-1995: American National Standards for Electric Power Systems and Equipment - Voltage Ratings (60 Hz)." Tech. Rep., 1995.
- [99] C. Brice, "Comparison of Approximate and Exact Voltage Drop Calculations for Distribution Lines," *IEEE Transactions on Power Apparatus and Systems*, vol. PAS-101, no. 11, Nov. 1982, pp. 4428–4431. doi: 10.1109/TPAS.1982.317346
- [100] IEEE, "<http://ewh.ieee.org/soc/pes/dsacom/testfeeders/index.html>."
- [101] I. S. 1459-2000, "IEEE Trial-use standard definitions for the measurement of electric power quantities under sinusoidal, non sinusoidal, balanced or unbalanced conditions, 2000." Tech. Rep., 2000.
- [102] IEEE, "Std. 1459-2010: IEEE Standard Definitions for the Measurement of Electric Power Quantities Under Sinusoidal, Nonsinusoidal, Balanced, or Unbalanced Conditions," Tech. Rep., 2010.
- [103] C. I. Budeanu, "Puissances Reactives et Fictives," *Institut Romain de l'énergie*, 1927.
- [104] L. S. Czarnecki, "What is Wrong with the Budeanu Concept of Reactive and Distortion Power and Why it Should be Abandoned," *IEEE Transactions on Instrumentation and Measurement*, vol. IM-36, no. 3, Sep. 1987, pp. 834–837. doi: 10.1109/TIM.1987.6312797
- [105] W. Xu, X. Liu, and Y. Liu, "An Investigation on the Validity of Power Direction Method for Harmonic Source Determination," *IEEE Power Engineering Review*, vol. 22, no. 7, Jul. 2002, pp. 62–62. doi: 10.1109/MPER.2002.4312428
- [106] M. A. Pereira, "Power Flow in Electric Distribution Systems," Ph.D. dissertation, UNICAMP-Brazil, 1993.

Articles de revues internationales avec comité de relecture

Paru

IEEE transactions on Power Systems

Evaluation of the PMUs Measurement Channels Availability for Observability Analysis

R.J. Albuquerque, V.L. Paucar - Volume 28 Issue 3. August 2013.

Abstract: *Phasor measurement units (PMUs) equipped with global positioning system (GPS) receivers are the first devices capable of efficiently performing real-time monitoring of remote electrical power systems. Reliability of the monitoring system that exclusively uses PMUs is directly related to the reliability of each unit allocated on the system. As the failure of measurement channels is more common than PMU's failure, a probabilistic evaluation method of the PMUs measurement channels availability for electrical network observability analysis is proposed. In this method, the Markov process is adopted for estimating the measurement channels availability, as well as for determining an equivalent of the state space diagram of all possible operation states of channels for each unit. With the objective to assess the impact of the failure of measurement channels in the observability and reliability of the system, an algorithm that determines the optimal placement of PMUs using a modified binary search, the measurement channels availability for each unit, the global measurement availability, and the critical measurement channels for power system observability analysis was developed. Numerical results using the IEEE 14-bus, IEEE 30-bus, New England 39-bus, and IEEE 118-bus test systems are presented and discussed.*

International Conferences with review committee

Paru

CIREN 2015 - *Adaptive Weighted Least Squares-based Algorithm to Estimate Synchronized Measurements over Wide Frequency Range*
Lyon, FRANCE

R. Bhandia, **R.J. Albuquerque**, R. Caire, N. HadjSaid, D. Picault - Poster Session. *June 2015.*

IEEE PowerTech 2015 - Eindhoven *An Enhanced Adaptive Data Processing Technique for Computing Synchrophasor Measurements under Power System Frequency Variation*
NETHERLANDS

H. Almasalma, **R.J. Albuquerque**, R. Caire, N. HadjSaid - Oral presentation session. *June 2015.*

Appendix A

Discrete Fourier Transform and phasor representation

Let the input signal $y(t)$ be given by

$$y(t) = Y_m \cos(2\pi f_o t + \phi). \quad (\text{A.1})$$

Considering a data window with $\{n=0,1,2,\dots, N-1\}$ samples obtained at sampling period nT_s , Eq. (A.1) can be rewritten as

$$y[n] = Y_m \cos(2\pi f_o n T_s + \phi) = Y_m \cos\left(\frac{2\pi n}{N} + \phi\right). \quad (\text{A.2})$$

Applying the real part of the DFT for Eq. (A.2) provides

$$Y_r = \frac{\sqrt{2}}{N} \sum_{n=0}^{N-1} Y_m \cos\left(\frac{2\pi n}{N} + \phi\right) \cos\left(\frac{2\pi nk}{N}\right), \quad (k = 1) \quad (\text{A.3})$$

and using the following trigonometric identities

$$\cos(a + b) = \cos(a)\cos(b) - \sin(a)\sin(b) \quad (\text{A.4})$$

$$\sin(a)\cos(a) = \frac{1}{2}\sin(2a) \quad (\text{A.5})$$

Eq.(A.6) can be represented as follows

$$Y_r = \frac{Y_m \sqrt{2}}{N} \sum_{n=0}^{N-1} \left[\cos(\phi) \cos^2\left(\frac{2\pi n}{N}\right) - \frac{1}{2} \sin(\phi) \sin\left(\frac{4\pi n}{N}\right) \right]. \quad (\text{A.6})$$

Looking closely at Eq. (A.6) some conclusions are drawn:

$$\frac{Y_m \sqrt{2}}{2N} \sum_{n=0}^{N-1} \sin(\phi) \sin\left(\frac{4\pi n}{N}\right) = 0 \quad (\text{A.7})$$

and

$$\frac{Y_m \sqrt{2}}{N} \sum_{n=0}^{N-1} \cos(\phi) \cos^2\left(\frac{2\pi n}{N}\right) = Y_m \sqrt{2} \cos(\phi) \left[\frac{1}{N} \sum_{n=0}^{N-1} \frac{1}{2} + \frac{1}{N} \sum_{n=0}^{N-1} \frac{1}{2} \cos\left(\frac{4\pi n}{N}\right) \right] \quad (\text{A.8})$$

therefore, the first summation of the brackets is equal to $\frac{1}{2}$ and the second will be null. In

this way, Eq. (A.6) can be rewritten as

$$Y_r = \frac{Y_m\sqrt{2}}{2}\cos(\phi) = \frac{Y_m}{\sqrt{2}}\cos(\phi) \quad (\text{A.9})$$

A similar procedure may be realized for the imaginary part of the DFT, hence

$$Y_i = \frac{\sqrt{2}}{N} \sum_{n=0}^{N-1} Y_m \cos\left(\frac{2\pi n}{N} + \phi\right) \sin\left(\frac{2\pi nk}{N}\right), \quad (k=1) \quad (\text{A.10})$$

taking into account the trigonometric identities given by Eqs. (A.4)-(A.5), we have

$$Y_i = \frac{Y_m\sqrt{2}}{N} \sum_{n=0}^{N-1} \left[\frac{1}{2}\cos(\phi)\sin\left(\frac{4\pi n}{N}\right) - \sin(\phi)\sin^2\left(\frac{2\pi n}{N}\right) \right] \quad (\text{A.11})$$

once again some conclusions are drawn:

$$\frac{Y_m\sqrt{2}}{2N} \sum_{n=0}^{N-1} \cos(\phi)\sin\left(\frac{4\pi n}{N}\right) = 0 \quad (\text{A.12})$$

and

$$-\frac{Y_m\sqrt{2}}{N} \sum_{n=0}^{N-1} \sin(\phi)\sin^2\left(\frac{2\pi n}{N}\right) = -\frac{Y_m\sqrt{2}}{N}\sin(\phi) \left[\sum_{n=0}^{N-1} \frac{1}{2} - \sum_{n=0}^{N-1} \frac{1}{2}\cos\left(\frac{4\pi n}{N}\right) \right] \quad (\text{A.13})$$

therefore, the first summation is equal to $\frac{1}{2}$ and the second is null. Thereby, Eq. (A.11) can be rewritten as

$$Y_i = -\frac{Y_m\sqrt{2}}{2}\sin(\phi) = -\frac{Y_m}{\sqrt{2}}\sin(\phi). \quad (\text{A.14})$$

It is clear that the DFT can represent a phasor in terms of a limited number of samples inside a data window, providing the real and imaginary parts of the phasor, hence

$$Y_k = Y_r - jY_i. \quad (\text{A.15})$$

The mathematical formulation presented in the present appendix has been considered a nominal frequency component, i.e. $k=1$, however the estimation of the harmonic phasors ($k=2,3,\dots$) can be directly obtained.

Appendix B

Phasor estimation error due to leakage phenomenon

In order to determine the error on the synchrophasor estimate due to the pernicious leakage phenomenon let us assume the following assumptions:

- The fundamental frequency $f_o = 50$ Hz;
 - N represents the amount of samples extracted in D -cycles (being D a positive integer or positive real number);
 - The sampling frequency is given by $f_a = Nf_o/D$, thus the sampling period is $T_a = 1/f_a$.
- Let the input signal $y(t)$ be given by the complex exponential function as

$$y(t) = e^{j2\pi f_o t} \quad (\text{B.1})$$

Eq (B.1), evaluated at each sampling time nT_a , provides

$$y[nT_a] = e^{j2\pi f_o n T_a} \quad (\text{B.2})$$

where, taking into account the third assumption, leads to the following sequence

$$y[n] = e^{j2\pi f_o n \left(\frac{D}{Nf_o}\right)} = e^{j2\pi \frac{nD}{N}}, \quad (n \geq 0). \quad (\text{B.3})$$

Applying the DFT for the sampled sequence $y[n]$, gives

$$Y(k) = \sum_{n=0}^{N-1} e^{j\frac{2\pi nD}{N}} \times e^{-j\frac{2\pi nk}{N}} \quad (\text{B.4})$$

being k the frequency component. Therefore,

$$Y(k) = \sum_{n=0}^{N-1} e^{j\frac{2\pi n}{N}(D-k)}. \quad (\text{B.5})$$

Clearly, the Eq. (B.5) can be represented by a geometric series as

$$Y(k) = \sum_{n=0}^{N-1} a^n = 1 + a + a^2 + \dots + a^{N-1} = \frac{1 - a^N}{1 - a} \quad (\text{B.6})$$

thus,

$$Y(k) = \frac{1 - a^N}{1 - a} = \frac{1 - e^{j2\pi n(D-k)}}{1 - e^{j\frac{2\pi n(D-k)}{N}}} \quad (\text{B.7})$$

or,

$$Y(k) = \frac{[1 - \cos(2\pi n(D-k))] - j\sin(2\pi n(D-k))}{\left[1 - \cos\left(\frac{2\pi n(D-k)}{N}\right)\right] - j\sin\left(\frac{2\pi n(D-k)}{N}\right)}. \quad (\text{B.8})$$

Using the following trigonometric identity

$$1 - \cos(x) = 2\sin^2\left(\frac{x}{2}\right) \quad (\text{B.9})$$

Eq. (B.8) can be rewritten as

$$Y(k) = \frac{2\sin^2\left(\frac{2\pi(D-k)}{2}\right) - j\sin(2\pi(D-k))}{2\sin^2\left(\frac{2\pi(D-k)}{2N}\right) - j\sin\left(\frac{2\pi(D-k)}{N}\right)} \quad (\text{B.10})$$

that is

$$Y(k) = \frac{2\sin^2(\pi(D-k)) - j\sin(2\pi(D-k))}{2\sin^2\left(\frac{\pi(D-k)}{N}\right) - j\sin\left(\frac{2\pi(D-k)}{N}\right)}. \quad (\text{B.11})$$

Performing a division by 2 for each member of Eq. (B.11), results

$$Y(k) = \frac{\sin^2(\pi(D-k)) - j\frac{\sin(2\pi(D-k))}{2}}{\sin^2\left(\frac{\pi(D-k)}{N}\right) - j\frac{\sin\left(\frac{2\pi(D-k)}{N}\right)}{2}} \quad (\text{B.12})$$

and using the following trigonometric identity

$$\frac{1}{2}\sin(2x) = \sin(x)\cos(x) \quad (\text{B.13})$$

Eq. (B.12) can be rewritten as

$$Y(k) = \frac{\sin^2(\pi(D-k)) - j\sin(\pi(D-k)) \times \cos(\pi(D-k))}{\sin^2\left(\frac{\pi(D-k)}{N}\right) - j\sin\left(\frac{\pi(D-k)}{N}\right) \times \cos\left(\frac{\pi(D-k)}{N}\right)} \quad (\text{B.14})$$

resulting

$$Y(k) = \frac{[\sin(\pi(D-k)) - j\cos(\pi(D-k))] \times \sin(\pi(D-k))}{[\sin\left(\frac{\pi(D-k)}{N}\right) - j\cos\left(\frac{\pi(D-k)}{N}\right)] \times \sin\left(\frac{\pi(D-k)}{N}\right)}. \quad (\text{B.15})$$

Multiplying the Eq. (B.15) by the j operator, gives

$$Y(k) = \frac{[\cos(\pi(D-k)) + j\sin(\pi(D-k))] \times \sin(\pi(D-k))}{[\cos\left(\frac{\pi(D-k)}{N}\right) + j\sin\left(\frac{\pi(D-k)}{N}\right)] \times \sin\left(\frac{\pi(D-k)}{N}\right)} \quad (\text{B.16})$$

therefore,

$$Y(k) = \frac{e^{j\pi(D-k)}}{e^{j\frac{\pi(D-k)}{N}}} \times \frac{\sin(\pi(D-k))}{\sin\left(\frac{\pi(D-k)}{N}\right)}. \quad (\text{B.17})$$

Multiplying the numerator and the denominator of Eq. (B.17) by the following unitary factors $\frac{\pi(D-k)}{\pi(D-k)}$ and $\frac{\frac{\pi(D-k)}{N}}{\frac{\pi(D-k)}{N}}$, respectively, and performing a regrouping of the equation terms, provides

$$Y(k) = N \frac{e^{j\pi(D-k)} \frac{\sin(\pi(D-k))}{\pi(D-k)}}{e^{j\frac{\pi(D-k)}{N}} \frac{\sin\left(\frac{\pi(D-k)}{N}\right)}{\frac{\pi(D-k)}{N}}} \quad (\text{B.18})$$

where,

$$\text{sinc}(x) = \frac{\sin(x)}{x} \quad (\text{B.19})$$

hence,

$$Y(k) = N \times \frac{\text{sinc}(\pi(D-k))}{\text{sinc}\left(\frac{\pi(D-k)}{N}\right)} \times e^{j\pi(D-k)(1-1/N)}. \quad (\text{B.20})$$

Eq. (B.20) can be found in [25]. This equation shows that when the input signal frequency changes from f_o Hz to $(f_o \pm \Delta f)$ Hz, the obtained phasor undergoes two modifications caused by the magnitude and phase angle factors. Generally, the magnitude factor could be negligible because the frequency deviation will cause a barely perceptible variation on the magnitude estimate. Let the true system frequency be given by $f_m = 51$ Hz, a frequency component equal to $k = 1$ (fundamental frequency), and using $N=256$ samples by cycle, the effect of magnitude leakage in the phasor estimation into one observation window will be

$$\left[\frac{\text{sinc}(\pi(1.02-1))}{\text{sinc}\left(\frac{\pi(1.02-1)}{256}\right)} \right] = 0.9935 \quad (\text{B.21})$$

The parameter $D=1.02$ into the brackets of Eq. (B.21) represents a fractional cycle inside the observation window (51 Hz/50 Hz). Based on this assumption, one can observe that the amount of samples within the observation window will not necessarily impact on the magnitude factor. It is important to mention that the same result can be found for a system frequency of 49 Hz taking into account a fractional cycle of 0.98. Fig. B.1(a) would lead us to believe that the curves of the magnitude factor response to each frequency are overlapped, however, the zoomed Fig. B.1(b) shows the expected effect of shifting between them related to the fractional cycles (asynchronous sampling condition).

When $D > 1$ the curve shifts to the right and to the left when $D < 1$ being the displacement proportional to the frequency deviation from nominal frequency. The displayed magnitude leakage data point represents the real value of the magnitude estimate of $X(1)$, in which it could be obtained performing a multiplication between the correct magnitude, given by N in Eq. (B.20), and the obtained value in Eq. (B.21). In theory, even performing a recursive DFT-based phasor estimation, the magnitude attenuation (varying with time) could be disregarded, however, for practical applications, the leakage phenomenon introduces a second harmonic component that yields oscillations over the magnitude estimate varying with time, as shown in Subsection I.8.b.

Unfortunately, all prerogatives cited above are not applied in a straightforward manner for the phase angle factor because it is far more sensitive to the frequency deviation. For a system frequency at 51 Hz, the phase angle error is given by

$$\pi(1.02-1) \left(1 - \frac{1}{256} \right) = 0.06259 \text{ rad} \approx 3.58^\circ \quad (\text{B.22})$$

in which a symmetric value can be found for a system frequency of 49 Hz. Fig. B.2(a) shows the phase angle factor linear response, and the zoomed Fig. B.2(b) displays that the frequency deviations will shift the phase leakage data point to up when $D > 1$ and to down when $D < 1$, being also the displacement proportional to the frequency deviation

from nominal frequency. Applying a recursive DFT algorithm the phase angle to each recursive computation will depend upon the frequency deviation and the recursion order, therefore the result is a phasor estimate that rotates one complete circle per second in the complex plane. For a constant input signal frequency of 51 Hz the phasor rotates in the counterclockwise direction, whereas for 49 Hz the phasor rotates in a clockwise direction. As mentioned in the first chapter of this thesis, the sensibility of the phase angle estimate has been employed for accurate frequency estimation.

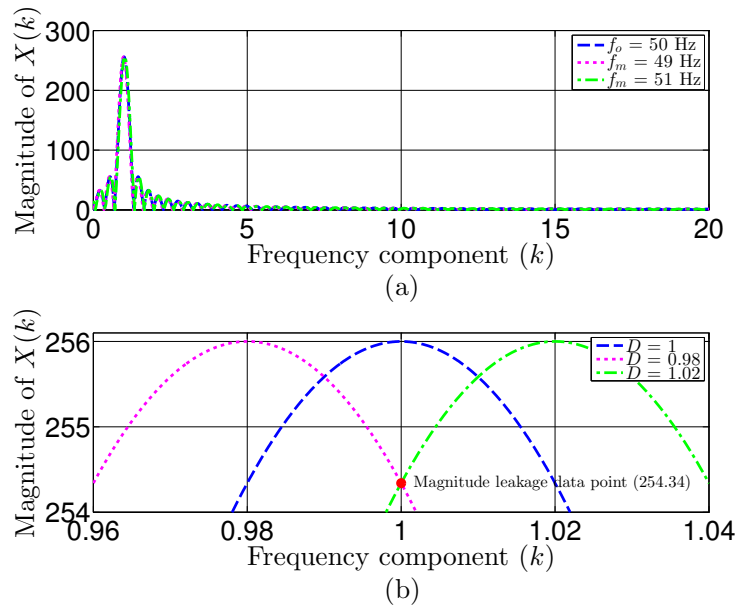


Figure B.1: (a) Magnitude factor response at 50 ± 1 Hz; (b) Zoomed view around $k=1$ to track the magnitude leakage data point.

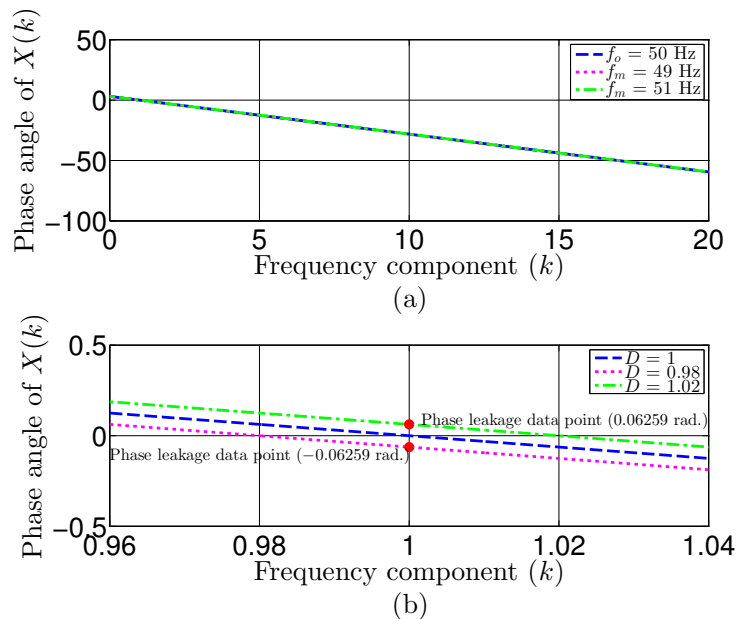


Figure B.2: (a) Phase angle factor response at 50 ± 1 Hz; (b) Zoomed view around $k=1$ to track the phase leakage data point.

Appendix C

Classical method for estimating fundamental positive-sequence phasor

The Fortescue's theorem states that any unbalanced three-phase system of vectors (voltage or current) may be represented into three balanced system of vectors called symmetrical components [84]. The balanced systems that compose the symmetrical components are termed as *positive-sequence system* (same sense of rotation as the original unbalanced system), *negative-sequence system* (opposite sense of rotation) and *zero-sequence* (vectors equal in magnitude and having the same phase position with respect to a given reference axis) [10], as illustrated in Fig. C.1.

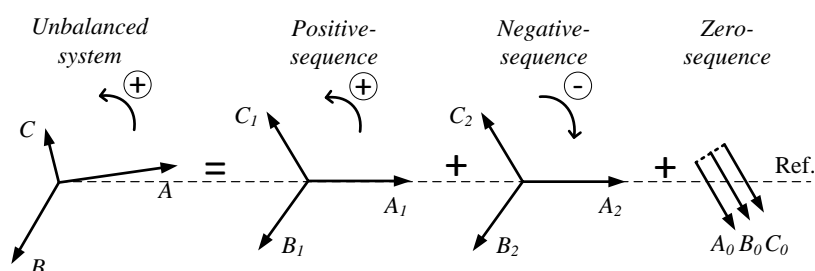


Figure C.1: Unbalanced three-phase system of vectors together with their symmetrical components.

Taking into account an unbalanced three-phase voltages system, the Fortescue's theorem can be written as follows

$$\begin{cases} V_A = V_{A0} + V_{A1} + V_{A2} \\ V_B = V_{B0} + V_{B1} + V_{B2} \\ V_C = V_{C0} + V_{C1} + V_{C2} \end{cases} \quad (\text{C.1})$$

in this way, performing some manipulations using the $a = 1\angle 120^\circ$ rotating operator, it is possible to solve the linear system (C.1) with respect to any symmetrical component. In order to exemplify this statement, let us consider the V_{A1} component. For this, the following identities are carried out: $V_{A0} = V_{B0} = V_{C0}$, $V_{B1} = a^2 V_{A1}$, $V_{C1} = a V_{A1}$, $V_{B2} = a V_{A2}$, and $V_{C2} = a^2 V_{A2}$. Hence, the linear system may be rewritten as (C.2), however, the second and third equations must be multiplied by a and a^2 in order to eliminate the zero and negative-sequence components, therefore

$$\begin{cases} V_A = V_{A0} + V_{A1} + V_{A2} \\ (V_B = V_{A0} + a^2V_{A1} + aV_{A2}) \times a \\ (V_C = V_{A0} + aV_{A1} + a^2V_{A2}) \times a^2 \end{cases} \quad (\text{C.2})$$

the resulting equation is given by

$$(V_a + aV_B + a^2V_C) = (1 + a + a^2)V_{A0} + 3V_{A1} + (1 + a + a^2)V_{A2} \quad (\text{C.3})$$

one can notice that the factor $(1+a+a^2)$ is null, thereby, the equation that describes the V_{A1} component is given by

$$V_{A1} = \frac{1}{3} (V_A + aV_B + a^2V_C) \quad (\text{C.4})$$

once calculated V_{A1} the other phasors V_{B1} and V_{C1} may be determined performing the following identities $V_{B1} = a^2V_{A1}$ and $V_{C1} = aV_{A1}$.

In [25], the recursive computation of positive-sequence component of three-phase signals is properly developed. Let us recall the procedure proposed in this reference through an example. Consider a constant input three-phase signals at the nominal frequency of the power system 50-Hz. The signals are sampled at a rate of 1800 Hz ($N=36$ samples by period of the fundamental frequency). In this case, the sampling angle is equal to $\theta=10^\circ$ ($360^\circ/36$). Recalling the recursive updating given by Eq. (I.95) and looking closely Eq. (C.4), the recursive updating of the component V_{A1} is given by

$$\begin{aligned} \hat{V}_{A1}^{N+r} &= \hat{V}_{A1}^{N+r-1} + \frac{\sqrt{2}}{3N} ((V_A(N+r) - V_A(r))e^{-j(r-1)\theta} \\ &+ (V_B(N+r) - V_B(r))e^{-j(12+r)\theta} + (V_C(N+r) - V_C(r))e^{-j(24+r)\theta}) \end{aligned} \quad (\text{C.5})$$

where r is the recursion index and the numbers 12 and 24 give the envisage phase shifts to comply with Eq.(C.4). Other components of voltage may be calculated in a similar manner for both balanced and unbalanced original three-phase systems.

Appendix D

Park's transformation-based fundamental positive-sequence phasor

In the present Appendix, the equations based on the Park's transformation for estimating fundamental-positive sequence phasor under specific scenarios particularly found in active distribution grids are outlined. The analyzed scenarios include balanced and unbalanced signals at nominal and off-nominal power frequency. In order to determine the equations let us consider the following assumptions:

- The nominal angular frequency $\omega_o = 2\pi f_o$;
- The off-nominal angular frequency $\omega = \omega_o + \Delta\omega$
- The sampling angle $\theta = \frac{2\pi}{N}$ (being N the number of samples inside a data window)
- The sampling period $T_s = \frac{1}{N \times f_o}$

Balanced input signal at nominal frequency

Let the sampled three-phase voltage input signal be given by

$$e_a(rT_s) = E_m \cos(\omega_o r T_s + \phi) \quad (\text{D.1})$$

$$e_b(rT_s) = E_m \cos(\omega_o r T_s + \phi - 120^\circ) \quad (\text{D.2})$$

$$e_c(rT_s) = E_m \cos(\omega_o r T_s + \phi + 120^\circ). \quad (\text{D.3})$$

being r the sample number or recursion index. Replacing Eqs. (D.1)-(D.3) into the Park's transformation equations given by

$$s_d = \kappa (e_a \cos(\theta) + e_b \cos(\theta - 120^\circ) + e_c \cos(\theta + 120^\circ)) \quad (\text{D.4})$$

$$s_q = -\kappa (e_a \sin(\theta) + e_b \sin(\theta - 120^\circ) + e_c \sin(\theta + 120^\circ)) \quad (\text{D.5})$$

the abc/dq transformation can be accomplished, hence

$$s_{d_r} = \kappa [E_m \cos(\omega_o r T_s + \phi) \cos(r\theta) + E_m \cos(\omega_o r T_s + \phi - 120^\circ) \cos(r\theta - 120^\circ) + E_m \cos(\omega_o r T_s + \phi + 120^\circ) \cos(r\theta + 120^\circ)] \quad (\text{D.6})$$

$$s_{q_r} = -\kappa [E_m \cos(\omega_o r T_s + \phi) \sin(r\theta) + E_m \cos(\omega_o r T_s + \phi - 120^\circ) \sin(r\theta - 120^\circ) + E_m \cos(\omega_o r T_s + \phi + 120^\circ) \sin(r\theta + 120^\circ)]. \quad (\text{D.7})$$

Using the following trigonometric identities

$$\cos(a)\cos(b) = \frac{1}{2} (\cos(a - b) + \cos(a + b)) \quad (\text{D.8})$$

$$\cos(a)\sin(b) = \frac{1}{2}(\sin(a+b) - \sin(a-b)) \quad (\text{D.9})$$

Eqs. (D.6)-(D.7) can be rewritten as

$$s_{d_r} = \frac{\kappa E_m}{2} [\cos(\omega_o r T_s + \phi - r\theta) + \cos(\omega_o r T_s + \phi + r\theta) + \cos(\omega_o r T_s + \phi - r\theta) \quad (\text{D.10}) \\ + \cos(\omega_o r T_s + \phi - 240^\circ + r\theta) + \cos(\omega_o r T_s + \phi - r\theta) + \cos(\omega_o r T_s + \phi + 240^\circ + r\theta)]$$

$$s_{q_r} = -\frac{\kappa E_m}{2} [\sin(\omega_o r T_s + \phi + r\theta) - \sin(\omega_o r T_s + \phi - r\theta) - \sin(\omega_o r T_s + \phi - r\theta) \quad (\text{D.11}) \\ - \sin(\omega_o r T_s + \phi - r\theta) + \sin(\omega_o r T_s + \phi + 240^\circ + r\theta) + \sin(\omega_o r T_s + \phi - 240^\circ + r\theta)].$$

Regrouping the terms yields

$$s_{d_r} = \frac{\kappa E_m}{2} [3\cos(\omega_o r T_s + \phi - r\theta) + \cos(\omega_o r T_s + \phi + r\theta) \quad (\text{D.12}) \\ + \cos(\omega_o r T_s + \phi - 240^\circ + r\theta) + \cos(\omega_o r T_s + \phi + 240^\circ + r\theta)]$$

$$s_{q_r} = \frac{\kappa E_m}{2} [3\sin(\omega_o r T_s + \phi - r\theta) - \sin(\omega_o r T_s + \phi + r\theta) \quad (\text{D.13}) \\ - \sin(\omega_o r T_s + \phi - 240^\circ + r\theta) - \sin(\omega_o r T_s + \phi + 240^\circ + r\theta)]$$

Looking closely at Eqs. (D.12)-(D.13) one can observe that

$$\cos(\omega_o r T_s + \phi + r\theta) + \cos(\omega_o r T_s + \phi - 240^\circ + r\theta) \quad (\text{D.14})$$

$$+ \cos(\omega_o r T_s + \phi + 240^\circ + r\theta) = 0$$

$$- (\sin(\omega_o r T_s + \phi + r\theta) + \sin(\omega_o r T_s + \phi - 240^\circ + r\theta) \quad (\text{D.15})$$

$$+ \sin(\omega_o r T_s + \phi + 240^\circ + r\theta)) = 0$$

hence, Eqs. (D.12)-(D.13) can be rewritten in a compact form as follows

$$s_{d_r} = \frac{3\kappa E_m}{2} \cos(\omega_o r T_s + \phi - r\theta) \quad (\text{D.16})$$

$$s_{q_r} = \frac{3\kappa E_m}{2} \sin(\omega_o r T_s + \phi - r\theta). \quad (\text{D.17})$$

All analyzes presented in the present Appendix use the κ coefficient equal to $\frac{\sqrt{2}}{3}$ aiming to transfer the RMS information of the three-phase signal to the dq -components. Due to the sampling clock be matched to the nominal power frequency the real and imaginary parts of the fundamental positive-sequence phasor may be directly obtained according to

$$s_{d_r} = \frac{E_m}{\sqrt{2}} \cos(\phi) \quad (\text{D.18})$$

$$s_{q_r} = \frac{E_m}{\sqrt{2}} \sin(\phi). \quad (\text{D.19})$$

Balanced input signal at off-nominal frequency

For the current scenario the previous analysis may be taken into account. For this, it is

only need to replace ω_o by ω into Eqs. (D.16)-(D.17), thus

$$s_{d_r} = \frac{E_m}{\sqrt{2}} \cos(\omega r T_s + \phi - r\theta) = \frac{E_m}{\sqrt{2}} \cos((\omega_o + \Delta\omega)r T_s + \phi - r\theta) \quad (\text{D.20})$$

$$s_{q_r} = \frac{E_m}{\sqrt{2}} \sin(\omega r T_s + \phi - r\theta) = \frac{E_m}{\sqrt{2}} \sin((\omega_o + \Delta\omega)r T_s + \phi - r\theta). \quad (\text{D.21})$$

Keeping in mind that the sampling clock and the power frequency are matched, one can reduce Eqs. (D.20)-(D.21) as follows

$$s_{d_r} = \frac{E_m}{\sqrt{2}} \cos(\Delta\omega r T_s + \phi) \quad (\text{D.22})$$

$$s_{q_r} = \frac{E_m}{\sqrt{2}} \sin(\Delta\omega r T_s + \phi) \quad (\text{D.23})$$

clearly, it can be seen that the real and imaginary parts of the phasor rotates according to the frequency deviation, as has been shown in Subsection I.8.b using DFT.

Unbalanced input signal at nominal frequency

Let the sampled unbalanced three-phase voltage input signal be given by

$$e_a(r T_s) = E_{m_a} \cos(\omega_o r T_s + \phi_a) \quad (\text{D.24})$$

$$e_b(r T_s) = E_{m_b} \cos(\omega_o r T_s + \phi_b - 120^\circ) \quad (\text{D.25})$$

$$e_c(r T_s) = E_{m_c} \cos(\omega_o r T_s + \phi_c + 120^\circ). \quad (\text{D.26})$$

One can note that the unbalanced concerns both amplitude and phase angle of the three-phase signal. Therefore, replacing Eqs. (D.24)-(D.25) into Eqs. (D.4)-(D.5) we can find generalized equations as given below

$$s_{d_r} = \frac{\sqrt{2}}{6} (E_{m_a} [\cos(\omega_o r T_s + \phi_a - r\theta) + \cos(\omega_o r T_s + \phi_a + r\theta)] \quad (\text{D.27})$$

$$+ E_{m_b} [\cos(\omega_o r T_s + \phi_b - r\theta) + \cos(\omega_o r T_s + \phi_b - 240^\circ + r\theta)]$$

$$+ E_{m_c} [\cos(\omega_o r T_s + \phi_c - r\theta) + \cos(\omega_o r T_s + \phi_c + 240^\circ + r\theta)])$$

$$s_{q_r} = -\frac{\sqrt{2}}{6} (E_{m_a} [\sin(\omega_o r T_s + \phi_a + r\theta) - \sin(\omega_o r T_s + \phi_a - r\theta)] \quad (\text{D.28})$$

$$+ E_{m_b} [\sin(\omega_o r T_s + \phi_b - 240^\circ + r\theta) - \sin(\omega_o r T_s + \phi_b - r\theta)]$$

$$+ E_{m_c} [\sin(\omega_o r T_s + \phi_c + 240^\circ + r\theta) - \sin(\omega_o r T_s + \phi_c - r\theta)])$$

Once again assuming a sampling clock matched with the power frequency Eqs. (D.27)-(D.28) can be rewritten in a compact form as follows

$$s_{d_r} = \frac{\sqrt{2}}{6} (E_{m_a} [\cos(\phi_a) + \cos(2\omega_o r T_s + \phi_a)] \quad (\text{D.29})$$

$$+ E_{m_b} [\cos(\phi_b) + \cos(2\omega_o r T_s + \phi_b - 240^\circ)]$$

$$+ E_{m_c} [\cos(\phi_c) + \cos(2\omega_o r T_s + \phi_c + 240^\circ)])$$

$$\begin{aligned}
s_{q_r} = & \frac{\sqrt{2}}{6} (E_{m_a} [\sin(\phi_a) - \sin(2\omega_o r T_s + \phi_a)] \\
& + E_{m_b} [\sin(\phi_b) - \sin(2\omega_o r T_s + \phi_b - 240^\circ)] \\
& + E_{m_c} [\sin(\phi_c) - \sin(2\omega_o r T_s + \phi_c + 240^\circ)])
\end{aligned} \tag{D.30}$$

Regardless of the type of unbalance (magnitude, phase angle, or both), it can be seen that the real and imaginary parts of the fundamental positive-sequence phasor is distorted by a 2th harmonic component.

Unbalanced input signal at off-nominal frequency

The generalized equations concerning unbalanced input signal at off-nominal frequency can be obtained just replacing ω_o in Eqs. (D.27)-(D.28) by ω , hence

$$\begin{aligned}
s_{d_r} = & \frac{\sqrt{2}}{6} (E_{m_a} [\cos((\omega_o + \Delta\omega)r T_s + \phi_a - r\theta) + \cos((\omega_o + \Delta\omega)r T_s + \phi_a + r\theta)] \\
& + E_{m_b} [\cos((\omega_o + \Delta\omega)r T_s + \phi_b - r\theta) + \cos((\omega_o + \Delta\omega)r T_s + \phi_b - 240^\circ + r\theta)] \\
& + E_{m_c} [\cos((\omega_o + \Delta\omega)r T_s + \phi_c - r\theta) + \cos((\omega_o + \Delta\omega)r T_s + \phi_c + 240^\circ + r\theta)])
\end{aligned} \tag{D.31}$$

$$\begin{aligned}
s_{q_r} = & -\frac{\sqrt{2}}{6} (E_{m_a} [\sin((\omega_o + \Delta\omega)r T_s + \phi_a + r\theta) - \sin((\omega_o + \Delta\omega)r T_s + \phi_a - r\theta)] \\
& + E_{m_b} [\sin((\omega_o + \Delta\omega)r T_s + \phi_b - 240^\circ + r\theta) - \sin((\omega_o + \Delta\omega)r T_s + \phi_b - r\theta)] \\
& + E_{m_c} [\sin((\omega_o + \Delta\omega)r T_s + \phi_c + 240^\circ + r\theta) - \sin((\omega_o + \Delta\omega)r T_s + \phi_c - r\theta)])
\end{aligned} \tag{D.32}$$

therefore, Eqs. (D.31)-(D.32) can be rewritten as follows

$$\begin{aligned}
s_{d_r} = & \frac{\sqrt{2}}{6} (E_{m_a} [\cos(\Delta\omega r T_s + \phi_a) + \cos(2\omega_o r T_s + \Delta\omega r T_s + \phi_a)] \\
& + E_{m_b} [\cos(\Delta\omega r T_s + \phi_b) + \cos(2\omega_o r T_s + \Delta\omega r T_s + \phi_b - 240^\circ)] \\
& + E_{m_c} [\cos(\Delta\omega r T_s + \phi_c) + \cos(2\omega_o r T_s + \Delta\omega r T_s + \phi_c + 240^\circ)])
\end{aligned} \tag{D.33}$$

$$\begin{aligned}
s_{q_r} = & \frac{\sqrt{2}}{6} (E_{m_a} [\sin(\Delta\omega r T_s + \phi_a) - \sin(2\omega_o r T_s + \Delta\omega r T_s + \phi_a)] \\
& + E_{m_b} [\sin(\Delta\omega r T_s + \phi_b) - \sin(2\omega_o r T_s + \Delta\omega r T_s + \phi_b - 240^\circ)] \\
& + E_{m_c} [\sin(\Delta\omega r T_s + \phi_c) - \sin(2\omega_o r T_s + \Delta\omega r T_s + \phi_c + 240^\circ)]) .
\end{aligned} \tag{D.34}$$

It is possible to see that this is the worst scenario because the real and imaginary phasor components will be distorted by a 2th harmonic component combined with an angular velocity related to the frequency deviation.

Appendix E

Feeder's data of the distribution grid model

In the present Appendix, the feeder's data of the distribution grid model of 18 nodes are presented. Tables E.1-E.2 show the bus and branch data for the base case, respectively. The tension base is equal to 20 kV and the power base is 1 MVA. The total impedance value (resistance and reactance) of each section has been directly represented in Table E.2. The feeder's data have been modified and adapted of the reference [106]. Below, one can find the definition of each parameter taking into account the IEEE Common Data Format (CDF).

- Type: 0 - Unregulated (load, PQ) and 3 - Hold voltage and angle (V-Theta)
- P_L : active power at the load point
- Q_L : reactive power at the load point
- P_G : active power generated
- Q_G : active power generated

Table E.1: Bus data

Bus	Type	P_L (pu)	Q_L (pu)	P_G (pu)	Q_G (pu)
1	3	0	0	3.6026	1.5403
2	0	1.229	0.505	0	0
3	0	0.080	0.039	0	0
4	0	0.036	0.017	0	0
5	0	0.671	0.325	0	0
6	0	0.176	0.085	0	0
7	0	0.064	0.031	0	0
8	0	0.266	0.129	0	0
9	0	0.072	0.035	0	0
10	0	0.108	0.052	0	0
11	0	0.124	0.060	0	0
12	0	0.028	0.014	0	0
13	0	0.158	0.024	0	0
14	0	0.136	0.064	0	0
15	0	0.098	0.022	0	0
16	0	0.078	0.012	0	0
17	0	0.101	0.032	0	0
18	0	0.118	0.025	0	0

Table E.2: Branch data

Bus (from)	Bus (to)	R (pu)	jX (pu)
1	2	0.000275	0.000353
2	3	0.002943	0.003773
3	4	0.003035	0.003891
4	5	0.000882	0.001132
5	6	0.000278	0.000254
5	9	0.001306	0.001674
6	7	0.000973	0.000890
7	8	0.002085	0.001908
9	10	0.001195	0.001533
9	13	0.007089	0.003536
10	11	0.006827	0.003405
11	12	0.003827	0.002105
13	14	0.006827	0.004505
14	15	0.002527	0.003205
15	16	0.004118	0.005125
16	17	0.001881	0.002334
17	18	0.001121	0.001212
8	12	–	–

UNITÉS DE MESURE DE PHASEUR DANS LE CADRE DES RÉSEAUX DE DISTRIBUTION ÉLECTRIQUE INTELLIGENTS

Résumé: Une infrastructure robuste de surveillance basée sur des mesures numériques classiques est souvent utilisée pour permettre une gestion efficace du réseau de distribution électrique, néanmoins les mesures de phaseurs synchronisés, également connu comme synchrophaseurs, sont particulièrement efficaces pour améliorer la capacité de gestion et la surveillance de ces réseaux. Le synchrophaseur est un phaseur numériquement calculé à partir des échantillons de données en utilisant une source temporelle absolue pour un horodatage extrêmement précis des mesures effectuées.

De ce fait, les applications des synchrophaseurs sont très nombreuses dans les réseaux électriques, en particulier dans les réseaux de transport. Ils permettent notamment de mesurer la différence angulaire entre les noeuds, l'estimation d'état linéaire, détecter l'îlotage, mesurer la stabilité oscillatoire, et détecter et identifier les défauts. Ainsi, nous pourrions être amenés à croire que pour apporter les avantages bien connus des mesures synchronisées vers les réseaux de distribution électriques, il serait seulement nécessaire de placer les Unités de Mesure de Phaseur, également connu par l'abréviation anglophone PMU, d'une manière directe dans l'environnement de la distribution électrique. Malheureusement, cette tâche n'est pas aussi évidente qu'elle n'y paraît.

Les réseaux de distribution électriques et les réseaux de transport ont des caractéristiques opérationnelles différentes, donc les PMUs dédiées aux réseaux de distribution doivent avoir des caractéristiques différentes de celles consacrées aux réseaux haute tension. Les réseaux de distribution intelligents possèdent des longueurs de ligne plus courtes en produisant une ouverture angulaire plus petite entre les noeuds adjacents. En outre, le contenu harmonique élevé et la déviation en fréquence imposent aussi des défis pour l'estimation des phaseurs. Les appareils synchronisés avancés dédiés pour la surveillance du réseau de distribution doivent surmonter ces défis afin de mener la précision des mesures au-delà des exigences actuelles.

Cette problématique globale est traitée et évaluée dans la présente thèse. La précision de l'estimation de phaseur est directement liée à la performance de l'algorithme utilisé pour traiter les données. Une grande robustesse contre les effets pernicioeux qui peuvent dégrader la qualité des estimations est fortement souhaitée. De ce fait, trois algorithmes adaptifs en fréquence sont présentés en visant l'amélioration du processus d'estimation des mesures de phaseurs dans les réseaux de distribution actifs. Plusieurs simulations en utilisant des signaux corrompus sont réalisées pour évaluer leurs performances dans des conditions statiques et/ou dynamiques.

Prenant en compte l'estimation précise des phaseurs, quatre applications potentielles sont présentées pour augmenter la perception, la compréhension et la projection des actions dans les réseaux de distribution. Des contributions sont apportées concernant le circuit équivalent de Thévenin vu par le point de couplage commun (PCC) entre la production décentralisée et les réseaux de distribution. Des contributions sont également apportées pour les équivalents dynamiques externes et l'évaluation de la chute de tension dans les réseaux moyenne-tension radiaux, ainsi que l'évaluation de la problématique des harmoniques pour l'amélioration de la méthode classique nommée PH (puissance active harmonique) pour détecter à la fois la principale source de pollution harmonique et le vrai flux de puissance harmonique sous déviation en fréquence.

Le sujet des mesures de phaseurs synchronisés dans le réseaux électrique de distribution est encore peu exploré et les questionnements quant à son applicabilité sont communs, néanmoins cette thèse vise à fournir des propositions pour contribuer à l'avènement de mesures de phaseurs dans l'environnement de la distribution électrique.

Mots clés *Synchrophaseur; Unités de Mesure de Phaseur; Réseaux de distribution électrique intelligent; Algorithmes adaptifs en fréquence; Applications.*

PHASOR MEASUREMENT UNITS IN ACTIVE POWER DISTRIBUTION SYSTEMS

Abstract: Robust metering infrastructure based on classical digital measurements has been used to enable a comprehensive power distribution network management, however synchronized phasor measurements, also known as synchrophasors, are especially welcome to improve the overall framework capabilities. Synchrophasor is a phasor digitally computed from data samples using an absolute and accuracy time source as reference. In this way, since the absolute time source has sufficient accuracy to synchronize voltage and current measurements at geographically distant locations it is possible to extract valuable informations of the real grid operating status without full knowledge of its characteristics.

Due to this fact, applications of synchronized phasor measurements in wide-area management systems (WAMSs) have been achieved. Angular separation, linear state estimation, islanding detection, oscillatory stability, and disturbance location identification are some of the several applications that have been proposed. Thus, we could be lead to believe that to bring the well-known benefits of the synchronized measurements toward electric distribution grids it is only required to place in a straightforward manner conventional Phasor Measurement Units (PMUs) into the electric distribution environment. Unfortunately, this is not as simple as it seems.

Electric power distribution systems and high-voltage power systems have different operational characteristics, hence PMUs or PMU-enabled IEDs dedicated to distribution systems should have different features from those devoted to the high-voltage systems. Active distribution grids with shorter line lengths produce smaller angular aperture between their adjacent busbars. In addition, high harmonic content and frequency deviation impose more challenges for estimating phasors. Generally, frequency deviation is related to high-voltage power systems, however, due to the interconnected nature of the overall power system, frequency deviation can be propagated toward the distribution grid. The integration of multiple high-rate DERs with poor control capabilities can also impose local frequency drift. Advanced synchronized devices dedicated to smart monitoring framework must overcome these challenges in order to lead the measurement accuracy beyond the levels stipulated by current standard requirements.

This overall problematic is treated and evaluated in the present thesis. Phasor estimation accuracy is directly related to the algorithm's performance used for processing the incoming data. Robustness against pernicious effects that can degrade the quality of the estimates is highly desired. Due to this fact, three frequency-adaptive algorithms are

presented aiming to boost the phasor estimation process in active distribution grids. Several simulations using spurious and distorted signals are performed for evaluating their performances under static and/or dynamic conditions.

Taking into account accurate phasor estimates, four potential applications are presented seeking to increase situational awareness in distribution environment. Contributions are presented concerning online Thévenin's equivalent (TE) circuit seen by the Point of Common Coupling (PCC) between DERs and the grid side, dynamic external equivalents and online three-phase voltage drop assessment in primary radial distribution grids, as well as assessment of harmonic issues for improving the classical PH method (harmonic active power) to detect both the main source of harmonic pollution and true power flow direction under frequency deviation.

The issue of synchronized phasor measurements in electric power distribution systems is still underexplored and suspicions about its applicability are common, however this thesis aims to provide propositions to contribute with the advent of phasor measurements in electric distribution environment.

Keywords *Synchrophasor; Phasor Measurement Units; Active power distribution systems; Frequency-adaptive algorithms; Applications.*